Semiconductor Metal Oxide Based Gas Sensors Towards Monitoring of Environment and Human Health

Thesis submitted for fulfilment of the degree of

Doctor of Philosophy in Science

To

Department of Physics

Jadavpur University

By

Subhajit Mojumder

Registration no: SOPHY1110521

Date – 23.11.2021

Functional Materials and Devices Division

CSIR-Central Glass and Ceramic Research Institute

Jadavpur, Kolkata-700 032, India

August, 2024

Dedicated to my beloved parents

CERTIFICATE FROM THE SUPERVISOR

This is to certify that the thesis entitled "***Semiconductor Metal Oxide Based Gas Sensors Towards Monitoring of Environment and Human Health***" submitted by Mr. Subhajit Mojumder (Registration no: **SOPHY1110521** and Index no: **105/21/Phys./27**) who got his name registered on 23rd November 2021 for the award of Ph.D. (Science) degree of Jadavpur University, is absolutely based upon his own work under the supervision of Dr. Mrinal Pal, Chief Scientist, Functional Materials and Devices Division, CSIR- Central Glass and Ceramic Research Institute (CGCRI), Kolkata, West Bengal-700032, India and that neither this thesis nor any part of it has been submitted for either any degree/diploma or any other academic award anywhere before.

Mrinal Pal

Dr. Mrinal Pal 28/8/24

Chief Scientist & Head

Functional Materials and Devices Division

CSIR-Central Glass and Ceramic Research Institute

Jadavpur, Kolkata-700 032,

India

Dr. Mrinal Pal
Chief Scientist & Head
Functional Materials and Devices Division
CSIR-Central Glass & Ceramic Research Institute
Kolkata- 700 032

DECLARATION

This is to declare that the thesis entitled '***Semiconductor Metal Oxide Based Gas Sensors Towards Monitoring of Environment and Human Health"*** submitted by Mr. Subhajit Mojumder (Registration no: **SOPHY1110521** and Index no: **105/21/Phys./27**) to Jadavpur University , Kolkata, India in partial fulfilment for the award of the degree of Doctor of Philosophy is a record of work carried out by me at CSIR-Central Glass and Ceramic Research Institute, Jadavpur, Kolkata, India. The work, in full or in parts, has not been submitted to any other University/Institute for the award of any other degree. Any information/material used in the thesis from external sources has been appropriately acknowledged.

Subhajit Mojumder 28/08/24

Mr. Subhajit Mojumder
Functional Materials and Devices Division
CSIR-Central Glass and Ceramic Research Institute
Jadavpur, Kolkata-700 032,
India

Acknowledgments

At this significant juncture, I must first acknowledge my department. I feel truly blessed to have had the opportunity to conduct my Ph.D. research here, which has been both enjoyable and challenging, as well as immensely valuable. I would like to express my deepest gratitude to my supervisor, Dr. Mrinal Pal, who is also the head of my division (Functional Materials and Device Division, CSIR-CGCRI). I am extremely fortunate to have him as my advisor and mentor, and I am delighted to thank him sincerely for his exceptional supervision and support. The time and guidance he provided throughout my Ph.D. study are invaluable. He consistently supported and assisted me, regardless of my circumstances, throughout my entire Ph.D. tenure. I am particularly grateful to him for granting me the freedom to pursue my work during my Ph.D. research. I would like to extend my immense gratitude to Dr. Srabanti Ghosh (Sr. Pr. Scientist, CSIR-CGCRI), for her valuable suggestions, guidance and help throughout my entire Ph.D. journey. I would like to express my deep gratitude to Dr. Debdulal Saha (Principal Scientist, CSIR-CGCRI), Dr. Swastik Mondal (Senior Principal Scientist, CSIR-CGCRI), and Chandan Kumar Ghosh (Assistant Professor, Jadavpur University, India) for their invaluable suggestions and support throughout my Ph.D. journey.

I would like to express my gratitude to Dr. K. Muraleedharan (former Director, CSIR-CGCRI) and Dr. Suman Kumari Mishra (current Director, CSIR-CGCRI) for providing me with the opportunity to pursue my Ph.D. at this esteemed institute, equipped with its advanced facilities. I am extremely thankful to the Head of the Department of Physics at Jadavpur University for allowing me to register in their department. I also wish to acknowledge all the faculty members of this department who introduced me to various aspects of research topics during the coursework. Additionally, I am very grateful to Dr. Sunirmal Jana, Chief Scientist of the Specialty Glass Division at CSIR-CGCRI, for offering valuable suggestions as a member of the RAC committee during my Ph.D. work.

I would like to extend my heartfelt gratitude to my lab met and co-author Tanushri Das, for her invaluable contributions to my entire research in CGCRI. I am deeply appreciative of her insightful inputs, meticulous review, and unwavering support throughout the entire research process. It gives me great pleasure to express my gratitude to my senior fellows Dr. Nirman Chakraborty, Dr. Sagnik Das, and Dr. Navonil Bose for their invaluable discussions. They have

been a tremendous help to me in every situation, and I deeply appreciate their support. I am also thankful to all my junior and colleagues Sanjib, Prantik, Krishnendu, Saibal, Debal, Kamalesh, Sourav, and Pratyasha for their selfless assistance.

I now wish to extend my deepest gratitude to my Maa and Baba for their unwavering support. I also want to thank my sister, Parnika, and brother-in-law, Avikda. I would like to acknowledge that without Avikda's inspiration, it might not have been possible for me to pursue a research career after completing my master's, especially given the challenging family situation at that time. Most importantly, I am profoundly grateful to my beloved wife and long-standing friend, Jaya, for her unconditional love and unwavering belief in me. Words cannot fully express their contributions to my life. I also wish to sincerely thank Debarshri and Susovon, my longtime friends and companions since school days, for their support and encouragement throughout my studies and research life.

I am extremely thankful to INSPIRE, DST, Government of India (Grant No. DST/INSPIRE Fellowship/ IF190118) for providing me the financial support through a research fellowship to complete my research work.

Once again, I want to thank every one for their constant support, I could never have achieved this without them.

Subhajit Mojumder
June, 2024

ABSTRACT:

Over the past few decades, there has been significant scientific interest in semiconductor metal oxide (SMO) based chemiresistive gas sensors. SMO-based sensors offer numerous advantages compared to conventional gas sensing technologies, particularly in their ability to selectively detect different hazardous gases and volatile organic compounds in presence of several other interfering gases. Consequently, there is a rapidly growing demand for SMO-based sensors in the realms of breath analysis for disease detection, as well as indoor and outdoor air quality monitoring.

Breath analysis for disease detection is a comparatively new domain of research which holds significant promise. It is indeed feasible to detect early-stage health conditions in humans through non-invasive exhaled breath analysis. The major components of exhaled breath are N_2 (~ 79%), O_2 (~ 14-16%), and CO_2 (~ 4-6%). Although it also has about 1000 additional gases and volatile organic compounds (VOCs) in it, the majority of which are present in trace amounts (in ppm, ppb, ppt levels). Certain gases and volatile organic compounds (VOCs) have been recognized as indicators for various diseases and irregular physiological states such as diabetes, kidney disorders, and diverse types of cancer. The major challenge lies in detecting particular gases and volatile organic compounds (VOCs) at very low concentrations, amidst a complex mixture of numerous other compounds. Novel chemiresistive SMO-based gas sensors, with their high sensitivity and selectivity to different trace gases and VOCs at room temperature, offer promising solutions to tackle this challenge. Moreover, the substantial rise in environmental pollution, driven by rapid industrialization, population expansion, vehicular emissions, agricultural pesticide and insecticide use, as well as leaks of toxic chemicals and gases, poses a significant threat to ecosystems within the biosphere. Detecting air pollutants exceeding their safe thresholds is thus imperative for safeguarding human health. In addition to monitoring outdoor environmental conditions, indoor air quality monitoring is also crucial in modern life. Poor indoor and outdoor air quality can lead to various health issues ranging from respiratory problems, asthma, headaches, and fatigue to allergies, bronchospasm, and even cancer with prolonged exposure to hazardous environments.

Henceforth, there remains a significant potential for further research in the development of diverse functional SMO-based sensors, which are capable in selectively detecting trace amounts of various gases or volatile organic compounds (VOCs) of exhale breath with adequate sensitivity and resolution. The primary objective of my doctoral research is to fabricate diverse chemiresistive gas sensors based on various pure, doped, and heterojunction metal oxides with different crystal structures. Additionally, the research seeks to explore the impact of strategically incorporated dopants in pure metal oxides and the formation of heterojunction materials on the enhancement of gas sensing performance in semiconductor metal oxide-based sensors.

The whole thesis consists of eight different chapters which includes general introduction, literature review, five original research works, comprehensive collusion and future research scopes. In original research works various sensors were fabricated (Viz. ethanol sensor, acetone sensor, ammonia sensor, formalin sensor and CO gas sensor) for different purpose.

In first work, aluminium (Al) and yttrium (Y) were used as strategic dopant in ZnO crystal. The Al and Y- codoped ZnO based sensor exhibited enhanced sensitivity towards trace ethanol. Role of defect states, elevated surface area, particle size in enhancing the sensitivity of the codoped ZnO system were discussed in detailed.

In second work, Li doped ZnO based sensor was fabricated which showed selective sensing performance towards ammonia. Herein this work ammonia sensing mechanism was explained from theoretical point of view through Density Functional Theory (DFT) calculations. For later work in thesis ferrite materials were explored.

The third and fourth research work focuses on the synthesis of perovskite yttrium ferrite in various different crystal phase. In third part, formalin sensor was prepared for indoor air quality monitoring using hexagonal Yttrium ferrite which was synthesized through hydrothermal rote. Subsequently in fourth work highly sensitive and selective acetone sensor was fabricated from orthorhombic $YFeO_3$. The improved acetone sensing capabilities of orthorhombic Yttrium Ferrite (YFO) are elucidated through quantitative phase analysis, and the bivalency of iron across various phases of yttrium ferrite. Experimental results also verified through (DFT) calculations.

In the fifth research work heterostructure between metal oxide and ferrite (ZnO-$ZnFe_2O_4$) was synthesized for fabricating CO sensor. Advantages of heterojunction composite over the pristine metal oxides in gas sensing activity is discussed in detailed here in this part from both the experimental and theoretical point of view.

Chapter eight outlines the conclusions and potential directions for future research, focusing on the application of advanced materials such as Metal-Organic Frameworks (MOFs) and Covalent Organic Frameworks (COFs) in gas sensing technologies. Additionally, it addresses the development of a hand-held device utilizing the fabricated sensor, aimed at facilitating the commercialization of this sensor technology.

Table of Contents

List of Tables

List of Figures

Fig. 3. 8. BET plot of (a)AYZ-0; (b)AZ-1; (c)AYZ-1; (d)AYZ-3; (e)AYZ-5; (f)AYZ-7 nanoparticles. (g) Variation of BET specific surface area in the AYZ samples with increasing doping concentration.

Fig. 3. 9. (a) UV-Vis spectrum and Tauc plot for AYZ-5 sample (inset shows UV-Vis absorption spectra for all the samples); and (b) variation of band gap with increasing doping concentration.

Fig. 3. 10. Ultra-contrast thermal images of AYZ-5 sensor surface at (a) 3.8 V; (b) 4.3 V; (c) 4.6 V; (d) 5 V; (e) 5.3 V; and (f) 5.45 V

Fig. 3. 11. (a) Gas response of different AYZ nanoparticles at different operating temperatures; (b) Temperature influence on response of AYZ-5 sensor fitted with gaussian equation; and (c) Variation of base resistance of AYZ-5 sensor with change of operating temperature (°C).

Fig. 3. 12. I-V plots of different AYZ sensors at 350 °C.

Fig. 3. 13. (a) The response of different ZnO sensors towards 1, 5, 10, 25 ppm ethanol vapor at 350°C and constant 33% RH background; and (b) Variation of AYZ-5 sensor response (1ppm ethanol) and base resistance in different %RH background at 350°C.

Fig. 3. 14. (a) Dynamic response curves of AYZ-5 nanoparticles to different concentrations of ethanol vapor (300 ppb to 100 ppm) at 350 °C; and (b) suitability of AYZ-5 sensor for the detection of hepatic steatosis (fatty liver disease).

Fig. 3. 15. (a) Linear dependency of AYZ-5 sensor response to different low concentrations of ethanol vapor (1-50 ppm) at 350 °C and constant 33% RH background; (b) Transient resistance curve of AYZ-5 sensor in response to 1 ppm ethanol vapor at 350°C fitted with single-site Langmuir adsorption model; and (c) Repeatability plot of AYZ-5 sensor towards 5 ppm ethanol vapor at 350°C and 33% RH background (inset shows repetitive dynamic response curves for AYZ-5 sensor towards 5 ppm ethanol at 350° C and constant 33% RH background).

Fig. 3. 16. (a) Cross-sensitivity plot of AYZ-5 sensor towards other major gas volatiles at 350°C; **(b)** Long-term stability graph of the AYZ-5 sensor; and **(c)** Long-term stability graph of the base resistance of AYZ-5 sensor.

Fig. 3. 17. Schematic presentation of gas sensing mechanism.

Fig. 3. 18. Gaussian deconvolutions of the PL spectra of (a) AYZ-0; (b) AZ-1; (c) AYZ-5; and (d) AYZ-7.

Fig. 3. 19. W-H Plot of (a) AYZ-0; (b)AZ-1; (c) AYZ-5; (d) AYZ-7.

Fig. 3. 20. (a) O 1s of AYZ-0; (b) O 1s of AZ-1; (c) O 1s of AYZ-5; and (d) Variation of O_L (%), O_D (%), and O_C (%) in AYZ-0, AZ-1, AYZ-5 samples.

Fig. 3. 21. (a) Sensing response of AYZ-5 sensor towards different trace concentrations of ethanol in exhaled breath background. [H.B = Healthy Breath; EtOH = Ethanol.]; and (b) Relation between gas sensing response of AYZ-5 sensor towards ethanol mixed with ambient air and healthy human breath.

Fig. 4. 1. Schematic representation of material synthesis procedure.

Fig. 4. 2. Schematic presentation of the humidity-controlled gas sensing set up.

Fig. 4. 3. (a) unit cell's structure of bare ZnO. (b) bare NH_3. (c) supercell structure of NH_3 adsorbed ZnO. (d) unit cell's structure of bare Li doped ZnO. (e) bare NH_3. (f) supercell structure of NH_3 adsorbed Li doped ZnO.

Fig. 4. 4. (a) XRD characterization of all LZ samples, (b) Relative deviation of (101) peak from XRD patterns of all LZ samples, (c) Variation of crystallite size in different LZ samples.

Fig. 4. 5. FESEM images of (a-b) pristine ZnO (c-d) LZ-5 sample (e) EDX spectra of LZ-5.

Fig. 4. 6. (a, b) TEM image of LZ-0 in low and high magnification respectively, (c) HRTEM image of LZ-0, (d) SAED pattern of LZ-0, (e, f) TEM images of LZ-5 in low and high magnification (g) HRTEM image of LZ-5 (h) SAED pattern of LZ-5.

Fig. 4. 7. N_2 adsorption–desorption isotherms and corresponding BJH pore size distribution curve (inset) of (a) LZ-0, (b) LZ-1, (c) LZ-5, (d) LZ-15.

Fig. 4. 8. (a) UV-Vis absorption spectra of all LZ samples, (b) Tauc plot of all LZ samples (c) Variation of energy bandgap with varying doping concentration.

Fig. 4. 9. Deconvoluted RT-PL spectra of **(a)** LZ-0, **(b)** LZ-1, **(c)** LZ-5.

Fig. 4. 10. (a) XPS survey scan of LZ-0, LZ-1, LZ-5 (Li peak position corresponding to survey scan of LZ-5 sample is shown in the inset). (b) Li 1s peaks of LZ-1 and LZ-5 samples. (c) Zn 2p peaks corresponding to LZ-0, LZ-1, LZ-5 samples (deviation of Zn $2p_{3/2}$ peak with Li doping is shown in the inset), Deconvoluted O1s of (d) LZ-0, (e) LZ-1, (f) LZ-5.

Fig. 4. 11. (a) Transient photocurrent spectra of all the samples. (b) LSV curves of all the samples under continuous light illumination. (c) Nyquist plots of under visible light irradiation. Insets of (c): equivalent circuit models of the Nyquist plots.

Fig. 4. 12. (a) Variation of sensing response of LZ-0, LZ-1, LZ-5, LZ-15 sensors with temperature towards 1ppm ammonia gas concentration at 33% RH background, (b) Response of all LZ sensor towards varying ammonia concentration at optimum operating temperature. (c) Dynamic response curve of LZ-5 sensor towards 1 ppm ammonia at various humidity background (4% - 94% RH) at optimum operating temperature.

Fig. 4. 13. (a) Variation of gas sensing response of LZ-5 sensor towards 1 ppm ammonia at different %RH background. (b) Dynamic response curve of LZ-5 sensor towards different ammonia concentration at optimum condition. (c) Response of LZ-5 sensor towards 5 ppm ammonia for 5 consecutive cycles. (d) Variation of response with varying Nh_3 concentration of LZ-5 sensor. (e) ln(*Sg*) vs ln(*Cg*) curve of LZ-5. (f) Variation of response and base resistance of LZ-5 sensor with time. (g) Dynamic resistance curve (fitted with single-site Langmuir adsorption model) of LZ-5 towards 1 ppm ammonia gas. (h) Cross-sensitivity curve of LZ-5 at optimum operating condition. (i) Comparison of response of LZ-5 to 1 ppm ammonia in presence of acetone, ethanol, CO, H_2S, NO_2 at optimum operating condition.

Fig. 4. 14. (a) Schematic presentation of simulated breath study. (b) Response of LZ-5 sensor towards simulated breath having different trace concentrations of NH_3 [H.B = Healthy Breath]. (c) Simulated breath response of the LZ-5 sensor for five different breath samples.

Fig. 4. 15. Schematic presentation of ammonia sensing mechanism.

Fig. 4. 16. Variation of gas sensing response of LZ sensors with major influencing parameters.

Fig. 4. 17. PDOS of (a-b) Zn, O of bare ZnO respectively. (c-f) Zn, O, N, H of NH_3 gas absorbed ZnO respectively. (g-i) Zn, Li, O of Li doped ZnO respectively. (j-n) Zn, Li, O, N, H of NH_3 gas absorbed Li doped ZnO respectively.

Fig. 4. 18. (a-c) Band structure, spin polarised TDOS, total PDOS bare ZnO respectively. (d-f) Band structure, spin polarised TDOS, total PDOS of NH_3 gas absorbed ZnO respectively. (g-i) Band structure, spin polarised TDOS, total PDOS of Li doped ZnO respectively. (j-l) Band structure, spin polarised TDOS, total PDOS of NH_3 gas absorbed Li doped ZnO respectively.

Fig. 5. 1. Schematic diagram of the hexagonal $YFeO_3$ synthesis procedure.

Fig. 5. 2. Schematic diagram of the gas sensing procedure.

Fig. 5. 3. (a) XRD pattern of hexagonal $YFeO_3$ powder, (b) W-H plot of hexagonal $YFeO_3$, (c) FTIR spectra of the hexagonal $YFeO_3$ powder.

Fig. 5. 4. (a) XPS survey scan of hexagonal $YFeO_3$. HR-XPS spectra of (b) Y 3d, (c) Fe 2p, and (d) O 1s region of $YFeO_3$.

Fig. 5. 5. (a-b) FESEM micrograph of the synthesized material at different magnification.

Fig. 5. 6. (a) TEM micrograph, (b) HRTEM image, (c) EDX spectra of hexagonal $YFeO_3$ powder.

Fig. 5. 7. (a) Tauc plot of the sample (inset shows UV-Vis absorption spectra of the samples), (b) BET plot of $YFeO_3$ powder.

Fig. 5. 8. (a) I-V plots of YFO sensor at different operating temperature, (b) Ultra-contrast thermal images of YFO sensor surface at optimum operating temperature (240°C), (c) Variation of base resistance of the sensor with varying operating temperature, (d) Variation of response to 1 ppm formalin with varying operating temperature.

Fig. 5. 9. (a) Variation of response to 1 ppm formalin with background relative humidity (%RH), (b) Dynamic response and recovery curve of the YFO sensor towards 0.5-100 ppm formalin, (c) Response of the sensor towards different formalin concentration, (d) Fitting of experimental sensing response data with Freundlich adsorption isotherm at 240 ◦C.

Fig. 5. 10 (a) Repeatability study of the sensor towards 25 ppm formalin vapour, (b) Response and recovery time, (c) Long-term stability curve, (d) Selectivity curve of the sensor.

Fig. 5. 11 Schematic representation of the formalin sensing mechanism of hexagonal $YFeO_3$ sample (a) in air, (b) in HCHO.

Fig. 6. 1. (a) Schematic of synthesis procedure of $YFeO_3$**.** (b) Schematic presentation of gas measurement setup.

Fig. 6. 2. (a) XRD patterns of $YFeO_3$ sintered at different temperatures. The peak positions in reference diffraction patterns of the hexagonal (ICDD-00-048-0529) and orthorhombic (ICDD-04-015-9132) $YFeO_3$, secondary phase $Y_3Fe_5O_{12}$ (ICDD-01-077-1998) are also indicated by

gray and black lines, respectively. (b) correspondingly magnified XRD patterns around 2θ = 25º-36º. (c) Refined XRD plot of YF-10 sample using Xpert High scrore plus software.

Fig. 6. 3. FESEM images of (a) YF-7, (b) YF-8, (c) YF-10, (d) YF-12. (e-g) FESEM images of YF-10 sample in higher magnification. (h) EDS spectrum of YF-10 sample.

Fig. 6. 4. (a) FESEM image of the selected mapping area of YF-7 and the corresponding EDX colour mapping of (b) O, (c) Fe, (d) Y. (e) FESEM image of the selected mapping area of YF-10 and the corresponding EDX colour mapping of (f) O, (g) Fe, (h) Y.

Fig. 6. 5. (a) TEM image of YF-7 sample. (b) SAED pattern of YF-7. (c) HRTEM images of YF-7 corresponding to (101) plane. (d) TEM image of YF-10 sample. (e) SAED pattern of YF-10. (f) HRTEM images of YF-10 corresponding to (111) plane.

Fig. 6. 6. (a) XPS survey spec tra of YF-7. YF-10, YF-12. HR-XPS spectra corresponding to the Y 3d core-level of (b) YF-7, (e) YF-8, (h) YF-10, (k) YF-12. Fe 2p core-level of pure (c) YF-7, (f) YF-8, (i) YF-10, (l) YF-12. O1s core-level of (d) YF-7, (g) YF-8, (j) YF-10, (m) YF-12.

Fig. 6. 7. (a) EPR spectra of the samples. (b) Linear fitting of the BET plot of YF-7, YF-8, YF-10, YF-12 powder. (c) Tauc plot of YF-10 sample. (Insight UV-Vis absorption spectra for all the samples). (d-f) Tauc plot of YF-7, YF-8, YF-12 sample.

Fig. 6. 8. Deconvoluted PL spectra of (a) YF-7, (b) YF-10 and (c) YF-12.

Fig. 6. 9. (a) Variation of base resistance of different YF sensors with operating temperature of the sensor. (b) I-V characteristics of all YF based sensor. (c) Response behaviour of all the YF sensors against varying operating temperature towards 0.5 ppm acetone at constant 33% RH background. (d) Variation of base resistance and the response of YF-10 sensor towards 0.5 ppm acetone with varying background %RH. (e-f) Dynamic response curve of YF-10 sensor towards 100 ppb to 50 ppm acetone vapour at optimum operating temperature and constant 33%RH background. (g) Response behaviour of all the YF-10 sensors against varying acetone concentration at optimum operating temperature and constant 33 %RH background (inset-variation of the response of YF-10 sensor toward low acetone concentrate. (h) Repetitive response curve of YF-10 sensor towards 1 ppm acetone, (i) Long time stability curve of YF-10, long term stability of the base resistance of YF-10 sensor at optimum conditions.

Fig. 6. 10. (a) Response of YF-10 sensor towards various concentration of different gases. Transient response curve of the YF-10 sensor for various (b) ethanol, (c) ammonia, (d)

formaldehyde, (e) CO of different concentration. (f) Variation of ln(C_g) and ln(S_g) for 5 different gases. (g) PL emission peak of YF-10 sample in presence and absence of acetone.

Fig. 6. 11. (a-b) Schematic diagrams of YFO for acetone detection. (c-d) Corresponding energy band diagrams in air and in acetone.

Fig. 6. 12. (a) optimized structure of acetone adsorbed orthorhombic $YFeO_3$. (b) optimized structure of acetone adsorbed hexagonal $YFeO_3$. (c) Planar average charge density difference in the acetone adsorbed orthorhombic $YFeO_3$.

Fig. 6. 13. Fitting of dynamic resistance curve of YF-10 sensor in response to (a) 1 ppm acetone at 300 ◦C for response and recovery time measurement. (b) 5 ppm acetone, (c) 10 ppm acetone, (d) 25 ppm acetone, (e) 50 ppm acetone, (f) 1 ppm ethanol, (g) 1ppm ammonia, (h) 1 ppm formalin, (h) 1 ppm CO at 300 ◦C for response time measurement. (i) Variation of $1/\tau_{res}$ with varying concentration of different gases for obtaining kinetic rate constant for different VOCs at 350 ◦C operating temperature. (j) Variation of response time of YF-10 sensor for different gases of 1ppm concentration at350 ◦C operating temperature for obtaining activation energy (E_a) values for different interfering gases.

Fig. 6. 14. (a) Dynamics response curve of YF-10 sensor towards healthy breath (H.B.) and simulated breath of simulated breath having different concentration at 300º C operating temperature. (b) Response of YF-10 sensor towards 5 different simulated breath samples. (c) Breath sample collection in 1lt. tedlar bag. (d-e) Preparation of simulated breath sample.

Fig. 7. 1. Schematic of synthesis procedure of ZnO- ZFO heterostructure.

Fig. 7. 2. (a) XRD pattern of all the samples, (b) Magnified XRD pattern of all the samples in the 2θ=34.5º-37º

Fig. 7. 3. (a) FTIR spectra of all the samples, (b) FTIR spectra of ZZF-11 sample.

Fig. 7. 4. FESEM micrographs of (a) ZFO, (b) ZZF-31, (c-d) ZZF-11, (e) ZZF-13, (f) EDX spectra of ZZF-11.

Fig. 7. 5. EDS selected elemental colour mapping area of (a) ZFO, (b) ZZF-31, (c) ZZF-11 (d) ZZF-31 (O, Fe, Zn elements are shown in different colours).

Fig. 7. 6. TEM micrographs of (a) ZFO, (b) ZZF-31, (c) ZZF-13, (d) ZZF-11, (e) HRTEM image of ZZF-11.

Fig. 7. 7. (a) XPS survey scan of ZnO, ZFO, ZZF-11, ZZF-13, ZZF-31. (b) HR-XPS spectra of Zn2p region of all the samples.

Fig. 7. 8. HR-XPS spectra of Fe2p region corresponding to (a) ZFO (b)ZZF-31, (c) ZZF-11, (d) ZZF-13.

Fig. 7. 9. HR-XPS spectra of O 1s region corresponding to (a) ZnO, (b) ZFO, (c) ZZF-31, (d) ZZF-11, (e) ZZF-13, (f) EPR spectra of all the samples.

Fig. 7. 10. (a) N_2 adsorption-desorption isotherm of ZZF-11 (inset BET surface area curve of ZZF-11), (b) BJH pore size distribution curve of ZZF-11 sample, (c) Variation of surface area, pore volume and pore diameter of in ZnO, ZFO, ZZF-31, ZZF-11, ZZF-13 samples.

Fig. 7. 11. (a) UV-Vis adsorption spectra of all the samples, Tauc plot of (b) ZnO, (c) ZFO, (d) ZZF-31, (e) ZZF-11, (f) ZZF-13.

Fig. 7. 12. (a) Comparison of PL emission spectra of all the sample, Deconvoluted PL spectra of (b) ZnO, (c) ZFO, (d) ZZF-11.

Fig. 7. 13. The electronic band structure and atom-projected partial density of states for (a, d) ZnO, (b, e) ZFO, and (c, f) ZZF-11, respectively. The inlets shown in figure (d) and (e) are the zoomed view of the conduction band edges of ZnO and ZFO.

Fig. 7. 14. (a) Variation of the base resistance of the sensors with operating temperature, (b) Variatio of the response of the sensors with operating temperature, (c) Changes of the sensitivity of the ZZF-11 sensor with background humidity, (d) Response of different sensors towards different CO concentration at their optimal operating temperatures.

Fig. 7. 15. (a) Dynamic response curve of ZZF-11 sensor, (b) $\log(S_g)$ vs. $\log(C_g)$ curve for ZZF-11 sensor, (c) Repeatable response curve of ZZF-11 sensor towards 75 ppm CO gas at optimum operating condition, (d) Response and recovery time of ZZF-11 sensor towards 75 ppm CO gas.

Fig. 7. 16. (a) Modulation of sensitivity and base resistance of ZZF-11 sensor over the time period of 120 days, (b) Selectivity curve of ZZF-11 sensor over other interfering gases.

Fig. 7. 17. Schematic of the CO sensing mechanism of ZZF-11.

Fig. 7. 18. (a) Schematic presentation of band diagram of ZFO/ZnO heterostructure. (b) 3D picture of the differential charge density of the ZFO/ZnO interface, where the yellow and blue areas denote the gain and the loss of electrons, respectively, with the isosurface value of 0.4253 $e/Å^3$

Fig. 7. 19. Adsorption of CO on (a) ZnO. (b) ZFO. (c) ZZF-11 in a favorable configuration.

Abbreviations and Symbols

SMO	Semiconductor metal oxide
VOCs	Volatile organic compounds
ZnO	Zinc oxide
Y	Yttrium
Al	Aluminium
Li	Lithium
$YFeO_3$	Yttrium ferrite
$ZnFe_2O_4$	Zinc ferrite
C_3H_6O	Acetone
C_2H_5OH	Ethanol
NH_3	Ammonia
CH_2O	Formaldehyde/Formula
CO	Carbon monoxide
CO_2	Carbon dioxide
H_2O	Water
$C_4H_6O_6$	Tartaric Acid
$C_6H_8O_7$	Citric acid
XRD	X-ray diffraction
FESEM	Field-emission scanning electron microscopy
HRTEM	High-resolution transmission electron microscopy
FTIR	Fourier transform infra-red spectroscopy
XPS	X-ray Photoelectron Spectroscopy
BET	Brunauer-Emmett-Teller
UV-Vis	UV-Visible Spectroscopy
PL	Photoluminescence
DFT	Density Functional Theory
EDL	Electron depletion layer

CHAPTER-I

General Introduction

1.1 Overview

Sensors permeate both domestic and professional environments and are integral to daily routines and industrial operations. This discourse aims to elucidate the fundamental attributes of sensors, their functionalities, and their applicability to process control frameworks. At its core, a sensor embodies a device with the ability to detect and respond to stimuli. Contemporary sensor technology extends beyond mere physical perception and encompasses the faculties of sight, touch, hearing, olfaction, and gustation. The absence of sensors would render commonplace activities arduous, as evidenced by their role in regulating traffic lights at intersections and facilitating automatic door operations at commercial establishments.[1–3]

Within industrial settings, sensors serve as linchpins for monitoring and managing critical parameters such as temperature and pressure in batch processes. Conceptually, sensors are construed as devices capable of discerning alterations in their physical, electrical, or chemical properties, thereby generating corresponding electrical outputs. The key physical properties detectable by the sensors are level, temperature, flow, pressure, speed, and position.

1.2 Gas sensors

Gas sensors represent a critical subset of sensing technologies and play pivotal roles in identifying and quantifying gases in various environments. These devices serve diverse purposes, ranging from indoor and outdoor air quality monitoring to detecting adulterated food and even specific diseases through exhaled breath analysis. Their utility extends to applications in aerospace, laboratories, fuel cells, and advanced medical sciences.

Gas sensors operate based on the principle of detecting and measuring gas concentrations in their vicinity, thereby offering insights into potential health hazards or environmental risks. They can be broadly categorized into several types, based on their intended applications and operational mechanisms.

1.2.1 Major usage of gas sensors

I. Detection and monitoring of toxic gases: Gas sensors are instrumental in identifying hazardous gases, such as carbon monoxide (CO), sulphur oxides (SO_x), nitrogen oxides (NO_x), and ammonia (NH_3), which pose significant health risks even at low concentrations. Continuous monitoring of these gases is crucial for mitigating potential health hazards associated with prolonged exposure.

II. Detection of volatile organic compounds (VOCs): Gas sensors also facilitate the detection of volatile organic compounds, such as ethanol, acetone, toluene, and formaldehyde, which can adversely affect human health. Moreover, Certain VOCs serve as biomarkers for specific diseases, such as acetone for diabetes and ethanol for fatty liver disease, highlighting the diagnostic potential of gas-sensing technology.

III. Detection of inflammable gases: Gas sensors play a vital role in identifying combustible gases to prevent unwanted fires or explosions and to enhance safety in various industrial and domestic settings.

IV. Detection of freshness of food: Adulteration in various foods such as milk, eggs, oils, and meat can lead to the generation of several gases, VOCs (volatile organic compounds), and metabolites such as formaldehyde (HCHO), sodium hypochlorite (NaClO), carbonic acid (H_2CO_3), and citric acid. Detecting adulteration in foods and beverages is crucial from a human health perspective.

V. Indoor air quality monitoring: Indoor air contains various pollutants generated from sources like paint, coloured wood polish, etc., such as formaldehyde (formalin), benzene, toluene, xylene, acetone. These indoor air pollutants can induce several health hazards such as eye, nose, and throat irritation, headaches, and dizziness among people of all age groups. Long-term exposure to such toxic gases could also potentially damage the liver, kidneys, and lungs. Therefore, detecting these toxic gases is another crucial issue for ensuring human safety.

1.2.2 Different types of gas sensors

Different types of gas sensors are available in the market, each of which is characterized by distinct constructional and operational principles.

(i) Metal oxide semiconductor gas sensors: These sensors operate based on changes in the electrical conductivity of metal oxides in the presence of target gases.

(ii) Optical Gas Sensor: Optical sensors utilize light absorption or emission properties to detect gas molecules, offering high sensitivity and selectivity.[4]

(iii) Electrochemical gas sensors[5,6]

(iv) Capacitance-based gas sensors.[7–9]

(v) Calorimetric gas sensors: [8,9]

Calorimetric sensors detect gas concentrations by measuring changes in heat release or absorption during gas interactions.

(vi) Acoustic-based gas sensors: Acoustic sensors detect gas concentrations by analyzing changes in sound wave propagation caused by gas interactions.

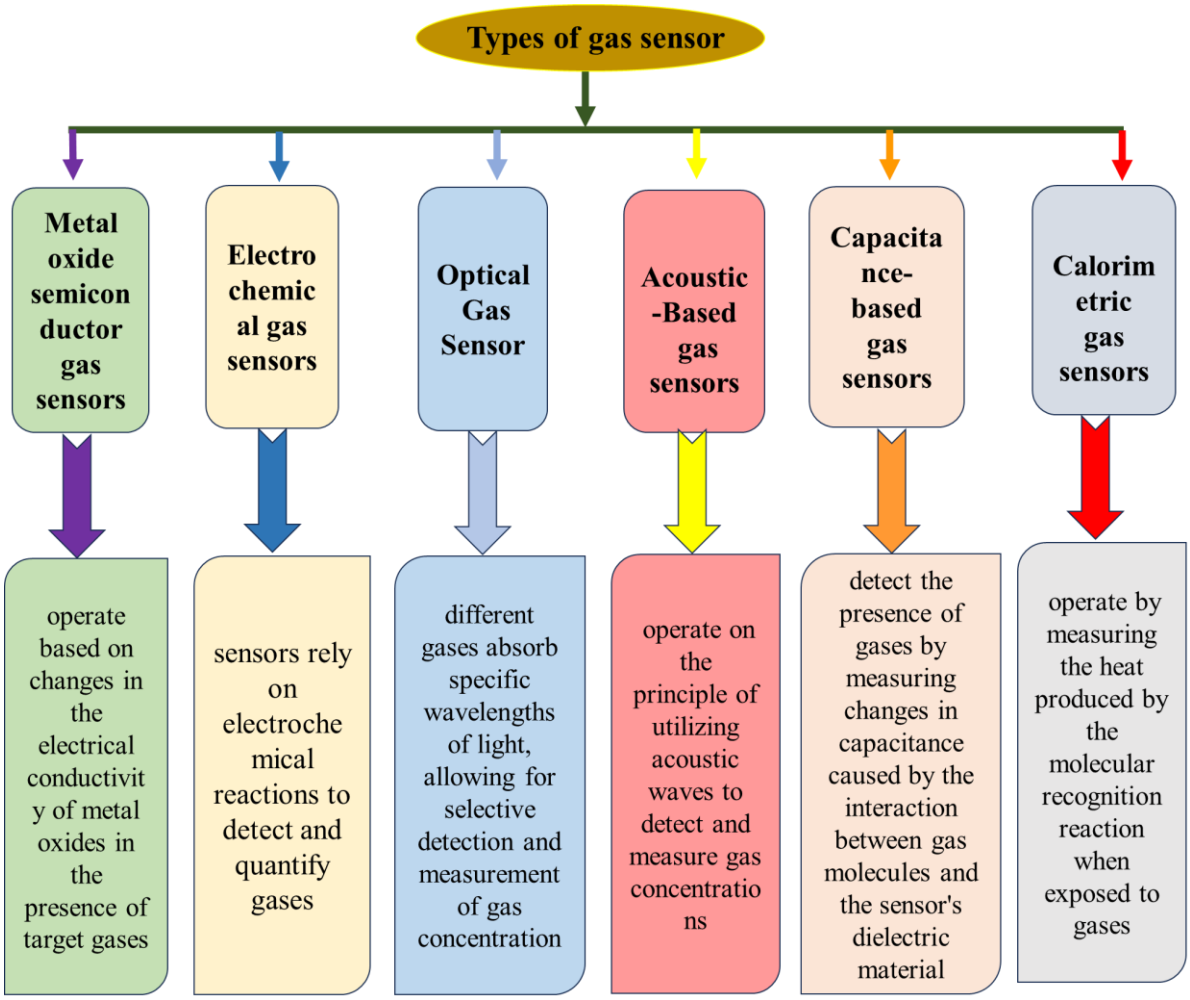

Fig. 1. 1. Types of gas sensors and their application field.

1.3 Semiconductor metal oxide based chemiresistive gas sensor

Among these different types of gas sensors over the last 50 years, semiconductor metal-oxide-based gas sensors have drawn significant attention within the scientific community. SMO-based sensors are widely utilized in various fields, such as detecting food adulteration,

monitoring environmental pollution, diagnosing human diseases, and sensing flammable gases. Chemiresistive SMO sensors have garnered significant interest from the scientific community, primarily because of their enhanced sensitivity, capability for real-time measurements, compact dimensions, cost effectiveness, portability, durability, and ease of operation. [10,11]

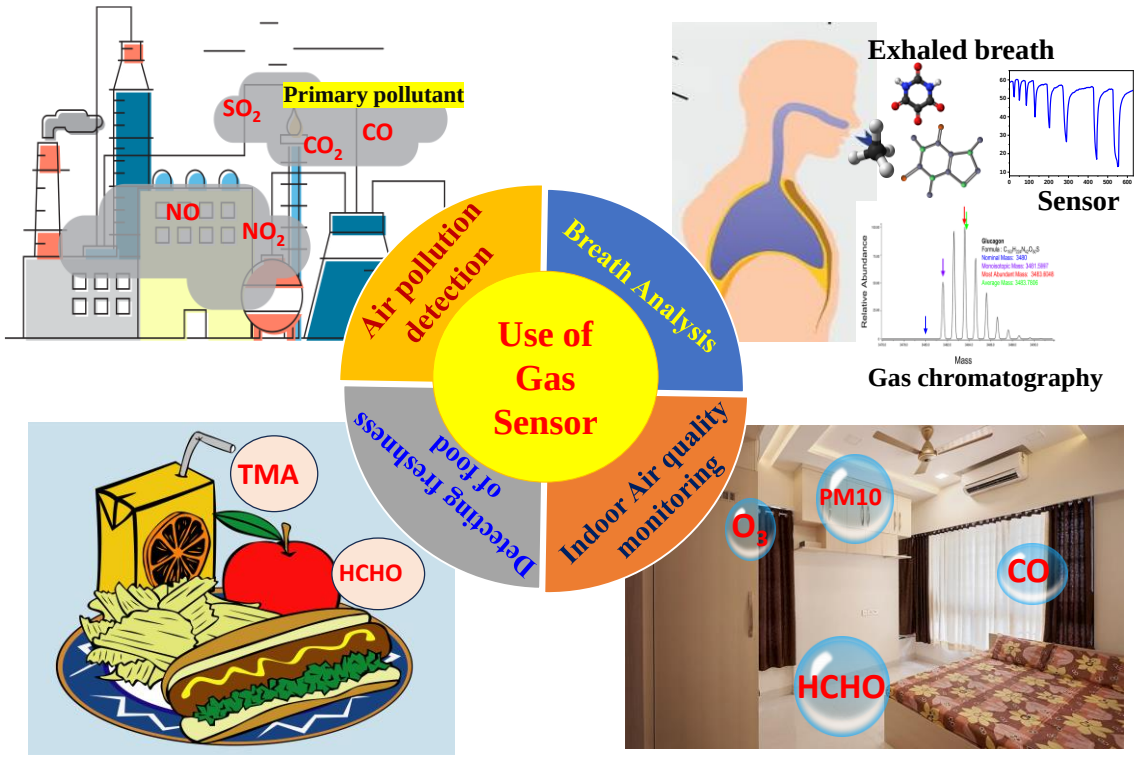

Fig. 1. 2. Schematic representation of various uses of gas sensors.

In recent years, air pollution, whether indoors or outdoors, has emerged as a significant threat to both human health and ecosystems. Air quality monitoring necessitates the detection of pollutants, such as sulphur oxides (SO_x), nitrogen oxides (NO_x), carbon monoxide (CO), and volatile organic compounds, such as benzene, toluene, and xylene (BTX), ensuring that their concentrations remain within acceptable limits. Comprehensive air quality monitoring mandates the deployment of portable sensors capable of conducting real-time measurements in diverse situations over prolonged durations. In this context, chemiresistive trace-gas-sensor-based handheld electronic noses (HENs) have emerged as optimal solutions for field applications. These HENs leverage chemiresistive principles to detect and quantify trace gas concentrations, offering portability, ease of use, and real-time data acquisition capabilities essential for effective air quality surveillance.[12,13]

Contemporary analytical and spectrophotometric methodologies, such as high-performance liquid chromatography and gas chromatography-mass spectrometry, exhibit precise capabilities for discerning the varieties and production of food contaminants. Nevertheless, SMO chemiresistors hold promise in substituting these cumbersome and costly apparatus.[14,15]

Exhaled breath primarily consists of nitrogen (approximately 79%), oxygen (approximately 14%-16%), and carbon dioxide (approximately 4%-6%). In addition to these major components, there are approximately 3000 other trace gases and volatile organic compounds (VOCs) present in parts per million (ppm), parts per billion (ppb), and even parts per trillion (ppt) concentrations. Among these gases and VOCs are acetone, ammonia, hydrogen sulphide, certain aldehydes, and alkanes, which serve as biomarkers indicating various diseases and abnormal physiological conditions.

The human body emits various biomarkers through exhaled breath, which serve as indicators of different diseases and disorders. Ammonia, crucial for metabolic processes, becomes toxic in excess and is removed through the urea or ornithine cycle. Elevated levels of breath ammonia may signal kidney failure, liver dysfunction, hepatic encephalopathy, or brain swelling. Nitric oxide, involved in cell signalling, increases in asthma and other conditions like liver transplant rejection and chronic obstructive pulmonary disease. Hydrogen sulphide, a gas transmitter, indicates asthma, airway inflammation, and oral health issues. Acetone, a byproduct of fat metabolism, rises in diabetes, diabetic ketoacidosis, and high-fat diets. Isoprene, linked to cholesterol production, is elevated in diabetes and lipid metabolism disorders. Methane, ethane, and pentane are produced by gut bacteria and lipid oxidation; their presence in breath indicates conditions like obesity, inflammatory bowel diseases, and cancer. Aldehydes, products of lipid peroxidation, increase in cancer patients and those with metabolic disorders like diabetes and Alzheimer's disease. Elevated aldehyde levels in breath serve as biomarkers for various diseases, including lung cancer. Monitoring these biomarkers in breath can provide valuable insights into the diagnosis and management of a range of health conditions.

Identifying these biomarkers among approximately 3000 other gases and volatile organic compounds (VOCs) in breath presents a significant obstacle. Advanced chemiresistive sensors based on semiconducting metal oxides (SMO) demonstrate promising capabilities in achieving high sensitivity and selectivity towards detecting trace gases and VOCs. In light of the increasing demand for these sensors, extensive research efforts have been conducted globally.

Evidently, the primary focus of extensive research efforts in the realm of SMO sensors revolves around the advancement of sensor technology, aiming for superior performance metrics including enhanced sensitivity, selectivity, stability, rapid response, and recovery times. To methodically engineer and innovate efficient sensor materials, a comprehensive understanding of the diverse physicochemical factors dictating sensing mechanisms and sensor efficacy is indispensable.

1.3.1 Working principle semiconductor metal oxide based chemiresistive gas sensors

semiconductor metal oxide based chemiresistive gas sensors operate by altering the physical properties of the sensing material when exposed to the target gas. At a specific temperature, oxygen molecules adhere to the surface due to defects or vacancies in the sensor material, trapping free electrons from the conduction band and creating potential barriers at grain boundaries. Upon exposer to the gas analyte, whether reducing or oxidizing, the resistance of the sensor changes. This change in resistance, relative to the base resistance of the material, determines response of the sensor. Essentially, resistance of the sensors changes during gas interaction which elucidates the sensor's ability to detect and respond to specific gas molecules, a fundamental principle underlying solid-state gas sensor functionality. There are different process involves during the whole gas sensing procedure are enlisted below,

[i] Over the gas sensing material, gas molecules are adsorbed.

[ii] Interaction takes place between the absorb gas and the active sensing material.

[iii] Finally gas molecules desorbed from the active sensing material

When gas is introduced to the active sensing material, the gas molecules diffuse into the active layer and are absorbed, adhering to the reactive surface. The adsorption of gas molecules on the active sensing material primarily occurs through three mechanisms: (a) Physisorption, where weak Van der Waals forces occur between the sensing material and gas molecules, without altering the surface's electronic structure; (b) Chemisorption, where a stronger chemical bond forms between the adsorbate and the sensing material, leading to changes in the electronic structure; and (c) Ionosorption, where adsorption involves the trapping of an electron or hole from the surface of the active material, resulting in the ionization of the gas molecules.

This ionization, caused by the trapping of electrons or holes from the sensing surface, significantly influences the sensing material's electronic structure. Chemisorption is distinguished by its strong bonding, while physisorption relies on weaker forces. Ionosorption

is a specialized form of chemisorption where adsorption leads to ionization of the adsorbate, profoundly impacting the electronic structure of the sensing material. Physisorption predominates at lower temperatures, while chemisorption occurs at higher temperatures subsequent to physisorption. Ionosorption, driven by electrostatic forces, plays a crucial role in solid-state gas sensors, as the entire process hinges on the adsorption and ionization of oxygen molecules into various species, such as O^-, O^{2-}, and O_2^-. These represent fundamental sensing mechanisms found in all chemiresistive gas sensors, providing understanding of gas-sensing processes applicable across various fields like environmental monitoring and medical diagnostics.

At low temperatures, oxygen molecules adhere to the sensing surface as O_2^-.. Upon reaching high temperatures, this O_2^-. dissociates into O^-. Given that gas sensing primarily occurs at the surface, the resulting peroxide O^- enhances the activity of the sensing surface. The sensor's sensitivity to gas analytes is enhanced by enhanced adsorption of oxygen molecules. Interaction between the gas molecule and the adsorbed oxygen ion prompts a shift in the resistance of the active sensing material, compared to its original state, termed as sensor sensitivity.

The gas sensing mechanism varies slightly depending on whether the gas analytes are reducing or oxidizing. For reducing gases, the interaction occurs between the physiosorbed oxygen on the active sensing material and the gas molecules. When oxygen molecules capture electrons from the conduction band, a depletion region is formed. Upon exposure to the test gas, additional free electrons are introduced into the conduction band, altering the sensor's resistance. In contrast, for oxidizing gases, donor vacancies are created due to the removal of lattice oxygen. These vacancies inject carriers into the sensing material's conduction band, resulting in changes in resistance.[16–19]

In semiconductor gas sensors, the majority carrier type, whether electrons or holes, dictates the sensor's response to different gas analytes. For n-type semiconductor materials, electrons are the majority carriers. When these materials interact with a reducing gas analyte, such as hydrogen or carbon monoxide, the electron concentration increases, leading to a decrease in resistance. Conversely, exposure to an oxidizing gas analyte, such as ozone or nitrogen dioxide, results in a decrease in electron concentration, causing an increase in resistance. In contrast, p-type semiconductor materials have majority carriers as holes. When subjected to an oxidizing gas analyte, the concentration of holes increases, leading to a rise in conductivity. Conversely, interaction with a reducing gas analyte reduces conductivity. This occurs as introduced

electrons combine with the positively charged holes, reducing their concentration and thereby increasing resistance. This behaviour is extensively discussed in Chapter III to Chapter VII. Thus, the response of semiconductor gas sensors to different gas analytes is contingent upon the type of majority carriers present in the semiconductor material, with n-type materials exhibiting contrasting behaviour to p-type materials. Step-wise gas sensing mechanism of SMO based gas sensors is schematically represented in Fig. 1. 3.

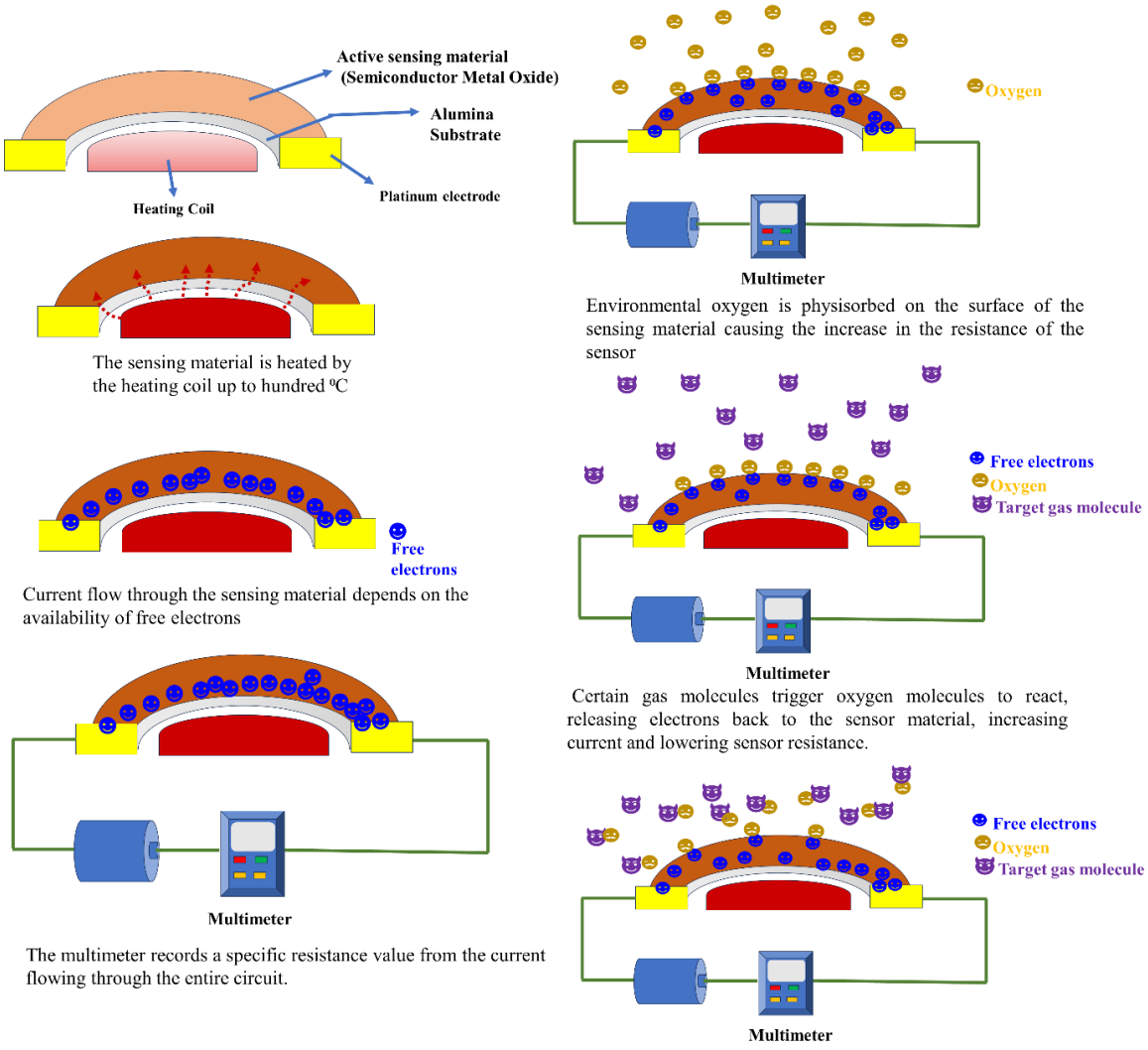

Fig. 1. 3. Stepwise schematic representation of gas sensing mechanism of SMO based gas sensors.

1.3.2 Gas sensing variables

(i) Sensitivity or response (S):

Chemiresistive sensors can be categorized into two types based on the behaviour of their active sensing material. If the resistance of the sensor increases in the presence of a gas, it is called p-type sensing response. Conversely, if the resistance of the sensor decreases in the presence

of certain gas molecules, it is called n-type response. The sensitivity of these two types of sensors is typically measured in terms of the change in resistance relative to their original baseline resistance in an ambient environment.[20,21]

For n-type of sensing material [33],

$$S_g = \left(\frac{R_g - R_a}{Ra}\right) \times 100\% \quad \text{..... (1)}$$

For p-type of sensing material [34],

$$S_g = \left(\frac{R_G}{R_a}\right) \quad \text{..... .....(2)}$$

(ii) Response time: It is defined as duration required for the sensor to achieve 90% of the peak alteration in resistance following the introduction of the test gas. [21]

(iii) Recovery time: It is defined as the time needed for the sensor to reach 90% of its initial resistance level after the test gas has been eliminated.

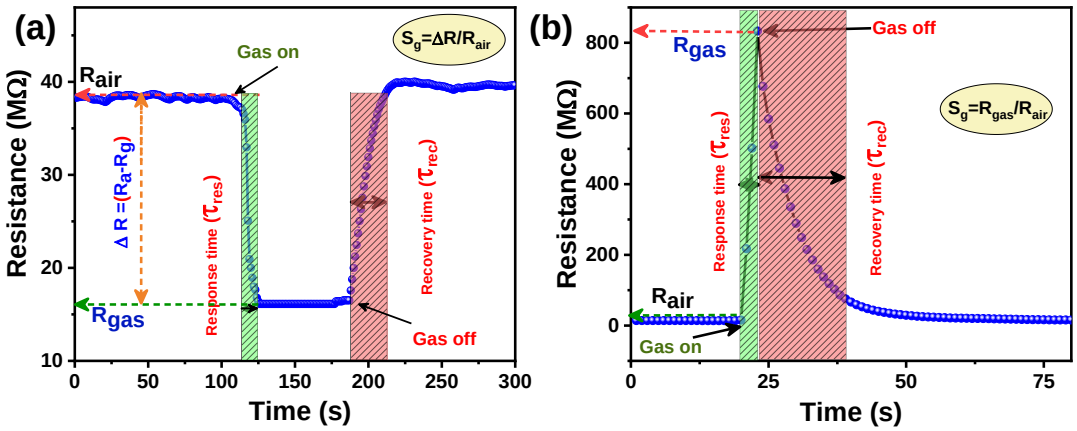

Fig. 1. 4. Dynamic gas sensing response curve of (a) n-type, (b) p-type sensor.

(iv) Operating temperature

The operational temperature is a crucial characteristic of any sensor, defining the temperature at which the sensor achieves its highest sensitivity to a specific concentration of the gas being analyzed. This operational temperature is contingent upon both the composition of the gas and the sensing material. Generally, the sensitivity of the gas sensing material is heavily reliant on the sensor's operational temperature. Initially, sensitivity increases with rising temperature until it reaches a peak, after which it diminishes with further temperature elevation. At lower operating temperatures, the active sites on the sample surface and the target gas molecules lack

the necessary energy for interaction. As temperature increases, sensitivity peaks when an equilibrium is established between the adsorption and desorption rates of gas molecules on the sample surface. Subsequent temperature increases result in a slower adsorption rate of gas molecules on the sensor surface compared to the desorption rate. [21–23]

(v) Selectivity: An essential parameter of an effective sensor is its selectivity towards a particular target gas at its optimal operating temperature. This implies that for a sensor to be practically viable, its response to a specific gas must be sufficiently high while exhibiting negligible response to other gases.

(vi) Stability: The long-term stability of a gas sensor is also a critical feature. It denotes the ability of sensor to maintain consistent performance throughout extended periods of testing.

1.3.3 Primary characteristics affecting the response of the chemiresistive gas sensor

(i) Particle size

Sensitivity of SMO based sensors can be significantly enhanced by reducing the particle size of the synthesized material. Gas sensing is primarily a surface catalytic oxidation-reduction-based phenomenon which highly relies on surface energy. As particle size diminishes, surface energy escalates, which in turn enhances the sensitivity and reduces the response and the recovery time of the fabricated sensors. Nonetheless, larger particle sizes generally diminish effective contact area between particles per unit volume resulting in reduced sensitivity.[24,25]

(ii) Morphology of the synthesized materials

Creating certain morphology out of SMO materials could increase the roughness, active furface area, porosity with in the active sensing material. Elevated surface area higher porosity would give rise to higher no of active sides for gas molecule interaction which results in enhancing the sensitivity of the SMO sensors

(iii) Specific surface area

The specific surface area plays a crucial role in amplifying sensitivity in SMO sensors. Increasing the specific surface area of synthesized SMOs directly enhances the surface-to-volume ratio. This elevation in surface-to-volume ratio provides a greater active surface area for interaction with gas molecules, thereby effectively boosting sensor sensitivity.[26,27]

(iv) Porosity

Porosity is a critical factor influencing the sensitivity as well as the response and recovery times of sensors. A greater number of pores within the sample material would increase the sensitivity of SMO sensors.[28,29]

(v) Doping with in the pure SMO

Pristine SMO based sensors often lack adequate selectivity. Doping of the pure SMO with any strategic dopant could alter electronic band structure which would modify its electrical response. Introducing doping agents such as noble metals, other oxides, polymers, rGO, CNT, etc., enhances selectivity and, in certain instances, also improves other sensor characteristics such as sensitivity, temporal stability, response and recovery times, among others.[30,31]

(vi) Crystalline phases and selectively exposed crystalline planes

The response to a specific gas is influenced by the electronic interaction between the gas molecules and various crystal facets. A stronger interaction typically results in a higher response to that gas. However, it is not always the case that gas molecules exhibit maximum interaction with the highest energy crystal facets. Sometimes, lower energy crystal facets may interact more strongly with a particular gas. In such scenarios, increasing the proportion of higher energy crystal facets could diminish sensor response. [32,33]

(vii) Humidity

Increased relative humidity in the air can occlude active sites on the sensing material, limiting interaction between gas molecules and the sensor. Generally, humidity has predominantly negative effects on chemiresistive sensing by impeding performance. Nevertheless, in rare instances, particularly with oxidizing gases, humidity can enhance sensitivity and improve response and recovery processes.[34,35]

(viii) Formation of heterojunction interface

The formation of heterojunctions, such as p-n, n-n, and p-p configurations, within metal oxides can greatly enhance sensitivity and response-recovery processes. The creation of a heterojunction interface typically reduces charge transfer resistance and improves electron-

hole separation in the composite metal oxide systems. Consequently, this promotes charge transfer-based surface catalytic processes, leading to increased sensitivity in SMO-based heterojunction sensors.[36,37]

1.3.4 Different types of semiconducting metal oxide as gas sensing materials: Comprehensive literature survey

In recent decades, binary metal oxides have been extensively investigated in the realm of gas sensing, particularly within the framework of semiconductor metal oxide (SMO) based gas sensors. Binary metal oxides are compounds formed by the chemical bonding of a metal atom with oxygen. Their appeal stems from several factors including their low synthesis costs, ready availability of raw materials, facile adjustability of band structure, and ease of morphological tuning, rendering them a preferred material choice. Notable examples encompass SnO_2, TiO_2, ZnO, NiO, WO_3, MoO_3, and In_2O_3 among others. However, despite demonstrating moderate sensitivity at elevated operating temperatures, conventional gas sensors based on pure binary metal oxides often exhibit deficiencies in selectivity. Moreover, their performance deteriorates significantly over prolonged periods of operation.

To mitigate these major drawbacks in pure binary metal oxide-based sensors researchers have used several dopants in the pure system. Introducing different dopant atoms in the pure metal oxide system generates several defect states in the system along with that electronic band structure of the pure system get modified. The modification in electronic structure changes the majority carrier density and surface chemistry of the active sensing materials. Additionally, presence of dopant in the pure metal oxide system also enhanced the active surface area of the sample. Adsorption and desorption kinetics on the surface of the doped samples gets modified due to alteration of electronic structure of the system. As cumulative effect of all of these changes sensitivity of the doped system increased substantially compare to the pure samples. In the following section a detail literature review is given discussing the gas sensing performance of pure and doped binary metal oxide based samples. [38–40]

1.3.4.I binary metal oxides-based sensors

L. Liao, et al. had synthesized ZnO with nanorods morphology which showed 2.6% response towards 100 ppm H_2S at 100 ºC [41]. Vahid et al. reported that Chromium loaded ZnO showed

27% response towards 150 ppm H_2S at 350 ºC operating temperature.[42] Fan f et al. had synthesized tubular hierarchical ZnO out of porous nanosheet by self-assembling and the fabricated sensor using this material had shown 1.6 folds response towards 2 ppm ethanol at 250 ºC operating temperature with response and recovery time of 14s, 18s respectively. [43] Ekasiddh et al. demonstrated that the introduction of Pt and Nb into ZnO nanostructures led to a notable enhancement in their ability to detect acetone. Specifically, ZnO:Pt and ZnO:Nb exhibited response levels of 188 and 224, respectively, when exposed to 1000 ppm of acetone at their optimal operating temperature.[44] Sett et al. synthesized ZnO nanorods doped with varying concentrations of cobalt using the hydrothermal method. Among these, the sensor based on 8% Co-doped ZnO exhibited the highest sensitivity to H_2 gas at 300 °C compared to all other sensors. This enhanced sensitivity was be attributed to its superior specific surface area. [45] Guoxing et al. had reported that Co-doped ZnO hierarchical microspheres exhibited selective sensing capabilities towards 1,2-dichloroethane, with rapid response and recovery times of 30 s and 5 s, respectively.[46] Li et al. synthesized hierarchical ZnO nanocages by treating MOF-5 which exhibited a high sensitivity to acetone, manifesting a response rate of 6.36 when exposed to 500 ppb of acetone at a temperature of 300°C.[47] Geng et al. had synthesized rGO-ZnO nanosheets based p-n junction which had exhibited ppb-level NO_2 sensing with significant sensitivity under white light illumination at room temperature.[48]

Z. Song et al, synthesized SnO_2 nanowire and rGO nanocomposite via Spin coating which had showed 33 folds response towards 50 ppm H_2S at room temperature with response time of 2s and recovery time of 292s with lower detection limit of 0.01 ppm.[49] Lin et al. had synthesized coral like nano porous-SnO_2 wet chemical method test coupled with annealing process. Subsequently, they tested sensors based on this material and observed an excellent response to various volatile organic compounds (VOCs) within the temperature range of 150–190 °C. Specifically, at 150°C, the sensor exhibited differential responses to VOCs in the following order: formaldehyde (HCHO) > ethanol (C_2H_5OH) > acetone (C_3H_6O) > methanol (CH_4O) > toluene (C_7H_8) > benzene (C_6H_6).[50] Bi et al. synthesized three-dimensional flower-like Pt-loaded hierarchical SnO_2 nanostructures using a hydrothermal route. Among the various compositions tested, the sensor containing 2.0 mol% Pt-doped SnO_2 exhibited the highest sensitivity to isopropanol with exceptional selectivity, particularly at an operating temperature of 250 °C.[51] Jia et al. had developed a nuclear shell structure within a PANI-T-SnO_2 nanotube composite material using argon plasma treatment techniques. Under ambient

conditions at room temperature and 50% relative humidity, the sensor based on the PANI-T-SnO_2 composite exhibited the highest sensitivity to ammonia (NH_3) with outstanding long-term stability.[52]

Wang et al. had prepared a 3D hierarchical TiO_2 nanoflower based gas sensor which showed highly sensitive and selective ethanol sensing properties with fast response and recovery time at room temperature. [53] Zhao et al. had synthesized C-doped TiO_2 nanoparticles through solvothermal route. Carbon doped TiO_2 nanoparticles-based sensor showed enhanced sensitivity towards ethanol at 170 ºC operating temperature. [54] Murali et al. had successfully prepared N-doped graphene quantum dots (NGQDs) decorating TiO_2 composite. The sensors made from these materials showed excellent nitrogen monoxide (NO) detection properties at room temperature. [55] Wang et al. had prepared La and V co-doped TiO_2 powders based sensor which exhibited selective methylbenzene sensing properties at optimum operating temperature of 300ºC. [56]

Miao et al. prepared NiO nano flower architectures through hydrothermal method and the fabricated sensor based on this material depicted enhanced sensitivity towards ethanol.[57] Liu et al. had synthesized flower-like NiO-decorated ZnO based sensor. Among various composition 8 wt % NiO-decorated ZnO based sensor showed maximum response to acetone at 375 ºC.[58] Chao et al. had fabricated NiO-In_2O_3 composite nanofibers based sensor which exhibited highly sensitive and selective response to 100 ppm ethanol gas at 300 ºC. [59] Nalage et al. had prepared PPy –NiO nano hybrid based sensor which showed towards excellent sensitivity to 100 ppm NO_2 at room temperature with fast response and recovery time. [60]

Lupan et al. had prepared CuO nanowire based sensor which showed highest response of 313 towards 100 ppm ethanol with excellent selective nature at 250 ºC operating temperature. [61] Rai et al. had synthesized Au@Cu_2O core–shell nanoparticles. The fabricated sensor out of that material showed 1.69 times higher sensitivity to 1000 ppm CO at 200 ºC than pure Cu_2O based sensor with relatively fast response and recovery time (3.7/6.45 min).[61,62] Wang et al. had prepared Cu_2O–CuO micro-flowers based sensor which exhibited maximum 5 folds response towards 100 ppb NO_2 at 187 ºC. [63] Roy et al. had synthesized MoS_2–Cu_2O composite based sensor which had showed 4.35 folds response towards 500 ppb acetone with a fast response and recovery time of 77s and 57s respectively at room temperature. [64]

M. Hjiri et al. had Synthesized α-Fe_2O_3 Nanoparticles via Hydrothermal Technique which had exhibited enhanced p-type NO_2 sensing properties at the operating temperature of 200 °C.[65] Q. Qin et al. prepared the ternary composite of γ-Fe_2O_3/SnO_2/RGO based sensor which responded to NO gas with response value equal to 4.09 in 12 s. [66] S. Liang et al. fabricated α-Fe_2O_3-graphene composite nanostructure-based sensor which showed enhanced ethanol sensing property.[67] B. Yang had synthesized Co_3O_4-decorated flower-like α-Fe_2O_3 microspheres which had showed enhanced sensitivity of 16.1 to 100 ppm ethanol at 170 °C with rapid response and recovery time of 3.3 s and 5.4 s respectively. [68]

A. M. Shboul et al. had prepared CuAc modified In_2O_3 Nanoparticles-based printed chemiresistive sensor which showed selective H_2S gas sensing response in high humid background environment. [69] B. Han reported that flower-like In_2O_3 synthesized through Hydrothermal route showed excellent chemiresistive isoprene sensing property up to 5 ppb concentration at 190 °C.[70] Chih-Wei Chen et al. had fabricated needle-like In_2O_3 based chemiresistive sensor which showed 35 folds p-type response to 10 ppm NO_2 at 100ºC operating temperature.[71] Z. H. Ma et al. reported that 3 mol% Pr-doped In_2O_3 nanoparticles based chemiresitive sensor showed 106 responses to 50 ppm ethanol at 240 °C.[72]

D. Kwak had fabricated MoO_3 nanoribbon-based chemiresistive sensor which exhibited substantial sensitivity of 0.72 towards 50 ppm NH_3 at 450 °C with a fast response time of 21s along with excellent selectivity among different cross sensing gases. [73] T. Thomas et al. deposited MoO_3 nanorods on silicon substrate to fabricate p-Si/ MoO_3 nano-hybrid system which showed excellent CO_2 at 250 °C.[74] P. Srinivasan had prepared α-MoO_3 nanorods based sensor which showed high sensitivity towards methylamine at 450 W with substantial selectivity.[73] Y. Liu had prepared MoO_3-SnO_2 nanocomposite based sensor which had showed high sensitivity of 12.7 to 100-ppm NH_3 at 280 °C with fast response and recovery time of 13s and 2s respectively.[75,76]

Over the past 5-10 years, there has been a noticeable shift in the selection of materials used as active sensing agents in gas sensing. Despite various approaches such as doping, metal ion modification, and the incorporation of conducting polymers to enhance the sensitivity and selectivity of metal oxide-based sensors, several limitations persist. Binary metal oxide-based sensors suffer from drawbacks including elevated operating temperatures, limited selectivity, inadequate resolution for distinguishing between different trace gas concentrations, prolonged

response and recovery times, and long-term instability. Recent research indicates that ferrite materials with diverse crystal structures such as perovskite, spinel, and garnet exhibit superior surface catalytic activity compared to binary metal oxides.

The perovskite structure of ferrites offers a higher density of active sites on their exposed surface area, facilitating the adsorption and desorption of various gases. Transition metal ions within perovskite ferrite materials commonly exhibit multiple valence states, promoting efficient charge transport and thereby enhancing their sensing capabilities. Additionally, the abundant morphology and porous structure of ferrite materials result in a large active surface area, providing ample sites for gas reactions. Furthermore, perovskite structures demonstrate significant chemical stability, ensuring sustained gas sensing performance over extended periods. The subsequent section provides a detailed literature review on chemiresistive gas sensors based on ferrites. [77–80]

1.3.4.II. Ferrite based sensors

P. Ghadage reported that 1-wt.% GO-loaded $BiFeO_3$ based gas sensor exhibited highly selective response of 89% towards 500 ppm acetone at 250 °C operating temperature.[81] S. Chakraborty et al. had fabricated pure $BiFeO_3$ based chemiresistive sensor which had exhibited 2.12 folds response towards 30 ppm CO at the optimum operating temperature of 350 °C with response time of 25s and recovery time of 13s.[82] S. Chakraborty et al. had prepared nanocrystalline bismuth ferrite based sensors which exhibited excellent sensing performance to acetone in high humid background.[83] X Liu et al. had synthesized Er doped $BiFeO_3$ nanoparticles and the sensor as prepared sensor using this material showed 43.2 response to 100 ppm acetone at 300°C. [84]

A.K. Yadav Fabrication of lanthanum ferrite-based gas sensor Which had exhibited 394% response towards 5000 ppm liquefied petroleum with response time of 100s and recovery time of 400s. [85] Y.M. Zhang et al. successfully produced a remarkably responsive formalin sensor utilizing Ag-doped $LaFeO_3$. This sensor exhibited a response ratio of 25 when exposed to 1 ppm formalin at a temperature of 90°C, demonstrating response and recovery times of 65 seconds and 60 seconds, respectively.[86] J. Zhang et al. reported that a sensor constructed from zinc-doped $LaFeO_3$ displayed a notable response rate of 38 when exposed to 100 ppm formaldehyde at 250°C, accompanied by response and recovery times of 100s each.[87]

Y. Wang et al. reported that perovskite-type $SrFeO_3$ oxide based gas sensor exhibited sensitive and selective C_2H_5OH sensing properties at 325°C. [88] M. Manikandan et al. had reported that sputtered $SrFeO_{2.97}$ based film exhibited highly sensitive and selective H_2S sensing nature at 60°C. [89]

Li Lv et al. reported that 0.5 % Sb-doped three-dimensional spherical $ZnFe_2O_4$ based sensor exhibited 35.5 response to 100 ppm N-butanol at 250 °C showcasing both high selectivity and stability.[90] Cao et al. had synthesized $ZnFe_2O_4$ nanorods through solid-state method having surface area 67.14 m^2g^{-1}. The prepared sensor using as synthesized material exhibited excellent response of 29.1% towards 100 ppm ethanol at 260 °C with fast response and recovery time of 2s and 7s respectively.[91] Yan et al. had prepared Au doped $ZnFe_2O_4$ microspheres via solvothermal method and 2 wt% Au doped $ZnFe_2O_4$ based sensor showed enhanced response towards H_2s at room temperature with response and recovery time of 46s and 629s respectively.[92]

M. M. Liu et al. had fabricated hydrothermally synthesized $SmFeO_3$ based sensor which showed an elevated response of 117 to 100 ppm ethylene glycol gas at 180 °C with excellent selectivity and repeatability. [93] A. Gaiardo et al. had fabricated $SmFeO_3$ Nanostructured based Gas Sensor which showed repeatable sensing performance towards CO gas at 350ºC. [94] H. Liu et al. had prepared $SmFeO_3$ planar electrode sensor which had showed 29.2 response to 30 ppm acetone under light illumination at 120 °C.[95]

P. Rao et al. fabricated Cu doped $NiFe_2O_4$ thin films-based sensor using spray pyrolysis deposition technique which showed elevated response to ethanol.[96,97] R. Kashyap et al. had prepared nickel ferrite ($NiFe_2O_4$) nanoparticles using auto-combustion route and the fabricated sensor utilizing the synthesized material showed 10% response to 100 ppm ammonia at 250 °C with the response and recovery time 100 s and 119 s respectively.[97]

To enhance the gas sensing capabilities of semiconductor metal oxide-based chemiresistive gas sensors, scientists are exploring the fabrication of composite materials combining binary metal oxides and ferrites. Recent studies indicate that heterojunction materials consistently exhibit superior responses compared to pristine metal oxides or pure ferrites. Research demonstrates

that composite materials utilizing two distinct metal oxides offer synergistic effects on surface catalytic and gas sensing properties. Typically, metal oxide heterostructures consist of two materials with disparate energy band gaps and electronic structures, facilitating enhanced charge separation and efficient charge transport.[98–101]

Therefore, heterojunction metal composites offer advantages over pure semiconductor metal oxides (SMOs). Despite the limited application of heterostructure materials in gas sensing, the following section discusses recent research on heterojunction-based gas sensing to provide insight into the current status of SMO-based gas sensing.

1.3.4.III. Heterojunction based sensors

$ZnO/BiFeO_3$ heterojunction interface modulation and rGO modification for detection of triethylamine Check for updates exhibited maximum 13.4 response to 10 ppm TEA at 112 °C, which were enhanced by 2.2 times than the pure ZnO based sensor.[102] Lifang He et al. had synthesized SnO_2-$ZnFe_2O_4$ spherical core-shell heterostructure and the detail sensing study revealed that the composite of $ZnFe_2O_4$ and SnO_2 in 1:0.7 ratio had showed maximum 120 response to 100 ppm acetone 210℃ with the lower detection limit of reach 0.1 ppm among all composition. [103] Z. Xia et al. had prepared SnO_2 quantum dot sensitized $LaFeO_3$ composites. Sensing study showed that $LaFeO_3$/2.5 wt% SnO_2 QDs composite exhibited maximum 31.5 response to 100 ppm HCOOH with a low detection limit of 1 ppm at 210 ℃ which was superior to both the SnO_2 QDs and pure $LaFeO_3$ based sensors. [103,104] Y Xu et al. had synthesized the $NiFe_2O_4$-NiO composite nanosheets with different Fe contents. The p-p heterojunction composite based sensors showed elevated acetone sensing response of 56.0 to 200 ppm of acetone which was much superior to the pure NiO and pure $NiFe_2O_4$ based sensors.[105] Y. Li et al. had prepared $ZnFe_2O_4$/α-Fe_2O_3 porous microrods based sensors. The composite based sensor had showed 42.4 response to 100 ppm TEA which was 20 times higher than the pure Fe_2O_3.[106]

1.4 Objectives and thesis outline

As discuss in this chapter development of semiconductor metal oxide based chemiresistive sensors drawn attention in the scientific community because of its easy useability for detecting disease by breath analysis and also detecting environmental pollution in the last decade or so.

The primary objective of the thesis is to develop SMO based chemiresistive sensor which could selectively detect certain gas or VOCs in presence of several other interfering gases.

Extensive literature review underscores the pivotal significance of selecting the appropriate material for the active sensing layer which significantly influences the sensitivity and selectivity of gas or VOC detection. Furthermore, beyond identifying materials for enhanced sensitivity, comprehending the gas sensing mechanism from an atomistic perspective is essential to elucidate why certain materials exhibit enhanced sensitivity to specific gases. Following a thorough literature survey, ZnO has been chosen as the active sensing material for the initial two studies (chapter 3 and 4). Various dopants were employed to enhance the sensitivity and selectivity of the sensors in these works.

Subsequently, transitioning from binary metal oxides, the focus shifted towards ferrite-based materials. Drawing from prior research, perovskite yttrium ferrite was selected as the sensing material. In chapter 5 and 6 detailed studies were performed to understand the gas sensing property of yttrium ferrite which were synthesized in different synthesis process and also in different phases Finally, in the concluding chapter, a heterojunction material combining binary metal oxide and ferrite was prepared. This study explored how the heterojunction material exhibited superior sensing performance compared to the individual pure materials.

Various synthesis methods including simple precipitation, sol-gel, hydrothermal, and reflux techniques was opted in the entire thesis work to produce desired nanostructures that enabled remarkable enhancement in their sensing properties. These nanostructures exhibited outstanding gas sensing performance towards diverse target gases such as ethanol, ammonia, formalin, acetone, and CO. A range of sophisticated characterization techniques including XRD, FESEM, TEM, EDX, XPS, FTIR, BET, UV-Vis, PL, and EPR were employed to analyze the phase, crystal structure, morphology, elemental and chemical composition, specific surface area, band gap energy, and presence of defect states in the synthesized samples. Subsequently, Taguchi-type sensors were fabricated utilizing the synthesized materials as active sensing elements, and a comprehensive investigation into their gas sensing characteristics was conducted.

Furthermore, the thesis explored the effects of dopants, morphology, presence of defect states, oxygen vacancies, multiple oxidation states, and modifications in the electric band structure on

gas sensing properties. This investigation was conducted from both experimental and theoretical perspectives.

The thesis is organized into eight chapters, structured as follows:

Chapter- I

This initial chapter commences with a general introduction to various types of sensors and their indispensability in daily life. Gas sensors, in particular, hold significant importance in today's world, finding applications ranging from detecting environmental hazardous gases to identifying volatile organic compounds (VOCs) in exhaled breath. Among the plethora of gas sensing techniques available, this research thesis focuses on SMO (Semiconductor Metal Oxide) based chemiresistive gas sensors. The chapter extensively covers the background of SMO-based chemiresistive gas sensor development, their principles, various parameters of gas sensors, and the underlying sensing mechanisms. Additionally, a literature review of gas sensing using different nanostructures is thoroughly discussed within this chapter.

Chapter- II

Chapter-II delves into various experimental methods for preparing selected nanoparticles and their corresponding characterization techniques. Different preparation methods such as sol-gel, hydrothermal, reflux, solution precipitation techniques are briefly elucidated. Moreover, characterization techniques including XRD, BET, FE-SEM, EDAX, TEM, UV-Visible, PL spectra, and FTIR spectra are discussed in detail, highlighting their roles in characterizing different samples.

Chapter- III

Excess ethanol in exhaled breath is an indicator of intoxication and a biomarker for fatty liver disease. Here in this work, Al and Y co-doped ZnO nanopowder based sensors were fabricated which would detect trace ethanol in human exhaled breath with high sensitivity and selectivity. The synthesized nanopowders were characterized using various sophisticated techniques, viz. XRD, XPS, FTIR, FESEM, EDX, BET surface area analysis, UV-Vis and PL spectroscopy. Among the different fabricated sensors 5% Y and 1% Al co-doped ZnO based sensor showed enhanced response of 62.8% to 1 ppm ethanol with ultra-fast response and recovery time of 0.77s and 8.1s respectively. Moreover, the optimized sensor exhibited

adequate selectivity along with long term stable response. Enhanced sensing performance was explained in terms of elevated surface area, higher amount of oxygen and donor defect states in the co-doped sample. Finally a simulated breath study were performed using the optimize sensor which delineates the fabricated sensor could detect ethanol in simulated breath sample as well which makes the fabricated sensor a potential candidate for both the detection of liver problem as well as commercial breath ethanol analyzer for drunken driving detection.

Chapter- IV

Trace ammonia sensor with high selectivity and sensitivity is essential for the early and non-invasive diagnosis of renal disease and helicobacter pylori-induced gastropathy. In this chapter, different Li- doped ZnO based sensors were fabricated among which 5-wt % Li doped ZnO based sensor showed maximum 43 % sensitivity to 1 ppm NH_3 with ultrafast response and recovery times of 0.72 s and 1 s respectively. Increased specific surface area, plentiful oxygen defects, and the presence of donor defects significantly contribute in improving the NH_3 sensing abilities of the doped samples. Additionally, the theoretical analysis through Density Functional Theory (DFT) demonstrates how the sensing of ammonia occurs by altering the electrical band. Finally, a simulated breath study was conducted to assess the real-time applicability of the sensor.

Chapter- V

Formalin (HCHO) is identified as one of the key toxic gas in indoor as well as out door environment which creates numerous numbers of health hazardous. In this chapter hydrothermally synthesized hexagonal $YFeO_3$ based sensor was fabricated which demonstrated a robust p-type response (approximately 3.12 times increase) to 1 ppm formalin, accompanied by an exceptionally rapid response time of 3s. The sensor also displayed a lower detection limit of 500 ppb at an optimal operating temperature of 240°C. The improved formalin sensing capabilities of the hexagonal $YFeO_3$ (YFO) based sensor can be attributed to a synergistic effect of an increased surface area, a reduced bandgap energy, and the existence of bivalent oxidation states of iron, along with the presence of oxygen defects.

Chapter- VI

Acetone is a breath bio marker of diabetes, so developing a highly sensitive and selective acetone sensor could save millions of life by early detection. In this chapter an acetone sensor

was developed using orthorhombic $YFeO_3$ which was synthesized via solution combustion route. Among different crystal phase of $YFeO_3$, orthorhombic $YFeO_3$ showed maximum 10.25 folds p-type response towards 1 ppm acetone with ultrafast response time of 0.2s. Co-existence of Fe^{2+} an Fe^{3+} ions, oxygen vacancies, in the samples were confirmed through detailed XPS study, which plays significant role in enhancing acetone sensing response of orthorhombic $YFeO_3$. The Eley-Rideal model has been utilized to elucidate the preference for acetone over other interfering gases. Density Functional Theory (DFT) calculations reveal that the adsorption energy, a crucial parameter for gas sensing performance of materials, is lower for the orthorhombic phase.

Chapter- VII

At the last part of the thesis ZnO-$ZnFe_2O_4$ heterojunction composites in different ratio were synthesized through two steps synthesis process. The developed sensors using the heterojunction samples reveals excellent CO sensing capabilities. Sensor based on ZnO and $ZnFe_2O_4$ in 50-50% molar ratio (ZZF-11) has showed significantly high response even to 1ppm CO gas (S= 29.4%) among all other pure and composite samples. Formation of heterostructure interface and transfer of charges at the interface was established through experimental and theoretical study. Various experimental results indicate that the presence of the highest ferric bivalence state, maximum defects, chemisorbed oxygen content, donor defect states, largest surface area, and stable photocurrent in the ZZF-11 sample collectively contribute to exhibiting the best sensing activity. The study highlights the promising potential of a CO gas sensor, which could serve as a vital tool in detecting air pollutants.

Chapter- VIII

the final chapter summarizes the key findings, the major conclusions and future direction for research in the field of SMO based chemiresistive gas sensor. The introduction of various strategic dopants into pure perovskite yttrium ferrite, along with the synthesis of different heterojunction composite materials, is discussed as a means to further enhance sensing capabilities. These advancements hold promise for continuous and point-of-care testing in the field of SMO-based sensing for both in breath analysis and environmental hazardous detection.

1.5 Reference

[1] M. Javaid, A. Haleem, R.P. Singh, S. Rab, R. Suman, Significance of sensors for industry 4.0: Roles, capabilities, and applications, Sensors International 2 (2021) 100110. https://doi.org/10.1016/j.sintl.2021.100110.

[2] M. Pirzada, Z. Altintas, Historical development of sensing technology, in: Fundamentals of Sensor Technology, Elsevier, 2023: pp. 3–16. https://doi.org/10.1016/B978-0-323-88431-0.00006-5.

[3] M. Javaid, A. Haleem, S. Rab, R. Pratap Singh, R. Suman, Sensors for daily life: A review, Sensors International 2 (2021) 100121. https://doi.org/10.1016/j.sintl.2021.100121.

[4] A. Airoudj, D. Debarnot, B. Bêche, F. Poncin-Epaillard, Design and Sensing Properties of an Integrated Optical Gas Sensor Based on a Multilayer Structure, Anal Chem 80 (2008) 9188–9194. https://doi.org/10.1021/ac801320g.

[5] W. Weppner, Solid-state electrochemical gas sensors, Sensors and Actuators 12 (1987) 107–119. https://doi.org/10.1016/0250-6874(87)85010-2.

[6] C.O. Park, J.W. Fergus, N. Miura, J. Park, A. Choi, Solid-state electrochemical gas sensors, Ionics (Kiel) 15 (2009) 261–284. https://doi.org/10.1007/s11581-008-0300-6.

[7] G. Korotcenkov, Materials for Capacitance-Based Gas Sensors, in: 2013: pp. 365–376. https://doi.org/10.1007/978-1-4614-7165-3_16.

[8] D.D.L. Chung, First review of capacitance-based self-sensing in structural materials, Sens Actuators A Phys 354 (2023) 114270. https://doi.org/10.1016/j.sna.2023.114270.

[9] L. Xu, A.P. Weber, G. Kasper, Capacitance-based concentration measurement for gas-particle system with low particles loading, Flow Measurement and Instrumentation 11 (2000) 185–194. https://doi.org/10.1016/S0955-5986(00)00018-2.

[10] M.V. Nikolic, V. Milovanovic, Z.Z. Vasiljevic, Z. Stamenkovic, Semiconductor Gas Sensors: Materials, Technology, Design, and Application, Sensors 20 (2020) 6694. https://doi.org/10.3390/s20226694.

[11] J.-H. Lee, Technological realization of semiconducting metal oxide–based gas sensors, in: Gas Sensors Based on Conducting Metal Oxides, Elsevier, 2019: pp. 167–216. https://doi.org/10.1016/B978-0-12-811224-3.00004-4.

[12] J. Zhang, Z. Qin, D. Zeng, C. Xie, Metal-oxide-semiconductor based gas sensors: screening, preparation, and integration, Physical Chemistry Chemical Physics 19 (2017) 6313–6329. https://doi.org/10.1039/C6CP07799D.

[13] A. Dey, Semiconductor metal oxide gas sensors: A review, Materials Science and Engineering: B 229 (2018) 206–217. https://doi.org/10.1016/j.mseb.2017.12.036.

[14] M. Motooka, S. Uno, Improvement in Limit of Detection of Enzymatic Biogas Sensor Utilizing Chromatography Paper for Breath Analysis, Sensors 18 (2018) 440. https://doi.org/10.3390/s18020440.

[15] J.H. Lee, M.S. Park, H. Jung, Y.-S. Choe, W. Kim, Y.G. Song, C.-Y. Kang, H.-S. Lee, W. Lee, Selective C2H2 detection with high sensitivity using SnO2 nanorod based gas sensors integrated with a gas chromatography, Sens Actuators B Chem 307 (2020) 127598. https://doi.org/10.1016/j.snb.2019.127598.

[16] P.T. Moseley, Progress in the development of semiconducting metal oxide gas sensors: a review, Meas Sci Technol 28 (2017) 082001. https://doi.org/10.1088/1361-6501/aa7443.

[17] X. Gao, T. Zhang, An overview: Facet-dependent metal oxide semiconductor gas sensors, Sens Actuators B Chem 277 (2018) 604–633. https://doi.org/10.1016/j.snb.2018.08.129.

[18] A. Staerz, U. Weimar, N. Barsan, Current state of knowledge on the metal oxide based gas sensing mechanism, Sens Actuators B Chem 358 (2022) 131531. https://doi.org/10.1016/j.snb.2022.131531.

[19] K.G. Krishna, S. Parne, N. Pothukanuri, V. Kathirvelu, S. Gandi, D. Joshi, Nanostructured metal oxide semiconductor-based gas sensors: A comprehensive review, Sens Actuators A Phys 341 (2022) 113578. https://doi.org/10.1016/j.sna.2022.113578.

[20] L. Liu, Y. Wang, Y. Liu, S. Wang, T. Li, S. Feng, S. Qin, T. Zhang, Heteronanostructural metal oxide-based gas microsensors, Microsyst Nanoeng 8 (2022) 85. https://doi.org/10.1038/s41378-022-00410-1.

[21] C. Wang, L. Yin, L. Zhang, D. Xiang, R. Gao, Metal Oxide Gas Sensors: Sensitivity and Influencing Factors, Sensors 10 (2010) 2088–2106. https://doi.org/10.3390/s100302088.

[22] S. Singh, S. S, P. Varma, G. Sreelekha, C. Adak, R.P. Shukla, V.B. Kamble, Metal oxide-based gas sensor array for VOCs determination in complex mixtures using machine learning, Microchimica Acta 191 (2024) 196. https://doi.org/10.1007/s00604-024-06258-8.

[23] J. Yoon, J. Kim, T. Kim, Y.J. Hong, Y.C. Kang, J. Lee, A New Strategy for Humidity Independent Oxide Chemiresistors: Dynamic Self-Refreshing of In_2O_3 Sensing Surface Assisted by Layer-by-Layer Coated CeO_2 Nanoclusters, Small 12 (2016) 4229–4240. https://doi.org/10.1002/smll.201601507.

[24] X. Wan, J. Wang, L. Zhu, J. Tang, Gas sensing properties of Cu_2O and its particle size and morphology-dependent gas-detection sensitivity, J. Mater. Chem. A 2 (2014) 13641–13647. https://doi.org/10.1039/C4TA02659D.

[25] M.A. Han, H.-J. Kim, H.C. Lee, J.-S. Park, H.-N. Lee, Effects of porosity and particle size on the gas sensing properties of SnO2 films, Appl Surf Sci 481 (2019) 133–137. https://doi.org/10.1016/j.apsusc.2019.03.043.

[26] S. Kanan, O. El-Kadri, I. Abu-Yousef, M. Kanan, Semiconducting Metal Oxide Based Sensors for Selective Gas Pollutant Detection, Sensors 9 (2009) 8158–8196. https://doi.org/10.3390/s91008158.

[27] M. Tereshkov, T. Dontsova, B. Saruhan, S. Krüger, Metal Oxide-Based Sensors for Ecological Monitoring: Progress and Perspectives, Chemosensors 12 (2024) 42. https://doi.org/10.3390/chemosensors12030042.

[28] Y. Yu, Y. Tan, W. Niu, S. Zhao, J. Hao, Y. Shi, Y. Dong, H. Liu, C. Huang, C. Gao, P. Zhang, Y. Wu, L. Zeng, B. Du, Y. He, Advances in Synthesis and Applications of Single-Atom Catalysts for Metal Oxide-Based Gas Sensors, Materials 17 (2024) 1970. https://doi.org/10.3390/ma17091970.

[29] S. Navale, M. Shahbaz, A. Mirzaei, S.S. Kim, H.W. Kim, Effect of Ag Addition on the Gas-Sensing Properties of Nanostructured Resistive-Based Gas Sensors: An Overview, Sensors 21 (2021) 6454. https://doi.org/10.3390/s21196454.

[30] N. Chakraborty, A. Sanyal, S. Das, D. Saha, S.K. Medda, S. Mondal, Ammonia Sensing by $Sn_{1-x}V_xO_2$ Mesoporous Nanoparticles, ACS Appl Nano Mater 3 (2020) 7572–7579. https://doi.org/10.1021/acsanm.0c01183.

[31] K. Suematsu, M. Sasaki, N. Ma, M. Yuasa, K. Shimanoe, Antimony-Doped Tin Dioxide Gas Sensors Exhibiting High Stability in the Sensitivity to Humidity Changes, ACS Sens 1 (2016) 913–920. https://doi.org/10.1021/acssensors.6b00323.

[32] J. Li, D. Xu, Tetragonal faceted-nanorods of anatase TiO2 single crystals with a large percentage of active {100} facets, Chemical Communications 46 (2010) 2301. https://doi.org/10.1039/b923755k.

[33] Y. Liang, Y. Yang, H. Zhou, C. Zou, K. Xu, X. Luo, T. Yu, W. Zhang, Y. Liu, C. Yuan, A systematic study on the crystal facets-dependent gas sensing properties of anatase TiO2 with designed {010}, {101} and {001} facets, Ceram Int 45 (2019) 6282–6290. https://doi.org/10.1016/j.ceramint.2018.12.110.

[34] L. Filipovic, A. Lahlalia, Review—System-on-Chip SMO Gas Sensor Integration in Advanced CMOS Technology, J Electrochem Soc 165 (2018) B862–B879. https://doi.org/10.1149/2.0731816jes.

[35] W. Liu, L. Xu, K. Sheng, X. Zhou, B. Dong, G. Lu, H. Song, A highly sensitive and moisture-resistant gas sensor for diabetes diagnosis with Pt@In2O3 nanowires and a molecular sieve for protection, NPG Asia Mater 10 (2018) 293–308. https://doi.org/10.1038/s41427-018-0029-2.

[36] J. Zhang, X. Jia, D. Lian, J. Yang, S. Wang, Y. Li, H. Song, Enhanced selective acetone gas sensing performance by fabricating ZnSnO3/SnO2 concave microcube, Appl Surf Sci 542 (2021) 148555. https://doi.org/10.1016/j.apsusc.2020.148555.

[37] W. Guo, L. Huang, X. Liu, J. Wang, J. Zhang, Enhanced isoprene gas sensing performance based on p-CaFe2O4/n-ZnFe2O4 heterojunction composites, Sens Actuators B Chem 354 (2022) 131243. https://doi.org/10.1016/j.snb.2021.131243.

[38] N. Chakraborty, S. Mondal, Dopant-mediated surface charge imbalance for enhancing the performance of metal oxide chemiresistive gas sensors, J Mater Chem C Mater 10 (2022) 1968–1976. https://doi.org/10.1039/D1TC05144J.

[39] K. Grossmann, U. Weimar, N. Barsan, Semiconducting Metal Oxides Based Gas Sensors, in: 2013: pp. 261–282. https://doi.org/10.1016/B978-0-12-396489-2.00008-4.

[40] J. Huang, Q. Wan, Gas Sensors Based on Semiconducting Metal Oxide One-Dimensional Nanostructures, Sensors 9 (2009) 9903–9924. https://doi.org/10.3390/s91209903.

[41] L. Liao, H.B. Lu, J.C. Li, H. He, D.F. Wang, D.J. Fu, C. Liu, W.F. Zhang, Size Dependence of Gas Sensitivity of ZnO Nanorods, The Journal of Physical Chemistry C 111 (2007) 1900–1903. https://doi.org/10.1021/jp065963k.

[42] V. Najafi, S. Zolghadr, S. Kimiagar, Remarkable reproducibility and significant sensitivity of ZnO nanoparticles covered by Chromium (III) oxide as a hydrogen sulfide gas sensor, Optik (Stuttg) 182 (2019) 249–256. https://doi.org/10.1016/j.ijleo.2019.01.015.

[43] F. Fan, P. Tang, Y. Wang, Y. Feng, A. Chen, R. Luo, D. Li, Facile synthesis and gas sensing properties of tubular hierarchical ZnO self-assembled by porous nanosheets, Sens Actuators B Chem 215 (2015) 231–240. https://doi.org/10.1016/j.snb.2015.03.048.

[44] E. Wongrat, N. Chanlek, C. Chueaiarrom, W. Thupthimchun, B. Samransuksamer, S. Choopun, Acetone gas sensors based on ZnO nanostructures decorated with Pt and Nb, Ceram Int 43 (2017) S557–S566. https://doi.org/10.1016/j.ceramint.2017.05.296.

[45] D. Sett, D. Basak, Highly enhanced H2 gas sensing characteristics of Co:ZnO nanorods and its mechanism, Sens Actuators B Chem 243 (2017) 475–483. https://doi.org/10.1016/j.snb.2016.11.163.

[46] G. Zhu, H. Xu, Y. Liu, X. Xu, Z. Ji, X. Shen, Z. Xu, Enhanced gas sensing performance of Co-doped ZnO hierarchical microspheres to 1,2-dichloroethane, Sens Actuators B Chem 166–167 (2012) 36–43. https://doi.org/10.1016/j.snb.2011.11.048.

[47] W. Li, X. Wu, N. Han, J. Chen, X. Qian, Y. Deng, W. Tang, Y. Chen, MOF-derived hierarchical hollow ZnO nanocages with enhanced low-concentration VOCs gas-sensing performance, Sens Actuators B Chem 225 (2016) 158–166. https://doi.org/10.1016/j.snb.2015.11.034.

[48] X. Geng, P. Lu, C. Zhang, D. Lahem, M.-G. Olivier, M. Debliquy, Room-temperature NO2 gas sensors based on rGO@ZnO1-x composites: Experiments and molecular dynamics simulation, Sens Actuators B Chem 282 (2019) 690–702. https://doi.org/10.1016/j.snb.2018.11.123.

[49] Z. Song, Z. Wei, B. Wang, Z. Luo, S. Xu, W. Zhang, H. Yu, M. Li, Z. Huang, J. Zang, F. Yi, H. Liu, Sensitive Room-Temperature H $_2$ S Gas Sensors Employing SnO $_2$ Quantum Wire/Reduced Graphene Oxide Nanocomposites, Chemistry of Materials 28 (2016) 1205–1212. https://doi.org/10.1021/acs.chemmater.5b04850.

[50] Z. Lin, W. Song, H. Yang, Highly sensitive gas sensor based on coral-like SnO2 prepared with hydrothermal treatment, Sens Actuators B Chem 173 (2012) 22–27. https://doi.org/10.1016/j.snb.2012.04.057.

[51] W. Bi, W. Xiao, S. Liu, Synthesis of Pt-doped SnO2 flower-like hierarchical structure and its gas sensing properties to isopropanol, J Mater Sci 56 (2021) 6095–6109. https://doi.org/10.1007/s10853-020-05655-7.

[52] A. Jia, B. Liu, H. Liu, Q. Li, Y. Yun, Interface Design of SnO2@PANI Nanotube With Enhanced Sensing Performance for Ammonia Detection at Room Temperature, Front Chem 8 (2020). https://doi.org/10.3389/fchem.2020.00383.

[53] M. Wang, Y. Zhu, D. Meng, K. Wang, C. Wang, A novel room temperature ethanol gas sensor based on 3D hierarchical flower-like TiO2 microstructures, Mater Lett 277 (2020) 128372. https://doi.org/10.1016/j.matlet.2020.128372.

[54] D. Zhao, X. Zhang, L. Sui, W. Wang, X. Zhou, X. Cheng, S. Gao, Y. Xu, L. Huo, C-doped TiO2 nanoparticles to detect alcohols with different carbon chains and their sensing mechanism analysis, Sens Actuators B Chem 312 (2020) 127942. https://doi.org/10.1016/j.snb.2020.127942.

[55] G. Murali, M. Reddeppa, Ch. Seshendra Reddy, S. Park, T. Chandrakalavathi, M.-D. Kim, I. In, Enhancing the Charge Carrier Separation and Transport via Nitrogen-Doped Graphene Quantum Dot-TiO $_2$ Nanoplate Hybrid Structure for an Efficient NO Gas Sensor, ACS Appl Mater Interfaces 12 (2020) 13428–13436. https://doi.org/10.1021/acsami.9b19896.

[56] Y. Wang, Y. Dai, Synthesis and gas sensing properties of La and V Co-doped TiO $_2$ thick film, Functional Materials Letters 11 (2018) 1850019. https://doi.org/10.1142/S1793604718500194.

[57] R. Miao, W. Zeng, Q. Gao, SDS-assisted hydrothermal synthesis of NiO flake-flower architectures with enhanced gas-sensing properties, Appl Surf Sci 384 (2016) 304–310. https://doi.org/10.1016/j.apsusc.2016.05.070.

[58] C. Liu, B. Wang, T. Liu, P. Sun, Y. Gao, F. Liu, G. Lu, Facile synthesis and gas sensing properties of the flower-like NiO-decorated ZnO microstructures, Sens Actuators B Chem 235 (2016) 294–301. https://doi.org/10.1016/j.snb.2016.05.064.

[59] C. Yan, H. Lu, J. Gao, G. Zhu, F. Yin, Z. Yang, Q. Liu, G. Li, Synthesis of porous NiO-In 2 O 3 composite nanofibers by electrospinning and their highly enhanced gas sensing properties, J Alloys Compd 699 (2017) 567–574. https://doi.org/10.1016/j.jallcom.2016.12.307.

[60] S.R. Nalage, S.T. Navale, R.S. Mane, Mu. Naushad, F.J. Stadlar, V.B. Patil, Preparation of camphor-sulfonic acid doped PPy–NiO hybrid nanocomposite for detection of toxic nitrogen dioxide, Synth Met 209 (2015) 426–433. https://doi.org/10.1016/j.synthmet.2015.08.018.

[61] O. Lupan, V. Postica, V. Cretu, N. Wolff, V. Duppel, L. Kienle, R. Adelung, Single and networked CuO nanowires for highly sensitive p-type semiconductor gas sensor applications, Physica Status Solidi (RRL) - Rapid Research Letters 10 (2016) 260–266. https://doi.org/10.1002/pssr.201510414.

[62] P. Rai, R. Khan, S. Raj, S.M. Majhi, K.-K. Park, Y.-T. Yu, I.-H. Lee, P.K. Sekhar, Au@Cu $_2$ O core–shell nanoparticles as chemiresistors for gas sensor applications: effect of potential barrier modulation on the sensing performance, Nanoscale 6 (2014) 581–588. https://doi.org/10.1039/C3NR04118B.

[63] N. Wang, W. Tao, X. Gong, L. Zhao, T. Wang, L. Zhao, F. Liu, X. Liu, P. Sun, G. Lu, Highly sensitive and selective NO2 gas sensor fabricated from Cu2O-CuO microflowers, Sens Actuators B Chem 362 (2022) 131803. https://doi.org/10.1016/j.snb.2022.131803.

[64] N. Roy, R. Sinha, H.B. Nemade, T.K. Mandal, Synthesis of MoS2-CuO nanocomposite for room temperature acetone sensing application, J Alloys Compd 910 (2022) 164891. https://doi.org/10.1016/j.jallcom.2022.164891.

[65] M. Hjiri, M. Aida, G. Neri, NO2 Selective Sensor Based on α-Fe2O3 Nanoparticles Synthesized via Hydrothermal Technique, Sensors 19 (2019) 167. https://doi.org/10.3390/s19010167.

[66] Q. Qin, D. Olimov, L. Yin, Semiconductor-Type Gas Sensors Based on γ-Fe2O3 Nanoparticles and Its Derivatives in Conjunction with SnO2 and Graphene, Chemosensors 10 (2022) 267. https://doi.org/10.3390/chemosensors10070267.

[67] S. Liang, J. Zhu, C. Wang, S. Yu, H. Bi, X. Liu, X. Wang, Fabrication of α-Fe2O3@graphene nanostructures for enhanced gas-sensing property to ethanol, Appl Surf Sci 292 (2014) 278–284. https://doi.org/10.1016/j.apsusc.2013.11.130.

[68] B. Yang, J. Liu, H. Qin, Q. Liu, X. Jing, H. Zhang, R. Li, G. Huang, J. Wang, Co3O4 nanoparticle-decorated hierarchical flower-like α-Fe2O3 microspheres: Synthesis and ethanol sensing properties, J Alloys Compd 727 (2017) 52–62. https://doi.org/10.1016/j.jallcom.2017.08.088.

[69] A.M. Al Shboul, R. Izquierdo, Printed Chemiresistive In_2O_3 Nanoparticle-Based Sensors with ppb Detection of H_2S Gas for Food Packaging, ACS Appl Nano Mater 4 (2021) 9508–9517. https://doi.org/10.1021/acsanm.1c01970.

[70] B. Han, J. Wang, W. Yang, X. Chen, H. Wang, J. Chen, C. Zhang, J. Sun, X. Wei, Hydrothermal synthesis of flower-like In2O3 as a chemiresistive isoprene sensor for breath analysis, Sens Actuators B Chem 309 (2020) 127788. https://doi.org/10.1016/j.snb.2020.127788.

[71] C.-W. Chen, Y.-T. Chen, W.J. Tseng, Morphology-dependent NO2 gas sensing for needle-like In2O3 chemiresistor nanosensors, Materials Science and Engineering: B 265 (2021) 115011. https://doi.org/10.1016/j.mseb.2020.115011.

[72] Z.-H. Ma, R.-T. Yu, J.-M. Song, Facile synthesis of Pr-doped In2O3 nanoparticles and their high gas sensing performance for ethanol, Sens Actuators B Chem 305 (2020) 127377. https://doi.org/10.1016/j.snb.2019.127377.

[73] D. Kwak, M. Wang, K.J. Koski, L. Zhang, H. Sokol, R. Maric, Y. Lei, Molybdenum Trioxide (α-MoO_3) Nanoribbons for Ultrasensitive Ammonia (NH_3) Gas Detection: Integrated Experimental and Density Functional Theory Simulation Studies, ACS Appl Mater Interfaces 11 (2019) 10697–10706. https://doi.org/10.1021/acsami.8b20502.

[74] T. Thomas, Y. Kumar, J.A. Ramos Ramón, V. Agarwal, S. Sepúlveda Guzmán, R. R, S. Pushpan, S.L. Loredo, K.C. Sanal, Porous silicon/α-MoO3 nanohybrid based fast and highly sensitive CO2 gas sensors, Vacuum 184 (2021) 109983. https://doi.org/10.1016/j.vacuum.2020.109983.

[75] Y. Liu, Z. Yuan, R. Zhang, H. Ji, C. Xing, F. Meng, MoO_3/SnO_2 Nanocomposite-Based Gas Sensor for Rapid Detection of Ammonia, IEEE Trans Instrum Meas 70 (2021) 1–9. https://doi.org/10.1109/TIM.2021.3124057.

[76] P. Srinivasan, J.B.B. Rayappan, Chemi-resistive sensing of methylamine species using twinned α-MoO3 nanorods: Role of grain features, activation energy and surface defects, Sens Actuators B Chem 349 (2021) 130759. https://doi.org/10.1016/j.snb.2021.130759.

[77] M. Enhessari, A. Salehabadi, Perovskites-Based Nanomaterials for Chemical Sensors, in: Progresses in Chemical Sensor, InTech, 2016. https://doi.org/10.5772/62559.

[78] R. Zhang, C. Qin, H. Bala, Y. Wang, J. Cao, Recent Progress in Spinel Ferrite (MFe2O4) Chemiresistive Based Gas Sensors, Nanomaterials 13 (2023) 2188. https://doi.org/10.3390/nano13152188.

[79] M.K. Tiwari, S. Chand Yadav, A. Kanwade, J.A. Kumar Satrughna, S.M. Rajore, P.M. Shirage, Advancements in lanthanide-based perovskite oxide semiconductors for gas sensing applications: a focus on doping effects and development, Analytical Methods 15 (2023) 5754–5787. https://doi.org/10.1039/D3AY01420G.

[80] M.A. Njoroge, N.M. Kirimi, K.P. Kuria, Spinel ferrites gas sensors: a review of sensing parameters, mechanism and the effects of ion substitution, Critical Reviews in Solid State and Materials Sciences 47 (2022) 807–836. https://doi.org/10.1080/10408436.2021.1935213.

[81] P. Ghadage, K.P. Shinde, D. Nadargi, J. Nadargi, H. Shaikh, M.A. Alam, I. Mulla, M.S. Tamboli, J.S. Park, S. Suryavanshi, Bismuth ferrite based acetone gas sensor: evaluation of graphene oxide loading, RSC Adv 14 (2024) 1367–1376. https://doi.org/10.1039/D3RA06733E.

[82] S. Chakraborty, M. Pal, Highly efficient novel carbon monoxide gas sensor based on bismuth ferrite nanoparticles for environmental monitoring, New Journal of Chemistry 42 (2018) 7188–7196. https://doi.org/10.1039/C8NJ01237G.

[83] S. Chakraborty, M. Pal, Highly selective and stable acetone sensor based on chemically prepared bismuth ferrite nanoparticles, J Alloys Compd 787 (2019) 1204–1211. https://doi.org/10.1016/j.jallcom.2019.02.153.

[84] X. Liu, J. Li, L. Guo, G. Wang, Highly Sensitive Acetone Gas Sensors Based on Erbium-Doped Bismuth Ferrite Nanoparticles, Nanomaterials 12 (2022) 3679. https://doi.org/10.3390/nano12203679.

[85] A.K. Yadav, R.K. Singh, P. Singh, Fabrication of lanthanum ferrite based liquefied petroleum gas sensor, Sens Actuators B Chem 229 (2016) 25–30. https://doi.org/10.1016/j.snb.2016.01.066.

[86] Y.M. Zhang, Y.T. Lin, J.L. Chen, J. Zhang, Z.Q. Zhu, Q.J. Liu, A high sensitivity gas sensor for formaldehyde based on silver doped lanthanum ferrite, Sens Actuators B Chem 190 (2014) 171–176. https://doi.org/10.1016/j.snb.2013.08.046.

[87] J. Zhang, Y.M. Zhang, C.Y. Hu, Z.Q. Zhu, Q.J. Liu, A Formaldehyde Gas Sensor Based on Zinc Doped Lanthanum Ferrite, Adv Mat Res 873 (2013) 304–310. https://doi.org/10.4028/www.scientific.net/AMR.873.304.

[88] Y. Wang, J. Chen, X. Wu, Preparation and gas-sensing properties of perovskite-type SrFeO3 oxide, Mater Lett 49 (2001) 361–364. https://doi.org/10.1016/S0167-577X(00)00400-6.

[89] M. Manikandan, B. Santhosh Kumar, T. Mukil Raj, S. Moorthy Babu, C. Venkateswaran, Gas-Sensing Characteristics of SrFeO3−δ Thin Film Probed by a Homemade Apparatus, J Electron Mater 47 (2018) 4678–4682. https://doi.org/10.1007/s11664-018-6339-x.

[90] L. Lv, P. Cheng, Y. Wang, L. Xu, B. Zhang, C. Lv, J. Ma, Y. Zhang, Sb-doped three-dimensional ZnFe2O4 macroporous spheres for N-butanol chemiresistive gas sensors, Sens Actuators B Chem 320 (2020) 128384. https://doi.org/10.1016/j.snb.2020.128384.

[91] Y. Cao, H. Qin, X. Niu, D. Jia, Simple solid-state chemical synthesis and gas-sensing properties of spinel ferrite materials with different morphologies, Ceram Int 42 (2016) 10697–10703. https://doi.org/10.1016/j.ceramint.2016.03.184.

[92] Y. Yan, P. Nizamidin, G. Turdi, N. Kari, A. Yimit, Room-temperature H2S Gas Sensor Based on Au-doped ZnFe2O4 Yolk-shell Microspheres, Analytical Sciences 33 (2017) 945–951. https://doi.org/10.2116/analsci.33.945.

[93] M.M. Liu, S.Y. Ma, L. Wang, Y.H. Cai, N.N. Ma, Highly sensitive and selective glycol gas sensor based on SmFeO3 microspheres, Ceram Int 49 (2023) 1108–1113. https://doi.org/10.1016/j.ceramint.2022.09.086.

[94] A. Gaiardo, G. Zonta, S. Gherardi, C. Malagù, B. Fabbri, M. Valt, L. Vanzetti, N. Landini, D. Casotti, G. Cruciani, M. Della Ciana, V. Guidi, Nanostructured SmFeO3 Gas Sensors: Investigation of the Gas Sensing Performance Reproducibility for Colorectal Cancer Screening, Sensors 20 (2020) 5910. https://doi.org/10.3390/s20205910.

[95] H. Liu, Y. Cao, W. Liu, J. Chen, J. Hu, Gas response of SmFeO3 planar electrode sensor to volatile organic compounds gases under light illumination, Mater Lett 326 (2022) 133009. https://doi.org/10.1016/j.matlet.2022.133009.

[96] P. Rao, R.V. Godbole, S. Bhagwat, Copper doped nickel ferrite nano-crystalline thin films: A potential gas sensor towards reducing gases, Mater Chem Phys 171 (2016) 260–266. https://doi.org/10.1016/j.matchemphys.2016.01.016.

[97] R. Kashyap, R. Kumar, S. Devi, M. Kumar, S. Tyagi, D. Kumar, Ammonia gas sensing performance of nickel ferrite nanoparticles, Mater Res Express 6 (2019) 125034. https://doi.org/10.1088/2053-1591/ab55b5.

[98] S. Yang, G. Lei, H. Xu, Z. Lan, Z. Wang, H. Gu, Metal Oxide Based Heterojunctions for Gas Sensors: A Review, Nanomaterials 11 (2021) 1026. https://doi.org/10.3390/nano11041026.

[99] F.-J. Meng, R.-F. Xin, S.-X. Li, Metal Oxide Heterostructures for Improving Gas Sensing Properties: A Review, Materials 16 (2022) 263. https://doi.org/10.3390/ma16010263.

[100] A. Staerz, X. Gao, F. Cetmi, Z. Ming, U. Weimar, T. Zhang, N. Barsan, Dominant Role of Heterojunctions in Gas Sensing with Composite Materials, ACS Appl Mater Interfaces 12 (2020) 21127–21132. https://doi.org/10.1021/acsami.0c05173.

[101] L. Liu, Y. Wang, Y. Liu, S. Wang, T. Li, S. Feng, S. Qin, T. Zhang, Heteronanostructural metal oxide-based gas microsensors, Microsyst Nanoeng 8 (2022) 85. https://doi.org/10.1038/s41378-022-00410-1.

[102] S. Bai, K. Tian, Y. Zhao, Y. Feng, R. Luo, D. Li, A. Chen, ZnO/$BiFeO_3$ heterojunction interface modulation and rGO modification for detection of triethylamine, J Mater Chem C Mater 10 (2022) 8015–8023. https://doi.org/10.1039/D1TC05498H.

[103] L. He, J. Hu, Q. Yuan, Z. Xia, L. Jin, H. Gao, L. Fan, X. Chu, F. Meng, Synthesis of porous ZnFe2O4/SnO2 core-shell spheres for high-performance acetone gas sensing, Sens Actuators B Chem 378 (2023) 133123. https://doi.org/10.1016/j.snb.2022.133123.

[104] Z. Xia, C. Zheng, J. Hu, Q. Yuan, C. Zhang, J. Zhang, L. He, H. Gao, L. Jin, X. Chu, F. Meng, Synthesis of SnO2 quantum dot sensitized LaFeO3 for conductometric formic acid gas sensors, Sens Actuators B Chem 379 (2023) 133198. https://doi.org/10.1016/j.snb.2022.133198.

[105] Y. Xu, Y. Fan, X. Tian, Q. Liang, X. Liu, Y. Sun, p-p heterojunction composite of NiFe2O4 nanoparticles-decorated NiO nanosheets for acetone gas detection, Mater Lett 270 (2020) 127728. https://doi.org/10.1016/j.matlet.2020.127728.

[106] Y. Li, N. Luo, G. Sun, B. Zhang, G. Ma, H. Jin, Y. Wang, J. Cao, Z. Zhang, Facile synthesis of ZnFe2O4/α-Fe2O3 porous microrods with enhanced TEA-sensing performance, J Alloys Compd 737 (2018) 255–262. https://doi.org/10.1016/j.jallcom.2017.12.068.

CHAPTER-II

Experimental Methods and Sample Characterizations

2.1 Overview

The primary step in manufacturing a semiconductor metal oxide (SMO)-based chemiresistive gas sensor involves synthesizing various nanoparticles with diverse nano structures. Synthesizing nanoparticles can be approached through two distinct methods: the top-down method and the bottom-up method. The top-down approach entails starting with bulk material and subsequently breaking it down into smaller particles, employing techniques such as ball milling, sputtering, and solid-state reactions. However, this method is accompanied by certain drawbacks including imperfect sample surfaces, broad particle size distributions, and irregular particle shapes and structures. On the other hand, the bottom-up approach involves commencing with atoms or molecules and constructing nanostructures from them, utilizing methods like co-precipitation, sol-gel, and hydrothermal processes. This approach is generally more favourable and convenient for synthesizing nanoparticles with regular shapes and sizes.

In addition to synthesis, the subsequent critical phase in nanomaterial research involves characterizing these materials to determine if the desired pure phase has been achieved. It's imperative to ascertain the precise chemical composition, including the chemical and oxidation states of the synthesized materials. Morphology and microstructure are equally crucial factors as they can profoundly impact the sensing capabilities of the material. Parameters such as active surface area, presence of defect states, and oxygen vacancies also play significant roles in influencing the gas sensing properties. Therefore, thorough characterization is essential for analysing the multifaceted physical and chemical attributes of the synthesized nanomaterials. By comprehensively understanding these characteristics, researchers can optimize their materials for specific applications, particularly in gas sensing technologies.

In this chapter, we delve into the various techniques employed for the synthesis and characterization of nanoparticles, shedding light on the methodologies and tools utilized to investigate their unique attributes and behaviours.

2.2 Nanoparticles preparation techniques

In the realm of nanotechnology, the process of creating nanomaterials encompasses two fundamental methodologies based on their synthetic mechanisms: the top-down approach and the bottom-up approach. The top-down approach entails the disintegration of bulk materials into nanoscale dimensions, essentially "carving out" nanostructures from larger materials. Conversely, the bottom-up approach involves the meticulous assembly of nanoscale building blocks to construct larger and more complex structures. [1,2]

Elaborating on this, in the top-down approach, larger materials are essentially deconstructed or resized into smaller components through various techniques such as

I. Mechanical milling or ball milling[4]
II. Laser ablation[4]
III. Etching[4]
IV. Sputtering[4]
V. Electro-explosion[4]
VI. Lithography[4][5]

This method offers precise control over the size and shape of the resulting nanostructures but may face limitations in scalability and uniformity. On the other hand, the bottom-up approach relies on the self-assembly or controlled synthesis of nanoscale constituents to form larger structures. This can involve different chemical and physical route such as sol-gel, Chemical vapor deposition (CVD), Chemical co-precipitation, Micro-emulsions, Hydrothermal method, Sonochemical method, Microwave method, Biological methods using plant extracts, enzymes, microorganisms, etc.

Among the array of synthesis techniques employed, the primary methods utilized throughout the study were sol-gel, co-precipitation, reflux, and hydrothermal techniques. These methods were chosen predominantly due to their cost-effectiveness and the absence of a requirement for expensive instrumentation during the synthesis process. The following section delves into the detailed processes of these commonly used synthesis techniques:

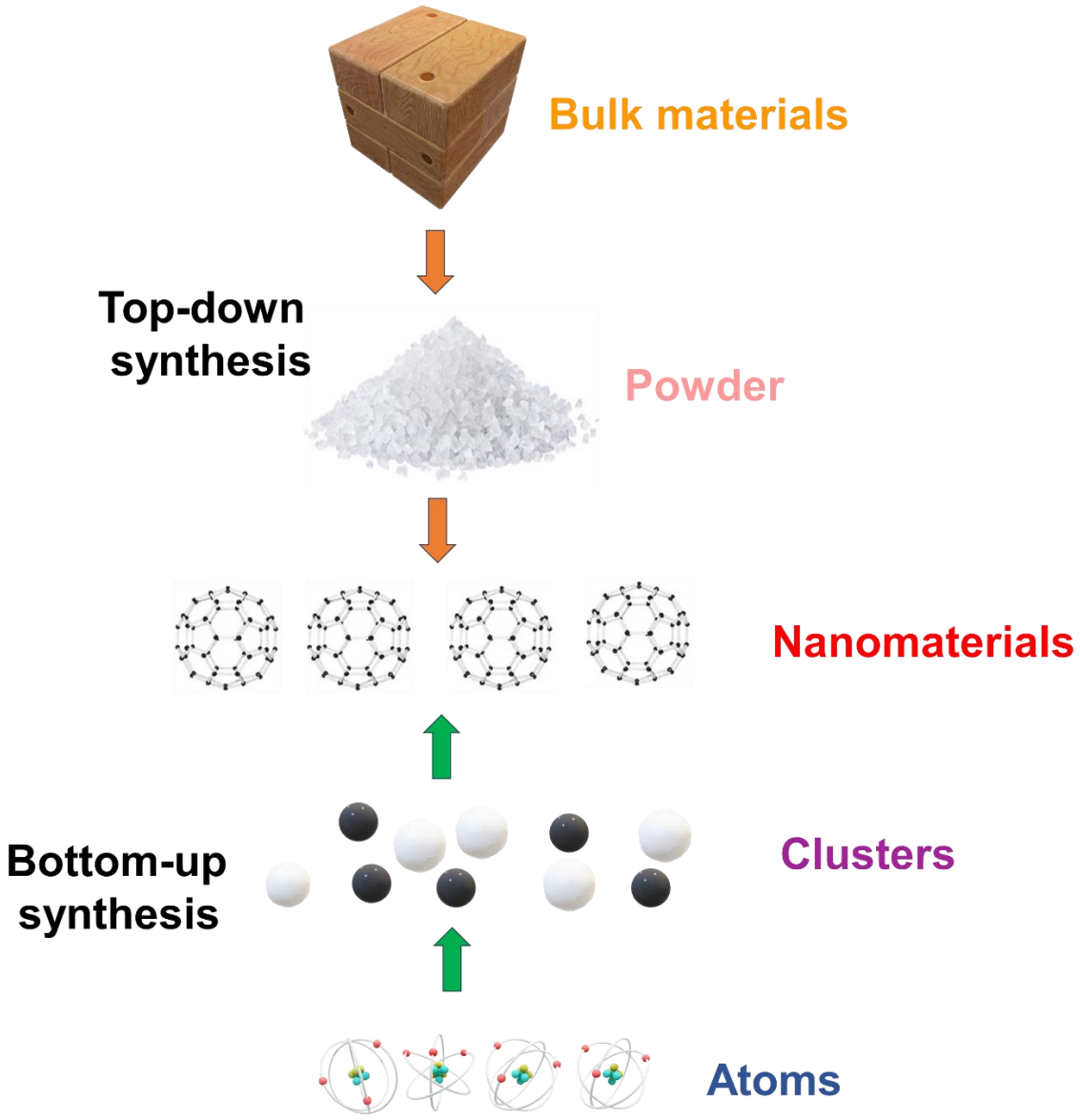

Fig. 2. 1. Steps of top-down and bottom-up synthesis route.

2.2.1 Sol-Gel Method:

A sol is a stable suspension of colloidal solid particles, typically ranging from 0.1 to 1 **µ**m in size, dispersed in a solvent. On the other hand, a gel refers to a continuous solid three-dimensional porous network surrounding a continuous liquid phase. The sol-gel process is an integral part of wet-chemical synthesis, particularly for producing metal oxide nanoparticles at the nanoscale. This method involves dissolving a molecular precursor, usually a metal alkoxide, in a solvent such as water or alcohol. Through hydrolysis or alcoholysis, triggered by heating and stirring, the precursor undergoes a transformation into a gel. The sol, under

vigorous stirring at low temperatures, transitions into a viscous gel phase. The resulting gel structure forms an interconnected porous rigid chain on a μm scale. This gel can then be subjected to drying and crushing processes to yield fine powders. The sol-gel process encompasses several sequential steps, including hydrolysis, polycondensation, drying, and thermal decomposition, all conducted at relatively mild temperatures. One of the key advantages of the sol-gel method lies in its capability to produce highly homogeneous composites with high purity. Furthermore, it allows for the simultaneous synthesis of different types of nanoparticles. Notably, this method is renowned for its ability to operate at lower temperatures compared to alternative techniques, rendering it particularly suitable for large-scale industrial production of nanomaterials.[3–5]

2.2.2 Co-precipitation Method

The co-precipitation technique involved simultaneous precipitating of multiple ions from a solution to form a solid phase. Initially, salts were dissolved in a specific solvent, followed by the addition of a base solution to induce precipitation. As the solute concentration reached saturation, a supersaturated phase emerged, prompting precipitation. Higher density of insoluble substances in the solution also facilitated precipitation. Nucleation occurred only when supersaturation transpired in soluble substances. Once nucleation initiated, crystals grew through a self-assembly process, wherein ionic species adsorbed onto nuclei. The resulting precipitate underwent filtration and drying at a defined temperature. Through this method, it possible to synthesize homogeneous materials with controlled stoichiometry. Further, the particle size also can be controlled while synthesis through this method. [6–8]

2.2.3 Reflux Method

In both the sol-gel and co-precipitation methods, the solvent and volatile components evaporate during heating of the solution. To address this issue, the reflux method is employed, wherein a closed vessel is utilized to conduct the reaction. The closed container allows the evaporated volatile components and solvents to condense back into the reaction vessel. The reflux method facilitates the completion of the chemical reaction through a repeated cyclic process. As a result of the closed environment, nanomaterials synthesized via the reflux method exhibit controlled size and form unique morphology. [9–11]

2.2.4 Hydrothermal Method

Over recent decades, the hydrothermal method has garnered extensive acceptance as a reliable technique for synthesizing various nanomaterials. This popularity stems from its capability to control the morphology, structure, and consequently the properties of nanomaterials through tailored synthesis conditions. It is widely acknowledged that the properties and potential applications of nanomaterials are influenced by their morphology. The hydrothermal method offers versatile options for modifying morphology, rendering it an attractive approach. Additionally, this method offers the potential for scaling up processes to meet industrial production requirements.[12–14]

2.3 Characterization techniques

This section encompasses a comprehensive overview of the various characterization techniques employed to assess various properties of the prepared sample. A plethora of sophisticated tools is available for studying the structural, morphological, optical, and electronic characteristics of materials. Among the arsenal of tools utilized for conducting these experiments, the following stand out:

1. X-ray Diffraction (XRD)

2. X-ray photoelectron spectroscopy (XPS)

3. Scanning Electron Microscopy (SEM)

4. Transmission Electron Microscopy (TEM)

5. Ultraviolet-visible spectroscopy (UV-vis study)

6. Photoluminescence spectroscopy (PL)

7. Fourier Transform Infrared Spectroscopy (FTIR)

8. Brunauer-Emmett-Teller (BET) spectroscopy

9. Electrical Characterization: Various electrical characterization techniques, such as conductivity measurements, Hall effect measurements, and impedance spectroscopy, are employed to investigate the electronic properties and charge transport mechanisms of the sample.

By employing a combination of these sophisticated characterization techniques, researchers can gain a comprehensive understanding of the structural, morphological, optical, and electronic properties of the prepared sample, facilitating the optimization of its properties for specific applications.

2.3.1 X-ray diffraction spectra (XRD)

X-ray diffraction method, commonly referred to as X-RD method, is utilized to determine the crystallographic structure of various materials. This structure specifies the nature of the crystal, identifying the spacing between lattice points, crystalite size, defects in crystal homogeneity or heterogeneity, and strain within the crystal. When X-rays are directed onto the sample, they are diffracted, creating a distinct pattern. From this pattern, crystallographic information is extracted. The size of nanomaterials can also be determined through X-ray methods. Shifts in XRD peaks indicate homogeneous strain, while broadening of peaks indicates heterogeneous strain. Homogeneous strain results in uniform distortion throughout the material, whereas heterogeneous strain leads to varying distortions throughout the material. According to Bragg's law, when X-rays interact with a crystal, they are diffracted from parallel planes within the crystal.

Bragg's law describes the relationship between the angles of incidence and of X-rays diffraction by a crystal lattice. It states that constructive interference of waves occurs when the path length difference between waves scattered by adjacent crystal planes is equal to an integer multiple of the wavelength of the waves. Mathematical equation of Bragg's law is given bellow

$$2d \sin\theta = n\lambda \quad \ldots\ldots\ldots\ldots\ldots\ldots \quad (1)$$

Where, n is the diffraction order , θ is the glancing angle, λ is the incoming wavelength, and d is the distance between the lattice plane.

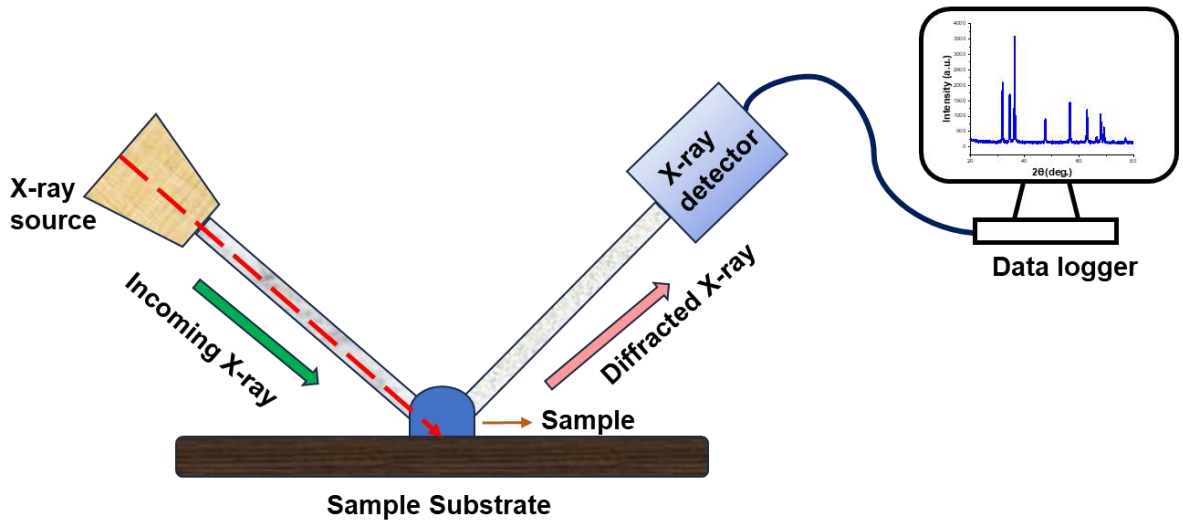

Fig. 2. 2. Schematic representation on the working principles of x-ray diffraction.

2.3.2 X-ray photoelectron spectroscopy (XPS)

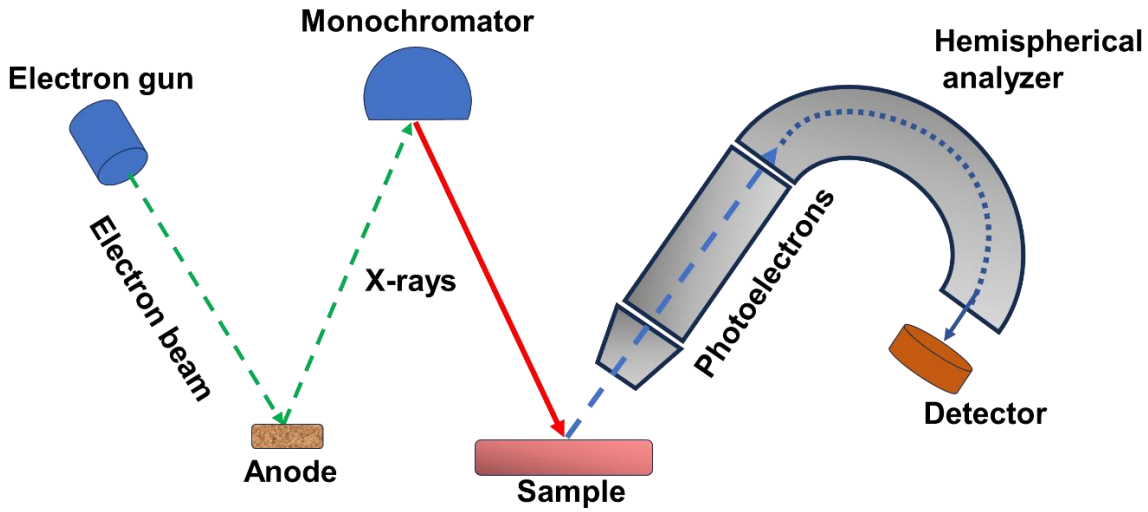

Fig. 2. 3. Schematic representation on the working principles of X-ray photoelectron spectroscopy.

X-ray photoelectron spectroscopy (XPS) is a surface-sensitive analytical technique utilized for quantitatively assessing the elemental composition of a sample [17]. Figure 2.6 illustrates the schematic of XPS. This technique enables the validation of oxidation state, chemical state, electronic state, and empirical formula of the elements present within a material. It involves

the measurement of the kinetic energy of electrons emitted from the sample surface upon excitation with mono-energetic X-rays. The kinetic energy (KE) of the emitted photoelectron is determined by the equation: given by,

$KE = h\nu - [E_B - \Phi]$ …… (2)

Here, E_B represents the binding energy of the electron, Φ denotes the work function of the sample, and $h\nu$ is the energy of the X-rays. The binding energy, intensity of a photoelectron peak, and chemical shift values are crucial parameters used to ascertain elemental identity, chemical state, and the percentage of dopants present in the sample.

2.3.3 Field emission scanning electron microscopy (FESEM)

Field-Emission Scanning Electron Microscopy (FESEM) is a crucial instrument in the realm of material science research, employed for the examination of material morphology. FESEM offers high-resolution imaging of various samples, typically achieving resolutions between 5 to 10 nano meters or magnifications ranging from 10 to 100,000 times. This technique utilizes an electron beam to generate images of the sample. The electron beam interacts with the sample, which is then captured by a detector and amplified before being displayed on a monitor. FESEM facilitates the detailed analysis of surface morphology, microstructure, surface roughness, and topography of materials. Additionally, it enables precise examination of particle size, shape, and distribution within a material. Moreover, the identification of chemical constituents present in the synthesized sample can be achieved through the integration of energy-dispersive X-ray spectroscopy (EDS) with FESEM instrumentation.

2.3.4 Transmission electron microscopy (TEM)

Transmission Electron Microscopy (TEM) is a sophisticated imaging technique utilized in scientific research, where a focused electron beam is transmitted through a thin sample. The process begins with an electron gun emitting electrons from a cathode filament via thermo-ionic emission. Subsequently, the emitted electrons are shaped and intensified by a series of magnetic lenses, akin to those found in optical microscopes, before being directed onto the sample surface. These electrons, primarily elastically scattered, traverse through the objective lens, which further focuses the beam. The magnification of the resulting image is controlled by a trio of lenses within the magnification system, along with the projector lens. The image is

then visualized on both a fluorescent screen and a monitor for analysis and observation. TEM offers unparalleled resolution and detail, enabling scientists to examine the fine structure and morphology of materials at the atomic level. Its ability to visualize samples with high contrast and resolution makes it indispensable in various fields, including materials science, nanotechnology, biology, and semiconductor research. By elucidating the microstructure and chemical composition of materials, TEM facilitates advancements in understanding fundamental properties and behaviors, driving innovation and discovery in science and technology.

2.3.5 Ultraviolet-visible spectroscopy (UV-vis study)

The principle behind UV-Visible (UV-Vis) spectroscopy is based on the interaction of molecules with light in the ultraviolet and visible regions of the electromagnetic spectrum. This technique relies on the fact that molecules absorb specific wavelengths of light due to electronic transitions. When molecules absorb light in the UV or visible range, they transition from a ground state to an excited state. The absorption of light by molecules leads to changes in their electronic structure, which can be detected and analyzed through UV-Vis spectroscopy[1][3][4]. In essence, UV-Vis spectroscopy measures the amount of discrete wavelengths of UV or visible light that are absorbed by a sample in comparison to a reference or blank sample. This absorption is influenced by the composition of the sample and provides valuable information about the components present and their concentrations. The technique is based on the energy required to promote electrons in a substance to a higher energy state, which results in the absorption of specific wavelengths of light corresponding to these electronic transitions[3]. The Beer-Lambert Law is fundamental to UV-Vis spectroscopy, relating the concentration of a solution, the path length that light travels through the solution, and the absorbance of light by the solution. This law allows for the quantification of the sample's concentration by measuring its absorbance at specific wavelengths, providing a direct relationship between absorbance and concentration[1][4][5].

2.3.6 Photoluminescence spectroscopy (PL)

Photoluminescence spectroscopy is another optical characterization technique which works on the basis of photoluminescent property of any material. When a photon with a wavelength appropriate to the sample's properties is directed onto the sample, the photons are absorbed, causing electrons to transition to higher energy states. Subsequently, these excited states return to their ground state over a specific period, emitting photons in the process. This emitted light, termed photo-excited luminescence, is captured and examined to glean insights into the characteristics of the photo-excited states within the material. This process allows for the extraction of valuable information regarding the behavior and properties of the excited states induced by photon absorption. Depending upon the required wavelength range, lasers or light-emitting diodes (LEDs) are generally used in PL- instrument as the source of excitation. Photomultiplier tube (PMT) or a charge-coupled device (CCD) camera are used as detector. PL spectroscopy plays an important role in studying electronic band structure, defects states, bandgap energy, life time of excited states, impurities in semiconducting materials along with other optical properties. Depending on the nature of emission photoluminescent is mainly dived into two categories, firstly fluorescence where emission from the material only exist during the time of excitation. Secondly, phosphorescence where emission stayed even after the excitation source is removed.

2.3.7 Fourier Transform Infrared Spectroscopy (FTIR).

In Fourier Transform Infrared (FTIR) Spectroscopy, vibrational spectroscopy is employed to analyze the local bonds within a composite material. When exposed to infrared (IR) radiation, molecules with a permanent dipole moment exhibit vibrations at characteristic frequencies corresponding to their vibrational modes. Even molecules without a permanent dipole moment can vibrate at specific frequencies. The reflected beams, resulting from the optical path difference between a fixed and a movable mirror, are directed through the sample. The light beam, now exhibiting frequency-dependent phase variations, is detected and converted into intensity variations using Fourier transform techniques, producing an interferogram. This interferogram is then processed using the Cooley-Tukey algorithm to generate a wavenumber-dependent spectrum. Compared to conventional IR spectrometers, FTIR offers higher resolution, faster data acquisition, and an improved signal-to-noise ratio.

2.3.8 BET (Brunauer-Emmett-Teller) method

The BET (Brunauer-Emmett-Teller) method serves as a crucial tool for determining the average surface area, pore volume, and pore diameter of solid materials through physical

adsorption of gas molecules on their surface [15]. This technique relies on multilayer adsorption and employs gases that do not chemically react with the sample surfaces as adsorbates. Typically, nitrogen (N2) is utilized as the probing gas at its boiling temperature (77 K) during BET spectroscopy. Although the concept of adsorption is rooted in Langmuir's theory of monolayer adsorption, in practice, the experiment follows multilayer adsorption processes.

2.4. Reference

[1] F.J. Heiligtag, M. Niederberger, The fascinating world of nanoparticle research, Materials Today 16 (2013) 262–271. https://doi.org/10.1016/j.mattod.2013.07.004.

[2] N. Baig, I. Kammakakam, W. Falath, Nanomaterials: a review of synthesis methods, properties, recent progress, and challenges, Mater Adv 2 (2021) 1821–1871. https://doi.org/10.1039/D0MA00807A.

[3] A. Amiri, Solid-phase microextraction-based sol–gel technique, TrAC Trends in Analytical Chemistry 75 (2016) 57–74. https://doi.org/10.1016/j.trac.2015.10.003.

[4] G. Bezzi, G. Celotti, E. Landi, T.M.G. La Torretta, I. Sopyan, A. Tampieri, A novel sol–gel technique for hydroxyapatite preparation, Mater Chem Phys 78 (2003) 816–824. https://doi.org/10.1016/S0254-0584(02)00392-9.

[5] A.E. Danks, S.R. Hall, Z. Schnepp, The evolution of 'sol–gel' chemistry as a technique for materials synthesis, Mater Horiz 3 (2016) 91–112. https://doi.org/10.1039/C5MH00260E.

[6] H. Al-Madhagi, V. Yazbik, W. Abdelwahed, L. Alchab, Magnetite Nanoparticle Co-precipitation Synthesis, Characterization, and Applications: Mini Review, Bionanoscience 13 (2023) 853–859. https://doi.org/10.1007/s12668-023-01113-1.

[7] Darwish, Kim, Lee, Ryu, Lee, Yoon, Synthesis of Magnetic Ferrite Nanoparticles with High Hyperthermia Performance via a Controlled Co-Precipitation Method, Nanomaterials 9 (2019) 1176. https://doi.org/10.3390/nano9081176.

[8] B. Wang, Q. Wei, S. Qu, Synthesis and Characterization of Uniform and Crystalline Magnetite Nanoparticles via Oxidation-precipitation and Modified co-precipitation Methods, Int J Electrochem Sci 8 (2013) 3786–3793. https://doi.org/10.1016/S1452-3981(23)14431-2.

[9] R. Jana, A. Dey, M. Das, J. Datta, P. Das, P.P. Ray, Improving performance of device made up of CuO nanoparticles synthesized by hydrothermal over the reflux method, Appl Surf Sci 452 (2018) 155–164. https://doi.org/10.1016/j.apsusc.2018.04.262.

[10] Y. Ding, X. Shen, S. Sithambaram, S. Gomez, R. Kumar, V.M.B. Crisostomo, S.L. Suib, M. Aindow, Synthesis and Catalytic Activity of Cryptomelane-Type Manganese Dioxide Nanomaterials Produced by a Novel Solvent-Free Method, Chemistry of Materials 17 (2005) 5382–5389. https://doi.org/10.1021/cm051294w.

[11] K. Mageshwari, S.S. Mali, T. Hemalatha, R. Sathyamoorthy, P.S. Patil, Low temperature growth of CuS nanoparticles by reflux condensation method, Progress in Solid State Chemistry 39 (2011) 108–113. https://doi.org/10.1016/j.progsolidstchem.2011.10.003.

[12] Y.X. Gan, A.H. Jayatissa, Z. Yu, X. Chen, M. Li, Hydrothermal Synthesis of Nanomaterials, J Nanomater 2020 (2020) 1–3. https://doi.org/10.1155/2020/8917013.

[13] W.L. Suchanek, R.E. Riman, Hydrothermal Synthesis of Advanced Ceramic Powders, in: 2006: pp. 184–193. https://doi.org/10.4028/www.scientific.net/AST.45.184.

[14] O. Schäf, H. Ghobarkar, P. Knauth, Hydrothermal Synthesis of Nanomaterials, in: Nanostructured Materials, Kluwer Academic Publishers, Boston, n.d.: pp. 23–41. https://doi.org/10.1007/0-306-47722-X_2.

CHAPTER-III

Y and Al Codoped ZnO-nanopowder Based Ultrasensitive Trace Ethanol Sensor: a Potential Breath Analyzer for Fatty Liver Disease and Drunken Driving Detection

Work is published in “Sensors and Actuators: B. Chemical 372 (2022) 132611”

3. 1 Introduction

Recently, trace ethanol sensing has attracted significant research interest owing to its multifarious applications, especially in exhaled breath analysis for detecting drunken driving and hepatic steatosis [1-4]. The concentration of ethanol in the exhaled breath of an otherwise healthy human being is less than 380 ppb. However, intoxication and fatty liver disease can elevate this up to 2300 ppb. In the past decade, numerous ethanol sensing techniques, viz. amperometric, electrochemical, optical, potentiometric, resistive [5-8] etc. have been reported. However, Precise measurement of trace ethanol vapor is only possible using sophisticated analytical techniques, such as, gas chromatography (GC), mass chromatography (MC), selected mass flow tube mass spectrometry (SIFT-MS), proton transfer reaction-mass spectrometry (PTR-MS), ion mobility spectrometry (IMS) [9-12] etc. However, these instruments are expensive, cumbersome, and require trained operators. Therefore, development of a sensitive, selective, fast, and layman-operable handheld electronic-nose (HEN) device for the detection of trace level ethanol is highly desirable. Semiconductor metal oxide (SMO)-based chemiresistive gas sensors are best suited for this application as they exhibit excellent sensing performance, and are rugged, cost-effective and compatible to HEN devices.

ZnO has emerged as a key technological oxide owing to its wide, direct band gap (3.3 eV), and high exciton binding energy (60meV). ZnO-based chemiresistive gas sensors are known to exhibit excellent sensitivity towards different trace gases and volatile organic compounds (VOCs), viz. acetone, ethanol, carbon monoxide, LPG, methanol, NO_x, H_2S etc. [13-18] Some of the interesting reports on ZnO-based trace ethanol vapor sensors are tabulated below (ref. Table 1).

Table-3. 1: ZnO-based trace ethanol vapor sensors

Material	**Ethanol vapor concentration of the response (ppm)**	**Respo-nse**	**Operating Temperature (°C)**	**Respo-nse time (s)**	**Recov-ery time (s)**	**Lower detection limit (ppm)**
In-doped three-dimensionally ordered macroporous ZnO [19]	100 ppm	88	250	25	10	5

5 wt% Sm_2O_3 loaded flowerlike ZnO [20]	100ppm	—	300	—	—	10
ZnO@In_2O_3 core-shell nanofibers [21]	5	3.7	225	3.7	52	5
Nanorod-assembled flower-like ZnO [22]	400	—	350	—	—	400
ZnO-In_2O_3 porous nanosheets [23]	5	3.5	350	3	8	1
Sol-gel derived ZnO [24]	100	38.46	175	219	220	500
15 wt % Ni- doped ZnO [25]	100	3.75	150	5	10	100
Au modified ZnO nanowires [26]	5	1.33	325	5	20	10
Hierarchical ZnO micro-rod and nano-tips [27]	50	47% and 59%	325	50-55	_	50
Neck-connected ZnO films [28]	50	124	375	120	70	_
1.08% Pt- decorated ZnO-nanorod [29]	500	5.12	260	6	95	0.50
Pt/ZnO nanorods/C_3N_4 nanosheets [30]	8	2.9	250	—	—	5
ZnO/SnO_2 Hollow spheres [31]	30	34.8	—	—	—	25
ZnO–CuO heterojunction [32]	200	3.32	108	62	83	100

It is observed that these sensors have multiple limitations, such as, inadequate detection lower limit [32], slow response/recovery times [24], cross-sensitivity [25], long-term instability [31], lack of repeatability [25] etc. Further, discussions on the sensing mechanisms are often cursory in the earlier reports.

Herein, we report for the first time a highly sensitive and selective Al and Y co-doped ZnO nanopowder based sensor for the detection of trace ethanol in exhaled breath. The nanopowder was synthesized by a facile cost-effective sol-gel method and characterized by multiple sophisticated techniques, such as, X-ray diffraction (XRD), X-ray photoelectron spectroscopy (XPS), Fourier transform infrared spectroscopy (FTIR), field emission scanning

electron microscopy (FESEM), energy dispersive X-ray spectroscopy, Brunauer–Emmett–Teller (BET) surface area analysis, UV-Vis spectroscopy, photoluminescence, infrared imaging, and current-voltage (I-V) measurement. The as synthesized nanopowders were exploited to fabricate thick film sensors that exhibited excellent sensitivity and selectivity to trace ethanol alongside fast response and recovery times, repeatability, and long-term stability. The sensor composition was optimized for maximum response and the enhanced sensor performance was attributed to doping-induced point defects and modified surface electronic states. The optimized sensor is suitable for a commercial breath ethanol analyzer.

3. 2. Experimental

3. 2. 1 Materials and Reagents

Zinc nitrate hexahydrate [$Zn(NO_3)_2{\cdot}6H_2O$], aluminium nitrate nonahydrate [$Al(NO_3)_3{\cdot}9H_2O$], Yttrium(III) nitrate hexahydrate [$Y(NO_3)_3{\cdot}6H_2O$], Polyethylene glycol [PEG-400], isopropyl alcohol [C_3H_8O], were procured from Sigma-Aldrich and used without further purification. Also, EMS (UK) make conducting gold paste (~75% Au), platinum wire (0.025 mm gauge), nichrome wire (38 standard wire gauge), inhouse make cylindrical α-alumina tubes (length 3 mm, OD = 2.2 mm, and ID = 1.1 mm), inhouse produced DI water, and custom-make plastic sensor-packaging cases were used for the synthesis and fabrication purposes.

3. 2. 2 Synthesis of nanopowders

Aluminium and yttrium co-doped ZnO nanoparticles were synthesized by a facile solution-precipitation method. Calculated amounts of zinc nitrate hexahydrate, aluminium nitrate nonahydrate, and yttrium nitrate hexahydrate were dissolved in DI water under continuous stirring. Thereafter, required quantities of PEG-400 were added drop wise into this solution. This solution was heated at 80°C under continuous stirring until a thick white precipitate was formed. The precipitate was dried at 120°C for 24 h. The amounts of reagents used for the synthesis of pristine and doped ZnO are given in Table- 3.2. The dried powder was calcined at 500°C for 5 h to obtain Al and Y co-doped ZnO nanoparticles. The synthesis process is schematically illustrated in Fig. 3. 1.

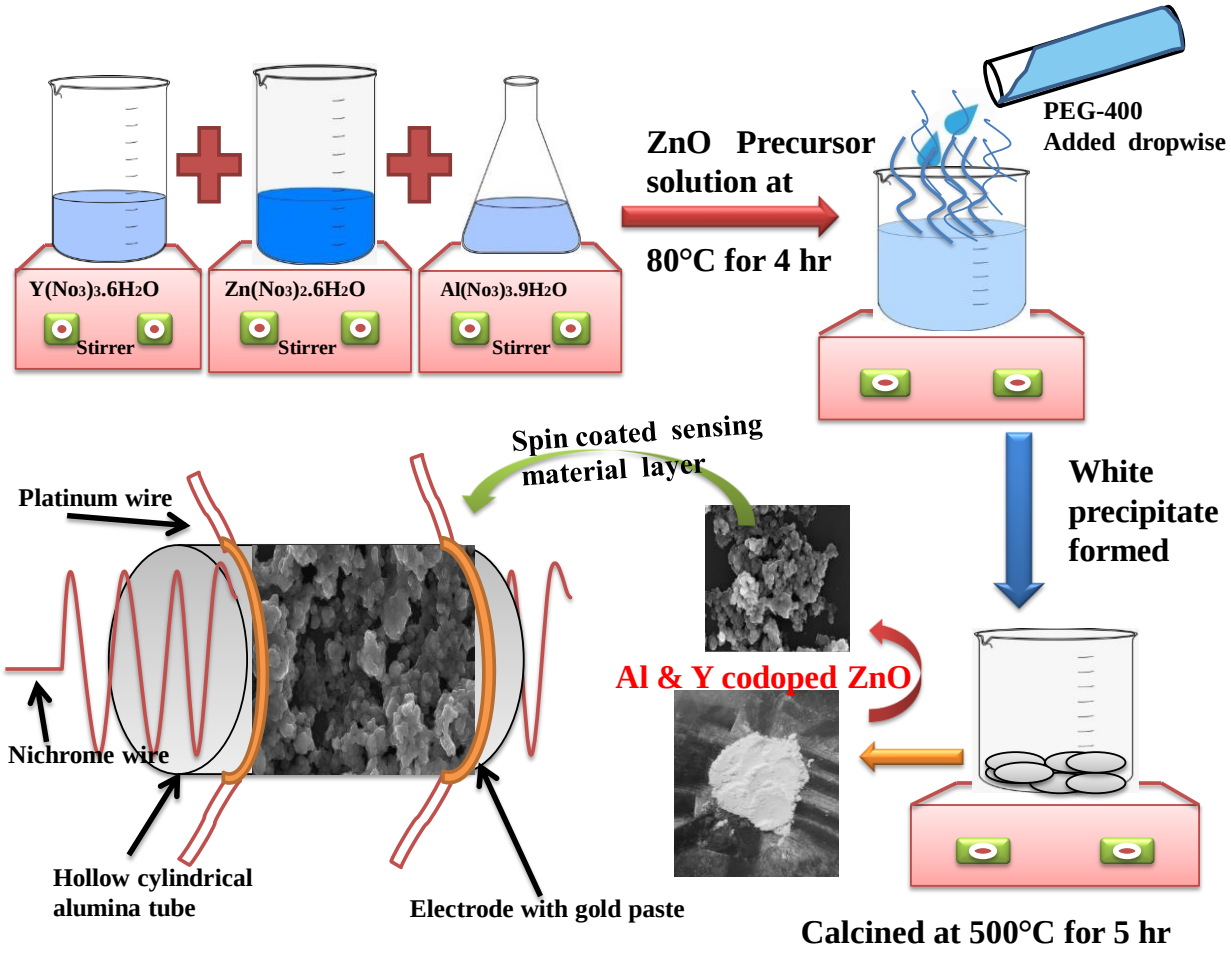

Fig. 3. 1. Schematic illustration of the nanomaterial synthesis process and sensor fabrication technique.

The sample nomenclatures, and the dopant concentrations in the different ZnO samples are listed in Table-3.2. Taguchi type thick film sensors were fabricated by a customized drop coating technique (ref. fig. 3.1) the details of which has been described elsewhere [33].

Table 3.2: Amounts of raw materials used for the synthesis of the different doped samples.

Weight of $Zn(NO_3)_2 \cdot 6H_2O$ (in gm)	Weight of $Al(NO_3)_3 \cdot 9H_2O$ (in gm)	Weight of $Y(NO_3)_3 \cdot 6H_2O$ (in gm)	Quantity of PEG-400 (in gm)	Sample Name	Dopant concentrations	
					Al(wt%)	Y(wt%)
2.974	—	—	11.3	AYZ-0	0	0
2.974	0.037	—	11.3	AZ-1	1	0
2.974	0.111	—	11.3	AZ-3	3	0
2.974	—	0.038	11.3	YZ-1	0	1
2.974	0.037	0.038	11.3	AYZ-1	1	1
2.974	0.037	0.114	11.3	AYZ-3	1	3
2.974	0.037	0.190	11.3	AYZ-5	1	5
2.974	0.037	0.266	11.3	AYZ-7	1	7

3.2.3 Materials Characterization

The as synthesized materials were characterized using different sophisticated techniques such as X-ray diffraction (XRD), X-ray photoelectron spectroscopy (XPS), Fourier transform infrared spectroscopy (FTIR), field emission scanning electron microscopy (FESEM), transmission electron microscopy (TEM), energy dispersive X-ray spectroscopy, Brunauer–Emmett–Teller (BET) surface area analysis, UV-Vis spectroscopy, photoluminescence, infrared (IR) imaging, and current-voltage (I-V) measurement. X'Pert pro MPD XRD (PANalytical) X-ray diffractometer having Cu Kα radiation (1.54 Å) was used for phase analysis of the synthesized nanopowders. Elaborate analyses of crystal structures of pure, Al doped and Al, Y co-doped ZnO powder samples were carried out by refinement of structural parameters using Rietveld method [34]. Le' Bail refinement [35] of the powder profile was carried out using the software Jana2006 [36] with $P6_3/mc$ space group, employing Pseudo Voigt polynomials for profile fitting and Legendre polynomials with 35 terms for background modelling. For doped samples, initial refinements with formula of pure ZnO yielded huge

difference between calculated and experimental data points. This was resolved by replacing some Zn with Al and Y species. Final refinements with damping factor 1 produced a good match between experimental and fitted values. A PHI 5000 Versa Probe II scanning XPS microprobe (ULVAC-PHI, U.S) with monochromatic AlKα (hv=1486.6 eV) radiations with a beam size of 100 μm and resolution of about 0.7 eV was used to carry out XPS study to learn the ionic states of the different elements in the samples. Pellets of nanopowder were prepared with KBr to conduct FTIR spectrometry (Nicolet 380) to determine the nature of different chemical bonds in the synthesized material. FESEM was conducted using a Carl Zeiss make Supra 35 V P microscope to determine particle size and morphology of the nanopowder. The specific surface area, pore volume and pore size of the nanopowder were calculated by BET technique (NovaWin, Quantachrome Instrument). UV-Vis study was conducted using a SHIMADZU UV–VIS-NIR spectrometer (UV-3600). Room temperature photoluminescence (PL) spectra were measured using a Horiba FluoroMax-4 spectrometer. Current-voltage (I-V) study was conducted to investigate the ohmic nature of the sensor contacts using an Agilent B2901A precision meter. IR imaging using a Fluke Ti27 infrared camera was conducted to accurately measure the operating temperature of the sensor. Gas sensing studies were carried out with a Keysight 34470A digital multimeter and the data was recorded with the help of a GUI enabled software (Keysight BenchVue). The sensor response was calculated using the following formula,

$$S(\%\ \text{responce}) = \left(\frac{R_g - R_a}{R_a}\right)\times 100 \quad \text{or} \quad S = \frac{\Delta R}{R_a}\times 100 \qquad \text{.....(1)}$$

where, R_a and R_g are sensor resistances at ambient air and target gas/vapor atmosphere, respectively.

3.2.4 Preparation procedure of all sample gases

Different concentrations of trace ethanol vapor and other vapors were prepared using a serial dilution technique [37].

3.2.4.1 Preparation procedure of ethanol vapour

Few desiccators were used to prepare different concentration of ethanol vapour (viz. 100 ppm, 50 ppm,25 ppm,10 ppm,5 ppm, 1 ppm, 0.5 ppm) to measure the response of as prepared sensor towards different concentration of ethanol. At first highest concentration of ethanol (viz. 100 ppm) vapour was prepared in one desiccator as stock sample and then lower ppm ethanol

vapour samples were prepared in different desiccators by diluting the stock sample by mixing required amount of normal air with it. The dilution of the stock sample was done using the following equation, $U_1 \times Y_1 = U_2 \times Y_2$ where U_1 is the volume of the stock desiccator, Y_1 is the concentration of ethanol vapour in the stock sample desiccator, U_2 is the volume of the small desiccator, and Y_2 is the concentration of ethanol vapour in the small desiccators.

3.2.4.2 Preparation procedure of acetone, ammonia, formalin vapour

100 ppm acetone, ammonia, formalin vapour was prepared in 3 different desiccators. Further 1 ppm acetone and ammonia vapour were prepared in different desiccators by diluting the stock sample in previously described process.

3.2.4.3 Preparation procedure of CO, NO, NO_2

Commercial gas cylinder of 5 ppm CO gas concentration balanced in N_2, 20 ppm NO gas concentration balanced in N_2 and 100 ppm NO_2 gas concentration balance in N_2 were used for cross sensitivity checking.

3.2.4.4 Preparation procedure of acetylene

Calculated amount of calcium carbide and DI water were mixed in closed desiccators for preparation of 500 ppm acetylene.

3.3 Results and discussion

3.3.1 Microstructural analysis

X-ray diffraction patterns of pure ZnO and Al/Y doped ZnO nanomaterials (ref. fig. 3.2(a)) can be indexed to hexagonal wurtzite ZnO (JCPDS No. 36–1451). No peak corresponding to aluminum or yttrium can be found in any of the diffraction patterns. This indicates that Al^{3+} or Y^{3+} ions have substituted Zn^{2+} in the crystal lattice of ZnO. Notably, average crystallite calculated using Debye Scherer's formula (ref. fig. 3. 2(b)) exhibited a monotonic decrease in average crystallite size with increase in doping concentrations of Al^{3+} or Y^{3+}. The calculated crystallite size of all the samples is shown in fig. 3. 2(b). With increased doping concentration of Y strain in the lattice increases. Thus, the crystallite size reduces which is reflected in broadening of peaks.

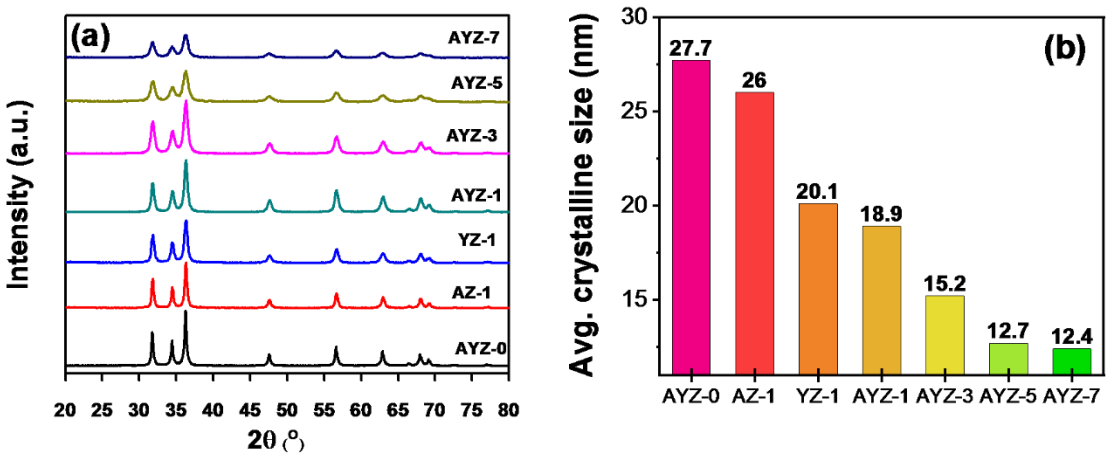

Fig. 3. 2. (a) XRD patterns of all AYZ samples; and (b) Change of particle size with increasing doping concentration.

Analyses of results obtained from Rietveld refinement reveal that on doping ZnO with Al and co-doping with Al, Y; there is a slight variation in lattice parameters and hence in the unit cell volume (ref. fig. 3. 3, Table-3. 3).

Table- 3.3: Crystallographic details of pure and doped ZnO samples

Crystallographic details	**S-1 (ZnO)**	**AZ-1 ($Zn_{0.72}Al_{0.28}O$)**	**AYZ-5 ($Zn_{0.692}Al_{0.106}Y_{0.106}O$)**	**AYZ-7 ($Zn_{0.68}Al_{0.118}Al_{0.118}O$)**
Space group	$P6_3/mc$	$P6_3/mc$	$P6_3/mc$	$P6_3/mc$
Lattice parameters: *a*(Å)	3.249(8)	3.246(10)	3.248(3)	3.249(2)
c(Å)	5.205(10)	5.201(16)	5.204(4)	5.205(4)
α, *γ* (degrees)	90, 120	90, 120	90, 120	90, 120
Unit cell volume, *V*($Å^3$)	47.601(14)	47.488(2)	47.566(7)	47.595(6)
Zn-O bond length (Å)	2.009(4)	1.968(12)	1.969(12)	1.999(4)

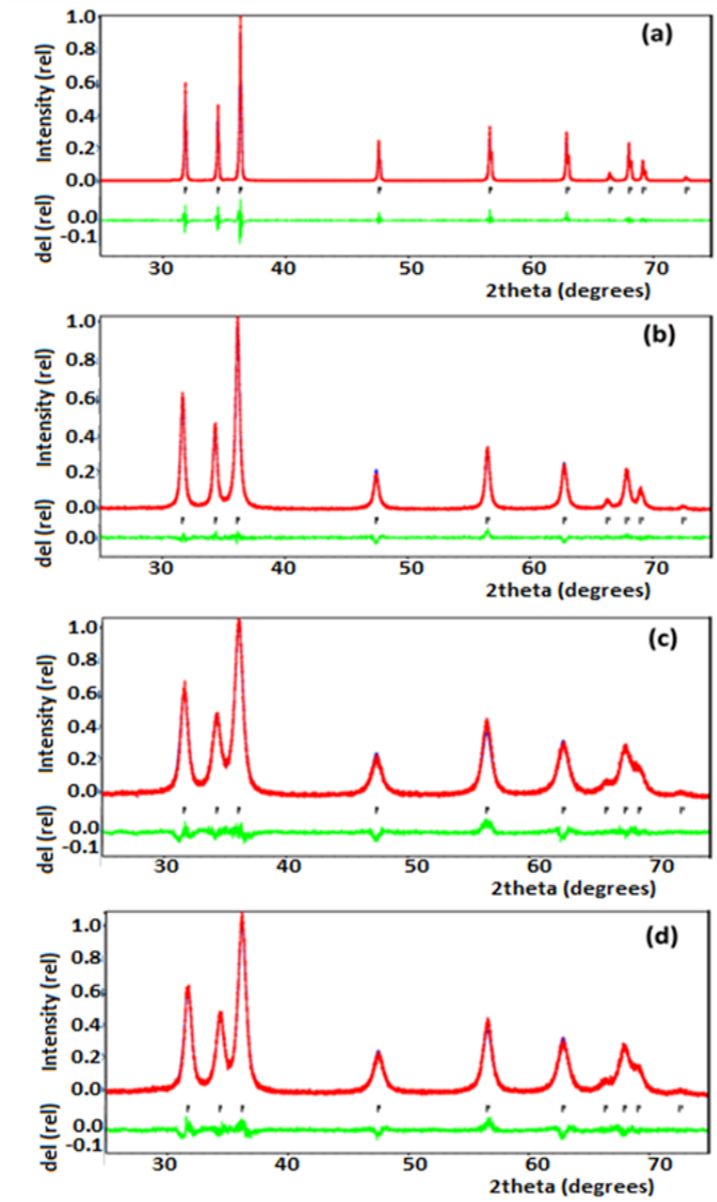

Fig. 3. 3. X-ray diffractograms of (a) ZnO; (b) AZ-1 ($Zn_{0.72}Al_{0.28}O$); (c) AYZ-5 ($Zn_{0.692}Al_{0.106}Y_{0.106}O$); and (d) AYZ-7($Zn_{0.68}Al_{0.118}Al_{0.118}O$) samples. Red points represent observed points, blue represents calculated points and green represents the difference between calculated and observed points. The Bragg reflections are shown using black lines.

In order to gain further insight into the structure of the as prepared samples Fourier transform infrared spectroscopy (FTIR) analysis was carried out in the wavenumber region of 400–4000 cm^{-1} at room temperature (ref. fig. 3. 4(a)). The FTIR spectra of AYZ-5 is shown in fig. 3. 4(b). The peaks at 478 cm^{-1}, 1385 cm^{-1}, 1634 cm^{-1}, 3437 cm^{-1} are observed in all the samples and are attributed to the stretching of Zn-O bond, C-H bond vibrations from organic

surfactant (PEG-400), bending vibration of absorbed water on the surface of the sample, and stretching and bending vibrations of surface – OH groups. [38] The peak observed at 1107 cm^{-1} in the Al-doped ZnO samples is assigned to Al–O bonds. [39] Further, the peaks observed at 680 and 780 cm^{-1} correspond to ZnO-Y bond. [40] Thus, FTIR analysis provides evidence for the formation of pure, and Al, Y –co-doped ZnO.

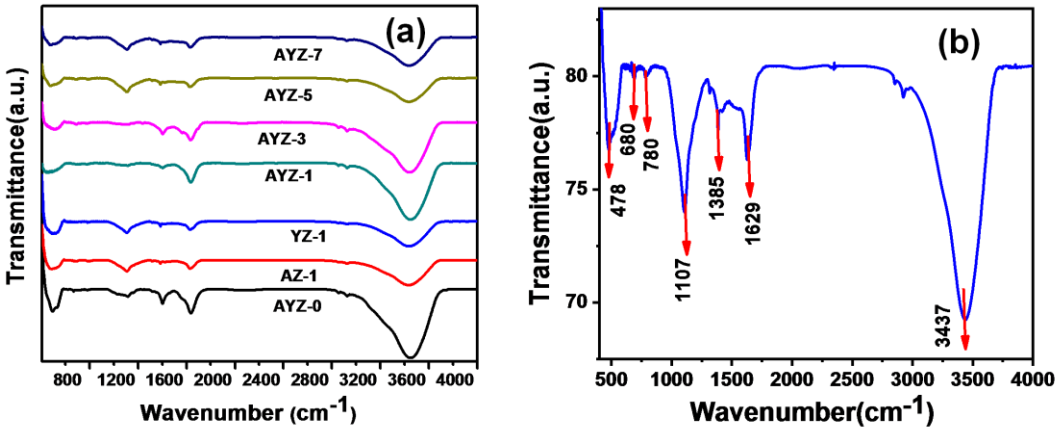

Fig. 3. 4. FTIR spectra of (a) different Al and Y doped ZnO; (b) 1 wt% Al and 5wt% Y codoped ZnO.

Fig. 3. 5(a)-(f) show the FESEM images of AYZ-0 to AYZ-7 samples, respectively. The nanoparticles in all the samples have nearly spherical morphology. Further, in all the samples significant proportion of pores are visible. PEG-400 plays an important part in controlling particle morphology and generating micropores. This is schematically represented in fig. 3. 5(g). The interaction of zinc species (Zn^{2+}) and PEG in the aqueous precursor mix leads to formation of solvated Zn (II)–PEG clusters. The zinc concentration is much higher in these clusters than in the bulk solution and therefore these clusters act as nuclei for growth. Continuous magnetic stirring and heating of the precursor mix yield completely hydrolyzed zinc species which attach onto the surface of these nuclei by oriented attachment mechanism. In order to attain minimum energy configuration these clusters self-assemble into spherical structures which further grow in size by Oswalt ripening mechanism. After calcination PEG burns out leaving behind porous spheres of pristine and doped ZnO[41- 42]. Average particle size was estimated using ImageJ software. It was observed that the particle size of the samples varies as a function of doping concentration (ref. fig. 3. 5(h)). This result is in agreement with the crystallite sizes calculated in XRD study.

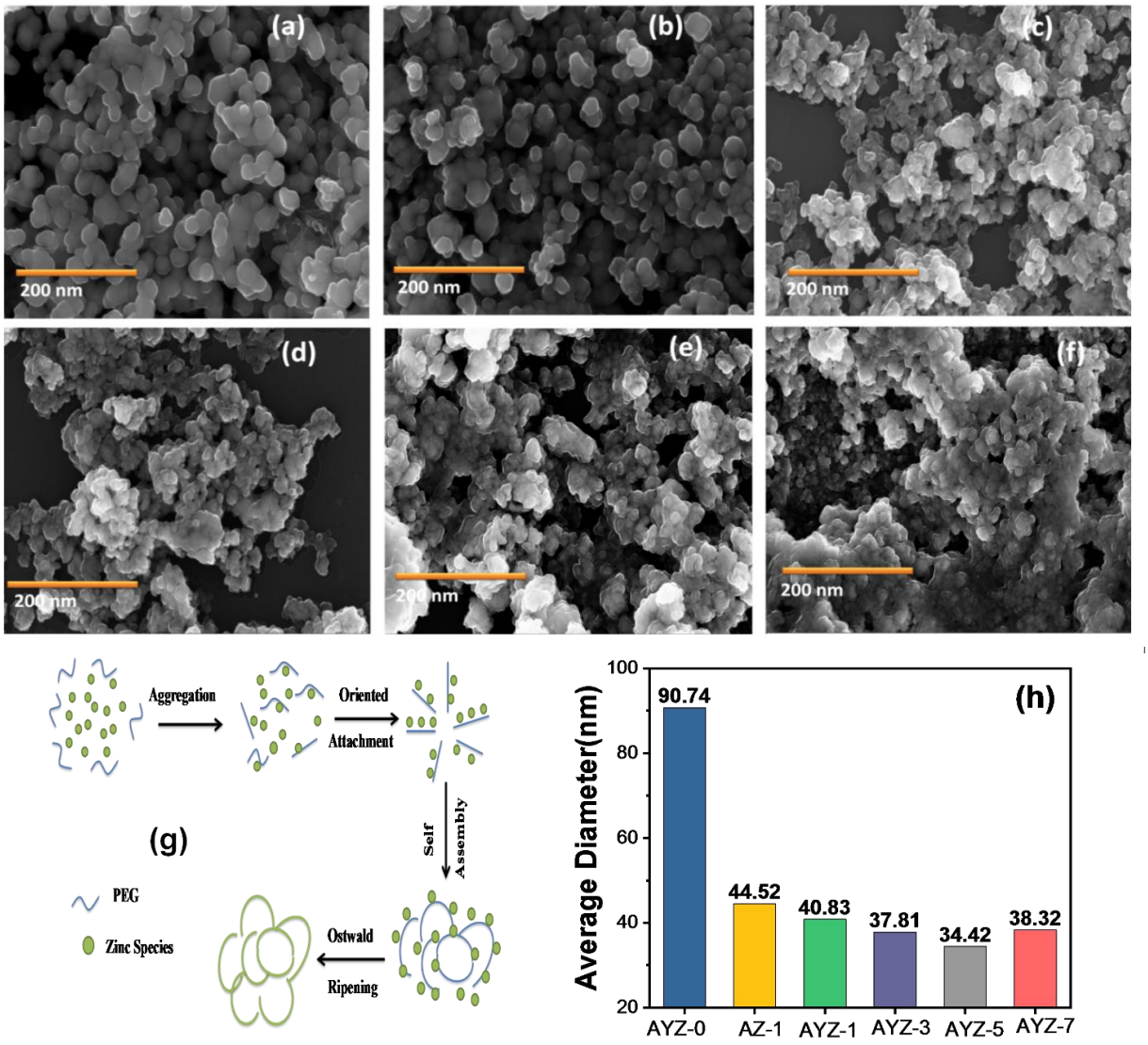

Fig. 3. 5. FESEM images of (a) AYZ-0; (b) AZ-1; (c) AYZ-1; (d) AYZ-3; (e) AYZ-5; (f) AYZ-7 nanoparticles; (g) schematic representation of the process for the formation of nearly spherical and porous ZnO nanostructures; and (h) variation of particle size with doping concentration.

Fig. 3. 6(e) shows the EDX spectrum of AYZ-5 sample. It is observed that the AYZ-5 sample contains Al, Y, Zn and O. Peaks corresponding to C and Cu originates from the C coated Cu grid on which the sample was coated for SEM study. No other peak for any impurity was observed. To further reveal the elemental distribution of Zn, O, Al, Y elements in the AYZ-0, AZ-1, AYZ-5, AYZ-7 corresponding elemental mapping was done as shown in Fig. 3. 6(a-d) respectively. It can be seen that Al, Y, Zn, O are homogeneously distributed throughout for

all the materials. The results obtained from EDX study are thus concomitant with the results obtained from XRD, and FTIR study.

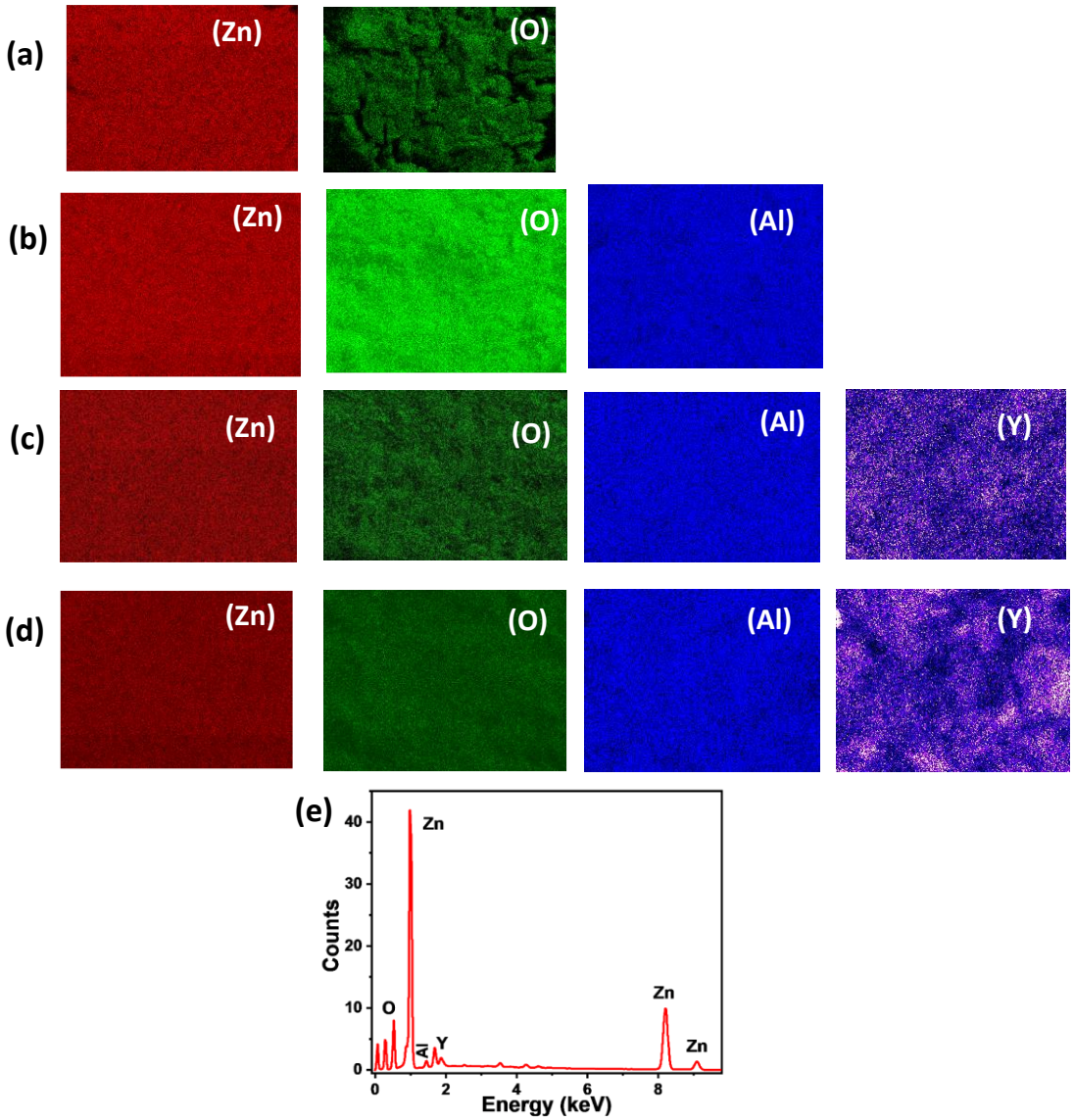

Fig. 3. 6. Elemental distribution of Zn, O, Al, and Y in (a) AYZ-0; (b) AZ-1; (c) AYZ-5; (d) AYZ-7 sample; (e) EDX spectra of AYZ-5.

Fig. 3. 7(a) shows the XPS survey scan spectra of AYZ-5 which discloses the presence of the peak corresponding to Zn 2p, Al 2p, Y 3d, C 1s, O 1s. C 1s peak came due to the adventitious carbon that was introduced due to the exposure of the sample to the atmosphere. In Fig. 3. 7(b) peak at 74.3 eV confirms the presence of Al^{3+} in the AYZ-5 sample.[43] In Fig. 3. 7(c) Y 3d spectra is deconvoluted into two peaks at 160.5 eV and 158.3 eV corresponding to the high binding state of Y $3d_{3/2}$ and low binding state of Y $3d_{5/2}$ respectively. These two

peaks are typical of Y_2O_3 suggesting the presence of Y^{3+} oxidation state in the sample.[44] In Fig. 3. 7(d), peaks with binding energies of 1021.51 and 1044.56 eV correspond to Zn $2p_{3/2}$ and Zn $2p_{1/2}$, respectively, which confirms the presence of Zn in the sample AYZ-5 exists in a divalent oxidation state. [45] It appears that for doped samples there is insignificant change in positions of Y, Al. However, a change around 0.5 eV is noticed for the position of Zn in case of Al-doped samples. This could be attributed to the differences of electron affinity between Al and Zn.

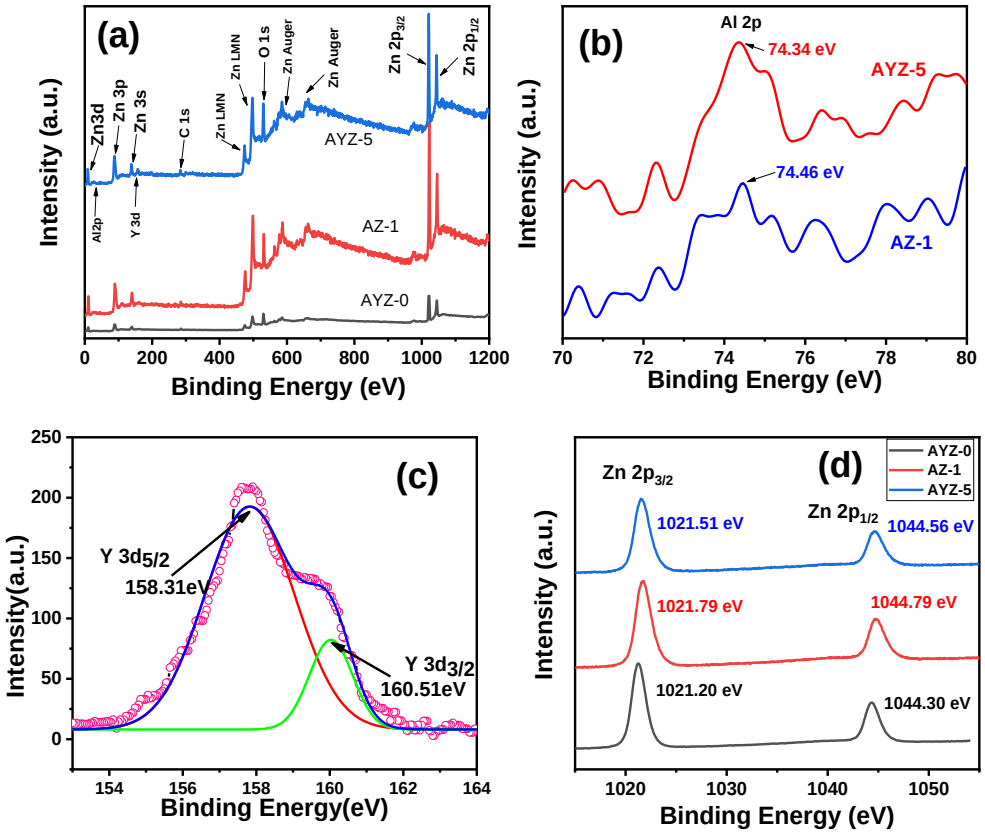

Fig. 3. 7. XPS spectra of (a) survey scan of AYZ-0, AZ-1, AYZ-5; (b) Al region of AZ-1, AYZ-5; (c) Y region of AYZ-5; and (d) Zn region of AYZ-0, AZ-1, AYZ-5.

Fig. 3. 8(a-f) shows the linear fitting of the experimental BET plots of all the samples with BET equation. Fig. 3. 8(g) diagrammatically shows the BET specific surface area of all the samples. It is observed that BET surface area increases with increasing doping concentrations, reaches a maximum at AYZ-5 and then decreases for the AYZ-7 sample. It appears that with increasing doping concentration strain in the crystal lattice increases leading to formation of smaller particles with higher specific surface area.[46] This This corroborate with FESEM study which shows that the particle size decreases with increasing doping

concentration, reaches a minimum at AYZ-5 sample and then decreases. Further, active sites for gas sensing increases with increasing specific surface area and thus maximum sensor response may be expected from AYZ-5 sample.

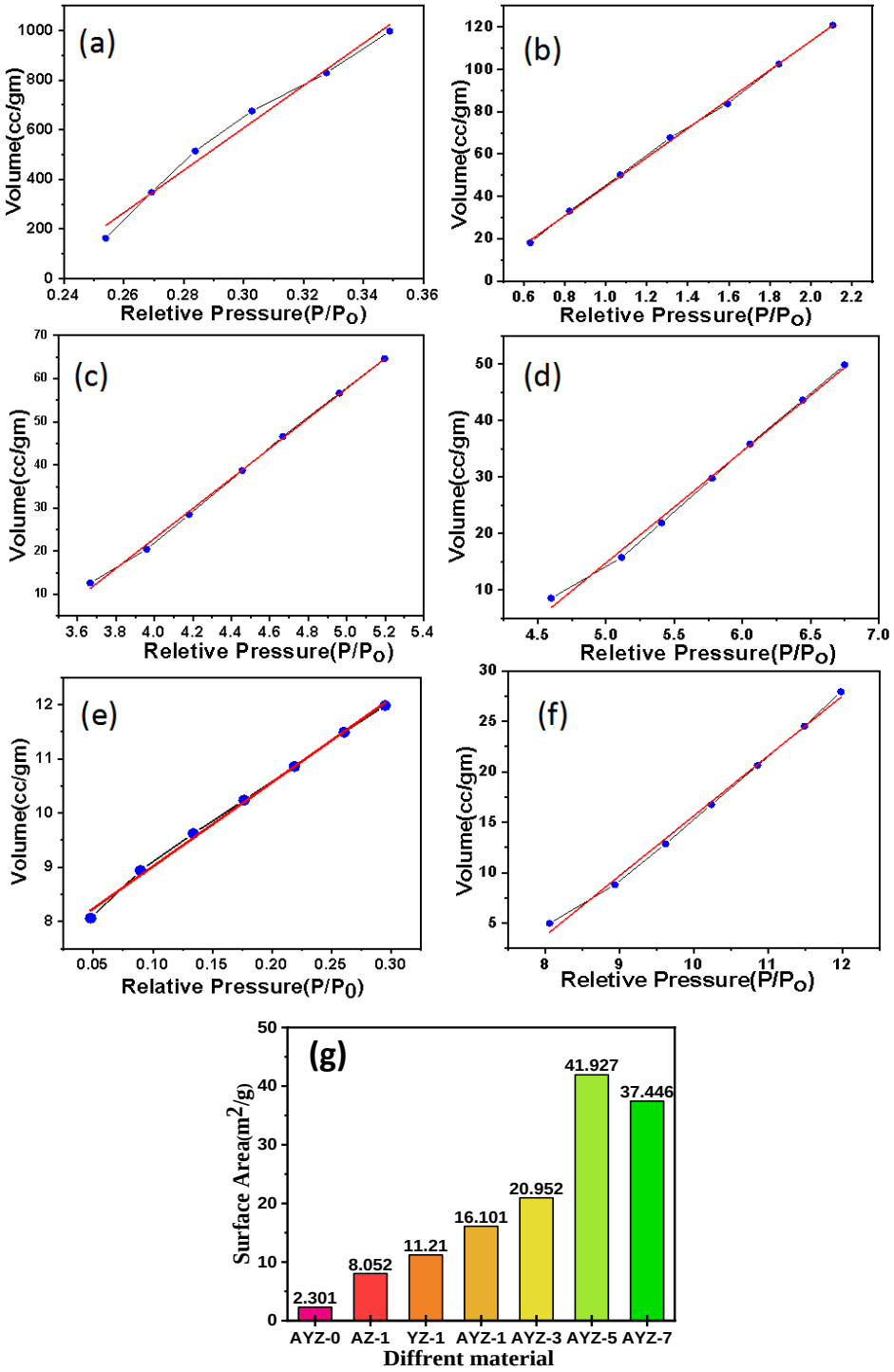

Fig. 3. 8. BETplot of (a)AYZ-0; (b)AZ-1; (c)AYZ-1; (d)AYZ-3; (e)AYZ-5; (f)AYZ-7 nanoparticles. (g) Variation of BET specific surface area in the AYZ samples with increasing doping concentration.

3.3.2 Optical study

UV-Vis spectroscopic analysis was conducted to determine the effect of doping on the band-gap of the AYZ samples. Fig. 3. 9(a) exhibits the UV-Vis spectrum and Tauc plot for AYZ-5 sample. The inset of Fig. 3. 9(a) shows the UV-Vis plot of all the other samples. It is observed that band gap increases with increasing doping concentrations (Fig. 3. 9(b)). Wide band gap of Al_2O_3 (7.1 eV) and Y_2O_3 (5.6 eV) dopants may be one plausible reason for such band gap enhancement [47- 48]. Further, with increasing doping concentrations particle size decreases. Thus, quantum confinement phenomenon may also contribute to increase the band-gap in doped samples. It is further observed that AZ-1 sample exhibits higher band-gap than YZ-1 sample. This may be attributed to higher band gap of alumina with respect to that of yttrium. Since gas sensing directly relates to the interaction of oxygen species and target gas molecules with the electronic states in the sensing oxide, the band-gap enhancement may play a vital role in dictating the sensing performance.

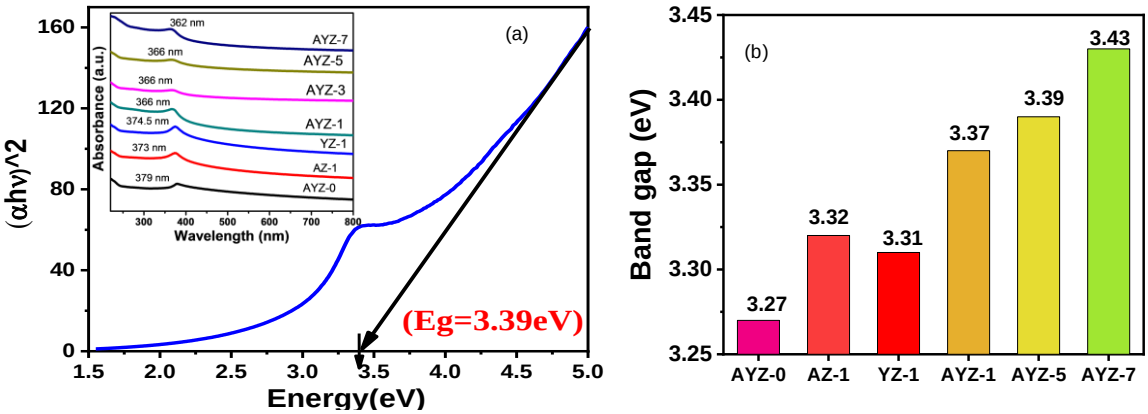

Fig. 3. 9. (a) UV-Vis spectrum and Tauc plot for AYZ-5 sample (inset shows UV-Vis absorption spectra for all the samples); and (b) variation of band gap with increasing doping concentration.

3.3.3 Electrical characterization and gas sensing behaviour

Operating temperature has profound effect on the sensing behavior and precise determination of the same is essential. Fig. 3. 10 (a-f) shows the thermal images of a typical AYZ sensor at different DC voltages applied across the heating coil. Further, it is important to

determine the optimum operating temperature at which maximum sensor response to target gas (here ethanol) is obtained. Fig. 3. 11 (a) shows the sensor response of the AYZ samples at to 1 ppm ethanol vapor at different operating temperatures at constant 33% RH background. Bell-shaped curves characteristic of chemiresistive sensors are observed for all the samples. Such bell-shaped curve originates from the interplay of multiple counteracting temperature dependent parameters described [49]. Further, it is noted that AYZ-5 sample shows highest response to 1 ppm ethanol at 350°C. To estimate the influence of temperature on response of AYZ-5 sensor, the response vs. operating temperature curve for AYZ-5 sensor has been fitted with following equation,

$$\boldsymbol{S(T) = S_0 + \frac{K}{\sigma\sqrt{2\pi}} e^{\frac{-(T-\mu)^2}{4\sigma^2}}} \quad \ldots\ldots\ldots\ldots\ldots\ldots\ldots\ldots \quad (2)$$

Where, S(T) is the response of the sensor at any temperature, S_0, K are two constants and **σ** is standard deviation. Estimated mean temperature (**μ**) is 350.6 ºC which exactly matches with optimum operating temperature (350ºC) of the AYZ-5 sensor (ref. fig. 3. 11 (b)). [50-51].

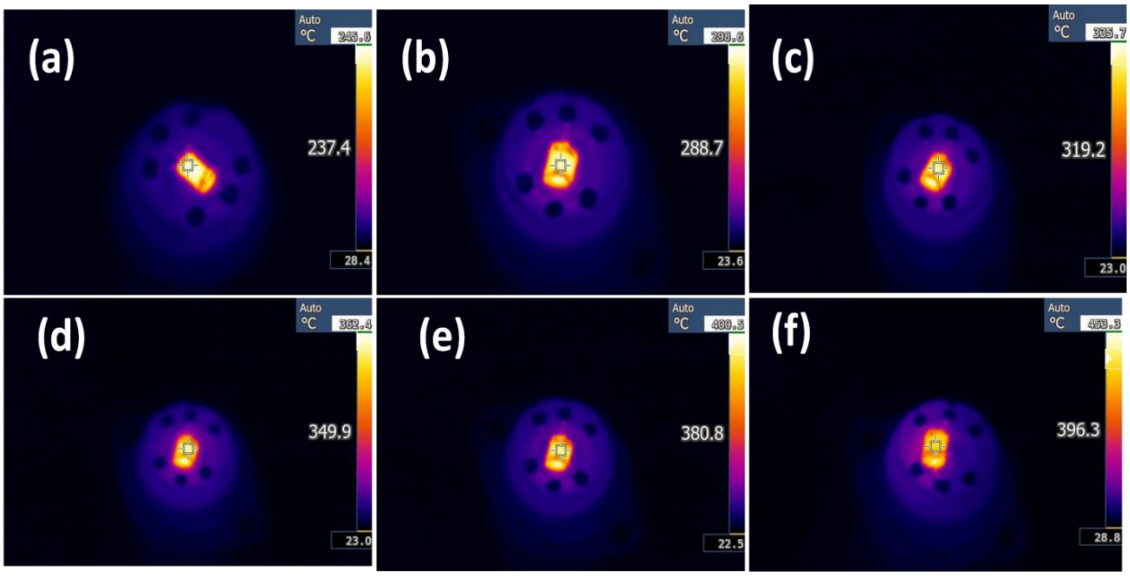

Fig. 3. 10. Ultra-contrast thermal images of AYZ-5 sensor surface at (a) 3.8 V; (b) 4.3 V; (c) 4.6 V; (d) 5 V; (e) 5.3 V; and (f) 5.45 V

Further, the variation of base resistance of the AYZ-5 sensor with the change of operating temperature is shown in Fig. 3. 11 (c). Base resistance shows an exponentially decreasing trend with increasing temperature which proves typical semiconducting nature of the material.

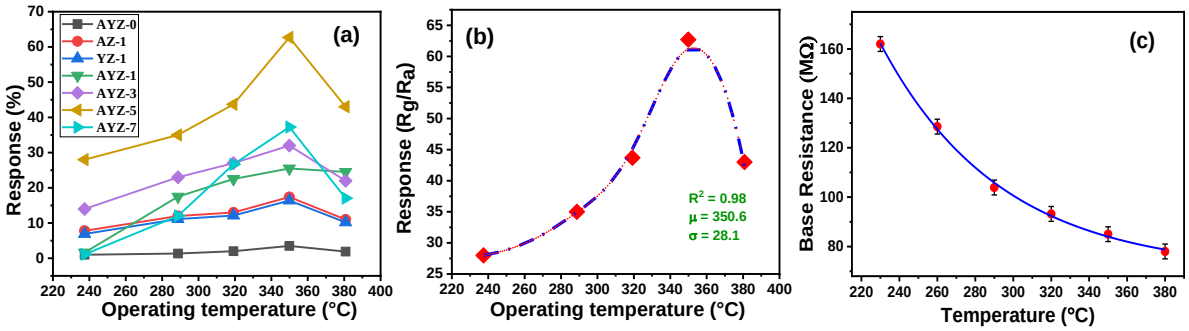

Fig. 3. 11. (a) Gas response of different AYZ nanoparticles at different operating temperatures; (b) Temperature influence on response of AYZ-5 sensor fitted with gaussian equation; and (c) Variation of base resistance of AYZ-5 sensor with change of operating temperature (°C).

The base resistances (R_a) of all the sensors in air atmosphere at 33% RH and 350°C have been listed in Table- 3. 4. It is observed that R_a for AZ-1 is lower than that of AYZ-0. However, with further increase in Al and/or Y concentration R_a increases rapidly. Aliovalent doping increases free electron concentration in the sensing material, thereby increasing the conductivity initially. FESEM study suggests that increase in doping concentration results into progressive decrease in grain size. This leads to increased scattering of the carrier free electrons at the grain boundary. Thus, with further increase in doping concentration R_a increases rapidly.

Table- 3. 4: Variation of the resistances of all the sensors at ambient air (R_a) at 350°C.

Sample Name	Resistance at ambient air (R_a) (MΩ)
AYZ-0	4.5
AZ-1	2.6
AZ-3	4.2
YZ-1	5.6
AYZ-1	12.1
AYZ-3	22.5
AYZ-5	88.5
AYZ-7	137.2

It is essential to confirm that ohmic contact is formed between the sensing oxide and contact metal (here gold electrode). This would ensure uninterrupted flow of charge carriers from the sensor to the external circuit, thereby generating proper and reliable sensor signal. The current-voltage (I-V) measurement of all the AYZ samples were conducted at the

optimized operating temperature of 350°C (ref. Fig. 3. 12) and it was observed that all the curves are sufficiently linear within the experimental range. Thus, ohmic nature of contacts in all the samples is confirmed.

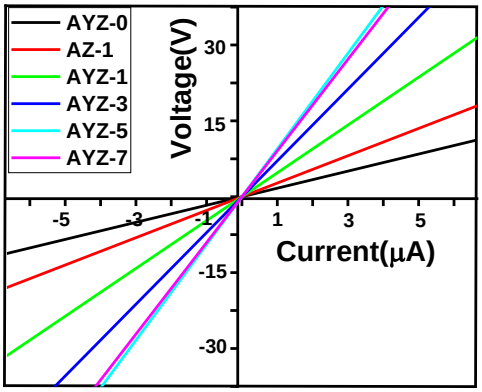

Fig. 3. 12. I-V plots of different AYZ sensors at 350 °C.

The response of different AYZ sensors to 1, 5, 10, and 25 ppm ethanol vapors at 350°C and 33% RH is plotted in Fig. 3. 13 (a). It was observed that 1 wt% Al doped ZnO sample (AZ-1) shows higher response than pristine ZnO sample (AYZ-0). However, 3 wt% Al doped ZnO (AZ-3) shows lower response as compared to AZ-1. Also, 1 wt% Y doped ZnO (YZ-1) exhibits higher response than pristine ZnO (AYZ-0) but it's lower than both AZ-1 and AZ-3. Therefore, keeping Al doping concentration constant at 1wt%, the doping concentration of Y was increased for co-doped samples. It was observed that, sensor response increases with increasing Y concentration, reached a maximum for AYZ-5 (5 wt% Y and 1 wt% Al doping). Thus, the beneficial effect of co-doping is unequivocally established.

Relative humidity (%RH) plays an important role in sensing response. Effect of humidity on gas sensing response and baseline of AYZ-5 sensor is shown in Fig. 3. 13 (b). Baseline resistance of the sensor shows negligible variation to different background %RH. The responses of the AYZ-5 sensor towards 1ppm ethanol in different %RH background (ranging from 3%RH to 94%RH) were measured as shown Fig. 3. 13(b). It delineates that humidity has inconsequential effect on the response of AYZ-5 sensor. The response data can be fitted well (adj. R^2 = 0.97) with the following equation,

$$S_g = a + b.(\%RH) \ldots\ldots\ldots\ldots\ldots\ldots (3)$$

where, "S_g" represents the sensing response, "a" is a constant, and "b" is the slope of the curve. "b" signifies the influence of humidity on sensor response at a fixed ethanol concentration. The slope of the curve (b=0.05) indicates that the response to 1 ppm ethanol changes by 0.05% with 1% change in background %RH. All other sensing response studies were conducted in 33% RH (as present in environment) background. [52-53]

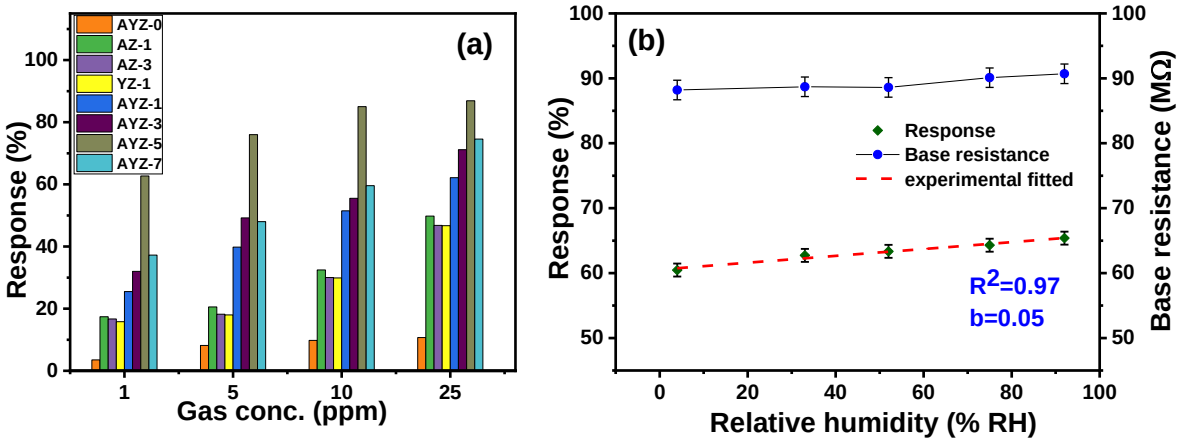

Fig. 3. 13. (a) The response of different ZnO sensors towards 1, 5, 10, 25 ppm ethanol vapor at 350°C and constant 33% RH background; and (b) Variation of AYZ-5 sensor response (1ppm ethanol) and base resistance in different %RH background at 350°C.

The dynamic response curves of the AYZ-5 sensor to various concentrations of ethanol vapor ranging from 300 ppb to 100 ppm at 350°C and 33% RH is shown in Fig. 3. 14(a). Clearly, the resolution (difference) in response of AYZ-5 sensor towards various concentrations of ethanol vapour is good enough for real device application. As mentioned earlier that the concentration of ethanol in healthy human breath is 380 ppb and in case of hepatic steatosis diseases it could escalate above 2.3 ppm (ref. Fig. 3. 14(b)).

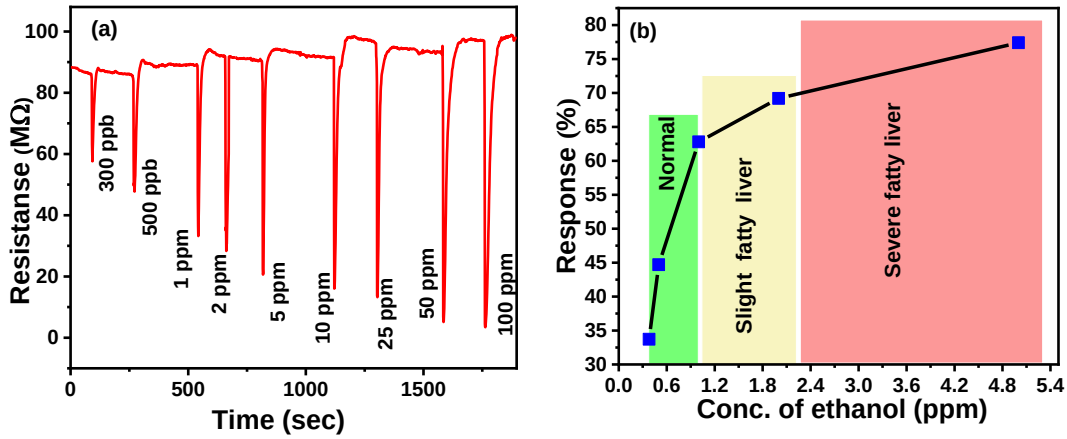

Fig. 3. 14. (a) Dynamic response curves of AYZ-5 nanoparticles to different concentrations of ethanol vapor (300 ppb to 100 ppm) at 350 °C; and (b) suitability of AYZ-5 sensor for the detection of hepatic steatosis (fatty liver disease).

It has been reported in previous literatures that the sensor response (S_g) of a semiconductor chemiresistive sensor can be represented by the following equation,

$$S_g = kC_g^{\beta}$$

$$\text{or}, \quad \ln(S_g) = \ln(K) + \beta \ln(C_g), \ldots\ldots\ldots\ldots (4)$$

where, "C_g" represents the target gas concentration, "k" is a constant, and "β" is an exponent that determines the sensor to target gas interaction strength. [54]. Fig. 3. 15(a) shows the log-log plot of S_g vs C_g for AYZ-5 sensor to different ethanol vapor concentration from 1 -50 ppm at 350°C and constant 33% RH background. The scatter plot could be fitted well with a straight line (adj. R^2 = 0.97) having a slope (β) of 0.09. Such low β value indicates that the ethanol molecules mostly physisorb on the sensor surface and O^{2-} ions play a major role in oxidizing the ethanol molecules.[55] Further, the linear fitting of the experimental data suggests fast recovery and reversibility of the sensor.

It is observed that the prepared sensor is ultrafast in nature. Accurate response and recovery times can be calculated by fitting the transient resistance curve of the AYZ-5 sensor at 350°C with the single-site Langmuir adsorption model (ref. Fig. 3. 15(b)). [33] The response transient (R(t)) can be fitted with the following equation,

$$R(t) = R_0(t) + R_1 e^{-\left(\frac{t}{\tau_{response}}\right)} \text{--------(5)}$$

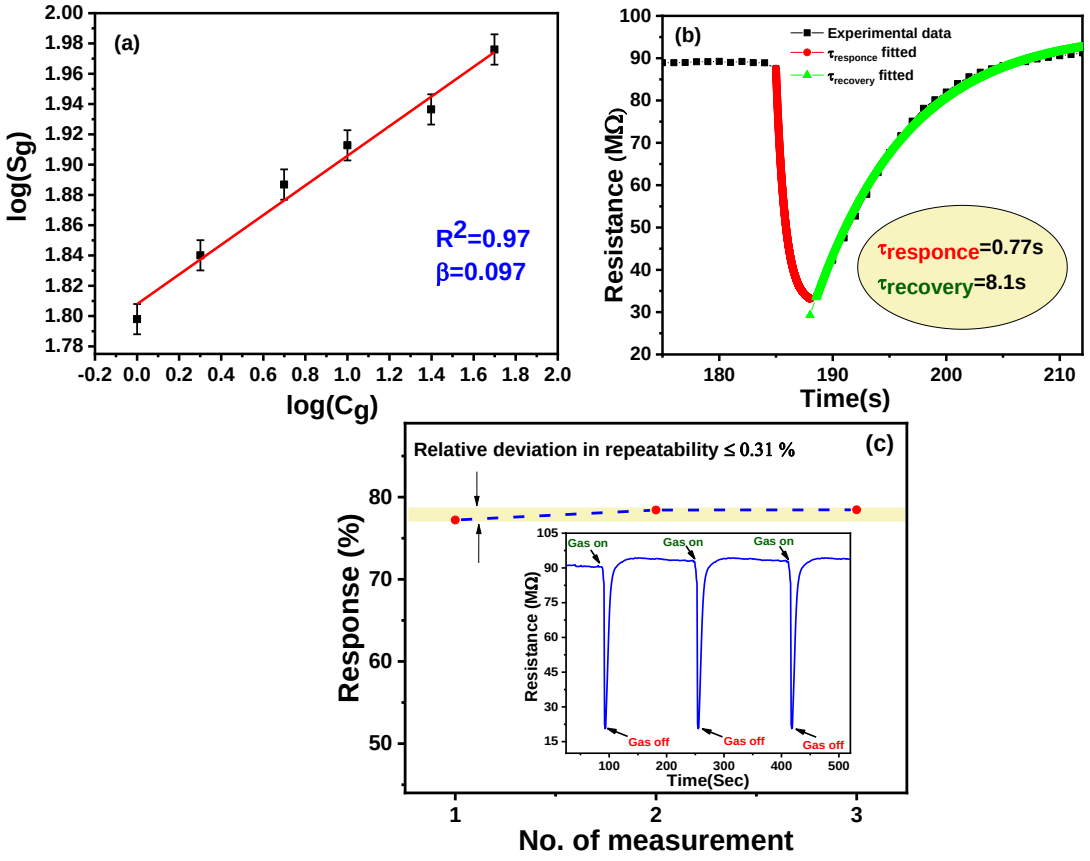

Fig. 3. 15. (a) Linear dependency of AYZ-5 sensor response to different low concentrations of ethanol vapor (1-50 ppm) at 350 °C and constant 33% RH background; (b) Transient resistance curve of AYZ-5 sensor in response to 1 ppm ethanol vapor at 350°C fitted with single-site Langmuir adsorption model; and (c) Repeatability plot of AYZ-5 sensor towards 5 ppm ethanol vapor at 350°C and 33% RH background (inset shows repetitive dynamic response curves for AYZ-5 sensor towards 5 ppm ethanol at 350° C and constant 33% RH background).

Where, R(t) is the sensor resistance at an instant t during response process, $R_0(t)$ is a constant, and $\tau_{response}$is the response time. Similarly, the recovery transient can be fitted by the following equation,

$$R'(t) = R_o(t) + R_1'\left(1 - e^{\left(\frac{-t}{\tau_{recovery}}\right)}\right) \text{--------(6)}$$

where, R′(t) is the sensor resistance at an instant t during recovery process, $R'_0(t)$ is a constant, and $\tau_{recovery}$ is the recovery time of the sensor. The response and recovery times ($\tau_{response}$ and

$\tau_{recovery}$) obtained by fitting the transient resistance curve by Eq. (5) and (6) are ~0.77 s and ~8.1 s, respectively. High specific surface area and porous nature of the nanoparticles, weak interaction indicating physisorption between the ethanol molecules and the sensor surface (ref. Fig. 3. 15), and enhanced charge transport through vacancy sites may be attributed to such ultrafast response and recovery process. This will be dealt in further details in a latter section.

Fig. 3. 15(c) shows three repetitive response and recovery cycles of AYZ-5 sensor in response to 5 ppm ethanol vapor at 350°C. Less than 0.31% relative deviation was observed amongst these three curves and this ensures repeatable and reliable measurement by the sensor.

Alongside repeatability, selectivity and temporal stability are two very important parameters in evaluating sensor response. Fig. 3. 16(a) shows the response of AYZ-5 sensor to different cross-interfering VOCs, such as, acetone, ammonia, carbon monoxide, NO, NO_2, formaldehyde, acetylene, and saturated moisture at 350°C. Clearly, AYZ-5 exhibits excellent selectivity to ethanol with respect to other interfering gases/VOCs. Further, the sensor exhibits long-term stable response towards 1 ppm ethanol vapor at 33% RH (ref. Fig. 3. 16(b)). Also, the base resistance of the sensor exhibits stability for at least 300 days (ref. Fig. 3. 16(c)). Such enhanced temporal stability can be attributed to high synthesis temperature (500°C) of the AYZ-5 nanopowder [56].

3.3.4. Gas sensing mechanism

Gas sensing mechanism of a semiconductor metal oxide-based chemiresistive sensor can be described in terms of the change in surface conductivity of the sensing film. There are two types of chemiresistive sensors, viz. n-type and p-type. At the operating temperature electrons from the defect/valence bands migrate to the conduction band. Atmospheric oxygen molecules due to their high electronegativity bind some of these electrons in the conduction band and thus ionsorb at the sensor surface as O_2^-, O^-, or O^{2-} [57]. Owing to such immobilization of free electrons, the resistivity of the sensor increases. When the sensor is exposed to a reducing gas, ethanol vapor for example, the oxygen species oxidize the reducing species, and revert the adsorbed electron back to the conduction band of the sensor. Thus, the resistance of the sensor decreases. Thereafter, atmospheric oxygen again ionsorb at the sensor surface, thereby restoring the original resistance, known as the base resistance of the sensor. The basic gas sensing mechanism is illustrated schematically in Fig. 3. 17.

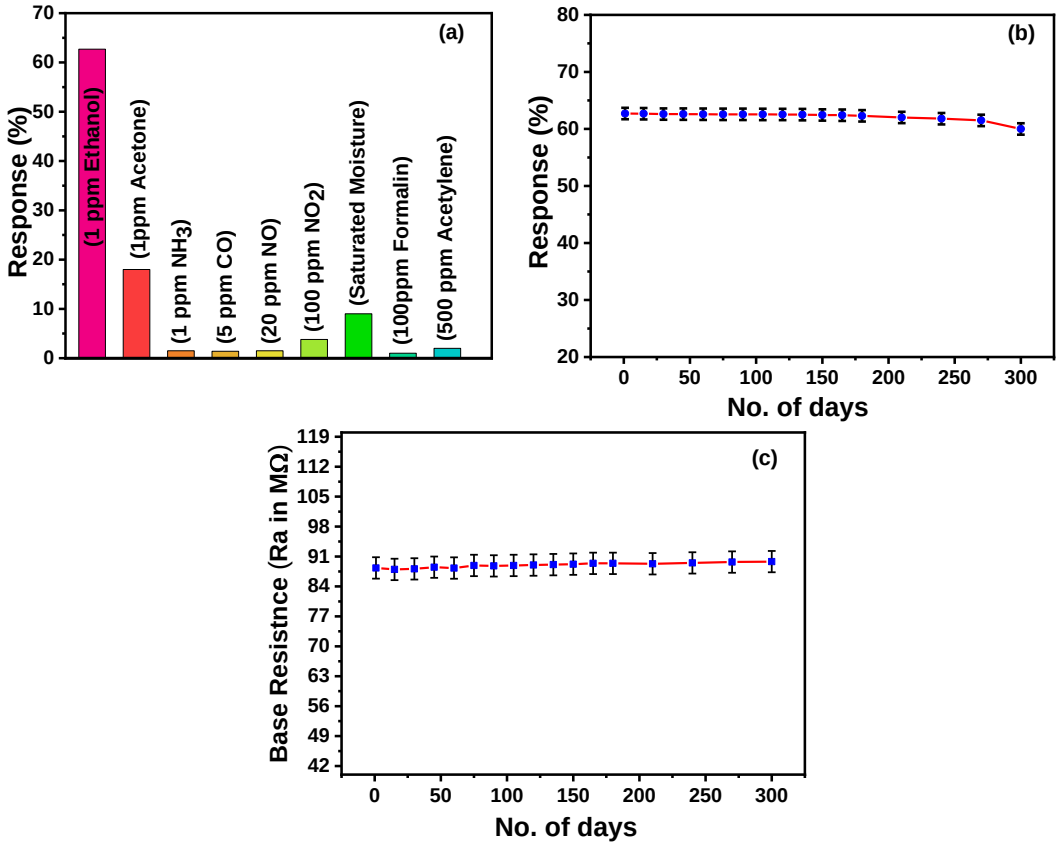

Fig. 3. 16. (a) Cross-sensitivity plot of AYZ-5 sensor towards other major gas volatiles at 350°C; **(b)** Long-term stability graph of the AYZ-5 sensor; and **(c)** Long-term stability graph of the base resistance of AYZ-5 sensor.

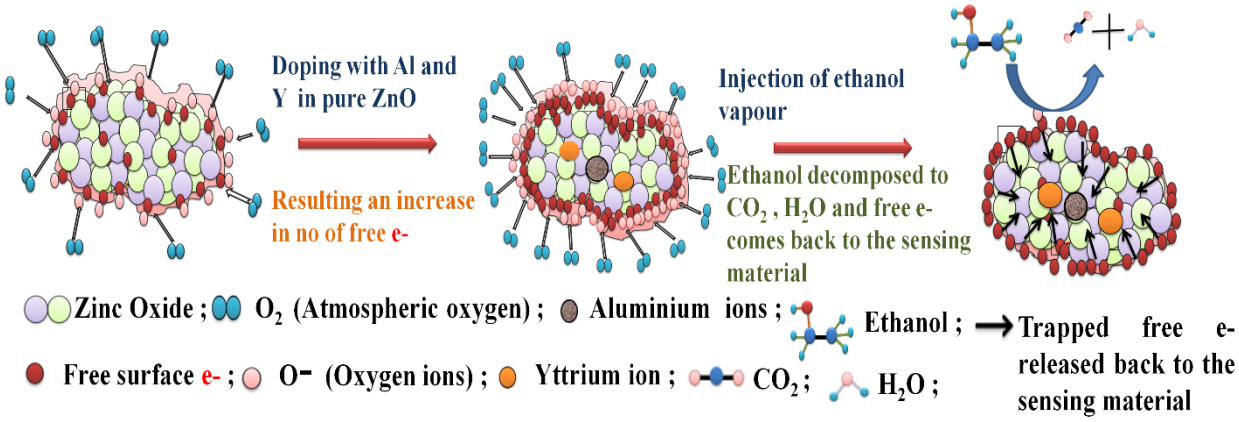

Fig. 3. 17. Schematic presentation of gas sensing mechanism.

The enhanced sensor response and selectivity to trace ethanol vapor of Al, Y co-doped ZnO sensors can be attributed to a complex interplay of multiple parameters, viz. increased

surface basicity, small particle size, high surface area and porosity, doping-induced point defects, and modification of surface electronic states.

3.3.4.1 Effect of Surface basicity

Depending on surface basicity ethanol molecules can interact with the metal oxide surface in two different pathways [58],

$C_2H_5OH \rightarrow C_2H_4 + H_2O$ (Acidic surface) …….. (7)

$C_2H_4 \rightarrow CO_2 + H_2O$……(8)

$C_2H_5OH \rightarrow CH_3CHO + H_2$ (Basic surface) …….(9)

$CH_3CHO \rightarrow CO_2 + H_2O$…….(10)

It may be noted that the C-H bond dissociation energy of ethylene (170 kcal/mol) is much higher than that of acetaldehyde (~87 kcal/mol). Thus, oxidation of acetaldehyde is easier than ethylene. Therefore, oxidation of ethanol is facilitated on basic surface [59]. Rare earth oxides are basic in nature and hence doping by yttrium may be construed as the prime reason for the selectivity of the sensor towards ethanol.

3.3.4.2 Effect of particle size, surface area, and porosity

It is observed from XRD (ref. fig. 2(b)) and FESEM (ref. fig. 3(h)) study that both crystallite size, and particle size decreases with increasing doping concentration, reaches a minimum at AYZ-5, and increases thereafter. The width of electron depletion layer (EDL) is strongly dependent upon the grain size [60]. The width of EDL increases with decreasing particle size. Accordingly, chemisorbed oxygen species at the surface increases. Also, with decreasing particle size surface to volume ration increases and this also allows increased surface chemisorption of oxygen species [61]. Further, porous nature of the nanoparticles allows the vapor and gas molecules to access the deep-seated oxygen species [62]. As a combined effect of all these the sensor is enabled to oxidize a greater number of reducing gas molecules. Thus, the sensitivity increases.

3.3.4.3 Effect of doping-induced enrichment in electron density

Points defects in Al, Y doped ZnO nanoparticles were investigated studying room temperature photoluminescence measurement using an excitation wavelength of 325 nm. Gaussian deconvolutions of the PL spectra for AYZ-0, AZ-1, AYZ-5, AYZ-7 are shown in Fig. 3. 18(a)-(d).

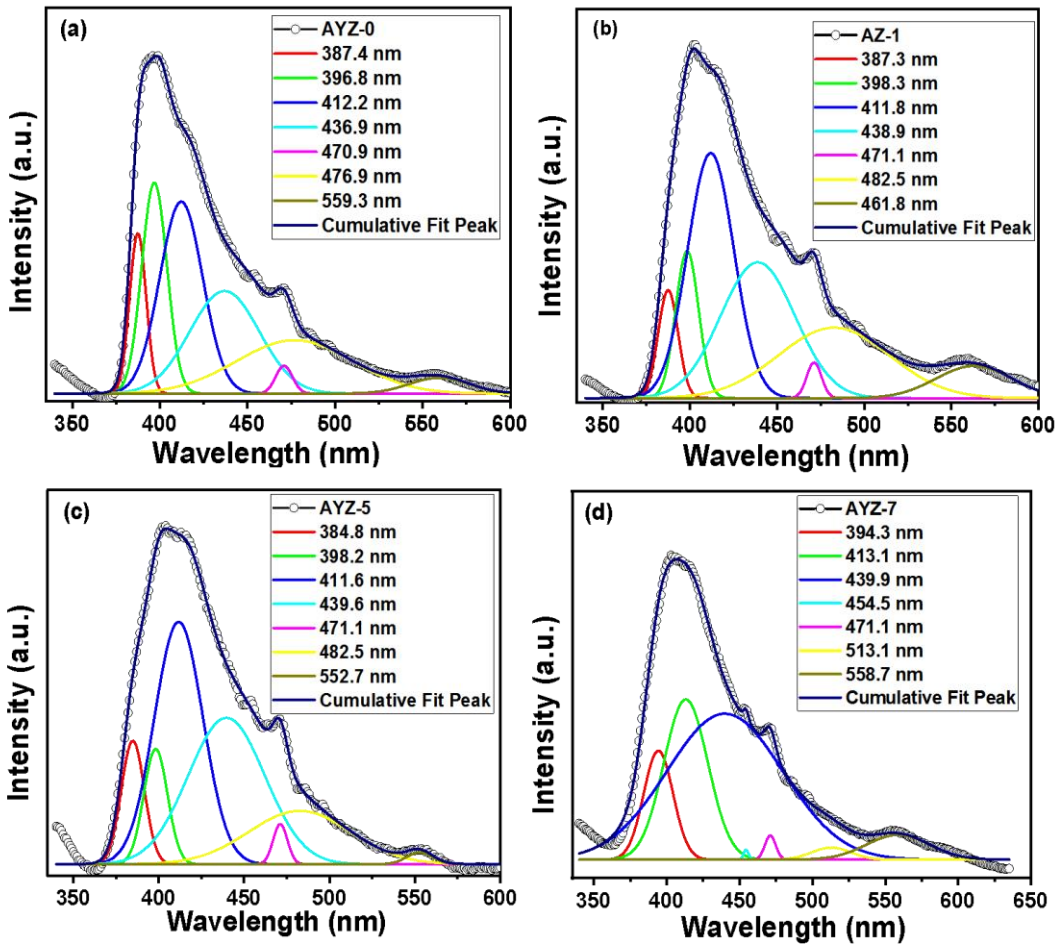

Fig. 3. 18. Gaussian deconvolutions of the PL spectra of (a) AYZ-0; (b) AZ-1; (c) AYZ-5; and (d) AYZ-7.

It is observed that seven different peaks appear around 385, 398, 411, 438, 471, 480, 555 nm corresponding to near-band-edge-emission, shallow donor levels, the shallow donor Zinc interstitial (Zn_i), Zinc Vacancies (V_{Zn}), the recombination of a conduction band electron and $V_O^{\cdot\cdot}$ center (which has two positive charges with respect to the normal site), Oxygen Vacancies (V_o), Oxygen interstitial (O_i) respectively. (ref. Table- 3. 5) [63]. Also, the near band-edge emission (NBE) of AZ-1 is blue shifted as compared to AYZ-0 sample. NBE for AYZ-5 is further blue-shifted as compared to AZ-1. It is plausible that replacement of Zn^{2+} by

Al^{3+} and/or Y^{3+} at the lattice site would induce free electrons that may fill up the lower part of the conduction band. Al, Y doping induced free electron generation may be explained with the help of defect chemistry and represented by Kröger–Vink notation as follows,

Replacing Zn^{2+} with Al^{3+}, $Al_2O_3 \xrightarrow{2ZnO} 2Al_{Zn}^{\bullet} + 2O_O^X + 2e^{/} + \frac{1}{2}O_2(g)$ ..... (11)

Replacing Zn^{2+} with Y^{3+}, $Y_2O_3 \xrightarrow{2ZnO} 2Y_{Zn}^{\bullet} + 2O_O^X + 2e^{/} + \frac{1}{2}O_2(g)$..... (12)

Donation of free electron to the bottom of conduction would lead to a band-gap widening manifested by the above-said blue-shift known as the Burstein -Moss (BM) shift [64]. Lattice strain may also induce such band-gap broadening. However, no substantial difference can be observed amongst the lattice strain of different samples calculated from their respective Williamson-Hall plots (ref. Fig. 19).

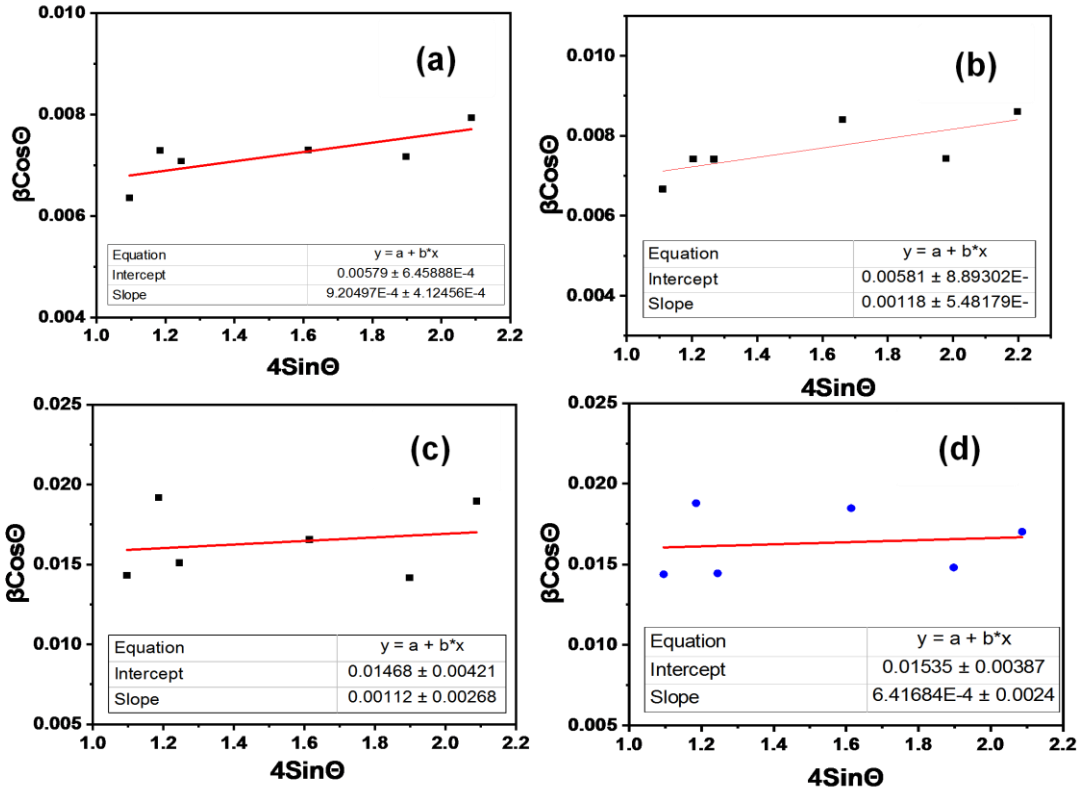

Fig. 3. 19. W-H Plot of (a) AYZ-0; (b)AZ-1; (c) AYZ-5; (d) AYZ-7.

Thus, lattice strain induced band-gap enhancement does not seem plausible. Nevertheless, increased free electron concentration would allow enhanced ionosorption of oxygen species on the sensor surface, thereby increasing sensor response.

Table- 3. 5: PL peaks for different ZnO samples.

Sl. No.	Peak centered at				Peak origin
	AYZ-0	**AZ-1**	**AYZ-5**	**AYZ-7**	
1	387.4	387.3	384.8	394.3	Near-band-edge-emission.
2	396.8	398.3	398.2	413.1	Shallow donor levels, which could not be excited to the conduction band because some excited electrons lose energy through phonon emission.
3	412.2	411.8	411.6	439.9	The shallow donor Zinc interstitial (Zn_i)
4	436.9	438.9	439.6	454.5	Zinc Vacancies (V_{Zn})
5	470.9	471.1	471.1	471.1	The recombination of a conduction band electron and center.
6	476.9	482.5	482.5	513.1	Oxygen Vacancies (V_o)
7	559.3	461.8	552.7	558.7	Oxygen interstitial (O_i)

3.3.4.4 Effect of oxygen vacancy

Oxygen defects play an important role in gas sensing mechanism. In order to investigate the variation of oxygen defects as a function of Y, Al codoping in ZnO, O 1s peaks in the XPS spectrum of AYZ-0, AZ-1, and AYZ-5 were deconvoluted into three Gaussian components, namely lattice oxygen (O_L), defect oxygen (i.e. oxygen vacancy, O_D) and hydroxyl oxygen (i.e. O^-, defined as O_C here), located at ~529.2 ± 0.5 eV (O_L), 531.5 ± 0.5 eV (O_D), and 532.5 ± 0.5 eV (O_C), respectively. (ref. Fig. 3. 20(a-c)). [65] Variation of O_L (%), O_D (%), and O_C (%) as a function of doping concentration is presented in Fig. 3. 20(d). The relative percentage of O_D and O_C is given by,

$$\eta_D = [\, S(O_D)/S(O_S) \,] \times 100 \ldots\ldots\ldots\ldots\ldots\ldots\ldots\ldots \quad (13.1)$$

$$\eta_C = [\, S(O_C)/S(O_S) \,] \times 100 \ldots\ldots\ldots\ldots\ldots\ldots\ldots\ldots \quad (13.2)$$

where $S(O_D)$, $S(O_C)$ and $S(O_S)$ are the intensity of the O_D peak, O_C peak, and the whole O 1s peak, respectively. From Fig. 3. 20 (d) it is observed that η_D increases with doping concentration and reaches maximum for AYZ-5 (~44.6%). On the other hand, the calculated values of η_c are 18.7%, 22.0%, and 31.8% for AYZ-0, AZ-1, and AYZ-5, respectively. It also

shows that AYZ-5 has the highest concentration of O_C that is expected to create maximum interaction with ethanol vapour at the sensor surface. Presence of maximum η_D and η_c is responsible for achieving maximum sensitivity in AYZ-5 which is consistent with the experimental results.

The relative percentages of donor defects (Zn_i and V_O) in different doped and undoped ZnO samples were calculated from their PL peak (around 410 nm for Zn_i, around 480 nm for V_o) intensities calculated from area under the respective peaks (ref. Fig. 3. 18) and are listed in Table-3. 6. It is observed that the donor percentage in AZ-1 (52.18%) is higher than that in AYZ-0. Further, AYZ-5 sample has higher donor concentration (66.3%) than AZ-1 sample. Thus, it may be concluded that the concentration of not only oxygen vacancies but all the donor defects increase with increasing doping concentration. However, in AYZ-7 sample the donor defect percentage decreases. It is plausible that in the presence of Al and/or Y the nucleation and growth process of the ZnO nanocrystals are affected in such a way that the generation of donor point defects are promoted. However, beyond a critical doping concentration (AYZ-5) the generation of donor defects are retarded (as in AYZ-7). Nevertheless, enhanced donor (oxygen vacancy) concentration would enhance free electron concentration at the elevated operating temperature and therefore would improve sensor response. Moreover, oxygen vacancies are highly favorable sites for oxygen chemisorption/ionsorption, thereby further enhancing sensor response.

Table- 3.6: Relative percentage of donor defects in different samples

Sample	**Donor percentage**
AYZ-0	48.21
AZ-1	52.18
AYZ-5	66.3
AYZ-7	26.34

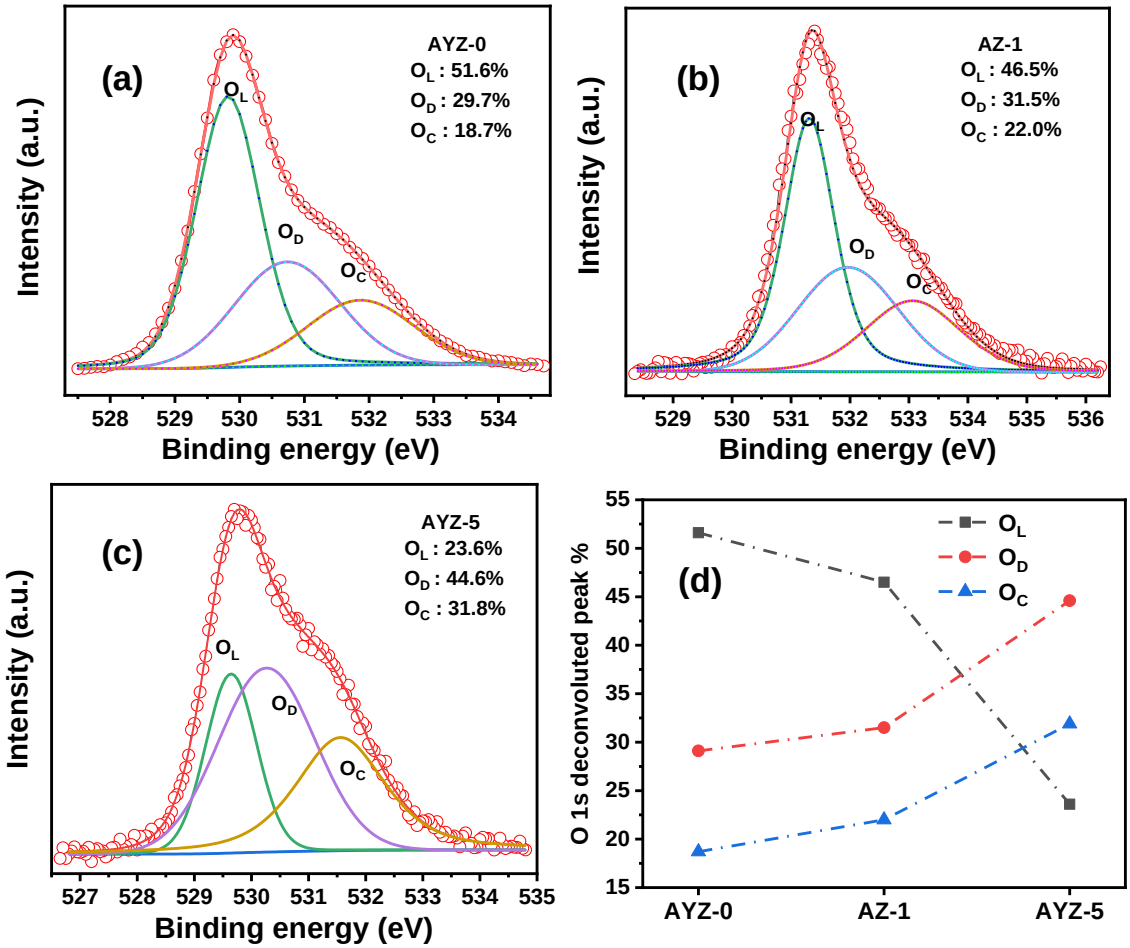

Fig. 3. 20. (a) O 1s of AYZ-0; (b) O 1s of AZ-1; (c) O 1s of AYZ-5; and (d) Variation of O_L (%), O_D (%), and O_C (%) in AYZ-0, AZ-1, AYZ-5 samples.

3.3.5 Simulated breath study

In order to demonstrate the reliability of AYZ-5 nanoparticle-based sensor, real and simulated (intoxicated/fatty liver) breath study was conducted. Different calculated amounts of ethanol vapor were mixed with healthy human breath in tedlar bags to simulate 1 ppm, 5 ppm, and 10 ppm ethanol containing human breath. The AYZ-5 sensor showed excellent resolution between healthy human breath and simulated breath with different trace ethanol concentrations (ref. Fig. 3. 21). Further, to describe the relationship between the sensing result and the previously established sensing calibration curve we have plotted a separate graph (ref. Fig. 3. 21 (b)) for three concentration taking data both from Fig. 14 (a) and Fig. 21 (a). This graph clearly demonstrate that sensitivity is always little higher in case of simulated breath. This indicates that our sensor is capable to detect trace amount of alcohol which is there our exhale

breath. Thus, this sensor may be suitable for real field applications in detecting drunken driving and/or fatty liver disease.

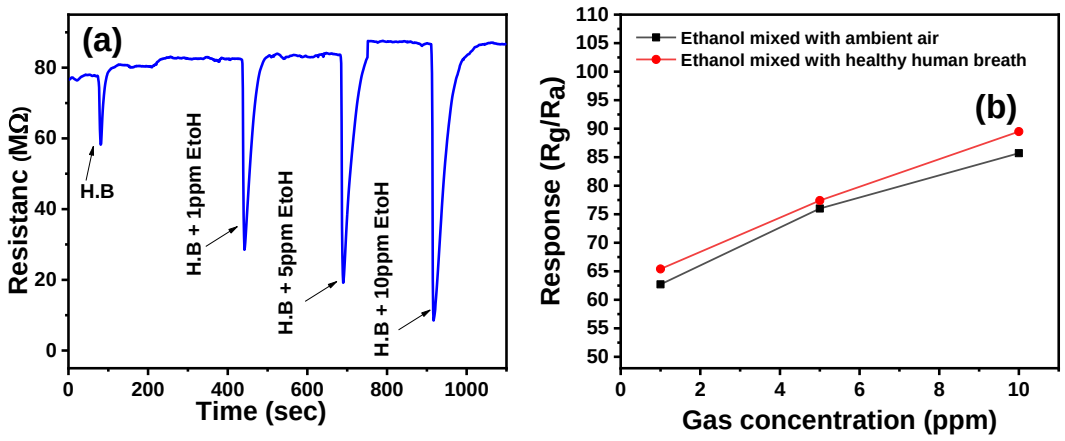

Fig. 3. 21. (a) Sensing response of AYZ-5 sensor towards different trace concentrations of ethanol in exhaled breath background. [H.B = Healthy Breath; EtOH = Ethanol.]; and (b) Relation between gas sensing response of AYZ-5 sensor towards ethanol mixed with ambient air and healthy human breath.

3.4 Conclusions

In summary, we report for the first time chemically prepared Al and Y co-doped ZnO nanopowder based highly sensitive and selective sensor for the detection of trace ethanol in exhaled breath. It was observed that AYZ-5 sensor exhibited highest n-type response to 1 ppm ethanol (62.8%) along with excellent selectivity to trace ethanol with respect to other interfering gases. Also, AYZ-5 sensor exhibited fast response (0.77 s) and recovery times (8.1 s), repeatability, and long-term stability of at least 10 months. Such high sensitivity and selectivity were attributed to high surface to volume ration due to reduced particle size and dopant induced point defects. Further, the AYZ-5 sensor showed excellent resolution between healthy human breath and simulated breath with different trace ethanol concentrations rendering it suitable for breath analysis applications towards drunken driving and fatty liver disease detection.

3.5 References

[1] L. A. Spacek, M.L. Mudalel, R.Lewicki, F. K. Tittel, T.H. Risby, J. Stoltzfus, J. J. Munier, S..F Solga, Breath Ammonia and Ethanol Increase in Response to a High Protein Challenge, J. Biomark., 20 (2015) 149-156.

[2] A. Umar, J.H. Lee, R. Kumar, O. Al-Dossary, A.A. Ibrahim, S. Baskoutas, Development of highly sensitive and selective ethanol sensor based on lance-shaped CuO nanostructures, Mater. Des., 105 (2016) 16–24.

[3] P.Shankar, J.B.B Rayappan, A. Monomer, Designer of ZnO Nanostructures (Nanobush & Nanowire) and Their Room Temperature Ethanol Vapor Sensing Signatures. ACS Appl. Mater. Inter., 9 (2017) 38135-38145.

[4] S.F. Solga, A. Alkhuraishe, K. Cope, A. Tabesh, J.M. Clark, M. Torbenson, P. Schwartz, T. Magnuson, A.M. Diehl, T.H. Risby, Breath Biomarkers and Non-alcoholic Fatty Liver Disease: Preliminary Observations, J. Biomark., 11 (2006) 174-183.

[5] P. Jacquinot, A. W. E. Hodgson, B. Müller, B. Wehrlib, P. C. Hauser, Amperometric detection of gaseous ethanol and acetaldehyde at low concentrations on an Au–Nafion electrode, Analyst, 124 (1999) 871–876.

[6] E. Pedrosa, N. Márcio, F. Bergamini, L. H. Marcolino-Junior, Improvement in the performance of an electrochemical sensor for ethanol determination by chemical treatment of graphite, J. Electroanal. Chem., 877 (2020) 114659.

[7] D. Liu, R. Kumar, F. Wei, W. Han, A. K. Mallik, J. Yuan, S. Wan, X. He, Z. Kang, F. Li, C. Yu, G. Farrella, Y. Semenova, Q. Wu, High sensitivity optical fiber sensors for simultaneous measurement of methanol and ethanol, Sens. Actuators B: Chem., 271 (2018) 1–82.

[8] L. Rotariu, C. Bala, V. Magearu, New potentiometric microbial biosensor for ethanol determination in alcoholic beverages, Anal. Chim. Acta., 513 (2004) 119–123.

[9] Y. H. Mohammed, J. M. Ghaidaa, H.H. Imad, Analysis of Bioactive Chemical Compounds of Nigella sativa Using Gas Ghromatography-Mass Spectrometry. J. Pharmacogn. Phytother., 8 (2016) 8−24.

[10] R. Teranishi, T.R. Mon, A.B. Robinson, P. Cary, L. Pauling, Gas Chromatography of Volatiles from Breath and Urine., Anal. Chem., 44 (1972) 18−20.

[11] M. Westhoff, P. Litterst, L. Freitag, W. Urfer, S. Bader, J.I. Baumbach, Ion Mobility Spectrometry for the Detection of Volatile Organic Compounds in Exhaled Breath of Patients with Lung Cancer:Results of A Pilot Study. Thorax, 64 (2009) 744−748.

[12] J.I. Baumbach, Ion Mobility Spectrometry Coupled with Multicapillary Columns for Metabolic Profiling of Human Breath, J. Breath Res., 3 (2009) 034001.

[13] J. E. Lee, C. K. Lim, H. J. Park, H. Song, S.Y. Choi, D.S. Lee, ZnO−CuO Core-Hollow Cube Nanostructures for Highly Sensitive Acetone Gas Sensors at the ppb Level, ACS Appl. Mater. Interfaces, 12 (2020) 35688−35697.

[14] P. Karthik, M. k. Manoj, V.Shanmugam, Boomadevi, R. K. Karn, V. Singh, P.K.Singh, K. Pandiyan, Studies on acetone sensing characteristics of ZnO thin film prepared by sol–gel dip coating, J. Alloys Compd. 673 (2016) 138-143.

[15] R. Wagner, D. Schönauer-Kamin, R. Moos, Novel Operation Strategy to Obtain a Fast Gas Sensor for Continuous ppb-Level NO_2 Detection at Room Temperature Using ZnO—A Concept Study with Experimental Proof, Sensors,19, 2019, 4104.

[16] P. S. Kolhe, A. B. Shinde, S.G. Kulkarni, N. Maiti, P. M. Koinkar, K. M. Sonawane, Gas sensing performance of Al doped ZnO thin film for H_2S detection J. Alloys Compd., 748 (2018) 6-11.

[17] A. Singh, A. Sharma , M. Tomar, V. Gupta, Growth of highly porous ZnO nanostructures for carbon monoxide gas sensing, Surf. Coat. Technol. 343(2018) 49-56.

[18] Y. Liu, X. Xu, Y. Chen, Y. Zhang, X. Gao, P. Xu, X. Li, J. Fang, W. Wen, An integrated micro-chip with $Ru/Al_2O_3/ZnO$ as sensing material for SO_2 detection, Sens. Actuators B: Chem. , 262 (2018) 26–34.

[19] Z. Wang, Z. Tian, D. Han, F. Gu, Highly Sensitive and Selective Ethanol Sensor Fabricated with In-Doped 3DOM ZnO, ACS Appl. Mater. Interfaces, 8 (2016) 5466−5474.

[20] M. Bagheri, N. F. Hamedani, A. R. Mahjoub, A. A. Khodadadi, Y. Mortazavi, Highly sensitive and selective ethanol sensor based on Sm_2O_3-loaded flower-like ZnO nanostructure, Sens. Actuators B: Chem., 191 (2014) 283–290.

[21] B.Y. Huang, Z.X. Zhang, C.H. Zhao, L.M. Cairang, J.L. Bai, Y.X. Zhang, X.M. Mu, J.W. Du, H. Wang, X.J. Pan, J.Y. Zhou, E.Q. Xie, Enhanced gas-sensing performance of ZnO@In2O3 core@shell nanofibers prepared by coaxial electrospinning, Sens. Actuator B-Chem., 255 (2018) 2248–2257.

[22] L. Zhu , Y. Li, W. Zeng, UV-enhanced ethanol sensor based on nanorod-assembled flower-like ZnO, Phys. E: Low-Dimens. Syst. Nanostructures, 94 (2017) 123-125.

[23] W. Yan, Y. Chen, X. Zeng, G. Wu, W. Jiang, D. Wei, M. Ling, K.W. Ng, Y. Qin, Ultrasensitive ethanol sensor based on segregated ZnO-In2O3 porous nanosheets, Appl. Surf. Sci., 535 (2021) 147697.

[24] A. Ahmadi Daryakenari, M. Ahmadi Daryakenari, Y. Bahari,and H. Omivar**,** Preparation and Ethanol Sensing Properties of ZnO Nanoparticles via a Novel Sol-Gel Method, ISRN Nanotechnology, 6 (2012) 879480.

[25] M. Sudha, S. Radha, S. Kirubaveni, R. Kiruthika, R. Govindaraj, N. Santhosh, Experimental study on structural, optoelectronic and room temperature sensing performance of Nickel doped ZnO based ethanol sensors, Solid State Sci.,78 (2018) 30-39.

[26] Y. Wu, T. Jiang, T. Shi, B. Sun, Z.R. Tang, G.L. Liao, Au modified ZnO nanowires for ethanol gas sensing, Sci. China Technol. Sci. , 60 (2017) 71–77.

[27] P. Das, B. Mondala, K. Mukherjee, Hierarchical zinc oxide nano-tips and micro-rod: Hydrothermal synthesis and improved chemi-resistive response towards ethanol, RSC Adv., 6 (2016) 1408–1414.

[28] T. Qi, X. Yang, J. Sun, Neck-Connected ZnO Films Derived from Core-shell Zeolitic Imidazolate Framework-8 (ZIF-8)@ZnO for Highly Sensitive Ethanol Gas Sensors, Sens. Actuator B-Chem., 283 (2019) 93-98.

[29] H. Tian, H. Fan, J. Ma, Z. Liu, L. Ma, S. Lei, J. Fang, C. Long, Pt-Decorated Zinc Oxide Nanorod Arrays with Graphitic Carbon Nitride Nanosheets for Highly Efficient Dual-Functional Gas Sensing., J. Hazard. Mater., 341 (2018) 102−111.

[30] L. Wang, H. L. Hao, F. Y. Wang, K. Yu, S. Wang, Polymer g-C_3N_4 wrapping bundle-like ZnO nanorod heterostructures with enhanced gas sensing properties , J.Mater. Res., 33(10) (2018) 1-10.

[31] J. Liu, T. Wang, B. Wang, P. Sun, Q. Yang, X. Liang, H. Song, G. Lu, Highly sensitive and low detection limit of ethanol gas sensor basedon hollow ZnO/SnO2spheres composite material, Sens. Actuator B-Chem., 245 (2017) 551–559.

[32] Y. Hu, X. Zhou, Q. Han, Q. Cao, Y. Huang, Sensing Properties of CuO-ZnO Heterojunction Gas Sensors, Mater. Sci. Eng. B: Solid-State Mater. Adv. Technol., 99(1) (2003) 41-43.

[33] T. Das, S. Das, M. Karmakar, S. Chakraborty, D. Saha, M. Pal, Novel barium hexaferrite based highly selective and stable trace ammonia sensor for detection of renal disease by exhaled breath analysis, Sens. Actuator B-Chem., 325 (2020) 128765.

[34] N. Chakraborty, P. Kumar Ghose, P. Rudra, S. Das, D. Saha, A. K. Mishra, A. Sanyal, S. Mondal, Dopant-induced cationic bivalency in hierarchical antimony-doped tin oxide nano-particles for roomtemperature SO_2 sensing. J. Mater. Chem. A 9(9) (2021) 21824-21834.

[35] A. L. Bail, Whole powder pattern decomposition methods and applications: A retrospection, Powder Diffr. 20 (2005) 316–326.

[36] V. Petricek, M. Dusek, L. Palatinus, Crystallographic Computing System JANA2006: General Features, Z. Kristallogr. 229(5) (2014) 345-352.

[37] S.Chakraborty, M.Pal, Improved ethanol sensing behaviour of cadmium sulphide nanoflakes: Beneficial effect of morphology , Sens. Actuator B-Chem., 242 (2017) 1155–1164.

[38] I.B. Elkamel, N. Hamdaoui, A. Mezni, R. Ajjel, L. Beji, Synthesis and characterization of Cu doped ZnO nanoparticles for stable and fast response UV photodetector at low noise current , J. Mater. Sci. Mater. Electron., 30 (2019) 9444–9454.

[39] A. Djelloul, M.s. Aida, Jamal Bougdira, Photoluminescence, FTIR and X-ray diffraction studies on undoped and Al-doped ZnO thin films grown on polycrystalline α-alumina substrates by ultrasonic spray pyrolysis, J. Lumin. ,130(11) (2010) 2113-2117.

[40] M. Thirumoorthi , J. T. J. Prakash, Structural, morphological characteristics and optical properties of Y doped ZnO thin films by sol–gel spin coating method, Superlattices Microstruct., 85 (2015) 237–247.

[41] X. Zhou, D. Zhang, Y. Zhu, Y. Shen, X. Guo, W. Ding, Y. Chen, Mechanistic Investigations of PEG-Directed Assembly of One-Dimensional ZnO Nanostructures, J. Phys. Chem. B, 110 (2006) 25734-25739.

[42] H.Y. Lin, J.L. Thomas, PEG-Lipids and Oligo (ethylene glycol) Surfactants Enhance the Ultrasonic Permeabilizability of Liposomes , Langmuir, 19 (2003) 1098-1105.

[43] J. Wang, Y, Li, Y. Kong, J. Zhou, J. Wu, X. Wu, W. Qin, Z. Jiao, L. Jiang, Non-fluorinated superhydrophobic and micro/nano hierarchical Al doped ZnO film: the effect of Al doping on morphological and hydrophobic properties, RSC Adv., 5, 2015, 81024.

[44] G.B. Sun, K. Hidajat, XS. Wu, Kawi, A crucial role of surface oxygen mobility on nanocrystalline Y_2O_3 support for oxidative steam reforming of ethanol to hydrogen over Ni/Y_2O_3 catalysts, Appl. Catal. B ., 81(3–4) (2008) 303-312.

[45] Y.C. Liang, C.C. Wang, Surface crystal feature-dependent photoactivity of ZnO-ZnS composite rods: Via hydrothermal sulfidation, RSC Adv., 8 (2018) 5063–5070.

[46] N. Naskar, M. F. Schneidereit, F. Huber, S.Chakrabortty, L. Veith, M. Mezger, L. Kirste, T. Fuchs, T. Diemant, T. Weil, R. J. Behm, K. Thonke, F. Scholz Impact of Surface Chemistry and Doping Concentrations on Biofunctionalization of GaN/Ga–In–N Quantum Wells, Sensors. 20(15) (2020) 4179.

[47] E. O. Filatova, A. S. Konashuk, Interpretation of the Changing the Band Gap of Al_2O_3 Depending on Its Crystalline Form: Connection with Different Local Symmetries, J. Phys. Chem. C, 119 (2015) 20755−20761.

[48] W. C. Wang, M. Badylevich, V. V. Afanas'ev, KU Leuven, A. Stesmans, C. Adelmann, S. Van Elshocht, J. A. Kittl, Mindaugas Lukosius , Ch. Walczyk, Ch. Wenger, Band alignment and electron traps in Y_2O_3 layers on (100)Si, Appl. Phys. Lett., 95(13) (2009) 132903-132903-3.

[49] S. Das, P. L. Mahapatra, P. P. Mondal, T. Das, M. Pal, D. Saha, A Highly Sensitive Cobalt Chromite Thick Film based Trace Acetone Sensor with Fast Response and Recovery Times for the Detection of Diabetes from Exhaled Breath, Mater. Chem. Phys. 262(1) (2021) 124291.

[50] J. Herrmann, G. Hagen, J. Kita, F. Noack, D. Bleicker, R. Moos, Multi-gas sensor to detect simultaneously nitrogen oxides and oxygen, J. Sens. Sens. Syst., 9, 2020, 327–335.

[51] K. Sahner, A. Schulz, J. Kita, R. Merkle, J. Maier, R. Moos, CO_2 Selective Potentiometric Sensor in Thick-film Technology Sensors, 8, 2008, 4774-4785.

[52] P. Chen, V. Rizzotto, A. Khetan, K. Xie, R. Moos, H. Pitsch, D. Ye, U. Simonb, Mechanistic understanding of Cu-CHA catalyst as sensor for direct NH_3-SCR monitoring: the role of Cu mobility, ACS Appl. Mater. Interfaces 11, 2019, 8097−8105.

[53] D. Biskupski, A. Geupel, K. Wiesner, M. Fleischer, R. Moos, Platform for a Hydrocarbon Exhaust Gas Sensor Utilizing a Pumping Cell and a Conductometric Sensor Sensors 2009, 9, 7498-7508.

[54] S. Chakraborty, M. Pal, Improved sensitivity of CdS nanoparticles by virtue of calcium doping: Promising candidate for monitoring alcohol in exhale human breath, Mater. Des., 126 (2017) 18–28.

[55] S. Chakraborty, M. Pal, Highly selective and stable acetone sensor based on chemically prepared bismuth ferrite nanoparticles, J. Alloys Compd. 787 (2019) 1204-1211.

[56] N.S. Baik, G. Sakai, K. Shimanoe, N. Miura, N. Yamazoe, Hydrothermal treatment of tin oxide sol solution for preparation of thin-film sensor with enhanced thermal stability and gas sensitivity, Sens. Actuators B Chem. 65 (2000) 97–100.

[57] N. Chakraborty, S. Das, V. Srihari, D. J. Mondal, D. Saha, S. Konar, A. K. Mishra, S. Mondal, Roles of structure and electron mobilization in enhanced ethanol sensing by Al doped SnO_2 nanoparticles, Mater. Adv., 2 (2021) 3760–3769.

[58] I. Stambolova, K. Konstantinov, S. Vassilev, P. Peshev, T. Tsacheva, Lanthanum doped SnO_2 and ZnO thin fifilms sensitive to ethanol and humidity, Mater. Chem. Phys. 63 (2000) 104–108.

[59] A.M. Maitra, Determination of solid state basicity of rare earth oxides by thermal analysis of their carbonates, J. Therm. Anal. 36 (1990) 657675.

[60] F. Lu, Y. Liu, M. Dong, X.P. Wang, Nanosized tin oxide as the novel material with simultaneous detection towards CO, H_2 and CH_4, Sens. Actuators B: Chem. 66 (2000) 225–227.

[61] S. Das, S. Mojumder, D. Saha, M. Pal, Influence of major parameters on the sensing mechanism of semiconductor metal oxide based chemiresistive gas sensors: A review focused on personalized healthcare, Sens. Actuators B: Chem. , 352(2) (2022) 131066.

[62] C. Wang, L. Yin, L. Zhang, D. Xiang, R. Gao, Metal oxide gas sensors: sensitivity and inflfluencing factors, Sensors 10 (2010) 2088–2106.

[63] S. Bai, T. Guo, Y. Zhao, R. Luo, D. Li, A. Chena, C. C. Liub, Mechanism enhancing gas sensing and first-principle calculations of Al-doped ZnO nanostructures, J. Mater. Chem. A, 1 (2013) 11335–11342.

[64] H. H. C. Lai, T. Basheer, V. L. Kuznetsov, R. G. Egdell, R. M. J. Jacobs, M. Pepper, P. P. Edwards, Dopant-induced bandgap shift in Al-doped ZnO thin films prepared by spray pyrolysis, J. Appl. Phys. 112 (2012) 083708.

[65] W. Guo, L. Huang, X. Liu, J. Wang, J. Zhang, Enhanced isoprene gas sensing performance based on p-$CaFe_2O_4$/n-ZnFe2O4 heterojunction composites, Sensors and Actuators: B. Chemical 354 (2022) 131243.

CHAPTER-IV

Improved Ammonia Sensing Performance Achieved Through Defect Modulation by Li Doping in Cauliflower-like ZnO for Exhaled Breath Analysis Towards Renal Diseases Detection: An Experimental Venture Supported by Ab-initio Calculation

Work is published in “Trends in Analytical Chemistry 180 (2024) 117896”

4.1 Introduction

Ammonia (NH3) in human exhaled-breath is identified as a key biomarker of renal /kidney related diseases. Our body generates urea as a by-product of metabolic activity. A person with kidney diseases suffers from incomplete regulatory reactions of urea, which increase urea content in blood. Excess urea in blood results in increased ammonia concentration in exhaled breath. Amount of ammonia in exhaled human breath resides around 0.25 ppm for healthy human being which may escalate above 5 ppm in a person suffering from severe renal disease.[1,2] Therefore, development of ultra-sensitive NH_3 sensor which could selectively sense the low concentration of ammonia in presence of several interfering gases (such as acetone, ethanol, CO, formalin etc.) and high humid atmosphere is an urgent demand of the society. Several analytical techniques (such as, Gas Chromatography-Mass Spectrometry (GC–MS), laser spectroscopy, Selected mass flow tube mass spectrometry (SIFT-MS) etc.) can be utilized for exhale breath ammonia detection.[3,4] However, all these instruments are very costly, cumbersome and needs trained manpower to operate.

Among other techniques semiconductor metal oxide (SMO) based chemiresistive gas sensing have attracted attention of researchers due to its cost effective and user-friendly nature.[5–7] Various SMO based ammonia sensors containing α-Fe_2O_3, V_2O_5, MoO_3, SnO_2, TiO_2, WO_3, Co_3O_4 and ZnO as sensing material have been previously studied. Especially, gas sensing performance of zinc oxide-based materials have been investigated extensively because of its wide band gap (E_g~3.1eV), high thermal stability. Moreover, it is relatively easy to modulate the band gap of ZnO and to produce different morphology with it. However, gas sensing performance of pristine ZnO could not meet the practical requirements. Tailoring the interstitial defect states and corresponding oxygen vacancies in ZnO system by means of strategic chemical doping is an effective way for enhancement of gas sensing performance of the ZnO based sensors.

Wang et al. and Mhlong et al. investigated the ammonia sensing capabilities of ZnO/NiO and ZnO/Pd nanocomposites. However, these materials exhibited insufficient low detection limits and prolonged response recovery, rendering them impractical for use in device. [14,15] Qi.et al. reported ammonia sensing behaviour of SnO_2/In_2O_3 nanofibers which could detect ammonia

up to 100 ppb but stability of the sensor was not reported properly. [17] Y lei et al. reported α-MoO_3 nanofibers based ultrasensitive ammonia sensor that could detect ammonia as low as 50 ppb but recovery time for that sensor was too long and long-term stability was also not checked. [18] In the last decade few researchers have published reports on ammonia sensing based on polymer based flexible sensors where mostly PANI and Polypyrrole were chosen as active sensing materials. Although polymer-based sensors showed good sensitivity in comparatively lower operating temperature, but these sensors pose a major setback of unstable base resistance which would also affect their sensing response.[8,9] Moreover, the previously reported work on ammonia sensing did not extensively examine sensing response of those fabricated sensors in varying background conditions. Though background RH% plays an influential role for breath analysis it was omitted in majority of literatures. The state-of–art of ammonia sensor and their performance are shown in Table- 4.1. While there are a large amount of research works on semiconductor metal oxide based chemiresistive gas sensing however those mostly focus on particular characteristics rather than providing a thorough analysis of all the key factors influencing sensor performance. Also, to the best of our knowledge there is hardly any study which extensively discussed the scope of real application possibilities of these sensors. In order to bridge this discrepancy, a detailed discussion on the effect of various factors that influence sensing performance and studies on real and simulated human exhale breath is need of the day.

In this work, pure and Li-doped cauliflower-like ZnO powder (LZ-0, 1, 5, 15) were synthesized via reflux technique with varying doping concentrations. The fabricated sensors using synthesized materials delineated excellent ammonia sensing performance. Among different doped samples, 5-wt % Li-doped ZnO (LZ-5) exhibited maximum of 43% n-type response towards 1 ppm ammonia which was almost 400% higher than pristine ZnO based sensor (LZ-0) at optimum operating condition with rapid response and recovery time (1.7s and 17s). This work delves into a detailed discussion on the impact of doping on SMO based gas sensor performance, covering particle morphology, porosity, surface area, oxygen and donor defects, charge separation, and charge transfer resistance. Moreover, the performance of LZ-5 sensor towards simulated breath was measured with real time exhaled breath samples, indicating its potential as a breath analyzer. Density functional theory (DFT) calculations were performed to understand the fundamentals of ammonia sensing process over the Li doped ZnO surface through adsorption energetics and electronic structures. Further DFT simulation study also

revealed adsorption energy of LZ-5 was significantly increased over LZ-0. A comprehensive experimental and theoretical investigation confirms the improved ammonia sensing of Li-doped ZnO sensor, suggesting its potential for renal disease detection as a breath analyzer.

Table- 4. 1: Sensing response of the previously reported NH_3 Gas Sensors

Material	**Concentration (ppm) @ Response (%)**	**Response time (s)**	**Recovery time (s)**	**Lower detection limit (ppm)**
α-Fe_2O_3/graphene [17]	10ppm@~13.5%	152s	648s	5 ppm
V_2O_5 nanosheets[18]	5 ppm@ 9.4%			0.4 ppm
V-doped SnO_2 [19]	10ppm@~77.7%	-	-	10ppm
ZnO [20]	400ppm@ ~17%	120~180	600~1200	
ZnO[21]	500 ppm @ 8%	360	-	
ZnO-rGO nanocomposite [22]	50 ppm @ 19.2%	50	250	
ZnO-NiO nanocrystals [23]	50ppm@ 42%	20s	90s	15 ppm
Pd-doped ZnO [24]	15ppm@ ~12%	198s	334s	30 ppm
ZnO/MoS2 nanocomposite [25]	5ppm@ ~23%	10s	11s	250 ppb
SnO_2/In_2O_3 nanofibers [26]	1ppm @ ~21folds	7s	10s	100 ppb
MoO_3 nanoribbons[27]	5ppm@ ~66%	21s	217s	100 ppb
Polypyrrole and Functionalized MWCNT Nanocomposites[28]	100ppm@ ~27%	16s	110s	5 ppm
Ppy/MWCNT rigid 200 3.07a 34 normal[29]	200ppm@ 3.07%	34s		
Ppy/SWCNT alumina rigid 750 1100a 415[30]	750 ppm@ 1100%	415s		
SWCNT@Ppy@PA[31]	1 ppm@ 2%	600-700s		

PPy (Flowers) PPy (Urchins) [32]	100 ppm@ 16.37% 100 ppm@ 34.25%	30s 23s	62s 67s	1ppm 1ppm
PPy/rGO [16]	1ppm@ 6.1%	60s		< 1
PPy-ZnO spherical nanocomposite [33]	100ppm@ 76%	45s		1ppm
PPy/sulfonated RGO Spherical nanocomosite[34]	0.001ppm@ 0.9%	48s		0.0002 ppm
polyaniline[35]	1ppm@ 3.33 folds	130s	195s	0.01 ppm
PSS doped ZIF-8-derived porous carbon/polyaniline hybrid film[36]	5.67 Hz/ppm	28s	17s	1 ppm
AlOOH microspheres.[37]	5ppm@ ~18.4%	57s	42s	0.5 ppm
Li doped ZnO [This work]	1ppm@ 43%	1.7s	17s	25 ppb

4.2 Materials and methods

4.2.1 Materials

Zinc nitrate hexahydrate ($Zn(NO_3)_2.6H_2O$, MW = 297.49 g/mol), lithium nitrate ($LiNO_3$, MW = 68.95 g/mol), polyethylene glycol (PEG-400), 2-butanol ($C_4H_{10}O$ MW = 74.12g/mol), sodium citrate ($C_6H_5O_7.3Na$, MW = 258.07 g/mol), isopropyl alcohol (C_3H_8O, Mw = 60.1 g/mol) were purchased from MERCK (India) and used without further purification. For the fabrication of the sensor module nichrome wire having 38 standard wire gauge, platinum wire having 0.025 mm gauge, conducting gold paste, tubular α-Al_2O_3 having dimensions (3mm X 2.2 mm X 1.1 mm), DI water, plastic made cylindrical sensor-cases were used.

4.2.2 Synthesis of the Li- doped ZnO nanoparticles

Pure and Li doped ZnO NPs were synthesized using reflux method. Zinc nitrate hexahydrate (0.1 mol) and calculated amount of lithium nitrate were dissolved in 100 ml DI water. 5ml polyethylene glycol, 5 ml 2-butanol and 0.01 mol sodium citrate were mixed with the solution. This mixture was kept under vigorous stirring for 2 hours before refluxing. The mixture was shifted to a round bottom refluxing pot and refluxed at 250°C for 5 hours. The refluxed solution was then centrifuged for 20 minutes at 1000 rpm and the precipitate was washed with ethanol for multiple times. For different doping concentrations, distinct batches were synthesized using similar methodologies. The washed powders were calcined at 500°C for 1 hour to obtained phased pure zinc oxide based samples. Names of different doped samples and their dopant contents were shown in Table- 4. 2. Schematic of synthesis procedure is shown in Fig. 4. 1.

Table- 4. 2: Name of different synthesized samples based on doping concentrations, and Variation of different oxygen content as calculated from XPS, BET surface area, Response to NH_3

Li - doping percentage (molar %)	**Samples identification no.**	**Lattice oxygen (O_L) (%)**	**Defect oxygen (O_D) (%)**	**Chemically adsorbed oxygen (O_C) (%)**	**BET surface area (m^2/g)**	**Response to 1 ppm NH_3**
0%	LZ-0	61.2	22.1	16.7	6.13	12
1%	LZ-1	58.3	30.6	11.1	27.9	28
5%	LZ-5	39.4	40.5	20.1	34.4	43.5
15%	LZ-15	-	-	-	10.9	29.5

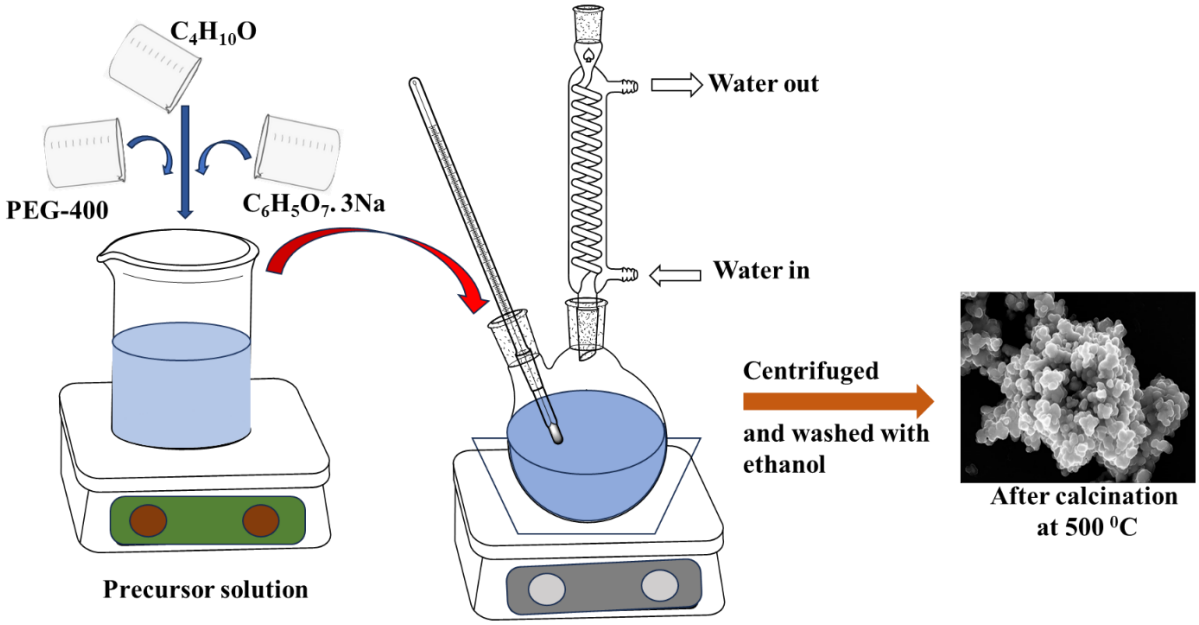

Fig. 4. 1. Schematic representation of material synthesis procedure.

4.2.3 Characterization

X-ray diffraction (XRD) patterns of the samples were analysed by X′ Pert pro MPD (PANalytical) X-ray diffractometer using Cu Kα radiation (1.54 Å) in the 2θ range from 20º to 80º for crystal structure and phase analysis of the synthesized samples. The morphology of the materials were analysed by field emission scanning electron microscope [FESEM, Supra 35 V P microscope (Carl Zeiss)] and transmission electron microscope [TEM Tecnai G230ST (FEI)]. Brunner−Emmet−Teller (BET) measurements were carried out using Quantachrome Instruments version 3.0 for estimation of surface area, pore size and distribution of the samples. Surface electronic states of the different elements of the samples were analysed by the X-ray photo electron spectroscopy using a PHI 5000 Versa Probe II scanning XPS microprobe (ULVAC-PHI, U.S). Elemental composition of the materials were investigated by energy-dispersive X-ray spectroscopy (EDX Oxford Instrument and EDAX Inc., attached to the FESEM). Optical band gap of the samples was measured from UV-Vis spectroscopy (SHIMADZU UV–VIS–NIR spectrometer (UV-3600)). Photoluminescence spectra of the pristine and doped samples were recorded using Horiba FluoroMax-4 spectrometer for analysing the defect states in the doped samples. An Agilent B2901A precision meter was used to performed the Current-voltage (I-V) study of the fabricated sensors to check the ohmic nature of the sensor contacts. A Keysight 34470A digital multimeter along with a GUI enabled software (Keysight BenchVue) was used to collect the gas sensing data of the sensors. The thin films of the materials had been prepared on FTO coated glass substrate. A potentiostat-

galvanostat (ZIVE, SP1) was used to measure the photoelectrochemical (PEC) response. A three-electrode set-up, a Pt electrode as a counter electrode, Ag/AgCl electrode as a reference electrode and an FTO substrate with coated thin film as a working electrode had been used for the measurement. The Xenon light source with an intensity of 150 mW/cm^2 was employed for all the measurements. Linear sweep voltammogram (LSV) was performed at 10 mVs^{-1} scan rate. Photocurrent density and stability were checked *via* Transient photocurrent under chopped conditions. The solution and charge transfer resistance at the electrode-electrolyte interface were calculated by measuring Electrochemical Impedance Spectroscopy (EIS) from 100KHz to 0.01Hz. ZMAN 2.5 software was used to fit the EIS data to calculate the solution charge transfer (R_{ct}) resistance.

4.2.4 Fabrication and measurement of the sensor

Taguchi type sensor module was fabricated using the as prepared pure and doped ZnO nanopowders. A small amount of the synthesized powder was grounded in mortar pestle with isopropanol to make a slurry paste which was then spin coated on an alumina made hollow cylindrical tube. Gold paste and Pt-wire were used to fabricate the electrode over an alumina tube and a nichrome wire was inserted inside the alumina tube to act as a heating coil during gas sensing measurements. Finally, a six-pin plastic socket and a plastic cap with double mesh were used to fabricate the sensor modules.

The fabricated sensor was placed inside a 10L glass desiccator. Saturated aqueous salt solutions were kept at the bottom of the desiccator to maintain definite %RH inside the desiccator. List of saturated salts used to generate certain %RH background are given in Table- 4. 3. Vacuum grease was used to make the inside environment of the desiccator air tight. Sensor was put on a base which delivered a varying DC voltage to generate the operating temperature for the sensor. Other electrodes were connected to the multimeter which recorded the transient resistance of the sensor. Commercially available gas cylinders were used for sensing measurements. Commercially available N_2 gas cylinder and Alicat made mass flow meter (MFC) were used to generate different concentrations for sensing performance. Gas sensing measurement set up is show schematically in the Fig. 4. 2.

Table- 4. 3: %RH generated corresponds to specific saturated salt solutions

Salt	**%RH**
Silica gel	4
Magnesium chloride ($MgCl_2$)	33
Sodium dichromate ($Na_2Cr_2O_7$)	52
Sodium chloride (NaCl)	75
Potassium sulphate (K_2SO_4)	95

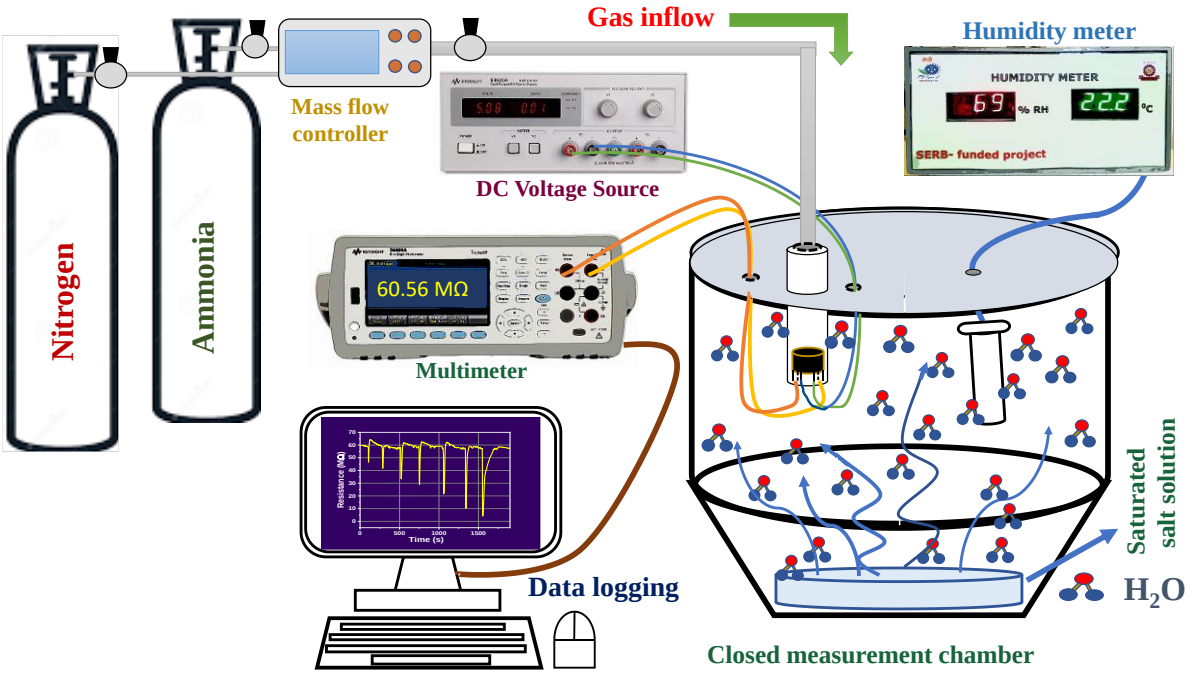

Fig. 4. 2. Schematic presentation of the humidity-controlled gas sensing set up.

4.2.5 Computational details

DFT calculations were carried out utilizing the Vienna ab initio simulation package (VASP) with spin polarization and the projector augmented technique (PAW) to comprehend the gas sensing mechanism of the sensor. The Perdew-Burke-Ernzerh (PBE) exchange-correlation ultra-soft potentials were used. Using various cell sizes and k-points, the geometrical structures of pure ZnO, Li doped ZnO, (ref. Fig. 4. 3(a), (d)) and bare NH_3 were optimized (ref. Fig. 4.

3(b), (e)). A (8×8×5) Monkhorst-Pack k-point grid and a cut off energy of 520 eV were used for pure and Li doped ZnO. For bare NH_3, a (5 × 5 × 5) Monkhorst-Pack k-point grid and the same cut off energy were used. The optimization aimed to achieve the lowest single-point ground state energy, with atomic displacements restricted to ~5×10^{-4} Å and stress restricted to ~0.02 GPa. Convergence was ensured by setting the EDIFF parameter to 10^{-6} eV and the force EDIFG parameter to 10^{-3} eV in both calculations. In the supplemental material, additional information regarding the calculations is provided. An NH_3 molecule was positioned on the O atom of the (101) surface of ZnO and Li doped ZnO system, as illustrated in Fig. 4. 3(c) and Fig. 4. 3 (f). Finally, the adsorption energy (E_{ad}) of the NH_3 molecule on the pristine and Li doped ZnO surface was calculated using following equations;

$$E_{ad} = E_{(NH3+ZnO)} - E_{(ZnO)} - E_{(NH3)} \quad \text{..... (1)}$$

$$E_{ad} = E_{(NH3+ZnO/Li)} - E_{(ZnO/Li)} - E_{(NH3)} \text{..... (2)}$$

Where $E_{(NH3+ZnO)}$, $E_{(ZnO)}$, and $E_{(NH3)}$ represent the total ground state minimum energies of the NH_3 plus ZnO system, bare ZnO, and the bare NH_3 system, respectively. Similarly, $E_{(NH3+Li-ZnO)}$, $E_{(Li-ZnO)}$, and $E_{(NH3)}$ represent the total ground state minimum energies of the NH_3 plus Li-doped ZnO system, bare Li-doped ZnO, and the bare NH_3 system, respectively.[31]

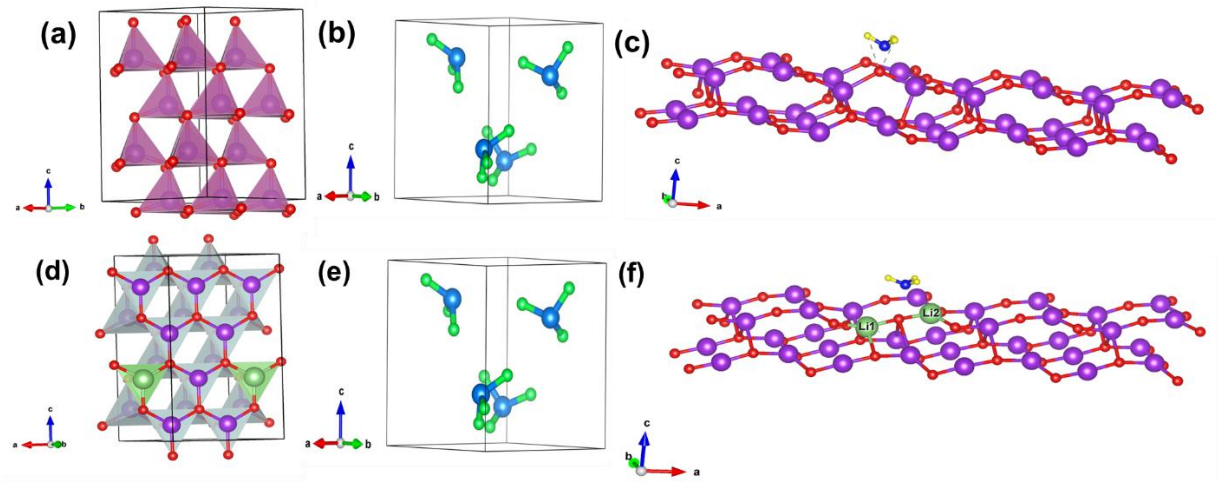

Fig. 4. 3. (a) unit cell's structure of bare ZnO. (b) bare NH_3. (c) supercell structure of NH_3 adsorbed ZnO. (d) unit cell's structure of bare Li doped ZnO. (e) bare NH_3. (f) supercell structure of NH_3 adsorbed Li doped ZnO.

4.3 Result and discussion

4.3.1 Structural, morphological, optical, electrochemical characterization

The indexed X-ray diffraction pattern of the prepared pure, Li doped ZnO nanopowders (LZ-0, LZ-1, LZ-5, LZ-15) are shown in Fig. 4. 4(a). All the peaks match well with the standard data of ZnO (JCPDS-Card no. 36-1451). No extra peak for any impurity is observed in LZ-0, LZ-1, LZ-5 samples. Few low intensity XRD peaks are found in the LZ-15 samples which indicates a very smaller fractions of lithium oxide are formed along with zinc oxide in the higher doped sample. The XRD pattern indicates the formation of phase-pure ZnO. The average crystallite size (D) is calculated using the Debye Scherer's formula,

$$D = (k\lambda/\beta \cos\theta) \quad \ldots\ldots\ldots\ldots\ldots\ldots (3)$$

where k is known as the Scherer's constant (k=0.94), λ is the X-ray wavelength (1.54178Å), β is full width at half maximum (FWHM) of the diffraction peak, and θ is the angle of diffraction. The average crystallite size decreases gradually with increasing doping concentration, but it exhibits an increase in the LZ-15 sample. (ref. Fig. 4. 4(c)). Furthermore, with increasing doping concentration, the (002) peak is gradually shifted towards lower angle. As shown in Fig. 4. 4(b) for LZ-1 sample deviation of the (002) peak is zero and it becomes nearly 0.06º and 0.08º for LZ-5 and LZ-15 sample, respectively. The deviation in the XRD peak position suggests that a few Li ions infiltrated the hexagonal wurtzite ZnO crystal during the synthesis process.

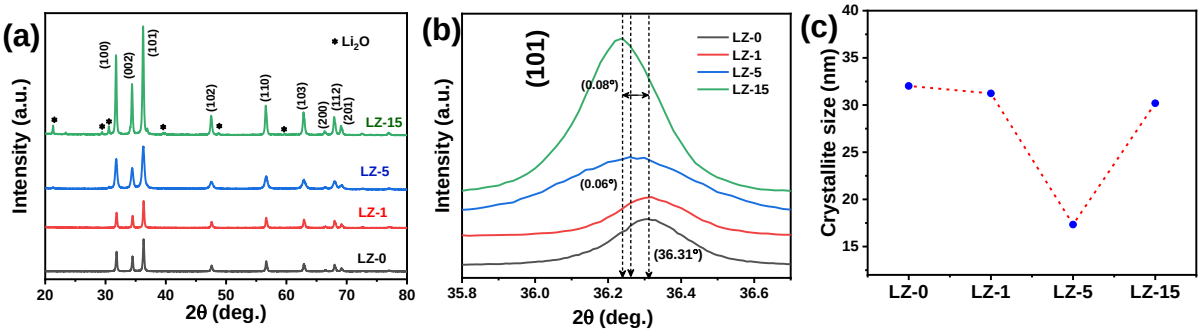

Fig. 4. 4. (a) XRD characterization of all LZ samples, (b) Relative deviation of (101) peak from XRD patterns of all LZ samples, (c) Variation of crystallite size in different LZ samples.

Fig. 4. 5 (a,c) represents the typical FESEM images of pristine (LZ-0) and 5 wt% Li doped ZnO (LZ-5) samples, respectively. LZ-0 sample exhibits 3D-sperical cauliflower like structure which takes more prominent shape in LZ-5 sample. The magnified FESEM images (ref. Fig. 4. 5 (b, d)) show that porous structure having curly edges was formed in both doped and undoped samples. Radius of the spherical structure is measured using ImageJ software. Average radius of the LZ-0 sample is ~1.63 **µ**m which further have reduced to ~1.32 **µ**m in LZ-5. Reduction in grain size owing to the Li doping is in well agreement with XRD results. The energy-dispersive X-ray spectroscopy (EDS) analysis was also performed to analyse the elements present in the material as shown in the Fig. 4. 5 (e). Though the EDS peaks corresponding to Zn, O and C were identified from EDS spectra, presence of Li was not detected through EDS analysis due to its smaller atomic number which is a limitation of EDS.

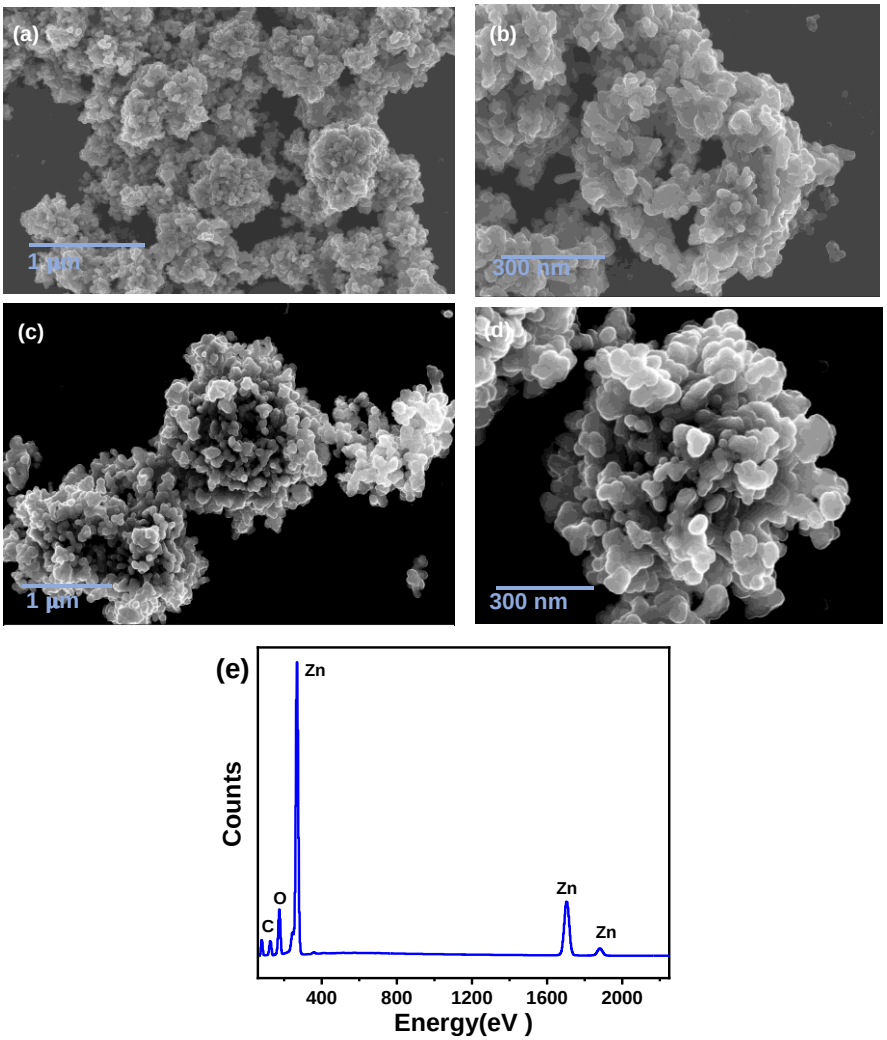

Fig. 4. 5. FESEM images of (a-b) pristine ZnO (c-d) LZ-5 sample (e) EDX spectra of LZ-5.

Typical TEM micrographs of LZ-0 and LZ-5 sample are shown in Fig. 4.6 (a) and Fig. 4.6 (e), respectively. The concurrence between the TEM and FESEM images is evident from the observed spherical shape with undulating edges. Highly magnified TEM images are shown in Fig. 4.6 (b) and Fig. 4. 6 (f) corresponding to LZ-0 and LZ-5 respectively which shows the clusters of ZnO nano petals. The length and widths of the nano petals of both the doped and undoped samples are calculated using ImageJ software. It is found that average length and width of LZ-0 sample was ~ 156 nm and ~ 84 nm, respectively. Further for LZ-5 sample average length of the petals increase to ~417 nm whereas width of the petals decreases to ~ 48 nm. The HRTEM images corresponding to LZ-0 and LZ-5 clearly delineates the lattice fringes as shown in Fig. 4. 6 (c) and Fig. 4. 6 (g), respectively. D-spacing values are measured using ImageJ software from the respective HRTEM images which are ~ 0.26 nm for both the samples. The 0.26 nm lattice spacing indicates the presence of (002) plane corresponding to the hexagonal wurtzite ZnO in both the samples. SAED pattern of LZ-0 and LZ-5 are shown in Fig. 4. 6 (d) and Fig. 4. 6 (h) which exhibits the (100), (101), (102), (002) lattice planes of ZnO. No extra diffraction planes or lattice fringes are observed in LZ-5 samples corresponding to lithium species which is in conformity with the XRD results.

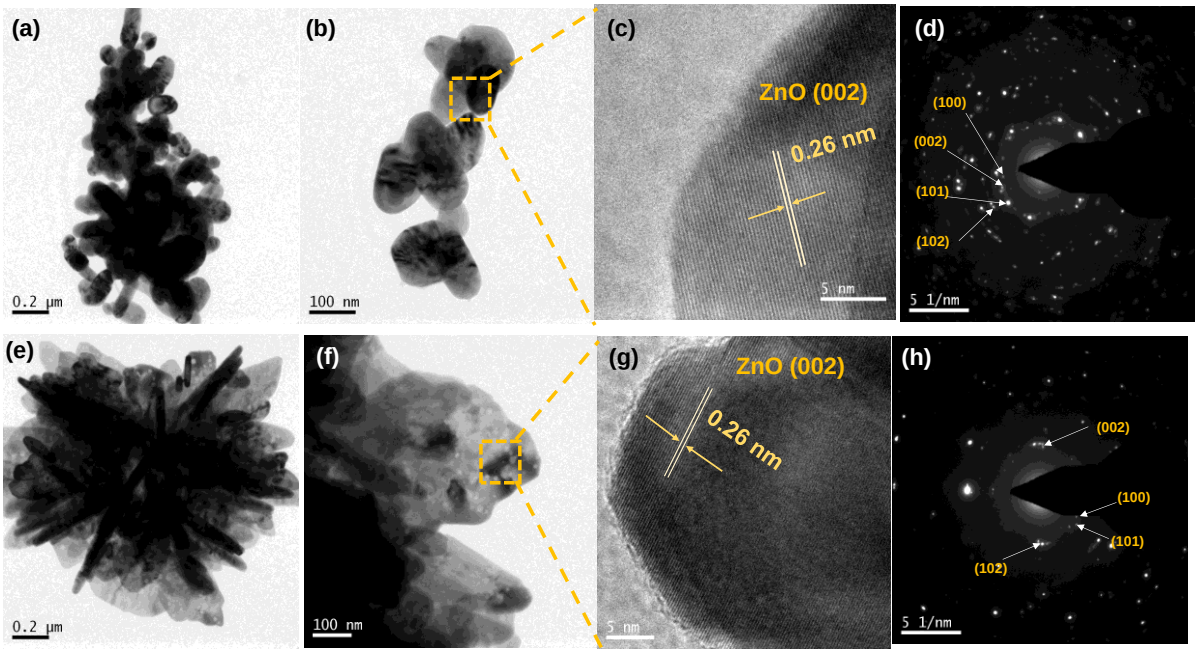

Fig. 4. 6. (a, b) TEM image of LZ-0 in low and high magnification respectively, (c) HRTEM image of LZ-0, (d) SAED pattern of LZ-0, (e, f) TEM images of LZ-5 in low and high magnification (g) HRTEM image of LZ-5 (h) SAED pattern of LZ-5.

Textural characteristics of as synthesized materials are analysed by N_2 adsorption–desorption testes. As shown in Fig. 4. 7 N_2 adsorption–desorption isotherms of LZ-0, LZ-1, LZ-5 are related to type IV isotherms which indicates the presence of mesopores in the samples. [32] Estimated specific surface area of LZ-0, LZ-1, LZ-5, LZ-15 samples are 6.1, 27.9, 34.4, 10.9 m^2/g, respectively. Enhancement of specific surface area with increasing doping concentration would definitely increase the adsorption of gas molecules over the sensing materials. Pore size distribution of the samples are calculated using Barrett–Joyner–Halenda (BJH) method which indicates pore sizes are distributed between 10~40 nm. Overall, presence of dopant in the pristine ZnO system enhanced the specific surface area as well as the pore size distribution which creates more active sites for ammonia adsorption over the doped sample. Thus, doping plays an influential role in enhancing gas sensing performance.

.

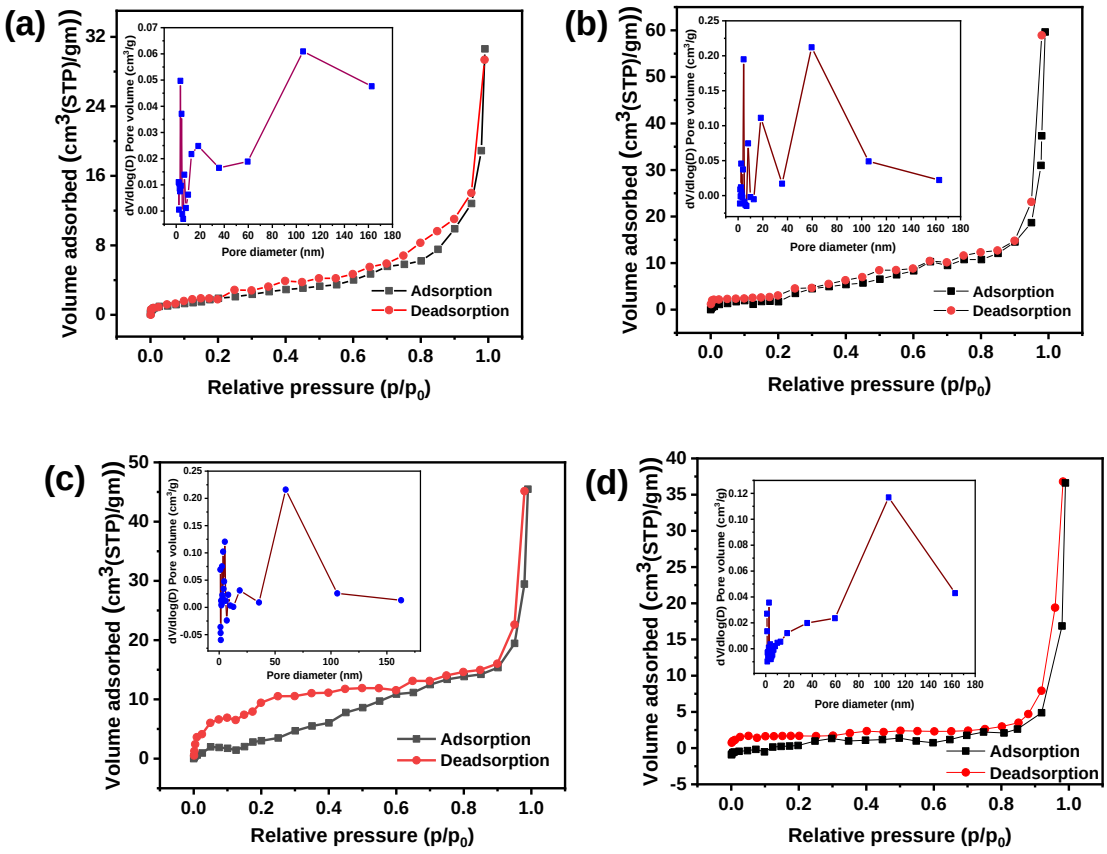

Fig. 4. 7. N_2 adsorption–desorption isotherms and corresponding BJH pore size distribution curve (inset) of (a) LZ-0, (b) LZ-1, (c) LZ-5, (d) LZ-15.

The Room temperature UV-Vis spectroscopy was performed to investigate the variation in energy bandgap due to lithium doping in pristine ZnO system. The UV-vis absorbance curves for pristine and doped samples are shown in Fig. 4. 8 (a). Band gap energies of all the samples are estimated using Tauc plot method as shown in Fig. 4. 8 (b). [33] Band gap energy of the LZ-0 sample is turned out to be 3.1 eV which is further red shifted with increasing Li doping concentration (ref. Fig. 4. 8 (c)). Generation of additional surface defects on the ZnO due to incorporation of Li creates defects energy levels in Li doped ZnO samples which could be accredited to the fact of decreases in energy level in doped samples.[34]Creation of additional defect energy levels due to doping is further being established by photo-luminance (PL) and XPS study on later sections.

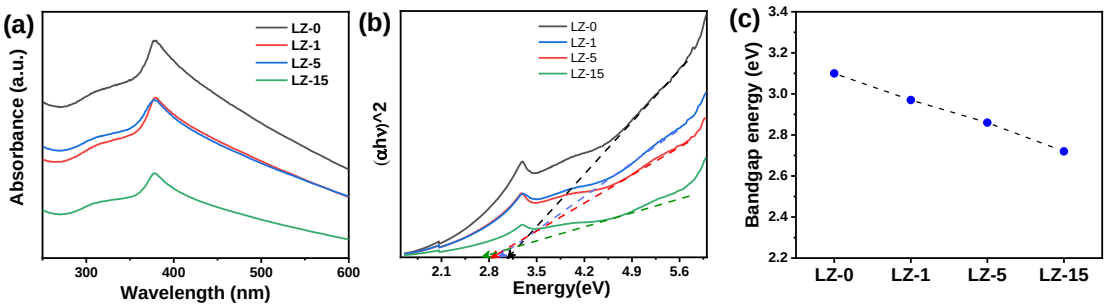

Fig. 4. 8. (a) UV-Vis absorption spectra of all LZ samples, (b) Tauc plot of all LZ samples (c) Variation of energy bandgap with varying doping concentration.

Room temperature photoluminescence study was performed to analyse the formation and Room temperature photoluminescence study was performed to analyse the formation and influence of defect states in the doped ZnO samples. Mainly there are two kinds of defects present in semiconducting metal oxides materials viz. donor defect and acceptor defect. All the samples (LZ-0, LZ-1, LZ-5) were excited by a He-Cd laser at 3.81eV (325nm) for room temperature PL measurement. All four samples showed broad emission peak in the region of 340nm - 630 nm. To analyse the variation of defect states with the variation of doping percentage, the RT PL spectra of doped and undoped samples are deconvoluted into six subpeaks which signifies seven different intrinsic defects states in ZnO (ref. Fig. 4. 9 (a-c)). Relative percentage of different peaks of all 4 samples are calculated from the area under the specific peak. Peak position and relative percentage of each peak of all 4 samples are given in

Table- 4. 4. All seven deconvoluted peaks centres are located in the UV and Visible range. Deconvoluted peak cantered around 3.24 eV is corresponding to the near bandage emission which is originated due to the recombination of free excitons. Other deconvoluted peak centres at the energy range of 3.04 eV (407 nm), 2.8 eV (430 nm), 2.7 eV (460 nm), 2.5 eV (495 nm), 2.3 eV (535 nm), 2.1 eV (590 nm) are corresponding to zinc interstitial (Zn_i^{+}), extended zinc interstitial (Zn_i^{++}), zinc vacancy (V_{zn}), single charge oxygen vacancies, excess oxygen present, Defect level emission respectively. Above these seven deconvoluted peaks, corresponding to zinc interstitial and oxygen vacancies are corresponding to donor defects in the sample. It is observed that donor defect content significantly increases in the doped samples (~55% in LZ-5) than the pristine ZnO (~39% in LZ-0). Higher amount of donor defects increases the amount of majority carrier in the samples which would be beneficial for the catalytic surface reactions. From the PL analysis it is observed that LZ-5 samples possess maximum amount of donor defects among all other sample which suggests that LZ-5 sample would be the maximum responsive towards the analyte gas. [35,36]

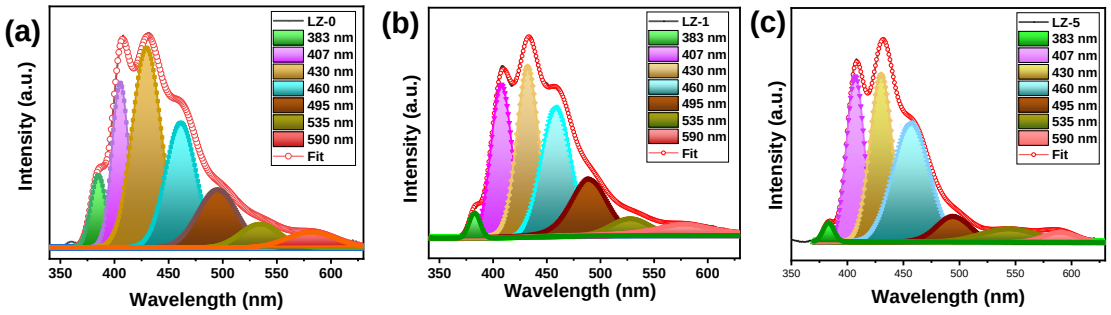

Fig. 4. 9. Deconvoluted RT-PL spectra of **(a)** LZ-0, **(b)** LZ-1, **(c)** LZ-5.

Chemical state and surface electronic compositions of LZ-0, LZ-1, LZ-5 samples were characterized by XPS study. Fig. 4. 10 (a) exhibits XPS survey scan of all 3 samples which indicate the presence of Zn, O, Li and C elements in the synthesized materials. [37] Fig. 4. 10 (b) shows two peaks at 1021.1 eV and 1044.2 eV for LZ-0 sample which are corresponding to Zn $2p_{3/2}$ and Zn $2p_{1/2}$ peaks of Zn^{2+} state. Simultaneously both the peaks are shifted nearly 0.2eV and 0.5 eV towards higher binding energies for LZ-1 and LZ-5 sample respectively as shown in the inset of Fig. 4. 10 (c). Gradual shift in the Zn 2p peak position with increasing dopant concentration indicates the electronic interaction between dopant and the ZnO. Similar trend is observed in Li 1s spectrum. Li 1s peak is observed near 55eV in LZ-1 sample which is further shifted by 0.2eV for LZ-5 sample which indicates that Li ions were successfully introduced in the ZnO lattice.[38]

Table – 4. 4: PL peak positions and corresponding relative percentage of each peaks in LZ-0, LZ-1, LZ-5.

Sl.no	Peak position (nm)	Originated due to	Peak percentage		
			LZ-0	**LZ-1**	**LZ-5**
1	382.7(LZ-0) 383(LZ-1) 383(LZ-5)	Near bend edge emission	2.1	6.3	1.6
2	407.7(LZ-0) 406.7(LZ-1) 407(LZ-5)	zinc interstitial (Zn_i^+)	20.9	17.5	22
3	432.1(LZ-0) 431(LZ-1) 430(LZ-5)	extended zinc interstitial (Zn_i^{++})	25.9	30.3	28.3
4	459(LZ-0) 460(LZ-1) 458.5(LZ-5)	zinc vacancy (V_{zn})	25.3	22.5	32.9
5	493(LZ-0) 494(LZ-1) 494(LZ-5)	single charge oxygen vacancies	15.3	13.5	6.5
6	532(LZ-0) 533(LZ-1) 536(LZ-5)	excess oxygen present	4.4	5.5	5.6
7	584(LZ-0) 585(LZ-1) 590(LZ-5)	Defect level emission	6.1	4.4	3.1

Surface oxidation states of oxygen are analysed by deconvoluting O1s spectra of all the synthesized materials into three gaussian peaks components corresponding to lattice oxygen (O_L), oxygen defect (O_D) and chemically adsorbed oxygen (O_C) species as shown in Fig. 4. 10 (d-f). The amount of different oxygen species (O_L, O_D, O_C) in pristine and doped samples are calculated using following equation and shown in Table- 4. 2.[35,39,40]

$$O_L\,(\%) = [A(O_L)/A(O_T)] \times 100 \quad \text{..... (4.1)}$$

$$O_D\,(\%) = [A(O_D)/A(O_T)] \times 100 \quad \text{.....(4.2)}$$

$$O_C\,(\%) = [A(O_C)/A(O_T)] \times 100 \quad \text{.....(4.3)}$$

where $A(O_L)$, $A(O_D)$, $A(O_C)$, and $A(O_T)$ are the area under the O_L peak, O_D peak, O_C peak, and the whole O 1s peak, respectively. Both the percentage of oxygen defects (O_D) and chemisorbed oxygen species (O_C) significantly increases in LZ-5 sample compare to pristine ZnO (LZ-0) sample. Effect of increasing oxygen defects amount in Li doped ZnO in gas sensing response is discussed in the later mechanism section.

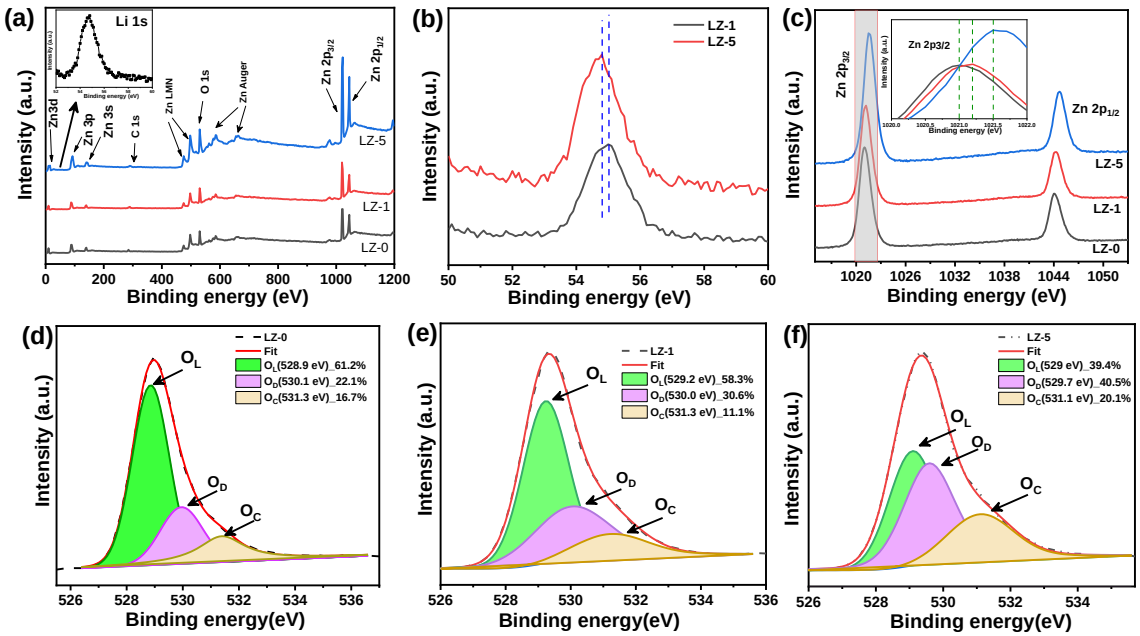

Fig. 4. 10. (a) XPS survey scan of LZ-0, LZ-1, LZ-5 (Li peak position corresponding to survey scan of LZ-5 sample is shown in the inset). (b) Li 1s peaks of LZ-1 and LZ-5 samples. (c) Zn

2p peaks corresponding to LZ-0, LZ-1, LZ-5 samples (deviation of Zn $2p_{3/2}$ peak with Li doping is shown in the inset), Deconvoluted O1s of (d) LZ-0, (e) LZ-1, (f) LZ-5.

Further to understand the charge separation ability of photogenerated electron-hole pairs in the Further to understand the charge separation ability of photogenerated electron-hole pairs in the pristine and Li-doped ZnO materials, a transient photocurrent response study was performed, as shown in Fig. 4. 11 (a). Transient photocurrent spectra clearly indicates that Li doping in pristine ZnO significantly reduces the photobleaching effect as well as improves the photo-stability of pure ZnO. Transient photocurrent spectra indicates that in comparison to other doped samples (LZ-1, LZ-15), the LZ-5 sample exhibited the highest photocurrent response, suggesting efficient charge separation which can be validated further with impedance spectra analysis. LSV curves of all the samples under continuous light illumination are shown in Fig. 4. 11 (b). LSV curves clearly indicate that current density significantly increases with Li doping which also indicate charge transfer resistance becomes low as well as enhanced charge carrier concentration and efficient charge separation. Although for higher doping concentration (LZ-15) current density further reduces, these trends exactly match with the transient photocurrent response study. Charge transfer resistance of the pure and Li-doped ZnO at the electrode-electrolyte interface has been studied using electrochemical impedance spectroscopy (EIS) in order to comprehend the origin of the highest possible efficiency of Li-doping. Fig. 4. 11 (c) illustrates the Nyquist plots for each sample. The smaller radius in the Nyquist plot suggests that charge transfer resistance of the LZ-5 sample is lowest among all four samples which also suggests that, in comparison to other compositions, the interfacial charge transfer process would occur more easily and smoothly in LZ-5 sample.[41–43]

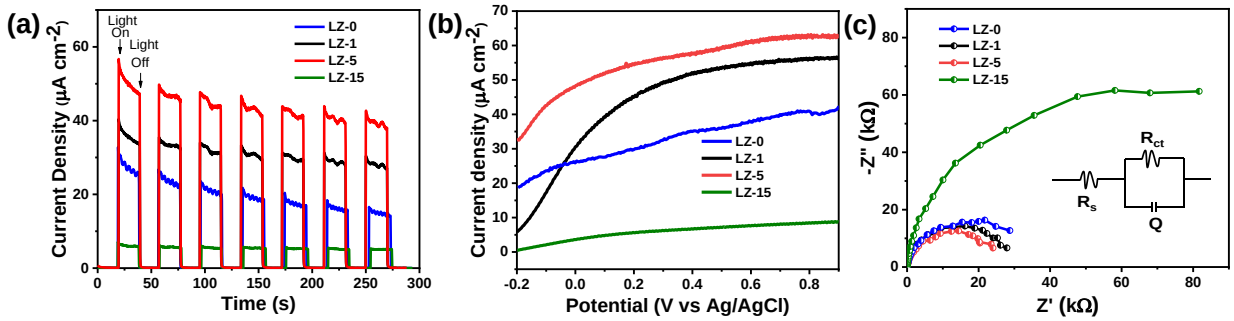

Fig. 4. 11. (a) Transient photocurrent spectra of all the samples. (b) LSV curves of all the samples under continuous light illumination. (c) Nyquist plots of under visible light irradiation. Insets of (c): equivalent circuit models of the Nyquist plots.

4.3.2 Gas sensing characteristics

Semiconductor metal oxides (SMO) based chemiresistive gas sensing takes place following a set of surface redox reactions. Resistance of the sensor either increase or decreases in presence of a certain gaseous environment with respect to its resistance in ambient air environment. The resistance of as fabricated zinc oxide based sensor in presence of ammonia vapour (R_{gas}) decreased with respect to the sensor resistance in ambient environment (R_{air}). Response of the sensors is calculated as follows[35],

$$S = \left(\frac{R_{gas} - R_{air}}{R_{air}}\right) \times 100\ \% \quad \ldots\ldots\ldots\ldots\ldots\ldots\ldots\ldots (5)$$

Working temperature of a sensor plays a crucial role in sensing response as it is a kinetically driven surface catalytic process. [44] Hence, response of pristine and Li doped ZnO based sensors towards 1 ppm ammonia was measured at constant 33% relative humidity background while varying temperature from 150-320ºC as shown in Fig. 4. 12 (a). Variation of sensor response with operating temperature looks like a gaussian shape. 5 % Li doped ZnO based sensor showed maximum 43% response towards 1 ppm ammonia at 240ºC which was nearly 400 % higher than pristine ZnO based sensor. Response of all the sensors towards 0.2, 0.5, 1, 5, 10 ppm ammonia was measured at optimum operating temperature and at constant 33% RH background. LZ-5 sensor showed maximum sensitivity for all different ammonia concentrations as shown in the Fig. 4. 12 (b). Response of LZ-15 sensor significantly was decreased with respect to LZ-5 sensor. Presence of impurity in wurtzite zinc oxide phase could lead to decrease in the response of the LZ-15 sensor.

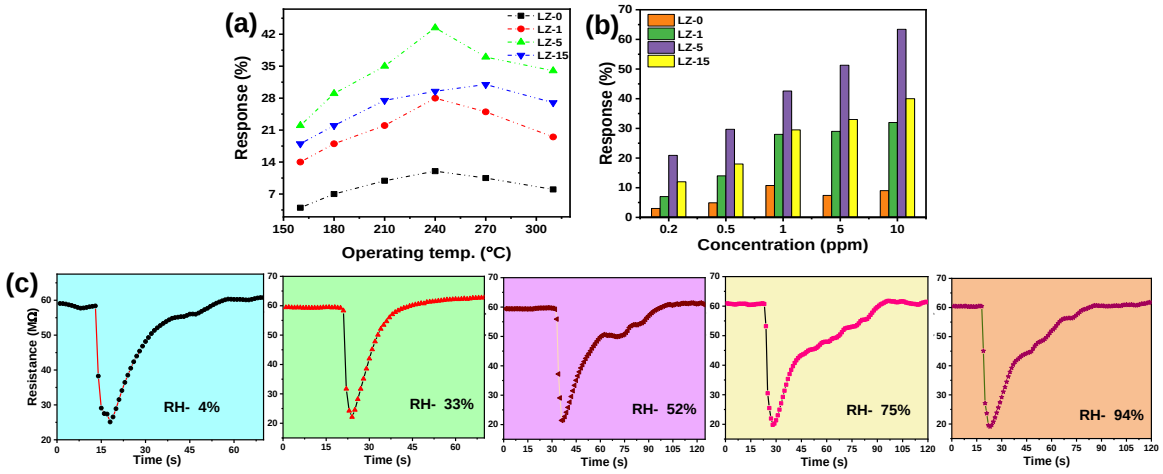

Fig. 4. 12. (a) Variation of sensing response of LZ-0, LZ-1, LZ-5, LZ-15 sensors with temperature towards 1ppm ammonia gas concentration at 33% RH background, (b) Response of all LZ sensor towards varying ammonia concentration at optimum operating temperature. (c) Dynamic response curve of LZ-5 sensor towards 1 ppm ammonia at various humidity background (4% - 94% RH) at optimum operating temperature.

As background humidity plays an influential role in gas sensing response. A rigorous study was performed to determine the variation of the sensing response with the varying background RH% for LZ-5 sensor. Response of LZ-5 sensor at different background humidity towards constant 10 ppm ammonia vapour at optimum operating temperature was measured as shown in Fig. 4. 12 (c). It can be seen that variation of base resistance of the sensor at different background humidity is almost negligible. It can also be inferred from the Fig. 4. 12 (c) that at this temperature response of LZ-5 sensor towards 10 ppm ammonia was increased from ~56.9% to ~68.3% as the background humidity was increased from 4% to 94%.

Variation of sensing response (S_g) with background humidity (% RH) shows a linear relationship which can be fitted with the following relation,

$$S_g = K + \nu.(\%\, RH) \quad \ldots\ldots\ldots\ldots\ldots\ldots\ldots \quad (6)$$

Where K is a constant and ν is the slope of the straight-line curve. Typical value of ν (=0.13%) indicates that with increase in 1% RH the response of the sensor increases nearly 0.13% for fixed 10 ppm ammonia (ref. Fig. 4. 13 (a)). All further gas sensing studies were done at constant 33% RH background. The dynamic response curve of the LZ-5 sensor towards various different ammonia vapour concentrations ranging from 0.2 ppm to 50 ppm at the optimum operating

temperature and fixed 33% RH background is shown in Fig. 4. 13 (b). LZ-5 sensor achieved ~93 % response for 50 ppm NH_3 vapour and moreover the sensor showed a high response of ~20% towards 0.2 ppm (200 ppb) NH_3 concentration at optimum condition. Response value of the sensor towards various different concentration is shown in Fig. 4. 13 (d) which is further extrapolated linearly (with $R^2 = 0.99$) towards the lower concentration range for calculating the lower detection limit (LDL) of the sensor. From inset of Fig. 4. 13 (d) it can be seen that the sensor could detect down to 25 ppb ammonia concentration with significantly high response (~16.2%). Transient response curve (Fig. 4. 13 (b)) also infers that resolution in sensing response of LZ-5 towards different ammonia concentration is also very good for practical applicability. Further 5 consecutive cycles with 5 ppm ammonia under optimum conditions were performed for LZ-5 sensor (ref. Fig. 4. 13 (c)) to investigate the repeatability of the sensor. The response of the sensor remains nearly unchanged for all 5 cycles. Freundlich adsorption isotherm model was used to understand nature of interaction between the gas molecules and the surface of the LZ-5 sensor at optimum operating condition. ln(*Sg*) vs ln(*Cg*) was fitted linearly (adj. $R^2 = 0.97$) using following equation for LZ-5 sensor,

$$\ln(S_g) = \ln(N) + \beta \ln(C_g) \quad \ldots\ldots\ldots\ldots\ldots\ldots\ldots\ldots (7)$$

where "Cg" represents the concentration of the target gas, "N" is a proportionality constant, and "β" is power of the exponent (ref. Fig. 4. 13 (e)). The value of "β" determines the strength of interaction between the surface of the sensor and the gas molecules. As shown in Fig. 4. 13 (e) the value of the "β" is equal to 0.25, which indicates that the incoming gas molecules majorly physiosorbed on the surface of the sensing material.[44] Further, linear relationship between $\ln(S_g)$ and $\ln(C_g)$ indicates reversible nature of sensor with fast recovery time. Again, base resistance and the response of the sensor towards 1 ppm ammonia at optimum operating temperature and 33%RH background were measured for more than 150 days. Changes in base resistance as well as response were not very significant over this time period. These results manifest supercilious reproducibility and long-term stable nature of the LZ-5 sensor at the optimum conditions (ref. Fig. 4. 13 (f)).

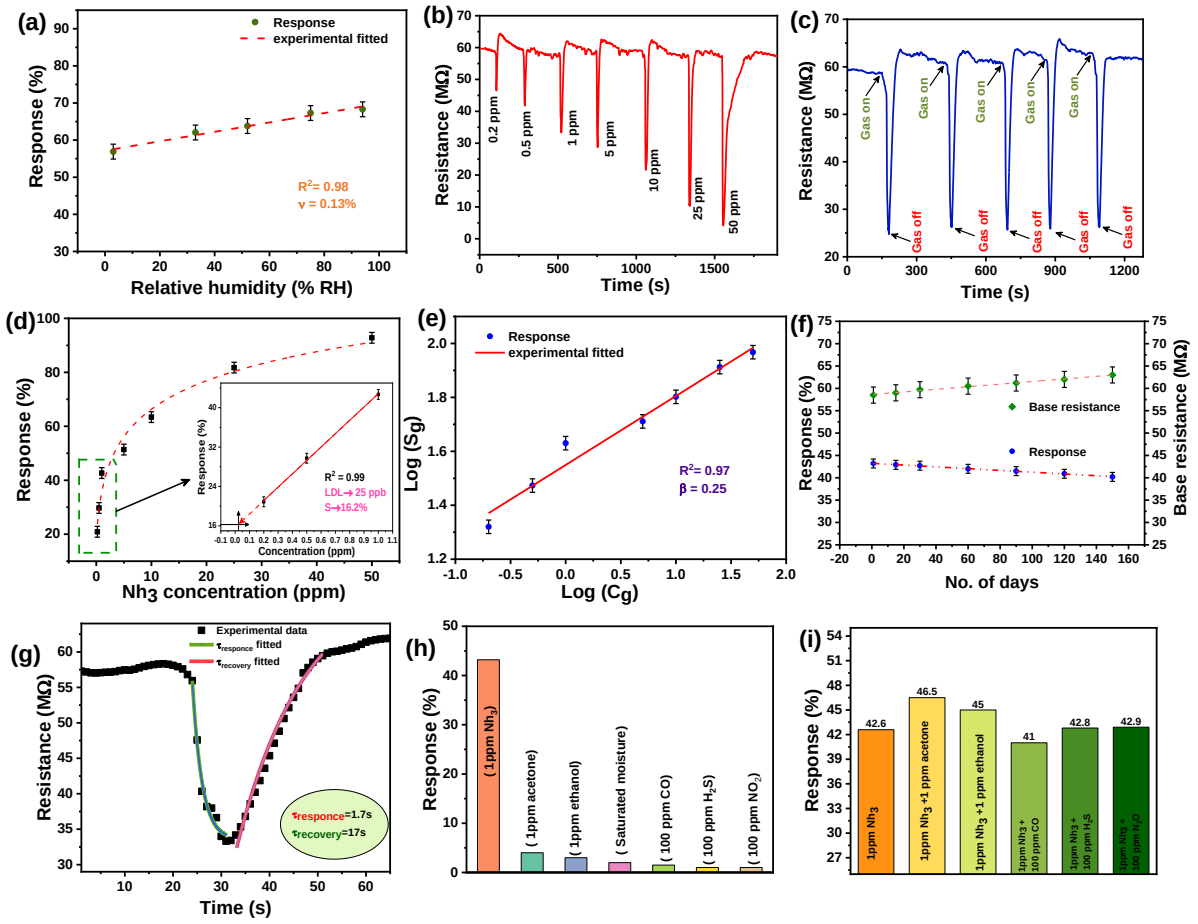

Fig. 4. 13. (a) Variation of gas sensing response of LZ-5 sensor towards 1 ppm ammonia at different %RH background. (b) Dynamic response curve of LZ-5 sensor towards different ammonia concentration at optimum condition. (c) Response of LZ-5 sensor towards 5 ppm ammonia for 5 consecutive cycles. (d) Variation of response with varying Nh_3 concentration of LZ-5 sensor. (e) ln(*Sg*) vs ln(*Cg*) curve of LZ-5. (f) Variation of response and base resistance of LZ-5 sensor with time. (g) Dynamic resistance curve (fitted with single-site Langmuir adsorption model) of LZ-5 towards 1 ppm ammonia gas. (h) Cross-sensitivity curve of LZ-5 at optimum operating condition. (i) Comparison of response of LZ-5 to 1 ppm ammonia in presence of acetone, ethanol, CO, H_2S, NO_2 at optimum operating condition.

Response and recovery time of the LZ-5 sensor is calculated from the transient resistance curve by means of fitting the curve with the single-site multi-exponential model.[45] The adsorption and desorption phases of sensor response are fitted with the following equation (8,9) respectively,

$$M(t) = M_0(t) + M_1 e^{-\left(\frac{t}{\tau_{response}}\right)} \quad \ldots\ldots\ldots\ldots\ldots\ldots\ldots\ldots (8)$$

$$M'(t) = M_0'(t) + \left(1 - e^{-\left(\frac{t}{\tau_{recovery}}\right)}\right) \ldots\ldots\ldots\ldots\ldots\ldots (9)$$

Where, $M_0(t)$ is base resistance, $M(t)$ is the transient resistance of the sensor during gas adsorption at a constant temperature, $M_0'(t)$ is conductance at stable response value, $M'(t)$ is transient resistance during recovery of the sensor at a constant temperature, $\tau_{response}$ and $\tau_{recovery}$ are the time constant of adsorption and desorption of the ammonia vapour. Response and recovery time as prevailed from the fitting data are ~1.7s and ~0.13s, respectively (ref. Fig. 4. 13 (g)). In comparison with the reported work in the literature the LZ-5 sensor shows ultrafast response and recovery nature.

Another challenging aspect towards fabricating a gas sensor for breath analysis is to control selectivity of the sensor. To examine the selectivity of the sensor, most commonly present gases in exhaled breath were chosen as interfering gases (viz. acetone, ethanol, CO, saturated moisture, H_2S, NO_2 etc.). The interfering gases were introduced to the LZ-5 sensor at optimum operating condition in succession. As shown in the Fig. 4. 13 (h)) the LZ-5 sensor showed incredibly high response towards ammonia with respect to other gases. In addition, in the practical scenario there may be few interfering gases coexist in the breath samples. Therefore, gas sensing response of the LZ-5 sensor was measured towards 1 ppm ammonia in presence of few interfering gases having 5 ppm concentration which is shown in Fig. 4. 13 (i)). The Figure shows that response of the LZ-5 sensor towards mixture gases does not varied significantly when compare with 1 ppm pure ammonia. These results delineate the reliability of the sensor as a potential breath analyser for exhaled ammonia detection to monitor kidney / renal related diseases.

4.3.3 Simulated breath study

Practical application capability of LZ-5 sensor was demonstrated by utilizing the real and simulated (ammonia mixed with healthy human breath) exhale breath study. Using a desiccator dilution technique, simulated breath samples with varying concentrations of trace ammonia were prepared. In particular, a unique method was used to produce a 1000 ppm ammonia vapor from liquid ammonia inside a large primary desiccator. A Tedlar gas sampling bag with a capacity of 1 liter was employed to collect exhaled breath from healthy individuals through one of its valves. The exhaled breath from healthy human subjects comprises nitrogen (N_2), carbon dioxide (CO_2), water vapor, and a myriad of volatile organic compounds (VOCs),

including ammonia. This collection serves as the foundational sample for the entire simulated breath study. Measured quantities of ammonia vapor were extracted from the main desiccator and introduced into the Tedlar bag through the alternate valve. The bag was then left undisturbed for 24h to create a simulated breath with a specific concentration of ammonia vapor thoroughly mixed into it. By using this methodology, simulated breath samples were made and put in separate Tedlar bags containing ammonia concentrations of 0.5 ppm, 1 ppm, and 5 ppm. Entire process of simulated breath sample preparation is shown graphically in Fig. 4. 14 (a). Impressive resolution between healthy human breath (H.B.) and simulated breath with various trace amount ammonia (H.B. + 0.5 ppm, H.B. + 1 ppm, H.B. + 5 ppm) was observed (ref. Fig. 4. 14 (b)). [45,46]To validate the simulated breath study, breath samples were collected from five distinct healthy individuals, and a comparative sensing study was conducted using the LZ-5 sensor for each participant. The results from each experimental set exhibited negligible variations across all cases, as illustrated in Fig. 4. 14 (c). Simulated breath study delineates the reliability of the fabricated sensor as a potential breath analyzer for renal diseases detection.

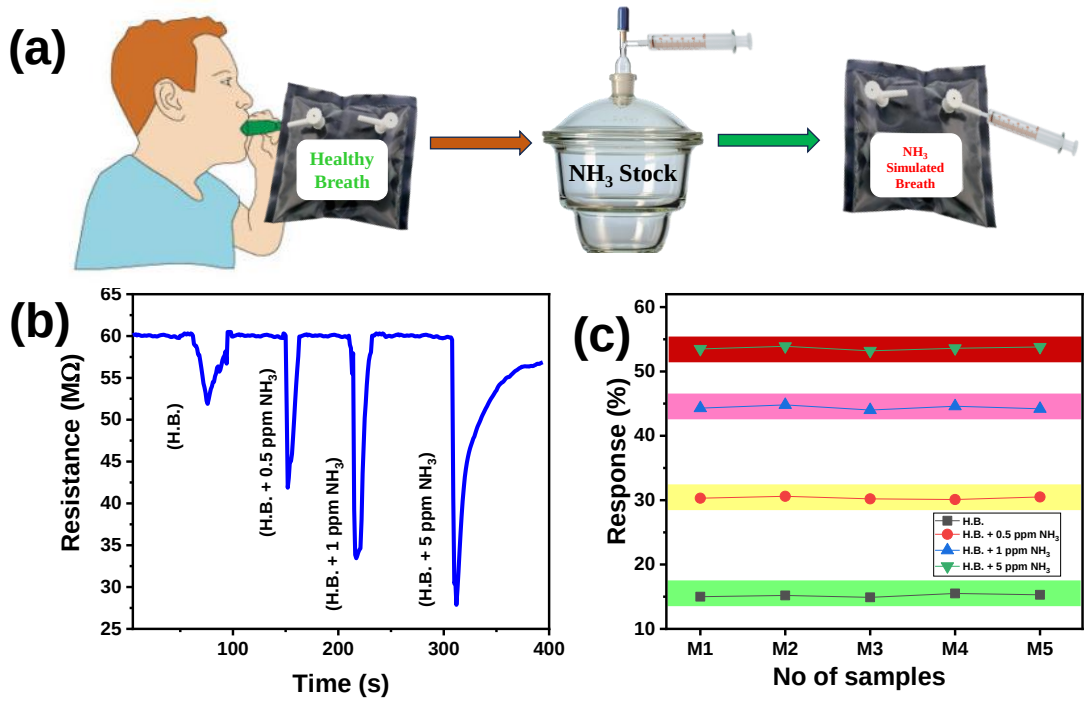

Fig. 4. 14. (a) Schematic presentation of simulated breath study. (b) Response of LZ-5 sensor towards simulated breath having different trace concentrations of NH_3 [H.B = Healthy Breath]. (c) Simulated breath response of the LZ-5 sensor for five different breath samples.

4.3.4 Gas Sensing Mechanism

The response of metal oxide semiconductor sensors primarily involves redox reactions at the surface of the sensing material, where electron transfer occurs between the surface of the sensing material and the target gas molecules. Composition and structure of the sensing material, analyte gas molecules, and the working temperature are the major influencing parameters for this surface redox reaction. Oxygen molecules of environment are initially adsorbed on Li doped ZnO material and converted to different ionic states O^-, O_2^-, O^{2-} by capturing electrons from the conduction band of the material.[44] As a result, the resistance of the material will increase. Since the operating temperature of prepared sensor is above 240°C, majorly adsorbed oxygen species would become O^-. Further, the ammonia molecules initially would react with the environmental humidity to convert into more energetically favorable NH_4^+ molecule as follows[47]:

$$NH_3(gas) + H_2O(ads) \rightarrow NH_4^+(ads) + OH^-(ads) \quad \ldots\ldots\ldots\ldots\ldots\ldots (10)$$

The produced NH_4^+ ions further react with the preabsorbed oxygen species O^- to generate nitric oxides and liberate electrons following the possible pathways:

$$2NH_4^+(ads) + 6O^-(ads) \rightarrow 2NO(ads) + 4H_2O(ads) + e^- \ldots\ldots\ldots\ldots\ldots\ldots (11)$$

These released electrons come back to sensing materials which in turn decreases the resistance of the sensor. Moreover, as discussed in equation (10) environmental humidity would play an influential role in ammonia sensing by generating more energetically favorable NH_4^+ species. Thus, presence of higher amount of humidity would increase sensing response through generation of excess NH_4^+ species.[47–49] Experimentally, we also observed sensitivity increases with increasing background %RH as shown in Fig. 4. 13 (a). Proposed sensing mechanism is shown schematically in Fig. 4. 15.

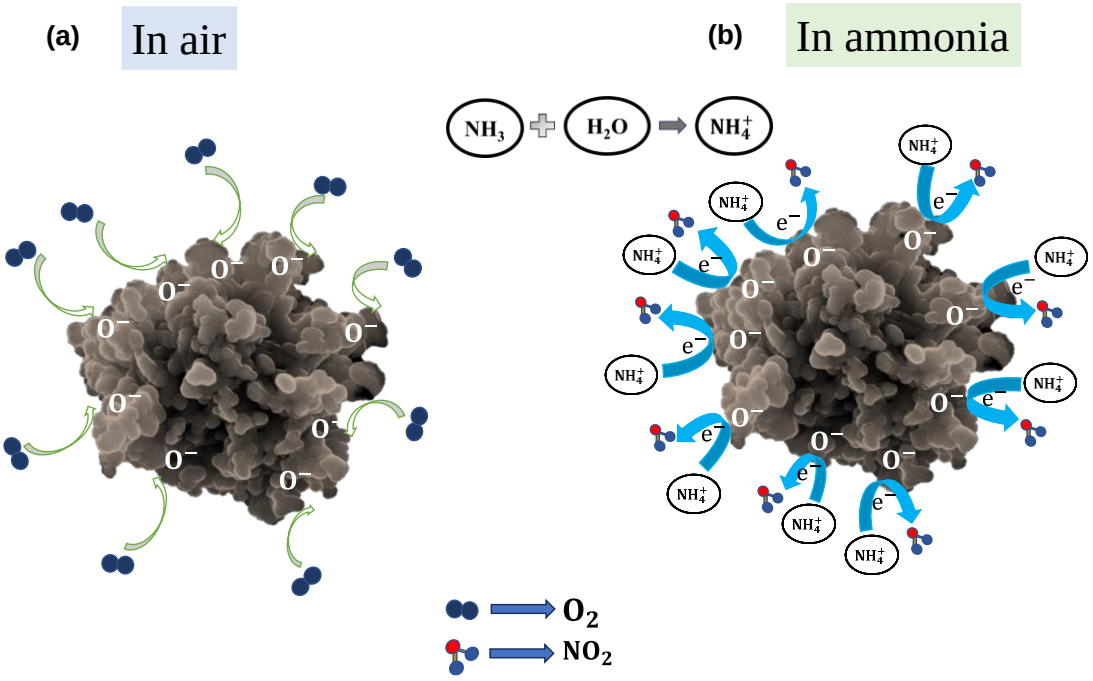

Fig. 4. 15. Schematic presentation of ammonia sensing mechanism.

The sensitivity of any SMO based sensor is majorly influenced by the presence of dopant, morphology, defect states, oxygen vacancies and active surface area. Li was introduced as dopant in ZnO crystal. Zn atoms in the system were substituted by the Li dopant which generated few oxygen vacancy sites on the doped system. The entire process can be written using the Kroger–Vink equation as follows:

$$Li_2O \xrightarrow{2ZnO} 2Li'_{Zn} + V_O^{\bullet\bullet} + O_O^X + \frac{1}{2}O_2(g) \quad \ldots\ldots\ldots\ldots\ldots\ldots (12)$$

Where Li'_{Zn} represents Li substituted in Zn site, $V_O^{\bullet\bullet}$is oxygen vacancy, O_O^X is oxygen ion with neutral charge. HR-XPS analysis also established that oxygen vacancy content was increased in the Li-doped ZnO system over the pure ZnO system.

PL analysis showed that the donor defects in the doped crystal was systematically increased with increasing doping concentration. As donor defects increases no of majority carrier was subsequently increased in the crystal. Therefore, greater no of environmental oxygen would pre-absorbed on the surface of the doped sample as O^- which would eventually increase the sensing response of the sensor. Increase of chemisorbed oxygen species with increasing Li concentration was verified by the XPS result (ref. Table- 4. 2). Higher vacancy sites could

induce high sensitivity and ultrafast sensing response and recovery by enhancing charge transport through vacancy sites. With doping active surface area increases which plays an influential role to enhance sensing performance by absorbing higher amount of gas molecules (ref. Table- 4. 2). [45] Furthermore, the photo electrochemical study indicates that both the stability and intensity of the photocurrent response were enhanced and became maximum in 5% Li doped ZnO based sample, indicating efficient charge separation. Electrochemical impedance spectroscopy illustrated that LZ-5 has the lowest charge transfer resistance, implying a smoother interfacial charge transfer process compared to other compositions.[42] Fig. 4. 16 graphically illustrates the correlation between variations in sensitivity and other influencing factors. On the other hand, excessive Li doping can introduce lattice disorder into ZnO, leading to the formation of Li_2O. The presence of Li_2O in the ZnO system can, to some extent, hampers electron transport. This is corroborated by the experimental observation of a reduced sensitivity value for the LZ-15 sensor.

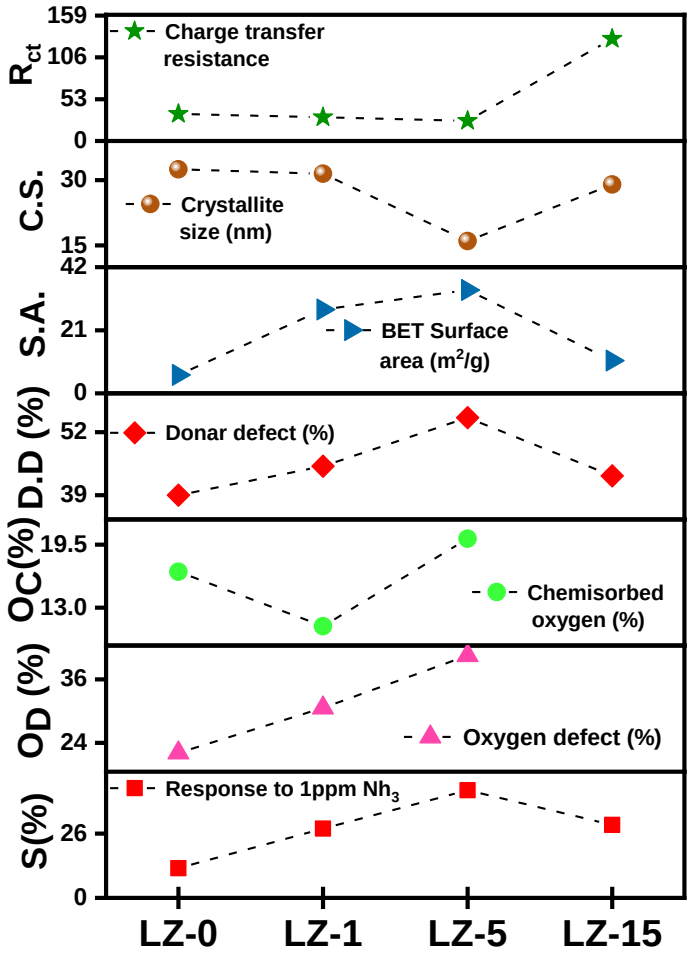

Fig. 4. 16. Variation of gas sensing response of LZ sensors with major influencing parameters.

In order to understand the effect of Li doping on sensing property of ZnO, we have calculated their band structures, total density of states (TDOS) and angular momentum projected partial density of states (PDOS) using ab initio density functional theory which provides deep insight about energy levels and electronic states in the absence and presence of NH_3. Presently, band structures have been calculated along several high symmetry k-points within the Brillouin zone. Prior to calculate the band structure, we have optimized unit cell parameters and they are found to be a = b = 6.57 and c = 10.61 Å in well agreement with experimental results indicating reliability of our calculation. Herein, top of the valence band maxima (VBM) is set to zero as reference for all other calculations. From calculated band structure (ref. Fig. 4. 18 (a)), it appears that ZnO has bandgap (E_g) ~ 3.21 eV with VBM and CBM energies ~ -0.7 and 2.51 eV respectively, at M-point. TDOS and PDOS of bare ZnO as shown in Fig. 4. 18 (b,c) and Fig. 4.17 demonstrate that upper part of the valence band is composed of O – $2p_x$, $2p_y$, and $2p_z$ orbitals, while lower part of conduction band is predominated by Zn – 4s orbitals. Band structure calculation reveals that Li doped ZnO (ref. Fig 18 (g)) exhibits E_g ~ 1.63 eV with VBM and CBM energies ~ -0.62 and 1.01 eV. Herein, lowering of CBM energy in Li doped ZnO may be attributed to more capturing of electrons at O atoms. Very briefly, Zn – O bond of ZnO is more covalent, rather than ionic due electronegativity of Zn ~ 1.65 and O ~ 3.44. Since, electronegativity of Li (0.98) is very less; hence Li substitution at cationic sites decreases electron concentration at cationic sites which in consequence reduces CBM energy. Similarly, enhanced electron concentration at anionic sites increases VBM energies. As for the adsorption of NH_3 molecule on pristine ZnO (101 surface), two different adsorption sites (N atoms on cationic and anionic sites) were simulated. Herein, our calculations reveal that NH_3 adsorption *via* N atom vertically at top of anionic sites (~ 1.84 Å) is more favourable than NH_3 adsorption on cationic sites having adsorption energy ~ 4.3 eV. The adsorption effect of NH_3 on ZnO and Li doped ZnO were investigated in order to understand the synergistic effect of Li doping in boosting ammonia sensing performance. Adsorption energies for pure ZnO and Li doped ZnO were calculated to be -4.27 eV and -5 eV, respectively. Adsorption process occurs more spontaneously in Li doped ZnO system, which plays key role in boosting the sensitivity of Li doped ZnO based sensor compared to pure ZnO based sensor, as indicated by greater negative value of adsorption energy. Hence, higher sensitivity of Li doped ZnO is assigned to the enhancement of electron concentration at anionic sites which facilitates charge transfer between NH_3 and cationic sites of Li doped ZnO and increases sensitivity.

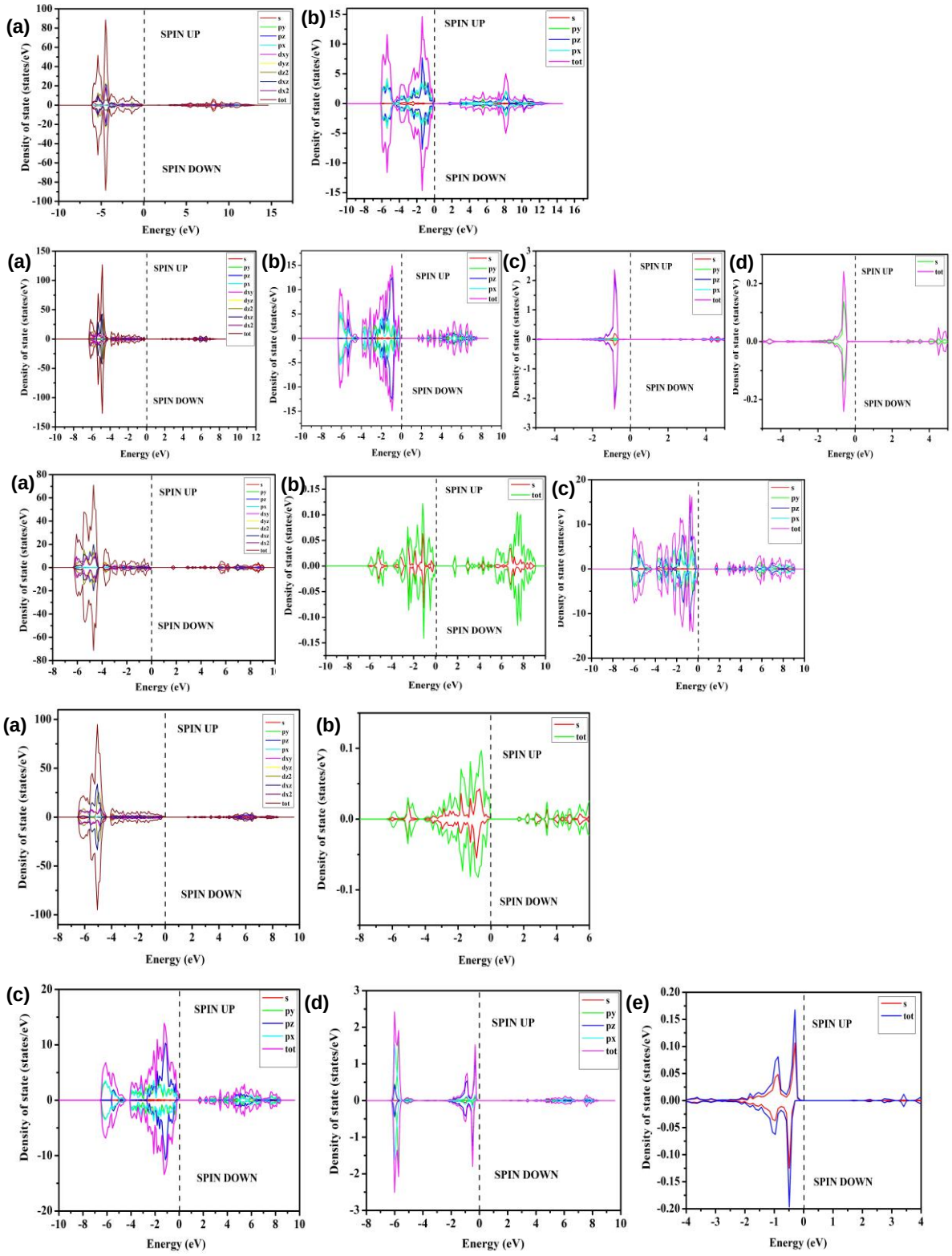

Fig. 4. 17. PDOS of (a-b) Zn, O of bare ZnO respectively. (c-f) Zn, O, N, H of NH_3 gas absorbed ZnO respectively. (g-i) Zn, Li, O of Li doped ZnO respectively. (j-n) Zn, Li, O, N, H of NH_3 gas absorbed Li doped ZnO respectively.

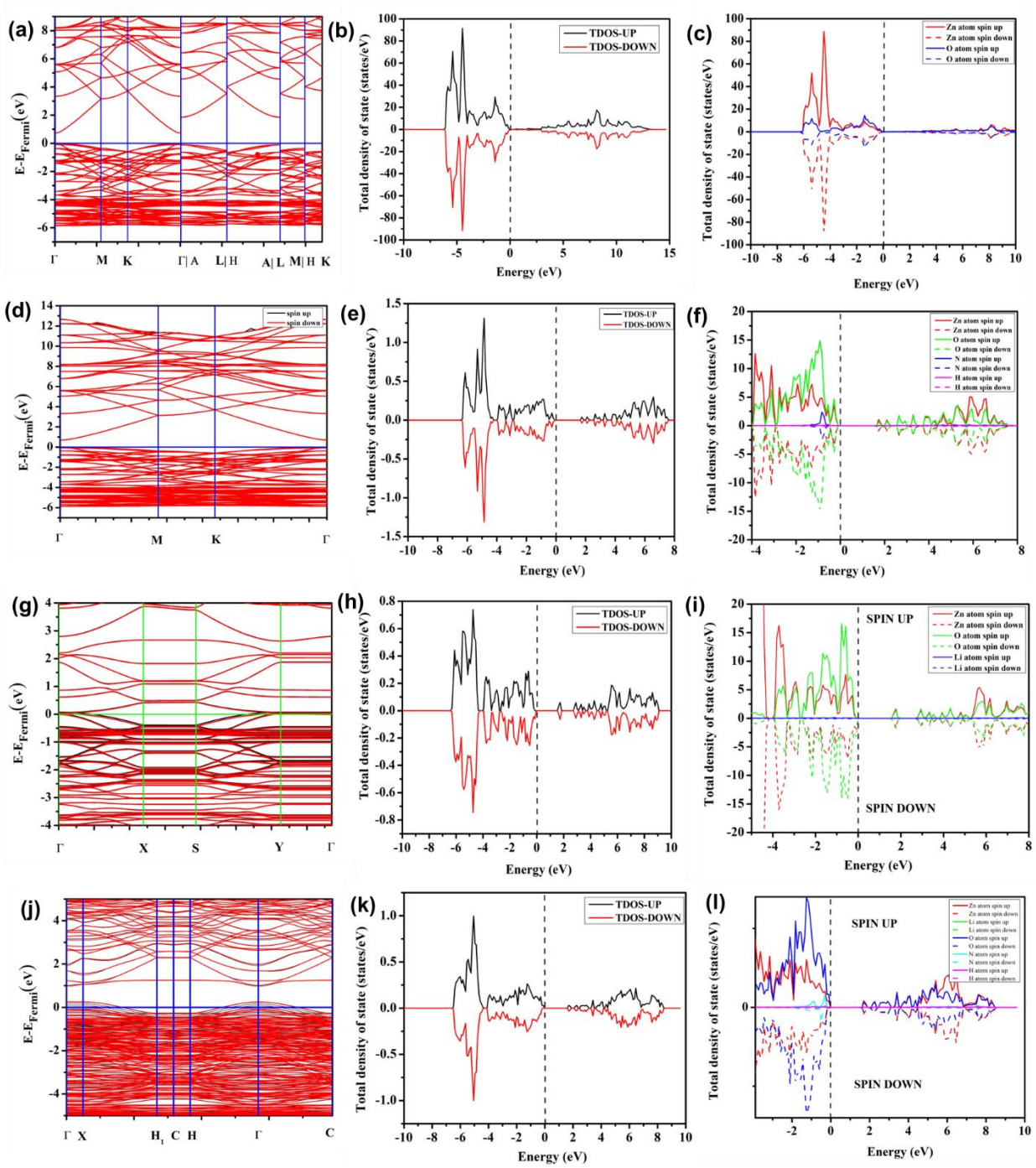

Fig. 4. 18. (a-c) Band structure, spin polarised TDOS, total PDOS bare ZnO respectively. (d-f) Band structure, spin polarised TDOS, total PDOS of NH_3 gas absorbed ZnO respectively. (g-i) Band structure, spin polarised TDOS, total PDOS of Li doped ZnO respectively. (j-l) Band structure, spin polarised TDOS, total PDOS of NH_3 gas absorbed Li doped ZnO respectively.

4.4 Conclusion

In conclusion, pure and Li doped cauliflower like ZnO nanoparticles were grown successfully using facile reflux technique. It was observed that doping of lithium produces a dramatic boost in sensing performance of pristine ZnO. Amongst other the 5-wt % Li doped ZnO (LZ-5) sample delineated the best sensing performance towards ammonia. The LZ-5 sensor exhibited the highest sensitivity (S = 43% towards 1 ppm ammonia), which was 400% higher than that of pristine ZnO (LZ-0). Additionally, it demonstrated a fast response time of 1.7 s and a recovery time of 17 s. In addition, LZ-5 was very selective towards ammonia, insensitive to moisture and stable over a period of six months. Significant enhancement in sensing performance with doping was explained in terms of larger surface area, generation of excess oxygen defects and donor content. Adsorption energy, estimated using DFT calculation, also support enhanced sensing performance of Li-doped sensor. Efficacy of practical application possibility of this sensor was checked using both real and simulated human exhale breath and found to be very encouraging. Overall, prepared Li-doped ZnO based sensor could be a promising candidate for exhale breath ammonia detection to monitor kidney related ailments.

4. 5. Reference

[1] A.T. Güntner, M. Righettoni, S.E. Pratsinis, Selective sensing of NH 3 by Si-doped α-MoO 3 for breath analysis, Sens Actuators B Chem 223 (2016) 266–273. https://doi.org/10.1016/j.snb.2015.09.094.

[2] S. Das, M. Pal, Review—Non-Invasive Monitoring of Human Health by Exhaled Breath Analysis: A Comprehensive Review, J Electrochem Soc 167 (2020) 037562. https://doi.org/10.1149/1945-7111/ab67a6.

[3] A. Amann, G. Poupart, S. Telser, M. Ledochowski, A. Schmid, S. Mechtcheriakov, Applications of breath gas analysis in medicine, Int J Mass Spectrom 239 (2004) 227–233. https://doi.org/10.1016/j.ijms.2004.08.010.

[4] T. Karl, P. Prazeller, D. Mayr, A. Jordan, J. Rieder, R. Fall, W. Lindinger, Human breath isoprene and its relation to blood cholesterol levels: new measurements and modeling, J Appl Physiol 91 (2001) 762–770. https://doi.org/10.1152/jappl.2001.91.2.762.

[5] L. Chen, J. Geng, Z. Guo, X.-J. Huang, Polyoxometalates-based functional materials in chemiresistive gas sensors and electrochemical sensors, TrAC Trends in Analytical Chemistry 167 (2023) 117233. https://doi.org/10.1016/j.trac.2023.117233.

[6] K. Wetchakun, T. Samerjai, N. Tamaekong, C. Liewhiran, C. Siriwong, V. Kruefu, A. Wisitsoraat, A. Tuantranont, S. Phanichphant, Semiconducting metal oxides as sensors for environmentally hazardous gases, Sens Actuators B Chem 160 (2011) 580–591. https://doi.org/10.1016/j.snb.2011.08.032.

[7] N. Chakraborty, A. Ghosh, S. Mojumder, A.K. Mishra, S. Mondal, Selectively activated suppressed quantum networks in self-assembled single atom-Ag catalyst-based room temperature sensors for health monitoring, J Mater Chem A Mater (2024). https://doi.org/10.1039/D4TA01888E.

[8] D. Maity, R.T.R. Kumar, Polyaniline Anchored MWCNTs on Fabric for High Performance Wearable Ammonia Sensor, ACS Sens 3 (2018) 1822–1830. https://doi.org/10.1021/acssensors.8b00589.

[9] X. Tang, J.-P. Raskin, N. Kryvutsa, S. Hermans, O. Slobodian, A.N. Nazarov, M. Debliquy, An ammonia sensor composed of polypyrrole synthesized on reduced graphene oxide by electropolymerization, Sens Actuators B Chem 305 (2020) 127423. https://doi.org/10.1016/j.snb.2019.127423.

[10] V. Haridas, A. Sukhananazerin, J. Mary Sneha, B. Pullithadathil, B. Narayanan, α-Fe2O3 loaded less-defective graphene sheets as chemiresistive gas sensor for selective sensing of NH3, Appl Surf Sci 517 (2020) 146158. https://doi.org/10.1016/j.apsusc.2020.146158.

[11] L. Van Duy, T.T. Nguyet, D.T.T. Le, N. Van Duy, H. Nguyen, F. Biasioli, M. Tonezzer, C. Di Natale, N.D. Hoa, Room Temperature Ammonia Gas Sensor Based on p-Type-like V2O5 Nanosheets towards Food Spoilage Monitoring, Nanomaterials 13 (2022) 146. https://doi.org/10.3390/nano13010146.

[12] N. Chakraborty, A. Sanyal, S. Das, D. Saha, S.K. Medda, S. Mondal, Ammonia Sensing by $Sn_{1-x}V_xO_2$ Mesoporous Nanoparticles, ACS Appl Nano Mater 3 (2020) 7572–7579. https://doi.org/10.1021/acsanm.0c01183.

[13] A. Kshirsagar, A.B. Joshi, A. Joshi, D.K. Avasthi, T.M. Bhave, S.A. Gangal, Comparative Study of Irradiated And Annealed ZnO Thin Films For Room Temperature Ammonia Gas Sensing, in: 2007 IEEE Sensors, IEEE, 2007: pp. 162–165. https://doi.org/10.1109/ICSENS.2007.4388361.

[14] A. Wei, Z. Wang, L.-H. Pan, W.-W. Li, L. Xiong, X.-C. Dong, W. Huang, Room-Temperature NH_3 Gas Sensor Based on Hydrothermally Grown ZnO Nanorods, Chinese Physics Letters 28 (2011) 080702. https://doi.org/10.1088/0256-307X/28/8/080702.

[15] V.S. Bhati, M. Hojamberdiev, M. Kumar, Enhanced sensing performance of ZnO nanostructures-based gas sensors: A review, Energy Reports 6 (2020) 46–62. https://doi.org/10.1016/j.egyr.2019.08.070.

[16] J. Wang, P. Yang, X. Wei, High-Performance, Room-Temperature, and No-Humidity-Impact Ammonia Sensor Based on Heterogeneous Nickel Oxide and Zinc Oxide Nanocrystals, ACS Appl Mater Interfaces 7 (2015) 3816–3824. https://doi.org/10.1021/am508807a.

[17] G.H. Mhlongo, D.E. Motaung, H.C. Swart, Pd2+ doped ZnO nanostructures: Structural, luminescence and gas sensing properties, Mater Lett 160 (2015) 200–205. https://doi.org/10.1016/j.matlet.2015.07.139.

[18] D. Zhang, C. Jiang, Y. Sun, Room-temperature high-performance ammonia gas sensor based on layer-by-layer self-assembled molybdenum disulfide/zinc oxide nanocomposite film, J Alloys Compd 698 (2017) 476–483. https://doi.org/10.1016/j.jallcom.2016.12.222.

[19] Q. Qi, P.-P. Wang, J. Zhao, L.-L. Feng, L.-J. Zhou, R.-F. Xuan, Y.-P. Liu, G.-D. Li, SnO2 nanoparticle-coated In2O3 nanofibers with improved NH3 sensing properties, Sens Actuators B Chem 194 (2014) 440–446. https://doi.org/10.1016/j.snb.2013.12.115.

[20] D. Kwak, M. Wang, K.J. Koski, L. Zhang, H. Sokol, R. Maric, Y. Lei, Molybdenum Trioxide (α-MoO_3) Nanoribbons for Ultrasensitive Ammonia (NH_3) Gas Detection: Integrated Experimental and Density Functional Theory Simulation Studies, ACS Appl Mater Interfaces 11 (2019) 10697–10706. https://doi.org/10.1021/acsami.8b20502.

[21] N. Van Hieu, N.Q. Dung, P.D. Tam, T. Trung, N.D. Chien, Thin film polypyrrole/SWCNTs nanocomposites-based NH3 sensor operated at room temperature, Sens Actuators B Chem 140 (2009) 500–507. https://doi.org/10.1016/j.snb.2009.04.061.

[22] S.G. Bachhav, D.R. Patil, Study of Polypyrrole-Coated MWCNT Nanocomposites for Ammonia Sensing at Room Temperature, Journal of Materials Science and Chemical Engineering 03 (2015) 30–44. https://doi.org/10.4236/msce.2015.310005.

[23] D.N. Huyen, N.T. Tung, T.D. Vinh, N.D. Thien, Synergistic Effects in the Gas Sensitivity of Polypyrrole/Single Wall Carbon Nanotube Composites, Sensors 12 (2012) 7965–7974. https://doi.org/10.3390/s120607965.

[24] W. Xuan Du, H.-J. Lee, J.-H. Byeon, J.-S. Kim, K.-S. Cho, S. Kang, M. Takada, J.-Y. Kim, Highly sensitive single-walled carbon nanotube/polypyrrole/phenylalanine core–shell nanorods for ammonia gas sensing, J Mater Chem C Mater 8 (2020) 15609–15615. https://doi.org/10.1039/D0TC04335D.

[25] S.D. Lawaniya, S. Kumar, Y. Yu, K. Awasthi, Ammonia sensing properties of PPy nanostructures (urchins/flowers) towards low-cost and flexible gas sensors at room temperature, Sens Actuators B Chem 382 (2023) 133566. https://doi.org/10.1016/j.snb.2023.133566.

[26] P. Singh, C.S. Kushwaha, V.K. Singh, G.C. Dubey, S.Kr. Shukla, Chemiresistive sensing of volatile ammonia over zinc oxide encapsulated polypyrrole based nanocomposite, Sens Actuators B Chem 342 (2021) 130042. https://doi.org/10.1016/j.snb.2021.130042.

[27] A. Shahmoradi, A. Hosseini, A. Akbarinejad, N. Alizadeh, Noninvasive Detection of Ammonia in the Breath of Hemodialysis Patients Using a Highly Sensitive Ammonia Sensor Based on a Polypyrrole/Sulfonated Graphene Nanocomposite, Anal Chem 93 (2021) 6706–6714. https://doi.org/10.1021/acs.analchem.1c00171.

[28] D. Lv, W. Shen, W. Chen, Y. Wang, R. Tan, M. Zhao, W. Song, One-step preparation of flexible citric acid-doped polyaniline gas sensor for ppb-level ammonia detection at room temperature, Sens Actuators A Phys 350 (2023) 114120. https://doi.org/10.1016/j.sna.2022.114120.

[29] D. Zhang, Z. Kang, X. Liu, J. Guo, Y. Yang, Highly sensitive ammonia sensor based on PSS doped ZIF-8-derived porous carbon/polyaniline hybrid film coated on quartz crystal microbalance, Sens Actuators B Chem 357 (2022) 131419. https://doi.org/10.1016/j.snb.2022.131419.

[30] H. Wu, X. Gong, W. Tao, L. Zhao, T. Wang, F. Liu, X. Yan, P. Sun, G. Lu, Humidity-activated ammonia sensor based on mesoporous AlOOH towards breath diagnosis, Sens Actuators B Chem 380 (2023) 133322. https://doi.org/10.1016/j.snb.2023.133322.

[31] Z.-Y. Song, Y.-Y. Li, W. Duan, X.-Y. Xiao, Z.-W. Gao, Y.-H. Zhao, B. Liang, S.-H. Chen, P.-H. Li, M. Yang, X.-J. Huang, Decisive role of electronic structure in electroanalysis for sensing materials: Insights from density functional theory, TrAC Trends in Analytical Chemistry 160 (2023) 116977. https://doi.org/10.1016/j.trac.2023.116977.

[32] M. Pandey, M. Singh, K. Wasnik, S. Gupta, S. Patra, P.S. Gupta, D. Pareek, N.S.N. Chaitanya, S. Maity, A.B.M. Reddy, R. Tilak, P. Paik, Targeted and Enhanced Antimicrobial Inhibition of Mesoporous ZnO–Ag $_2$ O/Ag, ZnO–CuO, and ZnO–SnO $_2$ Composite Nanoparticles, ACS Omega 6 (2021) 31615–31631. https://doi.org/10.1021/acsomega.1c04139.

[33] S. Chakraborty, M. Pal, Improved ethanol sensing behaviour of cadmium sulphide nanoflakes: Beneficial effect of morphology, Sens Actuators B Chem 242 (2017) 1155–1164. https://doi.org/10.1016/j.snb.2016.09.129.

[34] C. Yang, Z. Wang, T. Lin, H. Yin, X. Lü, D. Wan, T. Xu, C. Zheng, J. Lin, F. Huang, X. Xie, M. Jiang, Core-Shell Nanostructured “Black” Rutile Titania as Excellent Catalyst for Hydrogen Production Enhanced by Sulfur Doping, J Am Chem Soc 135 (2013) 17831–17838. https://doi.org/10.1021/ja4076748.

[35] S. Mojumder, T. Das, S. Das, N. Chakraborty, D. Saha, M. Pal, Y and Al co-doped ZnO-nanopowder based ultrasensitive trace ethanol sensor: A potential breath analyzer for fatty liver disease and drunken driving detection, Sens Actuators B Chem 372 (2022) 132611. https://doi.org/10.1016/j.snb.2022.132611.

[36] S. Bai, T. Guo, Y. Zhao, R. Luo, D. Li, A. Chen, C.C. Liu, Mechanism enhancing gas sensing and first-principle calculations of Al-doped ZnO nanostructures, J Mater Chem A Mater 1 (2013) 11335. https://doi.org/10.1039/c3ta11516j.

[37] S. Ullah Awan, S.K. Hasanain, M.F. Bertino, G. Hassnain Jaffari, Ferromagnetism in Li doped ZnO nanoparticles: The role of interstitial Li, J Appl Phys 112 (2012). https://doi.org/10.1063/1.4767364.

[38] S.H. Jeong, B.N. Park, S.-B. Lee, J.-H. Boo, Study on the doping effect of Li-doped ZnO film, Thin Solid Films 516 (2008) 5586–5589. https://doi.org/10.1016/j.tsf.2007.07.075.

[39] S. Mojumder, T. Das, D. Saha, M. Pal, Highly sensitive and selective chemiresistive temperature-dependent trace formalin sensor using hydrothermally grown hexagonal yttrium ferrite, Mater Chem Phys 319 (2024) 129329. https://doi.org/10.1016/j.matchemphys.2024.129329.

[40] T. Das, S. Mojumder, D. Saha, M. Pal, Enhanced ammonia sensing performance of barium hexaferrite enabled through Zn doping: Mechanistic study considering modulation of Fe2+/Fe3+ ratio and oxygen vacancy, Sens Actuators B Chem 406 (2024) 135358. https://doi.org/10.1016/j.snb.2024.135358.

[41] S. Ghosh, S. Bera, S. Sardar, S. Pal, F.V.A. Camargo, C. D'Andrea, G. Cerullo, Role of Efficient Charge Transfer at the Interface between Mixed-Phase Copper-Cuprous Oxide and Conducting Polymer Nanostructures for Photocatalytic Water Splitting, ACS Appl Mater Interfaces 15 (2023) 18867–18877. https://doi.org/10.1021/acsami.3c00090.

[42] W. Guo, L. Huang, X. Liu, J. Wang, J. Zhang, Enhanced isoprene gas sensing performance based on p-CaFe2O4/n-ZnFe2O4 heterojunction composites, Sens Actuators B Chem 354 (2022) 131243. https://doi.org/10.1016/j.snb.2021.131243.

[43] S. Vadivel, D. Maruthamani, A. Habibi-Yangjeh, B. Paul, S.S. Dhar, K. Selvam, Facile synthesis of novel CaFe 2 O 4 /g-C 3 N 4 nanocomposites for degradation of methylene blue under visible-light irradiation, J Colloid Interface Sci 480 (2016) 126–136. https://doi.org/10.1016/j.jcis.2016.07.012.

[44] T. Das, S. Mojumder, S. Chakraborty, D. Saha, M. Pal, Beneficial effect of Sn doping on bismuth ferrite nanoparticle-based sensor for enhanced and highly selective detection of trace formaldehyde, Appl Surf Sci 602 (2022) 154340. https://doi.org/10.1016/j.apsusc.2022.154340.

[45] S. Mojumder, T. Das, M. Mukherjee, D. Saha, A. Datta, M. Pal, Development of highly sensitive and selective trace acetone sensor using perovskite yttrium ferrite: Mechanism, kinetics and phase dependence study, Chemical Engineering Journal 477 (2023) 146855. https://doi.org/10.1016/j.cej.2023.146855.

[46] S. Sen, S. Maity, S. Kundu, Fabrication of Fe doped reduced graphene oxide (rGO) decorated WO3 based low temperature ppm level acetone sensor: Unveiling sensing mechanism by impedance spectroscopy, Sens Actuators B Chem 361 (2022) 131706. https://doi.org/10.1016/j.snb.2022.131706.

[47] T. He, S. Sun, B. Huang, X. Li, MXene/SnS_2 Heterojunction for Detecting Sub-ppm NH_3 at Room Temperature, ACS Appl Mater Interfaces 15 (2023) 4194–4207. https://doi.org/10.1021/acsami.2c18097.

[48] H.-I. Chen, C.-Y. Chi, W.-C. Chen, I.-P. Liu, C.-H. Chang, T.-C. Chou, W.-C. Liu, Ammonia sensing characteristic of a Pt nanoparticle/aluminum-doped zinc oxide sensor, Sens Actuators B Chem 267 (2018) 145–154. https://doi.org/10.1016/j.snb.2018.04.019.

[49] S. Kanaparthi, S. Govind Singh, Highly sensitive and ultra-fast responsive ammonia gas sensor based on 2D ZnO nanoflakes, Mater Sci Energy Technol 3 (2020) 91–96. https://doi.org/10.1016/j.mset.2019.10.010.

CHAPTER-V

Highly Sensitive and Selective Chemiresistive Trace Formalin Sensor Using Hydrothermally Grown Hexagonal Yttrium Ferrite

Work is published in “Materials Chemistry and Physics 319 (2024) 129329”

5.1 Introduction

Formaldehyde (HCHO), also known as formalin, which is extremely reactive and has a strong, pungent smell, has received a lot of attention from researchers as formalin has been classified as a human carcinogen by both the World Health Organization (WHO) and the Environmental Protection Agency (EPA)[1]. Long-term inhalation of this toxic vapor can cause a number of health problems, including nasopharyngeal cancer, an increased risk of leukemia, throat, and eye discomfort, shortness of breath, tightness in the chest, and many more.[2–4] Despite being toxic, formaldehyde is frequently utilized in food processing and color-making due to its strong reactivity and low cost. Additionally, it is used as a biocide, preservative, food, drugs, medical science, biotechnology, textiles, wood and plywood processing[5]. Due to its antiseptic qualities, formalin is employed as a hospital disinfectant.

Even though there are many low-concentration formalin sensing techniques (such as fluorometry and polarography, gas chromatography, and spectrophotometry) available in the market, however, their principal drawbacks reside in their high cost and difficult application processes.[6–9] The ease of manufacture, speed, precision, and low power consumption of metal oxide semiconductor (MOS) based chemiresistive gas sensors make them a very efficient technology compared to alternatives. Currently, conventional MOS materials like ZnO, In_2O_3, and SnO_2 exhibit outstanding formalin detection performance.[10–15] Recently scientist around the world reports few works on MOS-based formaldehyde. Table-5. 1 contains a list of notable reports. The principal drawbacks of these binary MOS-based formalin sensors are selectivity, long-term instability, and reductions in sensitivity in the presence of higher background moisture.[16,17] Pristine binary metal oxide-based sensors operate in much higher operating temperature. [18–20] Moreover, response towards trace formalin concentration is not adequate in most of these binary MOS-based sensors. In order to overcome the lacunas indicated above, researchers are currently diverting their attention away from binary oxide and toward higher-order oxides like spinel oxide or perovskite oxide, particularly ferrites. This is due to the fact that these substances have a lot of active sites and a lot of surface area that can enhance the diffusion channel and boost the adsorption of target gas molecules, enhancing their capacity to sense gases.[21–24]

Yttrium ferrite ($YFeO_3$), which has big coercivity, and good chemical stability, is one of the prominent magnetic materials that has received a lot of research. There are several reports in the literature on various application fields of $YFeO_3$ in diverse fields such as in microwave

devices, electromagnetic wave absorbers, phase shifter applications, leakage current, ferroelectric, and piezoelectric properties.[25–27] Although Yttrium Ferrite (YFO) has a wide range of uses in a variety of fields, its potential for gas sensing is still largely untapped. With a bandgap of 2-2.5 eV, YFO exhibits p-type semiconductor activity by nature. The variable bandgap, exceptional thermal stability, and effective transport characteristics of YFO have recently made it a highly promising material for gas sensing. However, up until this point, there has been no report on a chemiresistive formalin sensor based on yttrium ferrite.

In this study, hexagonal nanoparticles of $YFeO_3$ were synthesized through the hydrothermal technique. The resulting nanopowder underwent an extensive analysis employing X-ray diffraction (XRD), field-emission scanning electron microscopy (FESEM), transmission electron microscopy (TEM), high-resolution transmission electron microscopy (HRTEM), X-ray photoelectron spectroscopy (XPS), and Brunauer-Emmett-Teller (BET) analysis. Subsequently, a thick film sensor coating of $YFeO_3$ was deposited onto a tubular α-alumina substrate using a specialized drop coater to fabricate a Taguchi type chemiresistive sensor.
The sensor showed substantial p-type response of 3.12 folds to 1 ppm formalin at 240 ^{0}C. Furthermore, the sensor demonstrated exceptional differentiation ability among a range of low formalin concentrations, such as 0.5 ppm, 1 ppm, and 5 ppm. Additionally, it exhibits negligible cross-sensitivity, quick response and recovery times, and consistent stability over time. This sensor is a strong competitor for a wide range of industrial and environmental applications because of its exceptional detection skills, enduring stability, and constant repeatability. The improved formaldehyde sensing ability of the sensors based on the synthesized $YFeO_3$ nanoparticles can be attributed to the alteration of surface electronic states and the widening of the hole accumulation layer. This alteration is a result of the interaction between the gas impurities and the sensor's surface, leading to enhanced formaldehyde detection.

Table- 5. 1: comparative performance of various MOS-based chemiresistive formalin sensors in terms of sensing.

Sensor	**Response To formalin ($S = \frac{R_g}{R_a}$)**	**Operating temperature (°C)**	**Response time**	**Recovery time**
Sn-doped ZnO thin film[28]	2.9 folds to 50 ppm	25	10s	34s
SnO/SnO_2 nano-flowers[29]	~13 folds to 50 ppm	200	8s	33s
NiO/SnO_2 [30]	27.6 folds to 100 ppm	240	4s	18s
NiO nanosheets[31]	2.1 folds to 50 ppm	240	140 s	35 s
Sn-doped NiO[32]	145 folds to 100 ppm	225	30 s	160 s
CO- doped In2O3 nanoparticles[33]	23 folds to 10 ppm	130	60s	120s
Walnut-shaped $BiFeO_3$ microspheres[34]	3.1 folds to 25 ppm	240	20s	14s
$BiFeO_3$ - nanoparticles[35]	5.2 folds to 200 ppm	260	-	-
$LaFeO_3$ thin film [36]	1.4 folds to 1 ppm	120	5min	5 min
Sn- doped $BiFeO_3$ [37]	3.05 folds to 1 ppm	280	2.71s	25.22s
Zn- doped $LaFeO_3$ [38]	7 folds to 100 ppm	250	100s	100s
Ag– doped $LaFeO_3$ [39]	25 folds to 1 ppm	90	65s	60s
Pr-doped $BiFeO_3$ [40]	17.6 folds to 50 ppm	190	17s	19s

$CoFe_2O_4$- Co_3O_4 composite[41]	12.7 folds to 10 ppm	139	4s	9 s
Hexagonal $YFeO_3$ [This work]	3.12 folds to 1 ppm	240	2.3s	13.1s

5.2 Materials and methods

5.2.1 Materials

Iron nitrate nonahydrate ($Fe(NO_3)_3.9H_2O$), yttrium nitrate hexahydrate ($Y(NO_3)_3.6H_2O$), and tartaric acid ($C_4H_6O_6$) were procured from Merck, India. All of the chemicals were of analytical-grade purity and were utilized directly.

5.2.2 Synthesis of yttrium ferrite powder

A facile hydrothermal method was used to synthesize yttrium ferrite particles using procured precursor materials. $Y(NO_3)_3.6H_2O$ and $Fe(NO_3)_3.9H_2O$ were dissolved in 40 ml of DI water in a 1:1 molar ratio, and the mixture was agitated continuously for one hour using magnetic stirring. Required amount of tartaric acid was added to the solution to make the PH of the solution to 2. The entire mixture was then transferred to the autoclave and then kept in a muffle furnace at 180º C for 16 hours. The obtained product was ground into fine powders after being rinsed repeatedly with distilled water and alcohol and dried at 120 °C overnight. The dried powder was then sintered at 650°C for 1 hour, to produce the phase pure hexagonal $YFeO_3$. The detail synthesis procedure is shown schematically in Fig. 5. 1.

5.2.3 Characterization

X-ray diffraction (XRD) pattern of the synthesized material was obtained using the Panalytical X'Pert pro MPD XRD fitted with a Cu-Kα target (wavelength~1.5418Å) and nickel filter. Tecnai-made transmission electron microscope (G2 30ST (FEI)) and a Carl Zeiss Supra 35 VP field emission scanning electron microscope (FESEM) were used to examine the microstructure, morphology, and lattice fringes of the sample. ULVAC-PHI, US-made X-ray photoelectron spectroscopy was used to study the surface electronic states of the sample. The absorbance spectra were taken using a UV-Visible spectrophotometer (SHIMADZU, UV-3600) and the corresponding band gap energy of the material was estimated using Tauc plot

method. NovaWin, Quantachrome Instrument was used to conduct Brunauer-Emmett-Teller (BET) study to estimate the specific surface area of the synthesized nanopowder. Nicolet 380 Fourier Transform Infrared (FTIR) spectrometer was used to detect the presence of different functional bonds in the obtained powder. Agilent B2901A source meter and Keysight 34470A digital multimeter along with the computer-interfaced data logging facility were used to measure current voltage (I-V) characteristics and gas sensing response of the fabricated sensor with the synthesized hexagonal yttrium ferrite nanopowder as active sensing material.

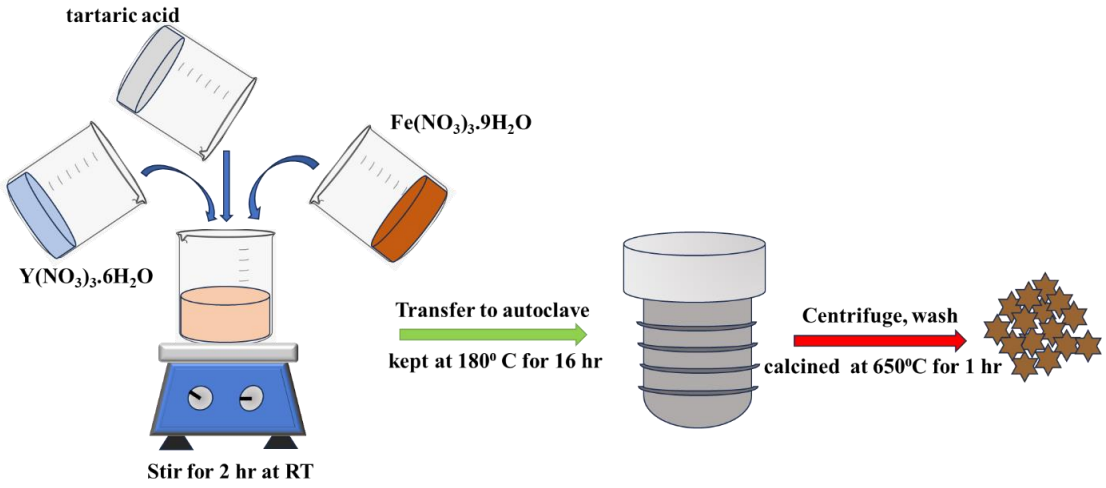

Fig. 5. 1. Schematic diagram of the hexagonal $YFeO_3$ synthesis procedure.

5.2.4 Fabrication of the sensor and measurement of the sensing performance

The as synthesized powder was used as active material for fabricating Taguchi-type thick film sensor where a 3.5 mm hollow cylindrical alumina tube was used as the substrate. Gold paste and Pt were used to fabricate the electrode of the sensor and a nichrome wire was inserted inside the hollow cylindrical substrate as a heating coil of the sensor. Further, the synthesized material was grinded using isopropanol to make a slurry paste which was drop coated on the cylindric substrate using a customized drop cotter. The sensor was air-dried at 60 °C for one hour after coating to eliminate any remaining traces of the isopropyl alcohol solvent. The constructed cylindrical substrate was welded within a polymeric sensor Schocket having a six-headed pin. Details of the sensor fabrication procedure are given in the earlier reports. [[42]] Finally, the fabricated sensor was used for the detail sensing measurements. The sensor module was attached to a base, where electrodes were connected to a Keysight multimeter and the

heating coil was connected to a DC voltage source. The sensor was heated by the applied voltage to the desired temperature, which was measured by a thermocouple. The resistance in ambient air (R_a), also known as the sensor's base resistance at this temperature, was recorded by the multimeter which was simultaneously entered into Keysight software on a computer. A commercially available nitrogen-balanced formalin gas cylinder was used for the sensing experiments. Further pure nitrogen gas cylinder and an alicat-made mass flow controller meter were used for diluting the high ppm formalin gas. For cross-sensing measurements different commercially available N_2 balanced gas cylinders viz. CO, H_2S, SO_2, NO_2, Benzene, Toluene were used. Schematic of the gas sensing measurement setup is shown in Fig. 5. 2. Response of the sensor was defined as,

$S = R_g/R_a$ …… (1)

where R_a is defined as the resistance of the sensor at ambient environment and R_g is defined as the resistance of the sensor when the gas was exposed over the sensor. [43]

5.3 Result and discussion

5.3.1 Material Characterization

X-ray diffraction pattern of as prepared Yttrium Ferrite particles is shown in Fig. 5. 3 (a). Several diffraction peaks were observed at $29.42^0, 30.38^0, 33.14^0, 42.76^0, 52.14^0, 61.58^0$, correspond to (100), (101), (102), (104), (110), (114) facets of hexagonal phase $YFeO_3$, respectively (ICDD card no. 00-048-0529). The subsequent XRD pattern showed no additional impurity peaks, indicating that hexagonal yttrium ferrite was synthesized with excellent phase purity.[44] The Debye-Scherrer formula was used to determine the average crystallite size, which was ~ 30.8 nm using the below equation,

$$D = \frac{(K\lambda)}{(ß \cos \varphi)}$$

Where, D, K, λ, ß are crystallites size, shape factor (0.89), wavelength of the X-ray source (here, 0.15406 nm), full width at half maxima of the diffraction peak for diffraction angle 2 ß (FWHM), and v is the Bragg angle. Further crystallite size of the synthesized sample was measured using W-H plot method which shows nearly same result (~28.05 nm) as of Debye-Scherrer formula. [45,46] W-H plot of hexagonal $YFeO_3$ is shown in Fig. 5. 3 (b).

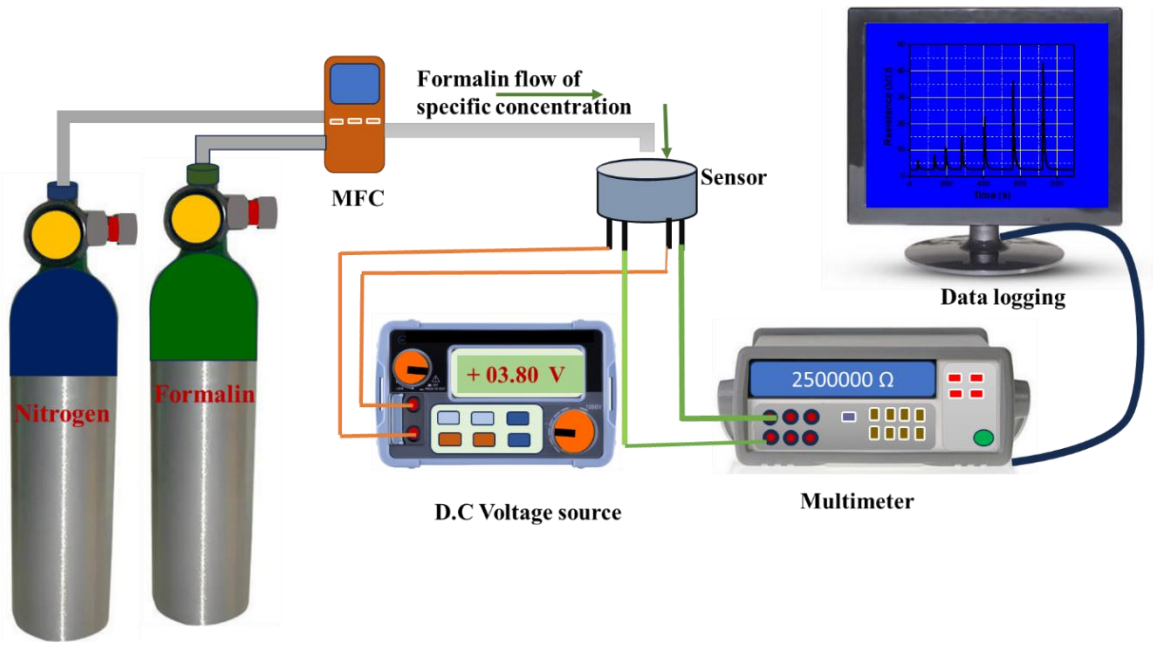

Fig. 5. 2. Schematic diagram of the gas sensing procedure.

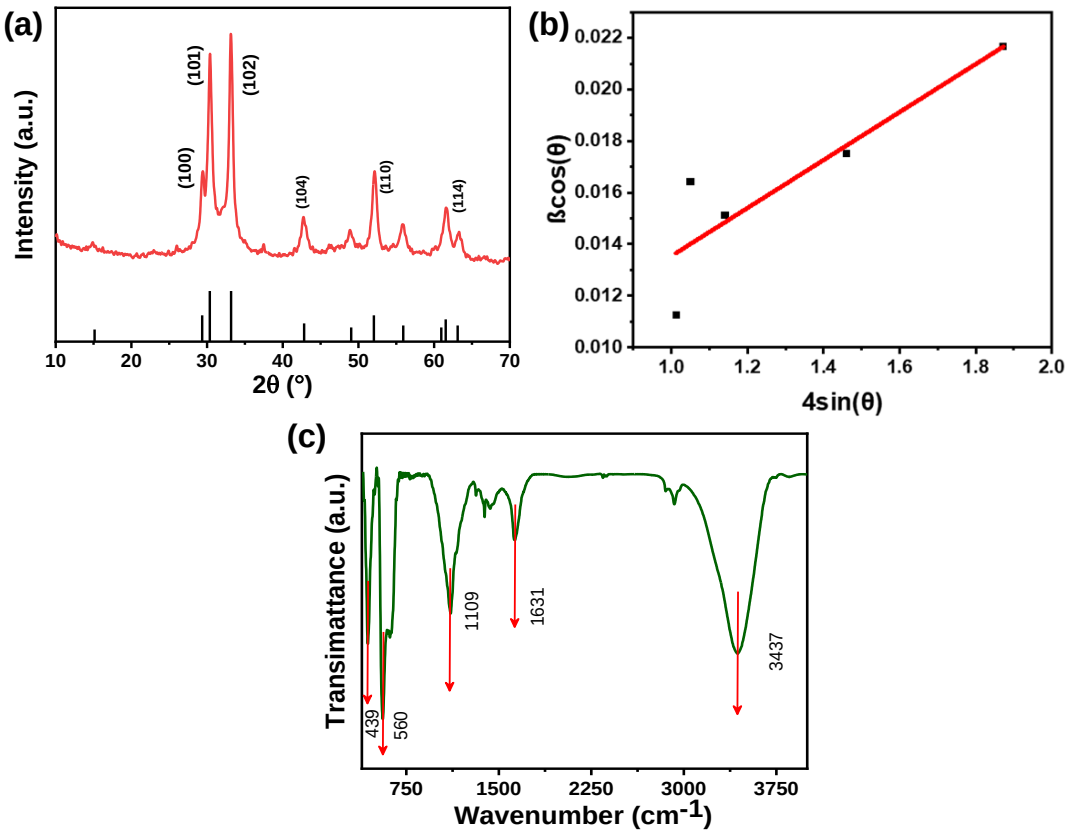

Fig. 5. 3. (a) XRD pattern of hexagonal $YFeO_3$ powder, (b) W-H plot of hexagonal $YFeO_3$, (c) FTIR spectra of the hexagonal $YFeO_3$ powder.

The purity of the $YFeO_3$ compound was further confirmed by FTIR studies as shown in Fig. 5. 3 (c). The wide peak at 3437 cm^{-1} is corresponding to the stretching vibrations of structural hydroxyl (OH) groups. The stretching vibrations of C=O, which correspond to the groups of tartaric, were associated with the intense peaks at 1628-1672 cm^{-1}. Further evidence that $YFeO_3$ pure phase was formed could be found in the peaks at 780 cm^{-1} and 560 cm^{-1}, which are caused by the vibration of octahedral FeO_6. The IR peaks below 1000 cm-1 corresponded to the vibrational bonds of Y- O or Fe-O.[47,48]

XPS survey spectra of the as synthesized $YFeO_3$ powder is shown in Fig. 5. 4 (a). The HR-XPS curves for the Y3d, Fe2p, and O1s spectra show that Y, Fe, and O are present in the sample (ref. Fig. 5. 4 (b,c,d))[47]. The Y 3d spectra showed two significant peaks with binding energies at about 156 eV and 159 eV respectively, corresponding to Y $3d_{5/2}$ and Y $3d_{3/2}$ which indicates Y is in the +3 valance state in $YFeO_3$.[47,49] Two primary Fe 2p3/2 and Fe 2p1/2 peaks were seen at binding energies of 710 eV and 724 eV respectively which indicate that iron is present in the sample as Fe^{3+}. XPS Fe2p deconvolution result (ref. Fig. 4(c)) reveals that the peaks at 710.2 eV and 723.6 eV are associated with bivalent iron (Fe^{2+}), the peaks at 713.1 and 726.5 eV are associated with trivalent iron (Fe^{3+}).[49,50] The coexistence of Fe^{2+} and Fe^{3+} ions is advantageous for enhancing electron transport efficiency. Fe^{3+} ions serve as electron traps, facilitating the conversion of some electrons into Fe^{2+} ions, thereby promoting electron transfer processes. To counterbalance this disparity in charge within the material, an increased generation of oxygen vacancies will occur. As shown in Fig. 5. 4 (d) HR-XPS spectra of the O1s region of the sample is deconvoluted into three distinct peaks at around 529 eV, 531eV and 532 eV corresponding to the crystal lattice oxygen, defect oxygen or oxygen vacancies and chemisorbed oxygen species respectively.[51] These oxygen vacancies, possessing positive charges, serve as active sites for sensing.

SEM was used to describe the microstructures of the synthesized samples. Fig. 5. 5 (a-b) shows the FESEM image, which shows that the accumulating of nanoparticles produces the final microstructure of the pure hexagonal $YFeO_3$. The YFO particles are in close proximity to one another, and there are clear pores in the agglomerated YFO structure. Due to agglomeration, it was difficult to accurately assess the particle size and morphology from this image.

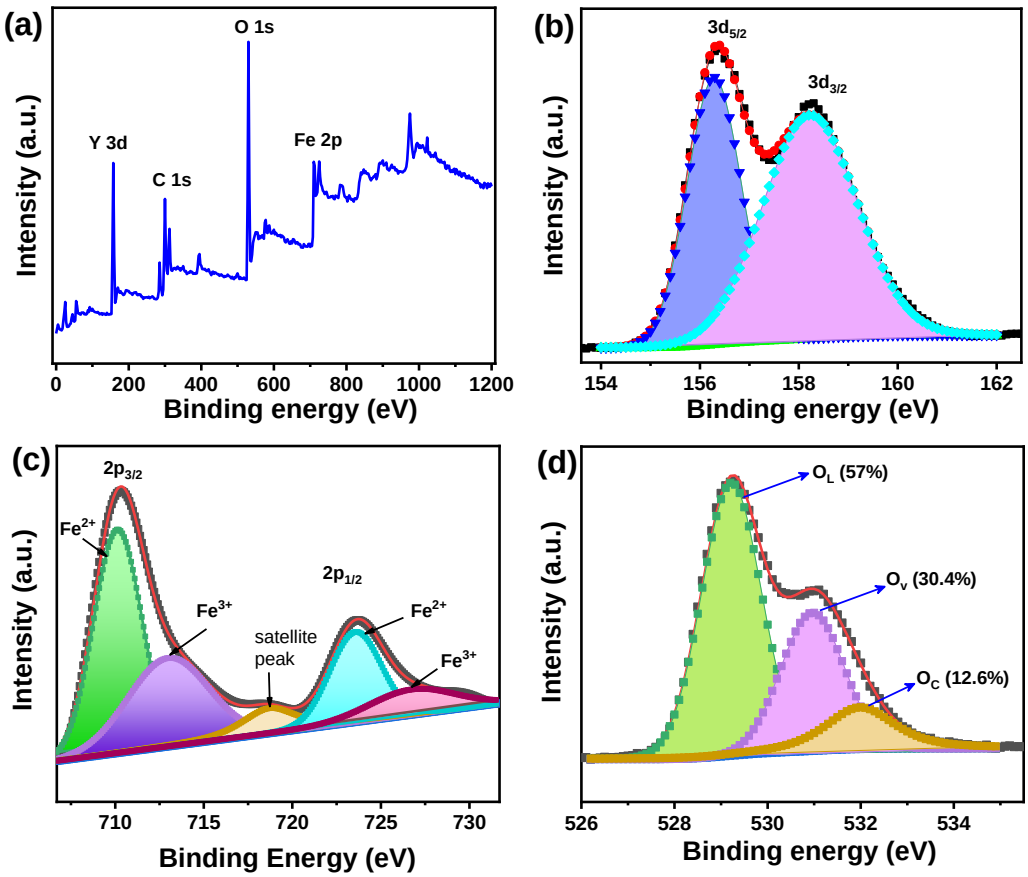

Fig. 5. 4. (a) XPS survey scan of hexagonal $YFeO_3$. HR-XPS spectra of (b) Y 3d, (c) Fe 2p, and (d) O 1s region of $YFeO_3$.

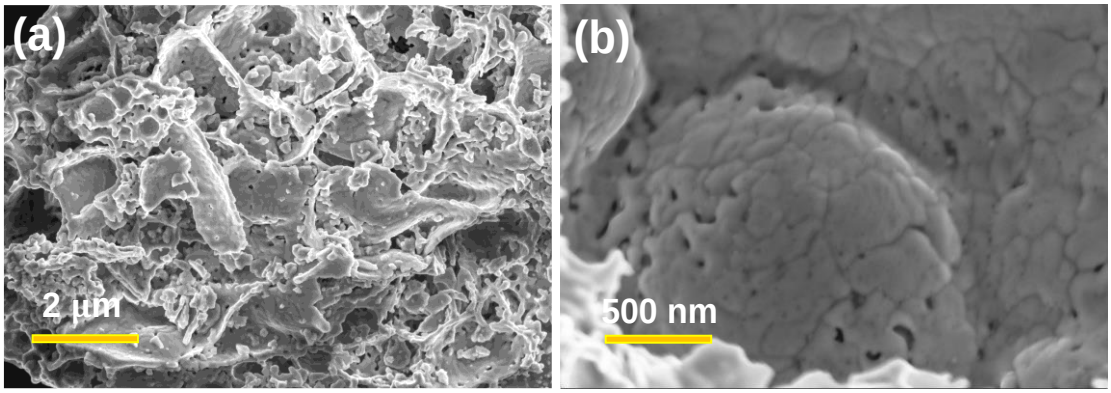

Fig. 5. 5. (a-b) FESEM micrograph of the synthesized material at different magnification.

TEM and HRTEM were utilized to describe the prepared samples in order to further examine their microstructure. The TEM patterns of the pure YFO are shown in Fig. 5. 6 (a). The TEM

micrograph reveals the agglomerated nature of the particles. The stack structure with glaring pore gaps between the particles of original YFO sample as presented in TEM is exactly resemble with FESEM. As observed from the TEM image of the material, the size of the particles falls within the range of 50 – 100 nm, which corroborates with the crystallite size of the material as calculated from X-ray diffraction results. A series of parallel lattice planes are seen in the HRTEM image (ref. Fig. 6 (b)), and their d-values (2.71 Å), as measured using imageJ software, line up well with the (102) plane, which also confirms the formation of hexagonal $YFeO_3$.

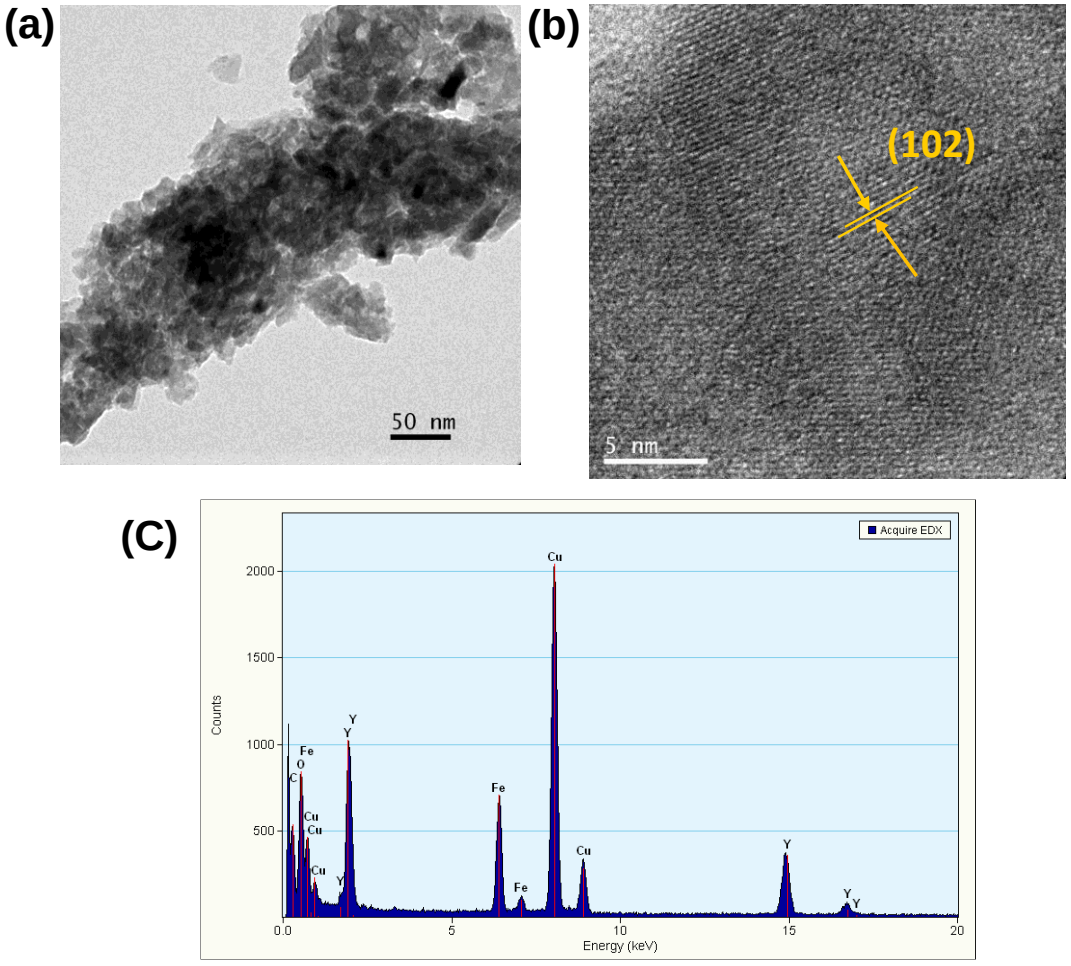

Fig. 5. 6. (a) TEM micrograph, (b) HRTEM image, (c) EDX spectra of hexagonal $YFeO_3$ powder.

EDS spectra corresponding to TEM micrographs is shown in the Fig. 5. 6 (c). Presence of yttrium, iron and oxygen in the synthesized sample. Further the peaks corresponding to C and

Cu in EDS spectra comes from the carbon coated copper grid which was used for the TEM analysis.

UV-visible spectrophotometer is utilized to investigate the optical properties of the synthesized materials, encompassing absorbance and band gap characteristics. UV-Vis absorbance spectra of the synthesized sample in the wavelength range of 300-1200 nm is shown in the inset of Fig. 5. 7 (a). The electronic change from the valence band to the conduction band can be generally associated with the substantial absorption. As depicted in the figure, YFO displays absorption peaks occurring around 730 nm. In accordance with this, synthesized YFO might function as an effective surface catalyst. Tauc plot method is employed to calculate the band gap of the material using following equation,

$$\alpha h\nu = A(h\nu - E_g)^{\frac{1}{2}} \quad \ldots\ldots\ldots\ldots\ldots\ldots\ldots\ldots\ldots\ldots\ldots\ldots (2)$$

Where α is the absorption coefficient, hν is the energy of the photon, E_g is the band gap energy of the sample and A is a constant. The estimated value of the bandgap of hexagonal $YFeO_3$ is nearly 2eV, which nearly matches with the previously reported value (ref. Fig. 5. 7 (a)).[52]

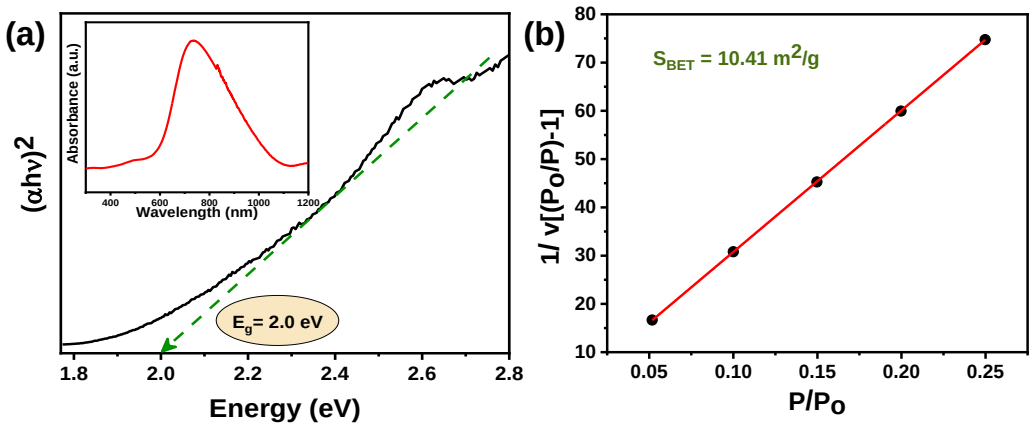

Fig. 5. 7. (a) Tauc plot of the sample (inset shows UV-Vis absorption spectra of the samples), (b) BET plot of $YFeO_3$ powder.

Fig. 5. 7 (b) shows the Brunauer–Emmett–Teller (BET) surface area curves of as synthesized YFO nanopowder. Calculated BET surface area for YFO nanopowder was 11.2 m^2/g when calcined at 650°C. The presence of a significant number of pores on the surface, as observed in the FESEM micrograph (ref. Fig. 5. 5 (b)), and smaller crystallite size may attribute to the elevated surface area of the as synthesized material.

5.3.2 Electrical and gas sensing study

Current voltage characteristics of the as fabricated sensor was measured at various operating temperature. The sensor showed a linear curve in the voltage range from -40v to +40v at each temperature which delineates that ohmic contact was formed between the active sensing material and the Au electrode. The slopes I-V characteristics curve at different operating temperature indicates that with increasing operating temperature the base resistance of the sensor decreases (ref. Fig. 5. 8 (a)). The ideality factor (I.F) for the I- V curves corresponding to each operating temperature are calculated from the slop of the I-V curve from the Fig. 5. 8 (a). Ideality factor shows an increasing trend as operating temperature of the sensor increases. I.F values of the I-V curves are 0.006, 0.012, 0.040, 0.075 corresponding to 150ºC, 200ºC, 240ºC, 300ºC. [53,54] Different operating temperatures were achieved by applying various DC voltages (1.0 V-4.5 V) across the heating coil inside the sensor. The accurate temperature was measured using thermal imaging of the sensor surface. Fig. 5. 8 (b) displays the ultra-contrast thermal pictures of the sensor surface at 3.7V. Further, the base resistance of the sensor at different operating temperatures was measured as shown in Fig. 5. 8 (c). The resistance-temperature curve fitted with the following equation….

$$R_T^{air} = R_0^{air} + A.exp^{\left(\frac{-t}{B}\right)} \text{ ……………………………… (3)}$$

where R_T^{air} is the base resistance of sensor at temperature T, R_0^{air} is the pre-exponential term, A and B are two constant. Fitting result clearly indicates that with increasing operating temperature conductivity of the sensing material increases exponentially which depicts the semiconducting nature of the material.

Since the active sensing material (YFO) is a typical semiconducting substance, operating temperature is a key factor in determining how well it responds for the purpose of sensing. Sensor responses to 1 ppm formalin vapor at different operating temperatures between 150°C and 300°C were measured to identify the optimal operating temperature (ref. Fig. 5. 8 (d)). The sensor showed maximum response to 1 ppm formalin at 240°C. Further gas sensing response of the sensor was measured at this optimal temperature. Background relative humidity (%RH) plays an influential role in sensing performance. Response of the sensor towards 1 ppm formalin was measured at different background %RH as shown in Fig. 5. 9 (a). In higher background conditions, the sensor's response slightly drops. A potential cause of this outcome could be the environment's excessive moisture, which might block the material's active sensing sites.

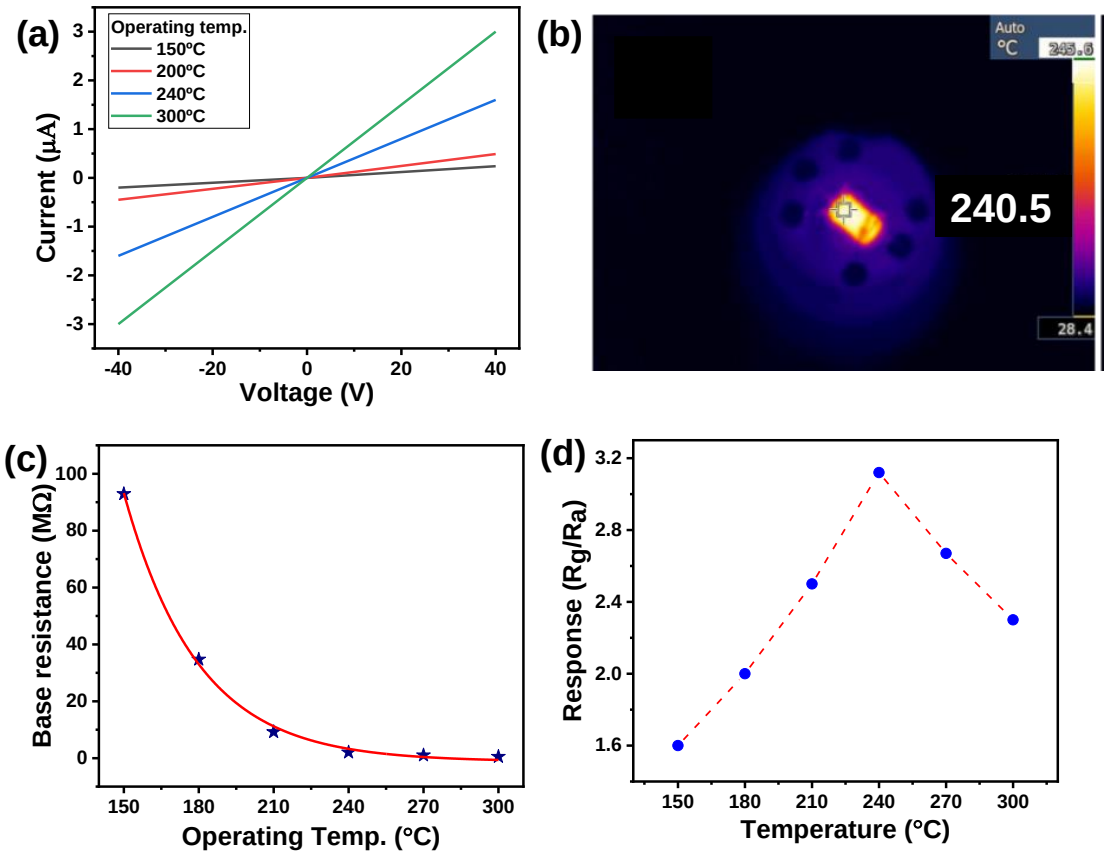

Fig. 5. 8. (a) I-V plots of YFO sensor at different operating temperature, (b) Ultra-contrast thermal images of YFO sensor surface at optimum operating temperature (240°C), (c) Variation of base resistance of the sensor with varying operating temperature, (d) Variation of response to 1 ppm formalin with varying operating temperature.

Further response of the sensor at various different formalin concentrations was measured and the corresponding dynamic response curve of the sensor was shown in Fig. 5. 9 (b). Response of the sensor corresponding to different formalin concentrations was calculated and the variation of sensing response with varying gas concentrations is shown in Fig. 5. 9 (c). This clearly delineates that the sensor shows remarkably good resolution in response for different gas concentrations. Further, the repeatability of any sensor is one of the major parameters for the fabrication of a commercially viable sensor. the repeatability of the sensor was measured by three consecutive cycles toward 25 ppm formalin as shown in Fig. 5. 10 (a). The fabricated sensor shows a very consistent response over three consecutive cycles. [55,56]

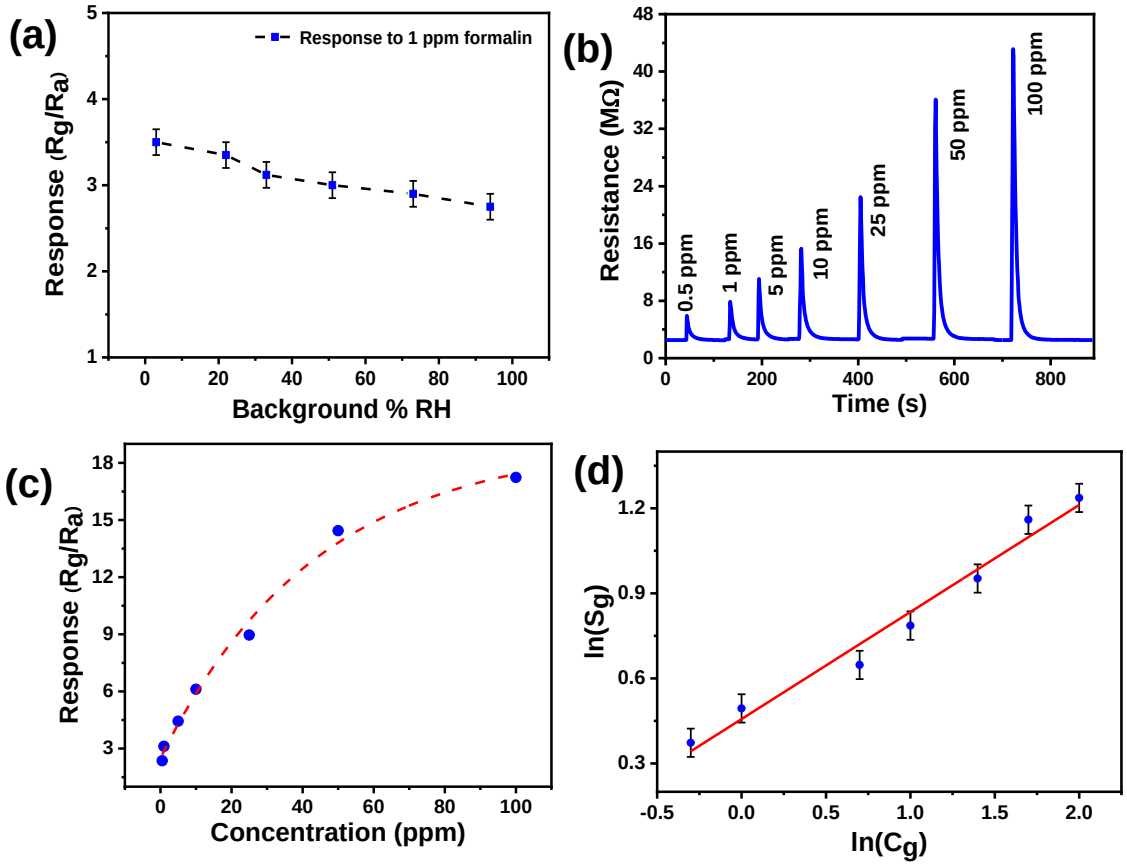

Fig. 5. 9. (a) Variation of response to 1 ppm formalin with background relative humidity (%RH), (b) Dynamic response and recovery curve of the YFO sensor towards 0.5-100 ppm formalin, (c) Response of the sensor towards different formalin concentration, (d) Fitting of experimental sensing response data with Freundlich adsorption isotherm at 240 ◦C.

The Freundlich absorption isotherm model has been used to ascertain the type of interaction between the ammonia gas molecules and the sensor surface. Equation for the Freundlich adsorption isotherm is shown below,

$$S_g = \alpha C_g^{\beta} \ \ldots\ldots\ldots\ldots\ldots\ldots\ldots\ldots\ldots\ldots\ (4)$$

$$\log(S_g) = \log\alpha + \beta\log C_g \ \ldots\ldots\ldots\ldots\ldots\ldots\ldots\ldots\ldots\ldots\ (5)$$

where S_g, α, C_g, β represent the response of the sensor, the proportionality constant, gas concentration, and the exponent respectively. Since the value of β is 0.37, it is clear that physisorption is occurring and only mild interactions between formalin molecules and the sensor surface are occurring[57]. Consequently, a thorough and rapid recovery may be anticipated (ref. Fig. 5. 9 (d)).

The fabricated sensor also showed rapid response and recovery time. The transient conductance of the sensor was fitted using the single site Langmuir absorption model in order to precisely determine the response and recovery durations. Transient response and recovery conductance were fitted with following equations (6) and (7) respectively,

$$C(t) = C_0(t) + C_1 e^{-\left(\frac{t}{\tau_{response}}\right)} \quad \text{..... (6)}$$

$$C^{\blacksquare}(t) = C_0^{\blacksquare}(t) + C_1^{\blacksquare}\left(1 - e^{\left(\frac{-t}{\tau_{recovery}}\right)}\right) \quad \text{..... (7)}$$

Where, $C(t)$ is the transient conductance at any time, $C^{\blacksquare}(t)$ is transient conductance G'(t) for the recovery process$C_0(t)$ is the base conductance, $C_0^{\blacksquare}(t)$ is the conductance at the end of the response process $\tau_{response}$ and $\tau_{recovery}$ are the response and recovery times respectively. Response and recovery times are 2.3 s and 13.1 s, respectively for 1ppm formalin gas, as determined by fitting the transient conductance curve by Eqs. (6) and (7) as shown in Fig. 5. 10 (b).

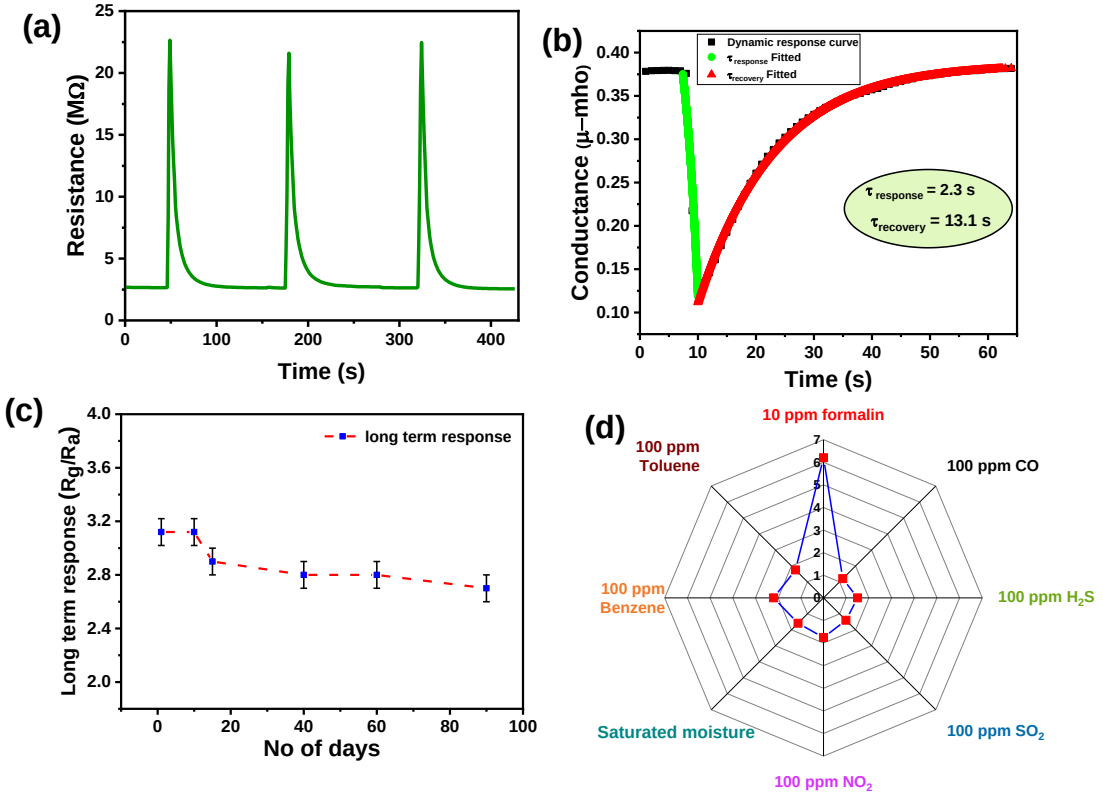

Fig. 5. 10 (a) Repeatability study of the sensor towards 25 ppm formalin vapour, (b) Response and recovery time, (c) Long-term stability curve, (d) Selectivity curve of the sensor.

For a sensor to be commercially viable, it must also be stable over the long term. The response of the YFO sensor at 240ºC stays essentially the same for a period of 100, as shown in Fig. 5. 10(c). Any sensor's selectivity is a key characteristic for real-time application. Selectivity of the sensor was checked with various interfering gases such as NO_2, SO_2, CO, H_2S, H_2, NH_3 as shown in Fig. 5. 10 (d). Sensor shows maximum response towards formalin over other interfering gases which demonstrates the potential of the sensor for selective formalin detection.

5.3.3 Formalin Sensing Mechanism

The YFO material, utilized in this investigation, demonstrated the typical traits of a p-type semiconductor. The interaction of gas molecules with the sensor's surface through adsorption and desorption processes is the main mechanism of its sensing performance. The atmospheric oxygen gets absorbed on the surface of the sensor and ionised by attracting electrons from its conduction band of the active sensing material. Depending on the surface temperature of the sensor, these oxygen molecules can form different ionic species (such O_2^- , $2O^-$ and O^{2-}). In this study the major adsorbed oxygen species on the surface will be O^- since the operating temperature of the sensor is 250 ^{0}C. As a result of decrease in electron concentration, the YFO sensor showed decrease in resistance when exposed to air since it's a p-type sensor. Equation (8.1-8.6) describes the adsorption procedure in detail. As shown in Equation (8.1-8.4)), when the sensor was exposed to formaldehyde (HCHO) gas, the HCHO molecules reacted with the previously adsorbed oxygen ions on the surface.[58–61] The active areas on the surface of the sensor were nearly occupied by HCHO molecules as the interaction between HCHO and the adsorbed oxygen continued to advance. Ultimately, HCHO will oxidise and produces CO_2, H_2O and also releases electrons. These released electrons will reintroduce into the conduction band of the sensing material and annihilate the holes accordingly to the equation 8.5 and 8.6 as seen in Fig. 5. 11 (a-b). The reduction in the concentration of holes will led to an increase in sensor resistance since its p-type in nature. As a result, the sensor's resistance increased to its maximum value, producing a clear detecting signal for the presence of HCHO.

$$O_2(gas) \rightarrow O_2(ads) \quad \text{..... (8.1)}$$

$$O_2\ (ads) + e^- \rightarrow O_2^-\ (ads)\ \ (T < 100^0C) \quad \text{..... (8.2)}$$

$$O_2^-\ (ads) + e^- \rightarrow 2O^-\ (ads)\ \ (100^0C < T < 300^0C) \quad \text{..... (8.3)}$$

$$O^-(ads) + e^- \rightarrow O^{2-}(ads)\ \ (T > 300^0C) \quad \text{..... (8.4)}$$

$$CH_2O\ (gas) + 2O^-\ (ads) \rightarrow CO_2 + H_2O + 2e^- \quad \text{..... (8.5)}$$

$h^+ + e^- \rightarrow null$..... (8.6)

When formalin gas is injected, it will adsorbed on the surface of $YFeO_3$ and interact with the adsorbed oxygen ions. On the surface of $YFeO_3$, the formalin gas molecules will simultaneously adsorb and desorb. Adsorption and desorption rates vary with operating temperature. At the optimum operating temperature adsorption rates becomes maximum. As a result, number of formalin molecules on the surface of the material become maximum at optimum operating temperature which intensifies the reaction between the incoming gas molecules and the oxygen ions. Hence maximum response (R_g/R_a) was achieved at the optimum operating temperature. Beyond the optimum operating temperature desorption rates of the formalin molecules become higher than the rate of adsorption, resulting in a decline in the response (R_g/R_a).

Additionally, at the optimum operating temperature, as the formalin concentration rises, more formalin molecules become adsorbed on the surface of $YFeO_3$ which results as higher amount charged transfer between the sensor surface and the absorbed gas molecules. However, there are only a finite number of free electrons on the surface of $YFeO_3$, and the amount of energy needed to undergo an electronic transition within $YFeO_3$ rises as well. Consequently, the response (R_g/R_a) rises with formalin gas molecule concentration, although rate of rising drops significantly.

When it comes to charge transfer-based surface catalytic characteristics, as synthesized $YFeO_3$ would have an advantage because of its lower band gap energy measured from UV vis spectra. Further as confirmed from XPS study iron is present in the synthesized material both in Fe^{2+} and Fe^{3+} oxidation states. It will be advantageous for increased electron transport as both Fe^{2+} and Fe^{3+} are present in the synthesized material.[62] More oxygen vacancies will be developed, which are positively charged and active sites for sensing, to balance out the material's charge imbalance. According to the results of the BET surface area analysis, the surface area of the synthesized material was reasonably high, which essentially aided in the gas adsorption and desorption process. This plays an influential role for giving elevated gas sensing response of the material. [63]

5.4 Conclusions

In this work, yttrium ferrite ($YFeO_3$) powder of pure hexagonal phase was successfully synthesized with a high degree of crystallinity using a hydrothermal technique. Differente

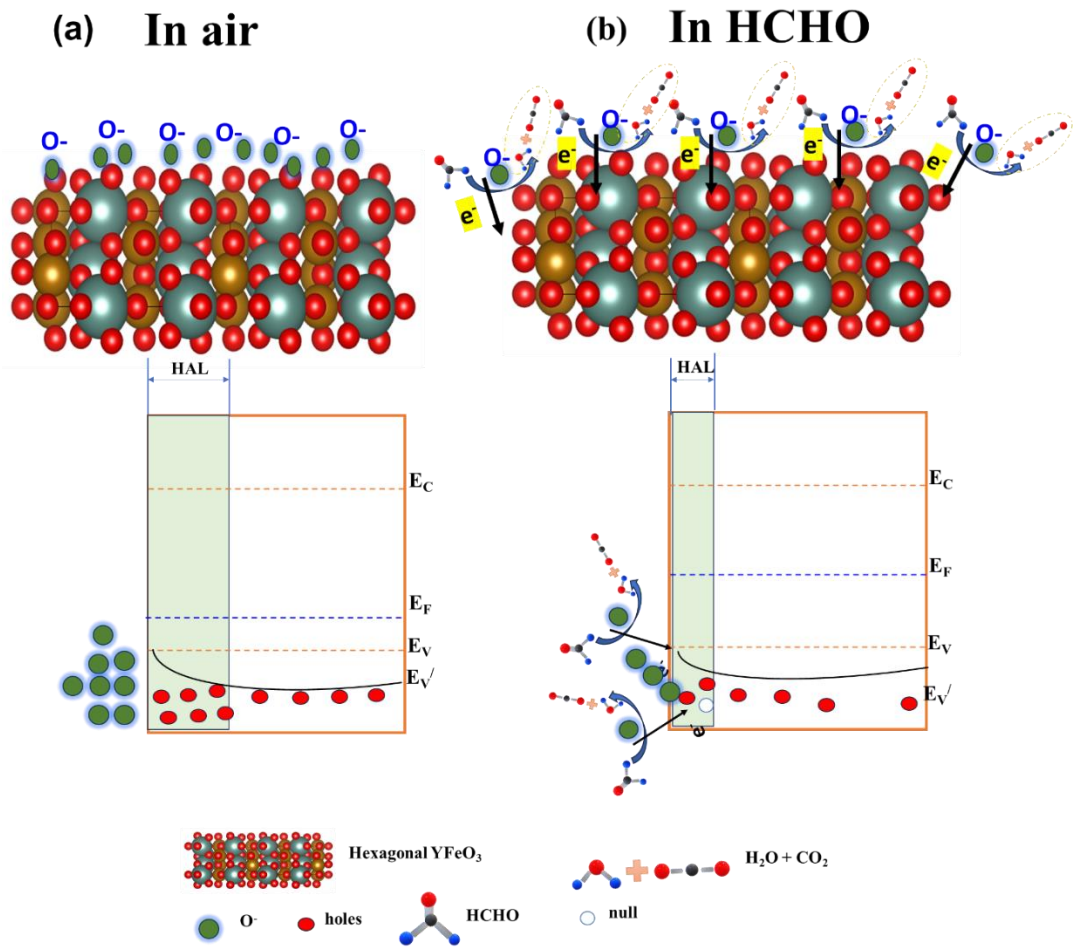

Fig. 5. 11 Schematic representation of the formalin sensing mechanism of hexagonal $YFeO_3$ sample (a) in air, (b) in HCHO.

offisticated techniques were employed to charecterize the synthesized material. Significantly, this study introduced for the first time a hexagonal yttrium ferrite-based chemiresistive sensor that showed highly selective and sensetive response towards formalin vapor. At an operational temperature of 240 ^{0}C, a response of around 3.12 times was achieved for 1 ppm formalin. The sensor also demonstrates rapid response and recovery characteristics, with response and recovery times of 2.3s and 13.1s respectively for 1ppm formalin gas. These sensors showcase minimal sensitivity towards probable interfering gasses/VOCs including moisture, remarkable stability, reproducibility, selectivity, rapid response and recovery times. The studydemonstrates that the elevated sensing response of the YFO sensor towards formalin vapor can be explicated by a synergistic interplay of multiple factors such as higher surface area, the existence iron in bivalent oxidation states, oxygen defects, and smal bandgap energy Prepared sensor possess high prospect in real-time application for monitoring of formaldeyde in different fields.

5.5 Reference

[1] X. Chu, X. Zhu, Y. Dong, W. Zhang, L. Bai, Formaldehyde Sensing Properties of SnO–Graphene Composites Prepared via Hydrothermal Method, J Mater Sci Technol 31 (2015) 913–917. https://doi.org/10.1016/j.jmst.2015.05.001.

[2] Z. Wang, H. Zhou, D. Han, F. Gu, Electron compensation in p-type 3DOM NiO by Sn doping for enhanced formaldehyde sensing performance, J Mater Chem C Mater 5 (2017) 3254–3263. https://doi.org/10.1039/C7TC00226B.

[3] D. Kukkar, K. Vellingiri, R. Kaur, S.K. Bhardwaj, A. Deep, K.-H. Kim, Nanomaterials for sensing of formaldehyde in air: Principles, applications, and performance evaluation, Nano Res 12 (2019) 225–246. https://doi.org/10.1007/s12274-018-2207-5.

[4] M. Koley, J. Han, V.A. Soloshonok, S. Mojumder, R. Javahershenas, A. Makarem, Latest developments in coumarin-based anticancer agents: mechanism of action and structure–activity relationship studies, RSC Med Chem 15 (2024) 10–54. https://doi.org/10.1039/D3MD00511A.

[5] L. Yang, C. Liu, W. Yuan, C. Meng, A. Dutta, X. Chen, L. Guo, G. Niu, H. Cheng, Fully stretchable, porous MXene-graphene foam nanocomposites for energy harvesting and self-powered sensing, Nano Energy 103 (2022) 107807. https://doi.org/10.1016/j.nanoen.2022.107807.

[6] Z. Bo, M. Yuan, S. Mao, X. Chen, J. Yan, K. Cen, Decoration of vertical graphene with tin dioxide nanoparticles for highly sensitive room temperature formaldehyde sensing, Sens Actuators B Chem 256 (2018) 1011–1020. https://doi.org/10.1016/j.snb.2017.10.043.

[7] D. Wang, M. Zhang, Z. Chen, H. Li, A. Chen, X. Wang, J. Yang, Enhanced formaldehyde sensing properties of hollow SnO 2 nanofibers by graphene oxide, Sens Actuators B Chem 250 (2017) 533–542. https://doi.org/10.1016/j.snb.2017.04.164.

[8] W.M. Moore, R.J. Edwards, L.T. Bavda, An Improved Capillary Gas Chromatography Method for Triethylamine. Application to Sarafloxacin Hydrochloride and GnRH Residual Solvents Testing, Anal Lett 32 (1999) 2603–2612. https://doi.org/10.1080/00032719908542991.

[9] J.F. Haskin, G.W. Warren, L.J. Priestley, V.A. Yarborough, Gas Chromatography. Determination of Constituents in Study of Azeotropes, Anal Chem 30 (1958) 217–219. https://doi.org/10.1021/ac60134a016.

[10] L. Zhao, Y. Chen, X. Li, X. Li, S. Lin, T. Li, M.N. Rumyantseva, A.M. Gaskov, Room Temperature Formaldehyde Sensing of Hollow SnO_2 /ZnO Heterojunctions Under UV-LED Activation, IEEE Sens J 19 (2019) 7207–7214. https://doi.org/10.1109/JSEN.2019.2916879.

[11] M. Sinha, S. Neogi, R. Ghosh, Temperature dependent selectivity switching from methanol to formaldehyde using ZnO nanorod based chemi-resistive sensor, Sens Actuators A Phys 357 (2023) 114405. https://doi.org/10.1016/j.sna.2023.114405.

[12] C.-S. Lee, H.-Y. Li, B.-Y. Kim, Y.-M. Jo, H.-G. Byun, I.-S. Hwang, F. Abdel-Hady, A.A. Wazzan, J.-H. Lee, Discriminative detection of indoor volatile organic compounds using a sensor array based on pure and Fe-doped In2O3 nanofibers, Sens Actuators B Chem 285 (2019) 193–200. https://doi.org/10.1016/j.snb.2019.01.044.

[13] W. Liu, X. Si, Z. Chen, L. Xu, J. Guo, L. Wei, G. Cheng, Z. Du, Fabrication of a humidity-resistant formaldehyde gas sensor through layering a molecular sieve on 3D ordered macroporous SnO2 decorated with Au nanoparticles, J Alloys Compd 919 (2022) 165788. https://doi.org/10.1016/j.jallcom.2022.165788.

[14] Swathilakshmi, S. Anandhan, Recent development in carbon dot-based gas sensors, Sensors & Diagnostics 1 (2022) 902–931. https://doi.org/10.1039/D2SD00074A.

[15] S. Kumar, C.S. Kushwaha, P. Singh, K. Kanojia, S.K. Shukla, Chemiresistive sensor for breath frequency and ammonia concentration in exhaled gas over a PVA/PANI/CC composite film, Sensors & Diagnostics 2 (2023) 1256–1266. https://doi.org/10.1039/D3SD00067B.

[16] T. Munawar, S. Fatima, K.M. Batoo, M.S. Nadeem, F. Mukhtar, S. Hussain, S.A. Khan, M. Koc, F. Iqbal, Enhanced charge carriers separation/transportation via S-scheme ZnCeS–ZnWO heterostructure nanocomposite for photodegradation of synthetic dyes under sunlight, Mater Chem Phys 314 (2024) 128938. https://doi.org/10.1016/j.matchemphys.2024.128938.

[17] F. Mukhtar, T. Munawar, K.M. Batoo, H. Khursheed, M.S. Nadeem, S. Hussain, J. Ponraj, M. Koc, F. Iqbal, Oxygen vacancies generation in CeO2 via Y/Nd co-doping with accelerated charge separation by decorating on rGO sheets for sunlight-driven photodegradation of hazardous dyes, Ceram Int 50 (2024) 11486–11499. https://doi.org/10.1016/j.ceramint.2024.01.049.

[18] F. Mukhtar, T. Munawar, M.S. Nadeem, M.N. ur Rehman, K. Mahmood, S. Batool, M. Hasan, K. ur Rehman, F. Iqbal, Enhancement in carrier separation of ZnO-Ho2O3-Sm2O3 hetrostuctured nanocomposite with rGO and PANI supported direct dual Z-scheme for antimicrobial inactivation and sunlight driven photocatalysis, Advanced Powder Technology 32 (2021) 3770–3787. https://doi.org/10.1016/j.apt.2021.08.022.

[19] F. Mukhtar, T. Munawar, M.S. Nadeem, M.N. ur Rehman, S. Batool, M. Hasan, M. Riaz, K. ur Rehman, F. Iqbal, Highly efficient tri-phase TiO2–Y2O3–V2O5 nanocomposite: structural, optical, photocatalyst, and antibacterial studies, J Nanostructure Chem 12 (2022) 547–564. https://doi.org/10.1007/s40097-021-00430-9.

[20] T. Das, S. Mojumder, D. Saha, M. Pal, Enhanced ammonia sensing performance of barium hexaferrite enabled through Zn doping: Mechanistic study considering modulation of Fe2+/Fe3+ ratio and oxygen vacancy, Sens Actuators B Chem 406 (2024) 135358. https://doi.org/10.1016/j.snb.2024.135358.

[21] P. Song, H. Zhang, D. Han, J. Li, Z. Yang, Q. Wang, Preparation of biomorphic porous LaFeO3 by sorghum straw biotemplate method and its acetone sensing properties, Sens Actuators B Chem 196 (2014) 140–146. https://doi.org/10.1016/j.snb.2014.02.006.

[22] P.M. Bulemo, I.-D. Kim, Recent advances in ABO3 perovskites: their gas-sensing performance as resistive-type gas sensors, Journal of the Korean Ceramic Society 57 (2020) 24–39. https://doi.org/10.1007/s43207-019-00003-1.

[23] S. Chakraborty, M. Pal, Highly efficient novel carbon monoxide gas sensor based on bismuth ferrite nanoparticles for environmental monitoring, New Journal of Chemistry 42 (2018) 7188–7196. https://doi.org/10.1039/C8NJ01237G.

[24] N. Chakraborty, S. Das, V. Srihari, D.J. Mondal, D. Saha, S. Konar, A.K. Mishra, S. Mondal, Roles of structure and electron mobilization in enhanced ethanol sensing by Al doped SnO_2 nanoparticles, Mater Adv 2 (2021) 3760–3769. https://doi.org/10.1039/D1MA00172H.

[25] M. Ismael, E. Elhaddad, D.H. Taffa, M. Wark, Synthesis of phase pure hexagonal YFeO3 perovskite as efficient visible light active photocatalyst, Catalysts 7 (2017). https://doi.org/10.3390/catal7110326.

[26] M.I. Díez-García, V. Celorrio, L. Calvillo, D. Tiwari, R. Gómez, D.J. Fermín, YFeO3 Photocathodes for Hydrogen Evolution, Electrochim Acta 246 (2017) 365–371. https://doi.org/10.1016/j.electacta.2017.06.025.

[27] S. Mojumder, T. Das, M. Mukherjee, D. Saha, A. Datta, M. Pal, Development of highly sensitive and selective trace acetone sensor using perovskite yttrium ferrite: Mechanism, kinetics and phase dependence study, Chemical Engineering Journal (2023) 146855. https://doi.org/10.1016/j.cej.2023.146855.

[28] S. Ishak, S. Johari, M.M. Ramli, Formaldehyde detection using Sn doped ZnO thin film, J Solgel Sci Technol 95 (2020) 265–275. https://doi.org/10.1007/s10971-020-05318-8.

[29] N. Li, Y. Fan, Y. Shi, Q. Xiang, X. Wang, J. Xu, A low temperature formaldehyde gas sensor based on hierarchical SnO/SnO2 nano-flowers assembled from ultrathin nanosheets: Synthesis, sensing performance and mechanism, Sens Actuators B Chem 294 (2019) 106–115. https://doi.org/10.1016/j.snb.2019.04.061.

[30] L. Xu, M. Ge, F. Zhang, H. Huang, Y. Sun, D. He, Nanostructured of SnO_2 /NiO composite as a highly selective formaldehyde gas sensor, J Mater Res 35 (2020) 3079–3090. https://doi.org/10.1557/jmr.2020.239.

[31] G. Li, X. Wang, H. Ding, T. Zhang, A facile synthesis method for Ni(OH)2 ultrathin nanosheets and their conversion to porous NiO nanosheets used for formaldehyde sensing, RSC Adv 2 (2012) 13018. https://doi.org/10.1039/c2ra22049k.

[32] Z. Wang, H. Zhou, D. Han, F. Gu, Electron compensation in p-type 3DOM NiO by Sn doping for enhanced formaldehyde sensing performance, J Mater Chem C Mater 5 (2017) 3254–3263. https://doi.org/10.1039/C7TC00226B.

[33] Z. Wang, C. Hou, Q. De, F. Gu, D. Han, One-Step Synthesis of Co-Doped In_2O_3 Nanorods for High Response of Formaldehyde Sensor at Low Temperature, ACS Sens 3 (2018) 468–475. https://doi.org/10.1021/acssensors.7b00896.

[34] K.M. Zhu, S.Y. Ma, S.T. Pei, Y. Tie, Q.X. Zhang, W.Q. Wang, X.L. Xu, Preparation, characterizaton and formaldehyde gas sensing properties of walnut-shaped BiFeO3 microspheres, Mater Lett 246 (2019) 107–110. https://doi.org/10.1016/j.matlet.2019.02.129.

[35] T. Tong, J. Chen, D. Jin, J. Cheng, Preparation and gas sensing characteristics of BiFeO 3 crystallites, Mater Lett 197 (2017) 160–162. https://doi.org/10.1016/j.matlet.2017.03.091.

[36] J. Hu, X. Chen, Y. Zhang, Batch fabrication of formaldehyde sensors based on LaFeO3 thin film with ppb-level detection limit, Sens Actuators B Chem 349 (2021) 130738. https://doi.org/10.1016/j.snb.2021.130738.

[37] T. Das, S. Mojumder, S. Chakraborty, D. Saha, M. Pal, Beneficial effect of Sn doping on bismuth ferrite nanoparticle-based sensor for enhanced and highly selective detection of trace formaldehyde, Appl Surf Sci 602 (2022). https://doi.org/10.1016/j.apsusc.2022.154340.

[38] J. Zhang, Y.M. Zhang, C.Y. Hu, Z.Q. Zhu, Q.J. Liu, A Formaldehyde Gas Sensor Based on Zinc Doped Lanthanum Ferrite, Adv Mat Res 873 (2013) 304–310. https://doi.org/10.4028/www.scientific.net/AMR.873.304.

[39] Y.M. Zhang, Y.T. Lin, J.L. Chen, J. Zhang, Z.Q. Zhu, Q.J. Liu, A high sensitivity gas sensor for formaldehyde based on silver doped lanthanum ferrite, Sens Actuators B Chem 190 (2014) 171–176. https://doi.org/10.1016/j.snb.2013.08.046.

[40] Y. Tie, S.Y. Ma, S.T. Pei, Q.X. Zhang, K.M. Zhu, R. Zhang, X.H. Xu, T. Han, W.W. Liu, Pr doped BiFeO3 hollow nanofibers via electrospinning method as a formaldehyde sensor, Sens Actuators B Chem 308 (2020) 127689. https://doi.org/10.1016/j.snb.2020.127689.

[41] N. Zhang, S. Ruan, F. Qu, Y. Yin, X. Li, S. Wen, S. Adimi, J. Yin, Metal–organic framework-derived Co3O4/CoFe2O4 double-shelled nanocubes for selective detection of sub-ppm-level formaldehyde, Sens Actuators B Chem 298 (2019) 126887. https://doi.org/10.1016/j.snb.2019.126887.

[42] T. Das, S. Das, M. Karmakar, S. Chakraborty, D. Saha, M. Pal, Novel barium hexaferrite based highly selective and stable trace ammonia sensor for detection of renal disease by exhaled breath analysis, Sens Actuators B Chem 325 (2020). https://doi.org/10.1016/j.snb.2020.128765.

[43] T. Das, S. Mojumder, S. Chakraborty, D. Saha, M. Pal, Beneficial effect of Sn doping on bismuth ferrite nanoparticle-based sensor for enhanced and highly selective detection of trace formaldehyde, Appl Surf Sci 602 (2022). https://doi.org/10.1016/j.apsusc.2022.154340.

[44] M. Wang, T. Wang, S.H. Song, M. Ravi, R.C. Liu, S.S. Ji, Effect of calcination temperature on structural, magnetic and optical properties of multiferroic YFeO3 nanopowders synthesized by a low temperature solid-state reaction, Ceram Int 43 (2017) 10270–10276. https://doi.org/10.1016/j.ceramint.2017.05.056.

[45] F. Mukhtar, T. Munawar, M.S. Nadeem, M. Naveed ur Rehman, S.A. Khan, M. Koc, S. Batool, M. Hasan, F. Iqbal, Dual Z-scheme core-shell PANI-CeO2-Fe2O3-NiO heterostructured nanocomposite for dyes remediation under sunlight and bacterial disinfection, Environ Res 215 (2022) 114140. https://doi.org/10.1016/j.envres.2022.114140.

[46] F. Mukhtar, T. Munawar, M.S. Nadeem, S.A. Khan, M. Koc, S. Batool, M. Hasan, F. Iqbal, Enhanced sunlight-absorption of Fe2O3 covered by PANI for the photodegradation of organic pollutants and antimicrobial inactivation, Advanced Powder Technology 33 (2022) 103708. https://doi.org/10.1016/j.apt.2022.103708.

[47] Y. Li, Y. Ma, Z. Wang, H. Liu, X. Wang, Y. Dong, W. Qian, Morphologically distinctive YFeO3 with near-infrared reflection and ferromagnetic characteristics, Journal of Materials Science: Materials in Electronics 33 (2022) 11318–11331. https://doi.org/10.1007/s10854-022-08105-z.

[48] C.-C. Wang, W.-T. Yu, Synthesis of yttrium iron garnet using polymer–metal chelate precursor, J Colloid Interface Sci 306 (2007) 241–247. https://doi.org/10.1016/j.jcis.2006.10.039.

[49] L. Wu, J.C. Yu, L. Zhang, X. Wang, S. Li, Selective self-propagating combustion synthesis of hexagonal and orthorhombic nanocrystalline yttrium iron oxide, J Solid State Chem 177 (2004) 3666–3674. https://doi.org/10.1016/j.jssc.2004.06.020.

[50] K. Wu, Y. Lu, Y. Liu, Y. Liu, M. Shen, M. Debliquy, C. Zhang, Synthesis and acetone sensing properties of copper (Cu2+) substituted zinc ferrite hollow micro-nanospheres, Ceram Int 46 (2020) 28835–28843. https://doi.org/10.1016/j.ceramint.2020.08.049.

[51] S. Mojumder, T. Das, S. Das, N. Chakraborty, D. Saha, M. Pal, Y and Al co-doped ZnO-nanopowder based ultrasensitive trace ethanol sensor: A potential breath analyzer for fatty liver disease and drunken driving detection, Sens Actuators B Chem 372 (2022). https://doi.org/10.1016/j.snb.2022.132611.

[52] H. Liu, T. Miao, W. Liu, J. Chen, B. Cheng, H. Qin, J. Hu, Highly sensitive acetone gas sensor based on YFeO3 planar electrode under multi-wavelength light illumination, Mater Lett 333 (2023) 133596. https://doi.org/10.1016/j.matlet.2022.133596.

[53] A.B.G. Trabelsi, K. V. Chandekar, Fatemah.H. Alkallas, I.M. Ashraf, J. Hakami, Mohd. Shkir, A. Kaushik, S. AlFaify, A comprehensive study on Co-doped CdS nanostructured films fit for optoelectronic applications, Journal of Materials Research and Technology 21 (2022) 3982–4001. https://doi.org/10.1016/j.jmrt.2022.11.002.

[54] K. V. Chandekar, T. Alshahrani, A. Ben Gouider Trabelsi, F.H. Alkallas, Mohd. Shkir, S. AlFaify, Novel rare earth yttrium doping effect on physical properties of PbS nanostructures: facile synthesis and characterization, J Mater Sci 56 (2021) 4763–4781. https://doi.org/10.1007/s10853-020-05539-w.

[55] Mohd. Shkir, Z.R. Khan, K. V. Chandekar, T. Alshahrani, I.M. Ashraf, A. Khan, R. Marnadu, R.A. Zargar, P. Mohanraj, M.S. Revathy, M.A. Manthrammel, M.A. Sayed, H.E. Ali, I.S. Yahia, E.S. Yousef, H. Algarni, S. AlFaify, M.F. Sanaa, Facile fabrication of Ag/Y:CdS/Ag thin films-based photodetectors with enhanced photodetection performance, Sens Actuators A Phys 331 (2021) 112890. https://doi.org/10.1016/j.sna.2021.112890.

[56] K. V. Chandekar, Mohd. Shkir, A. Khan, M.A. Sayed, N. Alotaibi, T. Alshahrani, H. Algarni, S. AlFaify, Significant and systematic impact of yttrium doping on physical properties of nickel oxide nanoparticles for optoelectronics applications, Journal of Materials Research and Technology 15 (2021) 2584–2600. https://doi.org/10.1016/j.jmrt.2021.09.072.

[57] S. Chakraborty, M. Pal, Highly selective and stable acetone sensor based on chemically prepared bismuth ferrite nanoparticles, J Alloys Compd 787 (2019) 1204–1211. https://doi.org/10.1016/j.jallcom.2019.02.153.

[58] J. Yang, W. Han, J. Ma, C. Wang, K. Shimanoe, S. Zhang, Y. Sun, P. Cheng, Y. Wang, H. Zhang, G. Lu, Sn doping effect on NiO hollow nanofibers based gas sensors about the humidity dependence for triethylamine detection, Sens Actuators B Chem 340 (2021). https://doi.org/10.1016/j.snb.2021.129971.

[59] Z. Wang, H. Zhou, D. Han, F. Gu, Electron compensation in p-type 3DOM NiO by Sn doping for enhanced formaldehyde sensing performance, J Mater Chem C Mater 5 (2017) 3254–3263. https://doi.org/10.1039/c7tc00226b.

[60] H. Gao, D. Wei, P. Lin, C. Liu, P. Sun, K. Shimanoe, N. Yamazoe, G. Lu, The design of excellent xylene gas sensor using Sn-doped NiO hierarchical nanostructure, Sens Actuators B Chem 253 (2017) 1152–1162. https://doi.org/10.1016/j.snb.2017.06.177.

[61] P. Rana, M. Narjinary, A. Sen, M. Pal, Beneficial effect of Pd and MWCNT co-loading in SnO_2 nanoparticles towards the low temperature detection of *n* -butane gas: synergistic effect on sensing performance, Sensors & Diagnostics 2 (2023) 909–917. https://doi.org/10.1039/D3SD00056G.

[62] N. Chakraborty, S. Mondal, Dopant-mediated surface charge imbalance for enhancing the performance of metal oxide chemiresistive gas sensors, J Mater Chem C Mater 10 (2022) 1968–1976. https://doi.org/10.1039/D1TC05144J.

CHAPTER-VI

Development of Highly Sensitive and Selective Trace Acetone Sensor Using Perovskite Yttrium Ferrite: Mechanism, Kinetics and Phase Dependence Study

Work is published in "Chemical Engineering Journal 477 (2023) 146855"

6.1 Introduction

Human exhale breath contains more than 1000 volatile organic compound (VOCs) and gases among which acetone is recognized as biomarker for diabetes. It's a life threating disease and throughout globe millions of people are suffering from diabetes. Detection and monitoring of exhale breath is very much required to save human life. Investigation shows that acetone vapor concentration in exhaled-breath of healthy person varies between 300-900 ppb which would increase to 1.8 ppm for mild-diabetic person and person with severe diabetic state amount of acetone vapour in exhaled breath could rise up to 10 ppm [1-4]. Again, acetone is also a by-product of lipolysis which can be used to track fat metabolism during diets or in different health conditions [5]. Furthermore, acetone is widely used as organic solvent in several industries like plastic, paint, rubber etc. Prolonged exposure to high acetone concentration environment could cause damage in liver, kidney and pancreas of healthy human body [6-7]. So, there is immense importance to develop a highly selective, sensitive acetone sensor which could sense ppb level acetone in presence of other interfering VOCs with significant resolution in the range of 300ppb -10ppm gas concentration.

Though different sophisticated techniques like gas chromatography-mass spectrometry (GC–MS), selected-ion flow tube mass spectrometry (SIFT-MS), ion mobility spectrometry (IMS), Proton Transfer Reaction-Mass Spectrometry (PTR-MS) could analyse the low concentration VOCs with sufficient precision, however they are not cost effective, bulk in size, needs skilled manpower and not suitable for portable use for real-time study [8-10]. One of the alternative ways to measure the concentration of VOCs semiconductor metal oxide (SMO) based chemiresistive gas sensors. Recent past SMO based gas sensors have gained immense research interest owing to their low production cost, easy processability, chemical versatility, good electrical properties, portability, and ease of chip-level integration [11,12]. Several SMO sensors based on ZnO [13-15], SnO_2 [16-18], In_2O_3 [19-21], MoO_3 [22-23], WO_3 [24], and α-Fe_2O_3 [25] have been explicitly explored for detection of acetone in exhaled human breath. However, gas sensing performance such as sensitivity, selectivity, response in different humid back ground, long term stability of these well explored binary metal oxide (A_xO_y) based sensors are not up to the mark for real-life applicability. Therefore, it is the need of the hour to extend research activity beyond these conventional binary metal oxide towards higher order oxides for better sensing performance.

Recently, perovskite type materials have gained enormous attention in the field of chemiresistive gas sensing due to their high thermal stability, narrow band gap, and high crystallinity. Moreover, valency control properties of the perovskite structure give an edge to these group of materials for showing better surface catalytic activity. Perovskites have a special structure of ABO_3 kind that exhibits flexibility in composition based on their A-site rare-earth or alkaline-earth metals, and B-site transition metals. Recent studies show that, among various perovskite structure perovskite ferrites are more responsive towards acetone vapour [26-39]. Generally, these perovskite ferrites have different phases which primarily depend on the synthesis conditions, presence of specific precursor and chelating agent during synthesis and the calcination temperature. Though there are ample number of reports in literature on acetone sensing behaviour of the perovskite ferrites ($AFeO_3$). However, to the best of our knowledge no literature is available on the details study on how different phases of these type of perovskite ferrites affect the acetone sensing phenomenon. Kinetics of the reactions take place over these types of materials have not been studied properly during the change of resistance in presence of certain VOCs and the ambient oxygen. Moreover, the reason behind greater response of a particular phase of $AFeO_3$ type materials towards acetone is not even explored till date. Also, no literature is available to the best of authors' knowledge on gas sensing behaviour of perovskite yttrium ferrite ($YFeO_3$).

In this work, highly sensitive and selective acetone sensors based on $YFeO_3$ are fabricated as a potential exhaled breath analyser for diabetes. With increasing sintering temperature hexagonal- $YFeO_3$ (YF-7) gradually transferred into orthorhombic- $YFeO_3$ (YF-10), as demonstrated by X-ray diffraction (XRD) and high-resolution transmittance electron microscopy (HRTEM). Orthorhombic $YFeO_3$ (YF-10) shows maximum response of 7.9 folds p-type response towards 0.5 ppm acetone vapour at 300ºC which in nearly 2.7 times higher than that of hexagonal $YFeO_3$ (YF-7) sensor. Detail XPS analysis indicates that phase transition causes generation of multiple co-existing host oxidation states in $YFeO_3$, making the charge imbalance in the host cationic instability which leads to enhanced surface reaction. Moreover, acetone sensing mechanism of orthorhombic $YFeO_3$ in the atomic scale is theoretically explained using density functional theory (DFT) simulations. In order to analyze the adsorption characteristics of the acetone gas molecule on $YFeO_3$, the quantitative charge transfer between the substrate and adsorbed molecule has been shown using the Bader charge analysis and planar averaged charge density calculations. The enhancement in acetone sensing performance of orthorhombic $YFeO_3$ over hexagonal $YFeO_3$ is explicitly explained by the change in

adsorption energy of acetone on orthorhombic $YFeO_3$ in comparison with the hexagonal phase. Further sensing kinetic analysis has been performed adopting Eley−Rideal model over the active surface of the sensor assuming that analyte molecules react with oxygen ions directly without fast adsorbing over the sensing surface. The kinetic parameters of the surface reactions such as sensitivity value (η), kinetic reaction rate (κr) and activation energy are determined which are used to discriminate between multiple interfering gases. Above theoretical modelling was used to explain the greater sensitiveness of $YFeO_3$ sensor towards acetone. Finally, sensing performance of YF-10 was measured with simulated breath samples which delineates the potential of YF-10 sensor as commercial breath acetone analyzer.

6.2 Materials and methods

6.2.1 Materials

Yttrium(III) nitrate hexahydrate ($Y(NO_3)_3.6H_2O$), iron(III) nitrate nonahydrate ($Fe(NO_3)_3.9H_2O$), and citric acid ($C_6H_8O_7$) were procured from Sigma-Aldrich and used directly as precursors to prepare YFO particles without further treatment.

6.2.2 Synthesis of yttrium ferrite powder

Pure perovskite, well-crystallized yttrium ferrite particles was synthesized using low temperature solution combustion process. $Y(NO_3)_3,6H_2O$, $Fe(NO_3)_3,9H_2O$ and citric acid were dissolved in deionized water in 1:1:2 molecular ratio under magnetic stirring at room temperature. Citric acid was used as complexing agent in aqueous solution for the formation of $YFeO_3$. The mixture was kept on continuous stirring at 100º C until all solvent gets evaporate and the solution converted into xerogel. Within a few minutes after completion of the combustion reaction a brown ash of the burnt dung was formed. The brunt brown ash was pre-fired at 300°C for 2h for preparing the precursor material. Finally, the floppy brown powder was ground in agate mortar and annealed in air at 600, 700, 800, 1000 and 1200 °C for 5h respectively, to obtain $YFeO_3$ powder which were named as YF-6, YF-7, YF-8, YF-10 and YF-12 respectively. The synthesis procedure is shown in Fig. 6. 1 (a) schematically.

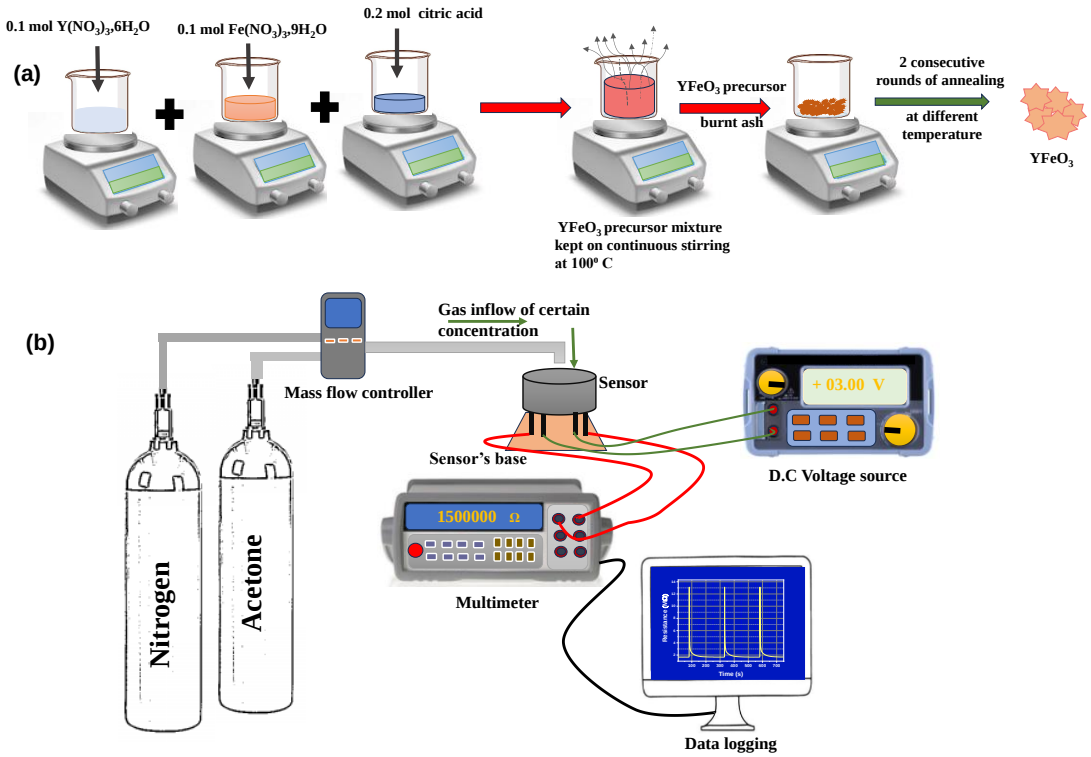

Fig. 6. 1. (a) Schematic of synthesis procedure of $YFeO_3$**.** (b) Schematic presentation of gas measurement setup.

6.2.3 Materials Characterization

The phase purity and crystal structure of the as-synthesized material was primarily examined using a X'pert pro MPD (PANanalytical) diffractometer system with Cu Kα incident radiation (λ=1.54056 Å, 20°-80°). Sample morphologies were observed using field emission scanning electron microscope (FESEM, Carl Zeiss Supra 35 V P microscope). Energy Dispersive X-ray (EDX) studies were performed on the sample using the same FESEM instrument to determine the composition of all the samples. Microstructural composition and selected area electron diffraction (SAED) pattern of the samples were analysed by high resolution transmission electron microscopy (TEM, FEI Tecnai G2 30ST instrument operated at 300 kV. Specific surface area of the samples was measured by Brunauer-Emmett-Teller study using NovaWin, Quantachrome Instrument. Optical bandgap was determined by using UV-Vis-NIR spectrometer (Shimadzu, UV-3600). Room temperature Photo-luminescence (PL) spectroscopic studies were conducted by a Fluoro Max-P (HORIBA Jobin Yvon) luminescence spectrophotometer. Study of Raman spectroscopy was conducted by Renishaw InVia

spectrophotometer using laser excitation of 514 nm. The oxidation states of the elements were analysed by X-ray photoelectron spectroscopy (XPS) using PHI 5000 Versa Probe II scanning XPS microprobe (ULVAC-PHI, U.S) with monochromatic AlKα (hv=1486.6 eV) radiations. Deconvolution of Y 3d, Fe 2p and O 1s core level spectra were carried out using peak fitting program (XPS-PEAK 4.1) by a combination of Gaussian–Lorentzian functions with the Shirley algorithm fitted background. Agilent B2901A precision source and the measurement unit were used to analyse electrical properties of the sensors by means of current-voltage (I-V) the measurement. Dynamic gas response and recovery characteristics of the as fabricated chemiresistive sensors were measured using a Keysight 34470A digital multimeter by virtue of measuring the change in resistance of the functional material.

6.2.4 Fabrication of the sensor prototypes

At first nearly 0.15 gm of as prepared materials (viz. YF-7,YF-8,YF-10,YF-12) were pestle with isopropanol to form a slurry paste. Subsequently the paste was coated on alumina tube (of length 3.2 nm, outer radius 0.5 mm and inner radius 0.25 mm) preassembled with Au-Pt electrodes (gold was used to create the electrode and Pt-wires were joined with the gold electrodes to establish the electrical contact). Next, the coated sensor substrates were kept at 100 ºC for 12 h for ageing. A Ni-Cr alloy was implanted through the hollow alumina substrate as joule's heating coil to modulate the operating temperature of the sensor. Finally, the sensor substrate along with the heating coil were welded onto a sensor socket having six pins. Schematic of the sensor fabrication procedure is shown in earlier reports [40-42].

6.2.5 Gas preparation and gas sensing measurement

Gas sensing measurements were performed in ambient air environment. Commercially available N_2 balanced acetone cylinder was used for measuring the sensing response of all the YFO based sensors and necessary dilutions of the acetone gas was performed using a Alicat made Mass Flow Controller (MFC) system by mixing required amount of nitrogen with the acetone gas. The entire gas sensing procedure is shown schematically in Fig. 6. 1(b). Similar process had been followed for measuring the response of YF based sensor towards other gases like Ammonia, CO, Formalin, Ethanol. The resistance of the sensing material increases in the gaseous environment (R_{gas}) with respect to its base resistance in ambient environment (R_{air}). Thus, gas sensing response was defined as follows,

$$S_{sensor} = R_{gas}/R_{air} \quad (1)$$

The response-recovery time was calculated as the time taken by the sensor to achieve 90% of the total resistance change in presence of and absence of certain gas respectively [43].

6.2.6 Computational Details

The First principles based density functional theory (DFT) has been carried out using the Vienna ab initio simulation package (VASP). To describe the electron exchange correlation, Perdew–Burke–Ernzerhof (PBE) within generalized gradient approximation (GGA) has been employed. The projector augmented wave (PAW) approach has been considered to take care of electron-ion interaction [44,45]. A plane wave basis set cut-off energy of 550 eV has been taken. The crystal structure has been relaxed taking care of the convergence criteria of energy ~ 10^{-5} eV and force ~ 0.02 eV/Å. In order to sample the 2D Brillouin zone, Monkhorst–Pack k-point mesh values of 5 × 5 × 1 has been used for geometry optimizations.

6.3 Results and discussion

6.3.1 Materials characterization

6.3.1.1 Structural and quantitative phase analysis

XRD patterns of as-synthesized $YFeO_3$ powders sintered at various temperatures are shown in Fig. 6. 2(a). Variation of crystallinity and growth of phases with varying sintering temperature are reflected in the XRD pattern. A broad XRD peak around 2θ=30º-35º indicates the amorphous nature for YF-6 sample. As sintering temperature increases from 600ºC to 700ºC crystallinity appears. All the XRD peaks for YF-7 samples matches well with hexagonal perovskite structure (ICDD card no.-00-048-0529) and no other peaks for any impurity is observed. Which indicates the formation of pure hexagonal $YFeO_3$ phase when calcined at 700ºC. With further increase in calcination temperature to 800ºC hexagonal phase appears to transformed to orthorhombic phase. Majority of the diffraction peaks for YF-8 sample can be indexed with orthorhombic $YFeO_3$ structure (ICDD-04-015-9132) and few peaks corresponding to hexagonal structure (ICDD-00-048-0529) indicating the formation of mixed phase at 800ºC temperature. All the diffraction peaks of YF-10, calcined at 1000 ºC matched well with orthorhombic perovskite structure (ICDD-04-015-9132). No other diffraction peaks corresponding to hexagonal phase or any other impurity phase were found which confirm the complete transformation to orthorhombic phase. However, with further increase in calcination temperature to 1200ºC, for YF-12 sample apart from the major orthorhombic $YFeO_3$ peaks

some very minor peaks corresponding to secondary phase $Y_3Fe_5O_{12}$ (ICDD-01-077-1998) are observed in the 2θ range from 25º to 36º. Presence of peaks corresponding to different crystal phase in XRD pattern in YF-7, YF-8, YF-10, YF-12 sample in the 2θ range from 25º to 36º is shown in the Fig. 6. 2(b).

To understand the phase transformation of $YFeO_3$ with calcination temperature quantitative phase analysis has been performed using Xpert High score plus software combined with the PDF-4+ database, from Rietveld refinement. All the refinable parameters were adjusted until the best fit of entire XRD pattern was achieved. Rietveld refinement method was used to calculate phase composition (wt%) for each identified phases in different samples according to the following equation,

$$W_P = S_P(ZMV)_P / \sum_{i=1}^{n} S_i(ZMV)_i \quad (2)$$

Where, W_P is the phase composition (% wt) of each identified phase: p; S is scale factor as derived from the Rietveld phase analysis, Z is number of formula units per unit cells; M is mass of the formula unit; and V is volume of the unit-cell (in Å) [46-48]. As calculated phase composition of Hexagonal or orthorhombic phase of $YFeO_3$ or secondary phase $Y_3Fe_5O_{12}$ in YF-7, YF-8, YF-10 and YF-12 samples are listed in Table- 6. 1 and refined XRD plot of YF-10 sample is shown in Fig. 6. 2(c). The result of quantitative phase analysis indicates that hexagonal $YFeO_3$ phase is metastable in nature which slowly transformed into thermodynamically more stable orthorhombic $YFeO_3$ phase at 1000ºC. Again, with further increase in calcination temperature a secondary phase ($Y_3Fe_5O_{12}$) started to form at 1200ºC. The crystallite size of the different samples were estimated using Debye-Scherer's formula which demonstrated a monotonic increase in average crystallite size from 8.2 nm to 36.7 nm with increasing calcination temperature (ref. Table 1)

6.3.1.2 Microstructural analysis

The morphologies of the as prepared samples were observed using FESEM, TEM and HRTEM. FESEM study was carried out at different magnification powers. The low magnified SEM images of YF-7, YF-8, YF-10, YF-12 are presented in Fig. 6. 3(a-d) which indicate the formation of porous structure. As calcination temperature increases from 700ºC to 1000ºC pores appeared to form regular hexagonal shape which apparently resembled a honeycomb. A porous structure was started to generate in relatively lower calcination temperature in YF-7 sample whereas the porous nature of the material was significantly increased in YF-10 sample and prominent honeycomb like shape was also formed in YF-10 sample. With further increase

in temperature the honeycomb structure started to collapse resulting in deformation of regular honeycomb shapes for YF-12. Formation of honeycomb morphology can be attributed to Ostwald ripening process. Nanoparticles formed in lower temperature in the beginning of the reaction get gradually cross-linked to form honeycomb like structure due the longer calcination period (5h at 1000ºC) at the cost of nanoparticles. During the solution combustion synthesis process pH of the precursor solution was kept at low value which helps in fast crystal growth that results in large crystal size of the prepared yttrium ferrite powders. A dichotomy between nucleation and crystal growth decides the final shape and size of the end product [49,50]. Fig. 6. 3(e, f) shows highly magnified SEM images of YF-10 materials which presents a clear, honeycomb-like structure where each side was surrounded by six hexagonal pores. Again, in Fig. 6. 3(g) inner wall of the pores are shown which resembles the roughness of the surface of the YF-10 material.

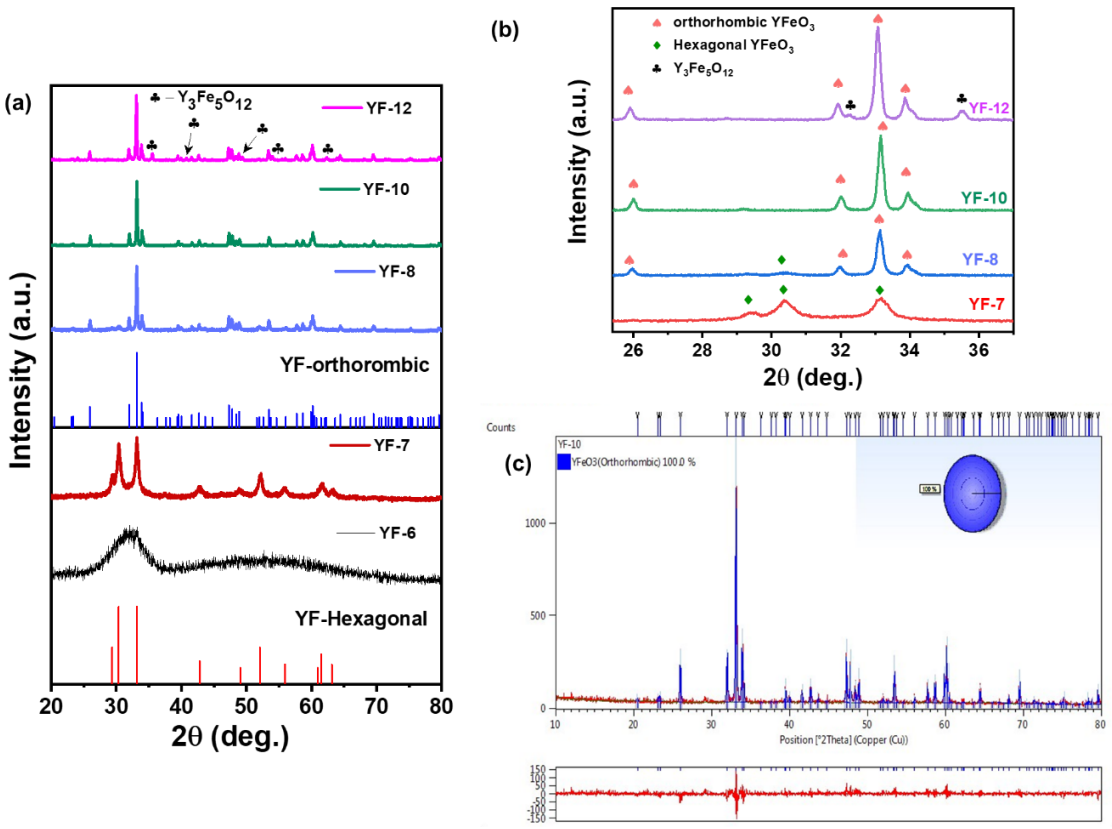

Fig. 6. 2. (a) XRD patterns of $YFeO_3$ sintered at different temperatures. The peak positions in reference diffraction patterns of the hexagonal (ICDD-00-048-0529) and orthorhombic (ICDD-04-015-9132) $YFeO_3$, secondary phase $Y_3Fe_5O_{12}$ (ICDD-01-077-1998) are also indicated by gray and black lines, respectively. (b) correspondingly magnified XRD patterns around 2θ = 25º-36º. (c) Refined XRD plot of YF-10 sample using Xpert High scrore plus software.

Table- 6. 1: Quantitative Crystal phase percentage (%) of all Samples along with Energy band gap, BET and XPS Results

Sample		**YF-7**	**YF-8**	**YF-10**	**YF-12**
Quantitive Crystal phase percentage (%)	$YFeO_3$(Hexagonal)	100	16.4	0	0
	$YFeO_3$(Orthorhombic)	0	83.6	100	97.8
	$Y_3Fe_5O_{12}$(Cubic)	0	0	0	2.2
Average crystallite size (nm)		8.2	27.8	31.2	36.7
Specific surface area (m^2/g)		4.29	4.76	5.85	5.28
Primary bandgap (eV)		2.61	2.56	2.50	2.38
Surface electronic states details	O_L (Lattice oxygen)	82.8%	61.9%	34.9%	40.0%
	O_D (Defect Oxygen)	13.7%	34.1%	56.2%	55.5%
	O_C (Chemiabsorbed Oxygen)	3.5%	4.0%	8.9%	4.5%
	Fe^{3+}: Fe^{2+} ratio (in percentage)	87.9:12.1	82.3:17.7	71.9:28.1	79.3:20.7

EDS spectrum of YF-10 sample indicates the presence of Y, Fe, O in the synthesized material (ref. Fig. 6. 3 (h)) and no other impurity peaks was found in the sample which confirms the purity of the synthesized material. Elemental composition of as synthesized hexagonal (YF-7) and orthorhombic (YF-10) yttrium ferrites were also studied from EDX spectroscopy using FESEM. As shown in Fig. 6. 4 (a)-(h) the EDX colour mapping of YF-7 (ref. Fig. 6. 4 (a)-(d))and YF-10 (ref. Fig. 6. 4 (e)-(h)) indicate that yttrium, iron and oxygen are distributed homogeneously in both the samples.

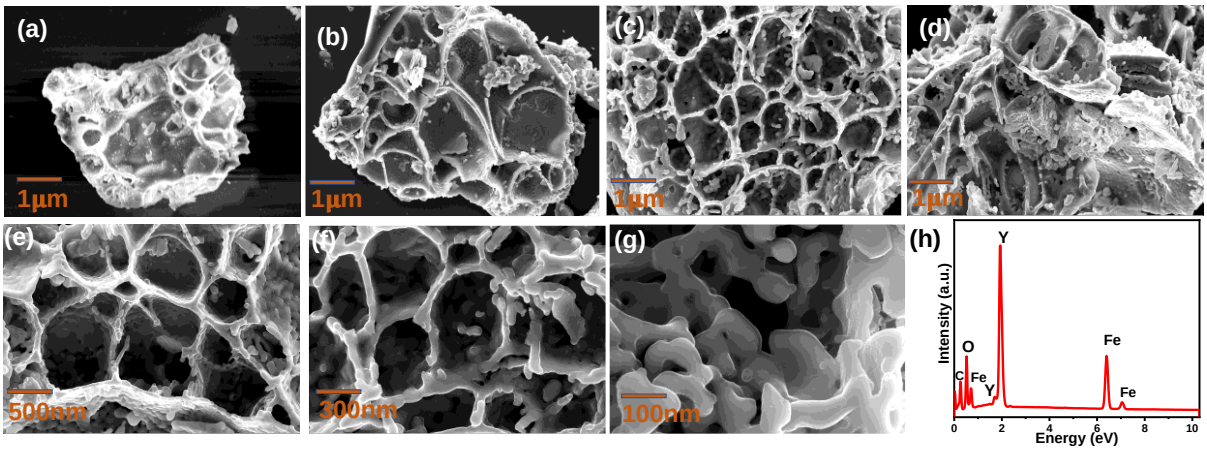

Fig. 6. 3. FESEM images of (a) YF-7, (b) YF-8, (c) YF-10, (d) YF-12. (e-g) FESEM images of YF-10 sample in higher magnification. (h) EDS spectrum of YF-10 sample.

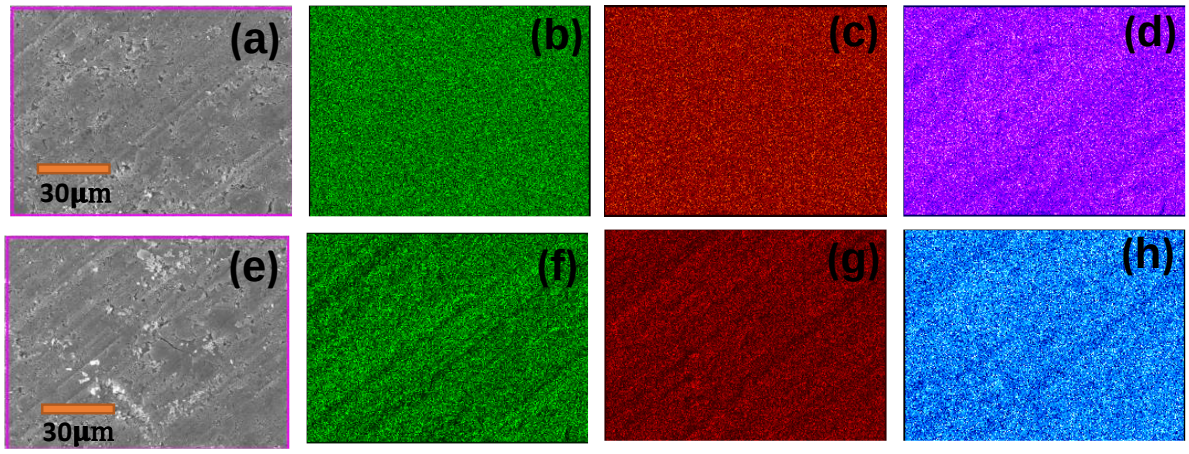

Fig. 6. 4. (a) FESEM image of the selected mapping area of YF-7 and the corresponding EDX colour mapping of (b) O, (c) Fe, (d) Y. (e) FESEM image of the selected mapping area of YF-10 and the corresponding EDX colour mapping of (f) O, (g) Fe, (h) Y.

The similar trend of formation of porous honeycomb like microstructures with increasing calcination temperature as observed in FESEM study, can also be noticed in the corresponding TEM images as shown in Fig. 6. 5 (a) and Fig. 6. 5 (d). Simultaneously, Selected area electron diffraction (SAED) and HRTEM images of YF-7 and YF-10 sample were analysed to verify the structure of prepared materials. Individual SAED of the YF-7 (ref. Fig. 6. 5 (b)) exhibit the (101), (102), (110) crystal planes of hexagonal $YFeO_3$. SAED pattern YF-10 (ref. Fig. 6. 5 (e)) could be indexed as (111), (121) (123) and (131) crystal surface corresponding to orthorhombic yttrium ferrite lattice. Thus, SAED pattern of YF-7 and YF-10 samples indicate the hexagonal

phase and orthorhombic phase of yttrium ferrite was formed respectively which perfectly matches with the XRD results. Interplanar spacing was also calculated from the HRTEM images of both YF-7 and YF-10 sample. As shown in the Fig. 6. 5 (c) interplanar spacing is measured to be 2.9 Å for YF-7 sample which is corresponding to the (101) plane of the hexagonal yttrium ferrite (ICDD card no.-00-048-0529) whereas in Fig. 6. 5 (f) interplanar spacing of YF-10 is measured to be 3.4 Å which is attributed to the (111) plane of the orthorhombic yttrium ferrite (ICDD-04-015-9132).

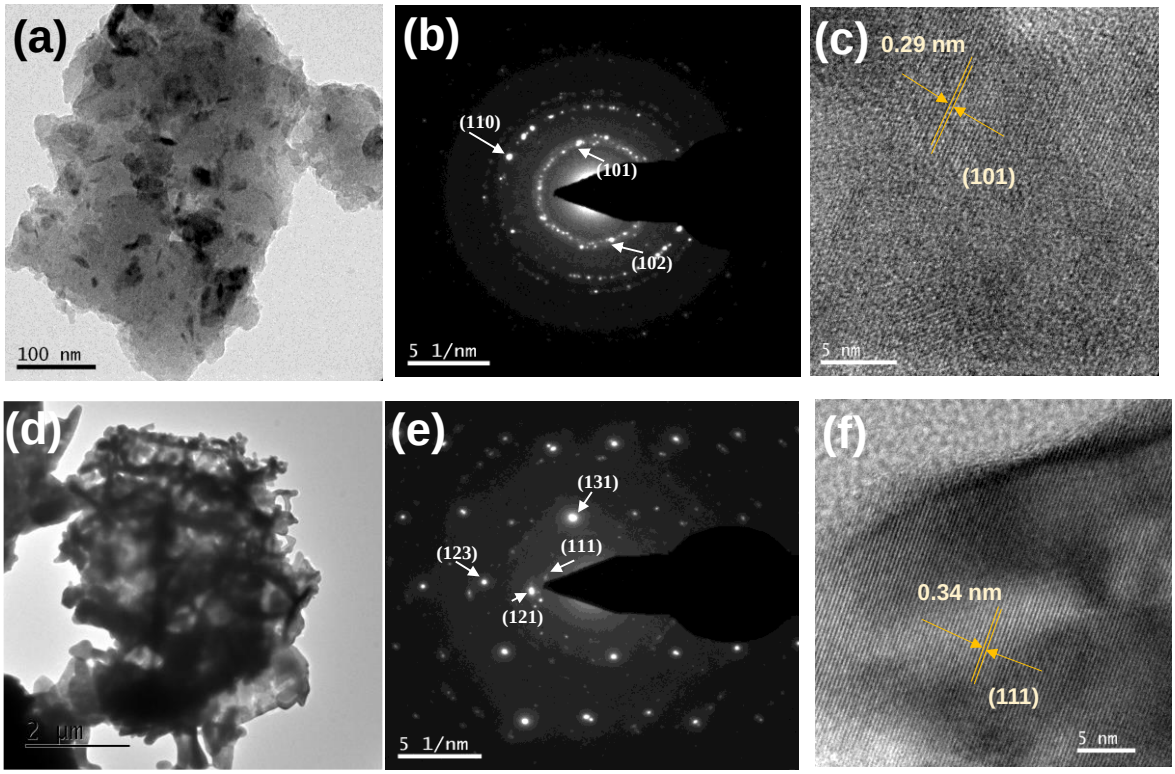

Fig. 6. 5. (a) TEM image of YF-7 sample. (b) SAED pattern of YF-7. (c) HRTEM images of YF-7 corresponding to (101) plane. (d) TEM image of YF-10 sample. (e) SAED pattern of YF-10. (f) HRTEM images of YF-10 corresponding to (111) plane.

6.3.1.3 Investigation on surface electronic states

Surface chemical compositions of all the samples were analysed by XPS study. Fig. 6. 6 (a) shows the wide scan spectra of YF-7, YF-8, YF-10, YF-12 samples which confirms the presence of Y, Fe, O in all the synthesized samples. Two peaks around 156.6 eV and 158.6 eV in the high-resolution XPS spectra for all three samples are identified as Y $3d_{5/2}$ and Y $3d_{3/2}$ of the Y 3d state, respectively [51]. The difference in energy of these two characteristic peaks of

Y 3d is nearly 2 eV, which indicates the presence of both Y^{3+} ion and Y–O bond in the synthesized materials, as presented in Fig. 6. 6 (b,e,h,k). High resolution XPS spectra of Fe 2p electronic state of all three samples are shown in Fig. 6. 6 (c,f,i,l). Two characteristic peaks of Fe $2p_{3/2}$ and Fe $2p_{1/2}$ around the binding energy of 710.8eV and 724.4 eV respectively could be assigned to the Fe–O bond. The signal peak at binding energy position 8.4eV higher than the principal Fe $2p_{3/2}$ peak is ascribed to the Fe^{3+} species [51,52]. Owing to the presence of the half-filled d orbital in Fe. Two distinct deconvoluted peaks are appeared in both the Fe $2p_{3/2}$ and Fe $2p_{1/2}$ which manifests that the oxidation state of the Fe element in the synthesized yttrium ferrite powder is comprised of Fe^{2+} and Fe^{3+} species [53]. As shown in Fig. 6. 6 (d,g,j,m), the high resolution XPS spectra of O1s are asymmetric in nature and can be deconvoluted in three characteristics peaks around 529.3 ± 0.6 eV, 530.1 ± 0.4 eV and 532.4 ± 0.3 eV, which are corresponding to O^{2-} ion in Y– O and Fe–O bonds of the yttrium ferrite structure (commonly known as lattice oxygen (O_L)), O defects (O_D), and chemisorbed oxygen (O_C), respectively [50,54,55]. Relative percentages of all the deconvoluted peaks (viz. Fe^{2+}, Fe^{3+}, O_L, O_D, O_C) in YF-7, YF-10, YF-12 are shown in Table 1.

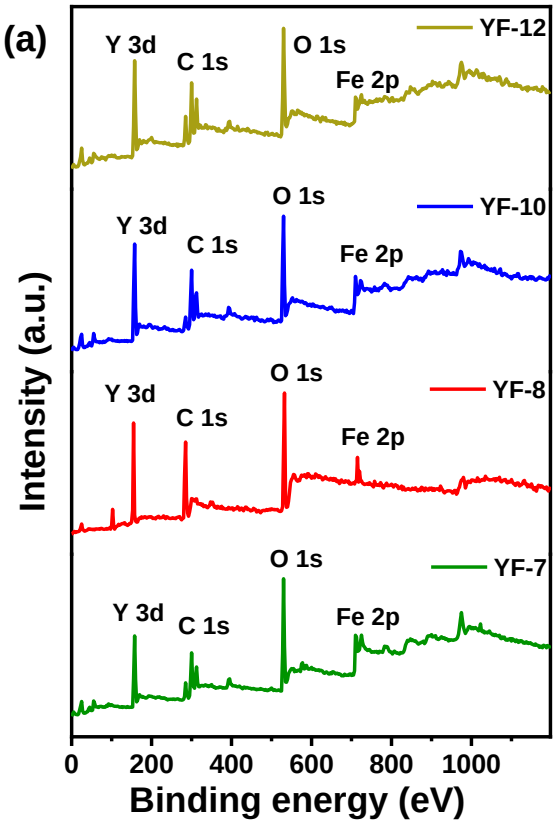

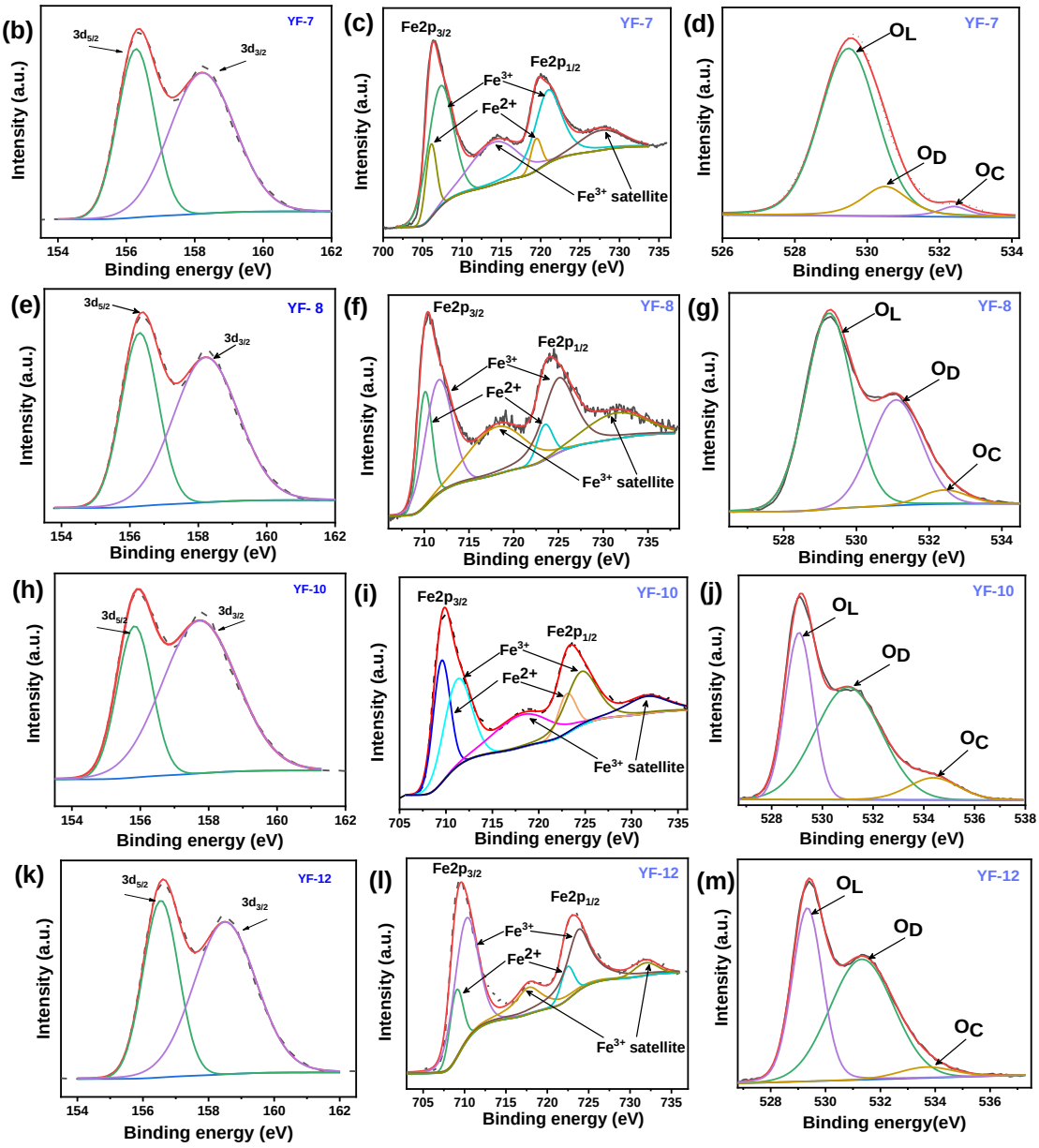

Fig. 6. 6. (a) XPS survey spec tra of YF-7. YF-10, YF-12. HR-XPS spectra corresponding to the Y 3d core-level of (b) YF-7, (e) YF-8, (h) YF-10, (k) YF-12. Fe 2p core-level of pure (c) YF-7, (f) YF-8, (i) YF-10, (l) YF-12. O1s core-level of (d) YF-7, (g) YF-8, (j) YF-10, (m) YF-12.

Electron paramagnetic resonance (EPR) spectra were utilized to confirm the existence of oxygen vacancies in all the materials as shown in Fig. 6. 7 (a). In all YF samples, the symmetrical signal at g = 2.01 was seen. Additionally, the oxygen vacancies signal strength rises from YF-7 to YF-8, reaches a maximum at YF-10, and then continues to fall at YF-12. The EPR study also delineates that YF-10 sample poses maximum oxygen vacancies [56,57].

6.3.1.4 BET surface area analysis

Specific surface area of the prepared samples was estimated from BET surface area study and delineated in Fig. 6. 7 (b). BET study reveals that with formation of porous honeycomb morphology with increasing calcination temperature from 800 ºC to 1000 ºC specific surface area also increases from 4.29 m^2/g (YF-7), 4.76 m^2/g (YF-8) to 5.85 m^2/g (YF-10). Again, for YF-12 sample surface area tends to decrease (5.28 m^2/g) as distortion in hexagonal morphology was observed at this temperature. Though the variation in surface area with varying calcination temperature is not very significant.

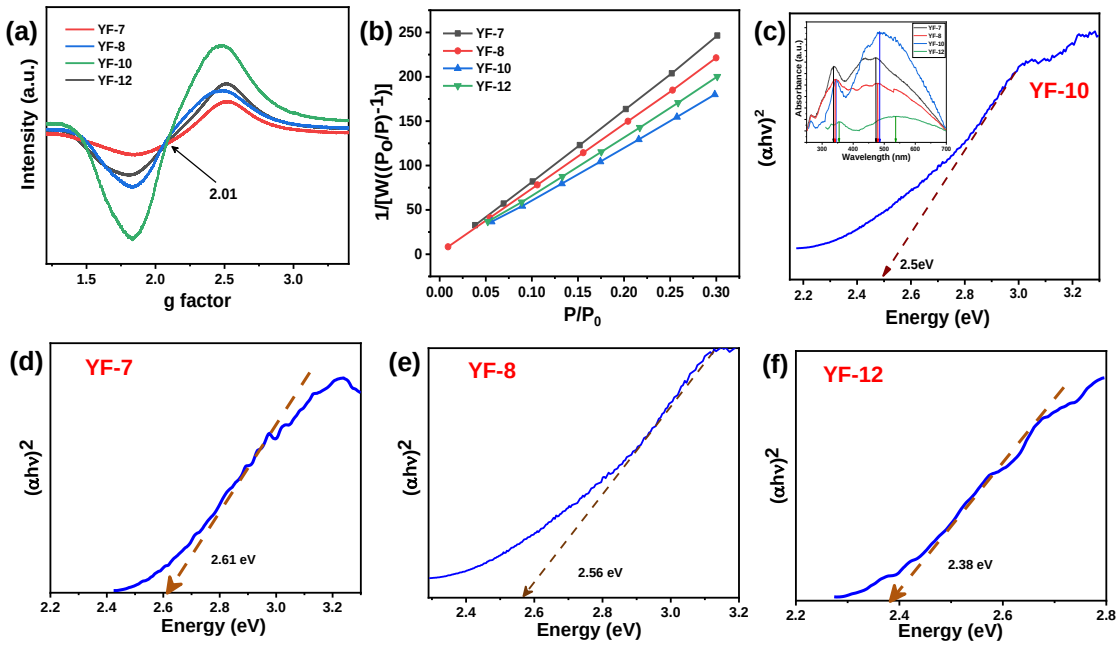

Fig. 6. 7. (a) EPR spectra of the samples. (b) Linear fitting of the BET plot of YF-7, YF-8, YF-10, YF-12 powder. (c) Tauc plot of YF-10 sample. (Insight UV-Vis absorption spectra for all the samples). (d-f) Tauc plot of YF-7, YF-8, YF-12 sample.

6.3.1.5 Spectroscopic study

Band gap energy of the samples calcined at various temperature were estimated from UV-vis spectroscopy and corresponding Tauc plot as shown in Fig. 6. 7 (c-f). It is observed that the band gap energy of the samples gradually decreases from 2.61 eV to 2.38 eV with the progression of calcination temperature from 700ºC to 1200ºC (ref. Table-6. 1). It is evident that band gap of pure hexagonal yttrium ferrite (YF-7) is relatively higher than the orthorhombic phase (YF-10). As indicated in XPS study with increasing calcination temperature more defect

states and unsaturated bonds grow on the surface of particle. The growth of these excess unsaturated bonds on the surface could modify the energy levels in the YF-10 sample.

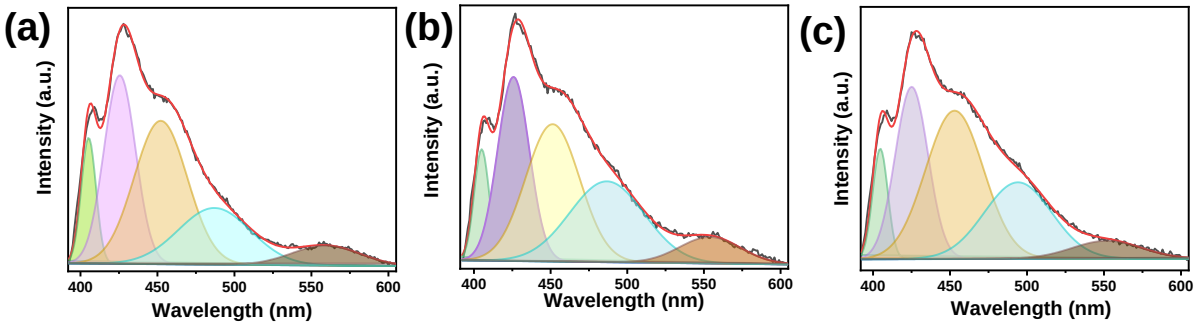

Fig. 6. 8. Deconvoluted PL spectra of (a) YF-7, (b) YF-10 and (c) YF-12.

The room temperature Photo-luminance emission spectra of YF-7, YF-10, and YF-12 were recorded after excitation at 375 nm as shown in Fig. 6. 8 (a-c). All three PL emission spectra are deconvoluted into 5 distinct peaks using a Gaussian-Lorentzian fit. The first deconvoluted peak around 405 nm can be attributed to near bend edge emission of the material. A strong blue emission peak around 425 nm is observed which is corresponding to the band-to-band electronic transition in perovskite ferrite materials. Peaks around 452 nm could arise due to the self-activated centre in the synthesized materials. Presence of excess Fe ions in the sample would also contribute to this most intense and broad emission peak. While emissions peak around 490 nm ought to the transition below the conduction band due to presence of defects in grain boundary or oxygen vacancies. Again, recombination of electrons which are trapped in the yttrium vacancies at deep levels could also contributes to this emission peak. Lastly peaks around 554 nm is corresponding to the oxygen defects in the samples [58-66]. Relative percentage of each PL peak are calculated from the area under the corresponding peak (ref. Fig. 6. 8 (a-c)) and are listed in Table- 6. 2.

Table- 6. 2: PL peak positions and corresponding relative percentage of each p eaks in YF-7, YF-10, YF-12.

Sl.no	**Peak position (nm)**	**Originated due to**	**Peak percentage**		
			YF-7	**YF-10**	**YF-12**
1	405(YF-7) 405(YF-10) 405(YF-12)	Near bend edge emission **(3.06 eV)**	7.5	6.3	8.9
2	425(YF-7) 426(YF-10) 425(YF-12)	Lattice deformation **(2.91 eV)**	25.9	13.6	28.6
3	452(YF-7) 451(YF-10) 453(YF-12)	Excess Fe ions Most intense peak (self activated centre in the synthesized materials) **(2.74 eV)**	33.0	23.9	36.5
4	487(YF-7) 487(YF-10) 494(YF-12)	Yttrium vacancies/ Transmission below the conduction band due to presence of defects in grain boundary or oxygen vacancies **(2.54 eV)**	26.7	27.8	19.6
5	558(YF-7) 554(YF-10) 552(YF-12)	Oxygen defects/ Defect level emission **(2.23 eV)**	7.1	28.4	6.4

6.3.2 Gas Sensing Properties

Variation of base resistance of yttrium ferrite thin film-based sensor with temperature is shown in Fig. 6. 9 (a). Exponentially decreasing trend of the curves clearly indicates semiconducting nature of the material. I-V characteristics curves showed linear relation (ref. Fig. 6. 9 (b) of current with increasing voltages at 300ºC which implies that typical Ohmic contact has been formed between sensing material and the electrodes [40].

Operating temperature plays significant role in gas sensing performance. Semiconductor metal oxide-based gas sensor requires sufficient thermal energy to activate reaction between analytes and surface of the sensing materials. In order to determine the optimum operating temperature of the sensors, sensing response was measured towards 0.5 ppm acetone gas at different temperature ranging from 260 ºC to 360 ºC for all the sensors in constant 33% RH background. As shown in Fig. 6. 9 (c) the sensors show enhanced response as temperature increases and becomes maximum at 300 ºC and start to decrease with further increase in temperature. At higher operating temperature the desorption rate of the analyte gas supplants the rate of gas adsorption which reduces the response of the sensor [67,68]. YF-10 shows maximum p-type response of 7.9 (R_g/R_a) towards 0.5 ppm acetone vapour at 300ºC which in nearly 2.7 times higher than that of YF-7 sensor. Accordingly, YF-10 sensor was taken for further detailed gas sensing performance measurement.

Humidity plays an influential role on gas sensing performance of any sensor. Moreover, human exhaled breath contains high amount of moisture. The fabricated sensor should show high response towards acetone even in saturated moisture background to be a potential breath analyser. Variation of base resistance of YF-10 sensor with different background humidity is shown in Fig. 6. 9 (d) which remains nearly unchanged with humidity variation. Again, response of YF-10 sensor towards 0.5 ppm acetone in different humidity background is measured (ref. Fig. 6. 9 (d)) which shows slightly decreasing trend in sensitivity with increasing background humidity. With increasing background humidity, the active sites on the sensor surface could be filled by the environmental moisture, which in turn reduces the number of actives sites for the acetone gas molecule and results in decreasing sensor response. This observation is in well agreement with literature [69-71]. All other sensor responses were measured in constant 33% RH background.

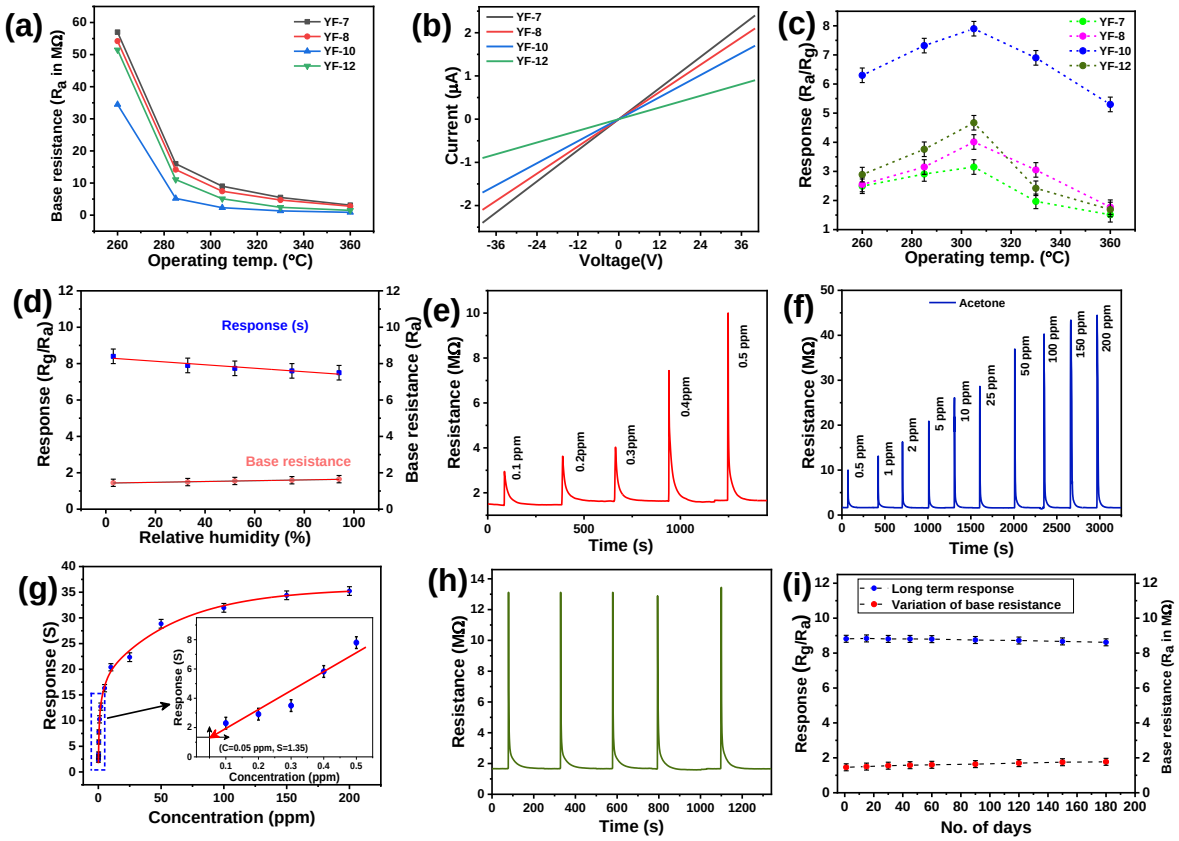

Fig. 6. 9. (a) Variation of base resistance of different YF sensors with operating temperature of the sensor. (b) I-V characteristics of all YF based sensor. (c) Response behaviour of all the YF sensors against varying operating temperature towards 0.5 ppm acetone at constant 33% RH background. (d) Variation of base resistance and the response of YF-10 sensor towards 0.5 ppm acetone with varying background %RH. (e-f) Dynamic response curve of YF-10 sensor towards 100 ppb to 50 ppm acetone vapour at optimum operating temperature and constant 33%RH background. (g) Response behaviour of all the YF-10 sensors against varying acetone concentration at optimum operating temperature and constant 33 %RH background (inset-variation of the response of YF-10 sensor toward low acetone concentrate. (h) Repetitive response curve of YF-10 sensor towards 1 ppm acetone, (i) Long time stability curve of YF-10, long term stability of the base resistance of YF-10 sensor at optimum conditions.

Fig. 6. 9 (e-f) shows the dynamic response and recovery curve of YF-10 sensor for different acetone concentration ranging from 0.1ppm to 200 ppm at optimum operating temperature. Sensor showed very significant sensitivity even towards 100 ppb acetone vapour (S= R_g/R_a =2.3). The response time (0.6s) and recovery time (2s) of YF-10 sensor for detecting 1 ppm acetone had significantly decreased in comparison with the YF-7 (3s, 15s respectively) sensor

for the same amount of gas concentration. Details procedure of the response and recovery time calculation is discussed in the letter section 3.3.(iii). Fig. 6. 9 (g) shows relationship of sensor response with increasing acetone concentration. Sensor shows relatively lower resolution for higher acetone concentration because number of free active sites on the materials surface cannot increase linearly with increasing acetone concentration. The inset of Fig. 6. 9 (g) shows how the response of YF-10 based sensor varies for lower acetone concentration which further liner fitted with following equation,

$$S = 13.1\rho + 0.23 \quad (3)$$

where S is the sensitivity and ρ is the acetone gas concentration. Estimated lower detection limit of acetone for YF-10 based sensor is found to be 150 ppt with nearly 1.35 folds p-type response. It is clearly visible that the sensitivity of the sensor almost saturates beyond 200 ppm. Technically, it is plausible to state that the upper detection limit of the sensor is 200 ppm above that concentration resolution of the sensor becomes very poor. Repeatability of the as prepared sensor was measured by three consecutive cycles of 1ppm acetone vapour, which showed excellent repetitive response of the sensor with relative deviation of ≤0.31% (ref. Fig. 6. 9 (h)) which delineates recyclability of the fabricated sensor with stable response value. Sensor's performance for a longer period of time is another crucial aspect for real life applicability of any sensor. Sensing response of YF-10 sensor towards 1 ppm acetone was measured for 180 days as shown in Fig. 6. 9 (i). Clearly, the YF-10 sensor showed stable response for 6 months.

The sensitivity of YF-10 sensor at 300 ºC towards five different target gases of various concentration ranging from 0.5ppm to 50 ppm was measured as shown in Fig. 6. 10 (a). Transient response curve of the sensor for various gases (Viz. ethanol, ammonia, formaldehyde, CO) are shown in Fig. 6. 10 (b-e). For each and every gas concentration YF-10 sensor had showed remarkably higher response towards acetone than any other interfering gases. Yamazoe and Shimanoe equation was employed to demonstrate dependency of gas sensing response with gas concentration as shown in following equation;

$$S_g = \alpha C_g^{\eta} \quad (4)$$

$$\log(S_g) = \log(\alpha) + \eta \log(C_g) \quad (5)$$

Where S_g is the sensor response, α is proportionality factor, C_g is the gas concentration [72]. Sensitivity (η) values of the YF-10 sensor at optimum operating temperature for different gases is obtained from the slope of the fitted straight line of $\log(S_g)$ versus $\log(C_g)$ plot as shown

in Fig. 6. 10 (f). Sensitivity values for acetone, ethanol, ammonia, formalin, CO are given in Table- 6. 4.

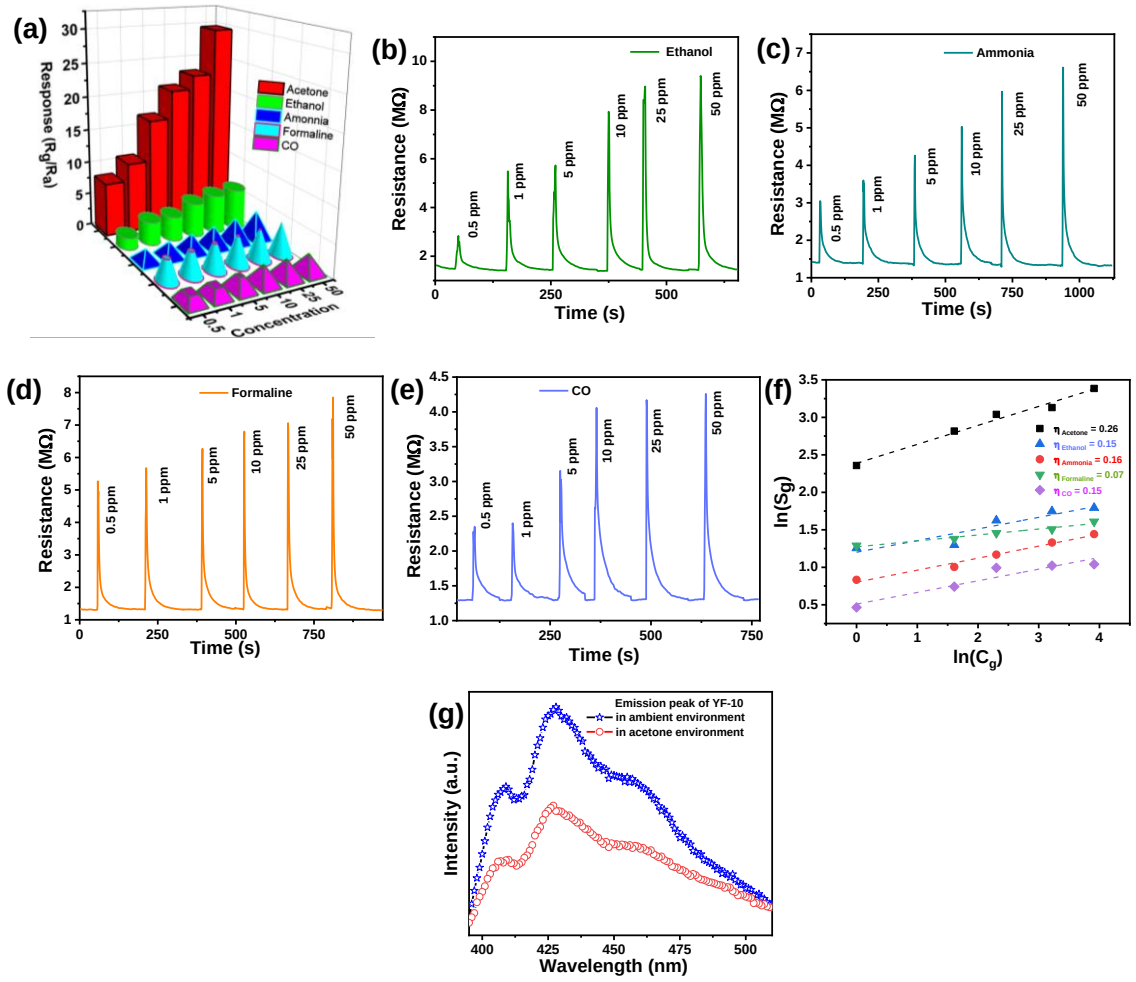

Fig. 6. 10. (a) Response of YF-10 sensor towards various concentration of different gases. Transient response curve of the YF-10 sensor for various (b) ethanol, (c) ammonia, (d) formaldehyde, (e) CO of different concentration. (f) Variation of $\ln(C_g)$ and $\ln(S_g)$ for 5 different gases. (g) PL emission peak of YF-10 sample in presence and absence of acetone.

Table- 6. 3: Literature based comparative study of trace level chemiresistive acetone vapor sensors

Material	**Response (R_g/R_a) (concentration ppm)**	**Operating Temperature (°C)**	**Response/Recovery time (s) (acetone concentration in ppm)**	**Lower detection limit (ppm)**
[13] Au doped ZnO Nanosphere	2 (0.5ppm)	170	27s/18s (100 ppm)	0.5
[14] Au/Pd-doped ZnO Nanorods	~1.5 (100 ppm) ~1.3 (75 ppm)	150	8s/5s (Au) 9/7s (Pd) (100 ppm)	0.005
[15] ZnO Nanofibers	~4 (1 ppm)	250	75s/25s (100 ppm)	1
[16] Tb doped SnO_2	~1.21 (0.05 ppm)	450	9s/-(20ppm)	0.05
[17] Pd, Au decorated SnO_2 nanosheets	6.6 (2ppm)	250	5s/4s (2 ppm)	0.10
[18] Ru-doped SnO_2 nanofibers	8.9 (5ppm)	200	1s/86s (100 ppm)	0.5
[19] Au modified In_2O_3 3D sphere	42.4 (5 ppm)	340	9s/15s (5 ppm)	0.20
[20] Pt@In_2O_3 nanowires	6.23 (1ppm)	320	11s/13s(1ppm)	0.01

[21] Pt-decorated In_2O_3 nanoparticles	~15.2 (1.56ppm)	150	25s	0.01
[22] MoO_3	(n-type) ~20% (1.25 ppm)	200	10s/120s (1.25 ppm)	0.40
[23] MoO_3 and In2O3 hollow spherical composites	~2 (1 ppm)	250	2s/50s (100 ppm)	1
[24] Au and Pd-decorated WO_3 nanorod	(n-type) 40% (200 ppm)	300	101s/96s (200 ppm)	200
[25] 3D α-Fe_2O_3 nanorods arrays @graphene oxide	~19 (50 ppm)	220	7s/8s (50 ppm)	5
[26] $BiFeO_3$ nanoparticles	~1.8 (1 ppm)	350	25s/17s (100 ppm)	1
[27] Ag-doped $BiFeO_3$	(n-type) 33% (1ppm)	350	65±10s/_ (25 ppm)	0.5
[28] $LiFeO_3$	~2.6 (20 ppm)	240	9s/18s (200 ppm)	20
[29] $LaFe_{0.99}P_{0.01}O_{3-\delta}$ nanosheets	~30 (100 ppm)	180	-	0.05
[30] $SmFeO_3$	~4.7 (0.5 ppm)	210	47s/10s (0.5 ppm)	0.5
[31] Sm doped $PrFeO_3$	~3.7 (5 ppm)	270	15s/16s (50 ppm)	5

[32] $PrFeO_3$	141.3 (200 ppm)	180	5s/5s	10
[33] Pd doped $NdFeO_3$	~5.5 (50 ppm)	140	18s/1s (50 ppm)	-
[34] $YFeO_3$ planar electrode	~23 (10 ppm)	110	-	10
[35] $YbFeO_3$	7.75 (30 ppm)	200	18s/25s	0.5
[36] p-$SmFeO_3$/p-$YFeO_3$	134 (30 PPM)	120	166s/228s	10
[37] Cu doped $ZnFe_2O_4$	~2.53 (1 ppm)	125	66s/136s (1 ppm)	0.5
[38] Ag-$ZnFe_2O_4$	~1.40 (0.8 ppm)	175	17s/148s (100 ppm)	0.8
[39] Pt decorated $CuFe_2O_4$ nanotubes	~3.80 (5 ppm)	300	17s/306s (100 ppm)	5
[This work] Orthorombic-$YFeO_3$	~10.3 (1 ppm)	300	0.2s/1.4s (1ppm)	0.1

6.3.3 Gas sensing mechanism and DFT calculation

Highly selective acetone sensing mechanism of the YF-10 sensor is discussed in three different segments for better clarity, as follows: (i) Surface electronic charge transfer mechanism, (ii) role of pure orthorhombic structure for enhanced sensing performance of YF-10, (iii) Gas sensing kinetics study to understand selectivity towards acetone.

(i) Surface electronic charge transfer mechanism

Yttrium ferrite showed a p-type semiconducting response where holes played the role of majority charge carrier. When the sensor is exposed to the ambient environment, oxygen

molecules are absorbed on the sensor surface and converted to O^-, O_2^-, or O^{2-} by immobilizing electrons drawn from the surface of the sensing material depending upon sensor's operating temperature. This results in increased hole accumulation layer (HAL) and subsequently resistance of the material decreases. When acetone is introduced over the surface of the sensor, these pre-absorbed oxygen ions react with the acetone vapour and produce carbon dioxide, vapour and free electrons as discussed elsewhere [13,15,26,27,73]. These free electrons are released back to the valance band where these electrons recombine with the holes, resulting the quenching of the hole accumulation layer and expansion of the insulating core (ref. equation 6-7). Thus, decrease in majority carrier concentration results as increase in resistance of the sensing material.

$$C_3H_6O + 8O^- \rightarrow 3CO_2 + 3H_2O + 8e^- \quad (6)$$

$$e^- + h^+ \rightarrow null \quad (7)$$

The shrinking of majority carrier (hole) accumulation layer upon exposer of acetone vapour is further experimentally established by photoluminescence study of the sensing material. Fig. 6. 10 (g) represents the PL spectra of YF-10 sample in ambient air environment and acetone gas environment, separately. PL intensity indicates recombination efficiency of electron and hole pairs. It is clearly shown in the fig PL peak intensity of YF-10 sample significantly decreases in acetone environment. The number of available majority carrier will be less for recombination. Hence, PL peak intensity diminished after acetone exposer. The whole process is depicted schematically in Fig. 6. 11.

(ii) role of pure orthorhombic structure for enhanced sensing performance of YF-10

As calcination temperature increases from 700ºC to 1000ºC a significant change in XPS spectra for Fe 2p peak is observed. Deconvolution of Fe 2p peak indicates that Fe^{2+} content increases from 12.1% for YF-7 to 28.1% for YF-10. Presence of both Fe^{2+} and Fe^{3+} will be beneficial for more electron transport. With the increase in calcination temperature some electrons are trapped by Fe^{3+} and converted into Fe^{2+}. To compensate this charge imbalance in the material, more oxygen vacancies are originated will be generated which are positively charged and active sites for sensing [74-78]. In case of YF-10 sample since Fe^{2+} is maximum it will have maximum oxygen vacancies which is also supported by both PL and EPR studies. Higher the oxygen vacancy adsorption of environmental oxygen of the surface will be higher which will give rise to maximum sensitivity. Accordingly, increasing oxygen vacancies in YF-10 sample induces greater number of chemisorbed oxygen species which is also responsible for enhanced gas sensing response in YF-10 sample. [79,80] However, in case of YF-12 sample concentration

of Fe^{2+} again decreases and subsequently concentration of defect oxygen as well as chemisorbed oxygen will decrease which in turn lead to decrease in sensing response. Moreover, formation of minor higher order phases in YF-12 sample could be a probable reason for the decrease of sensitivity.

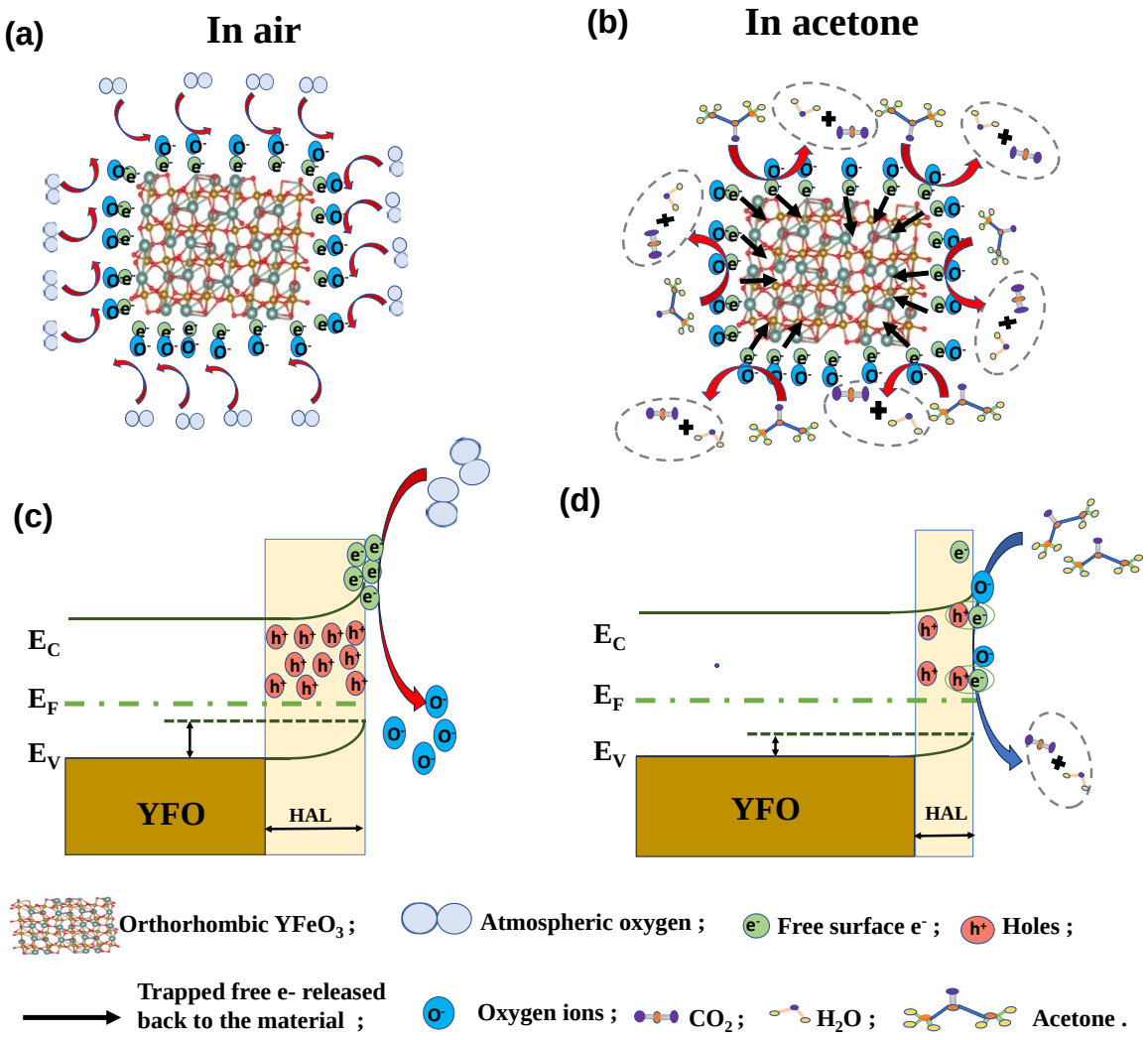

Fig. 6. 11. (a-b) Schematic diagrams of YFO for acetone detection. (c-d) Corresponding energy band diagrams in air and in acetone.

Relatively lower band gap energy of YF-10 as calculated from UV vis spectra would give an edge to the orthorhombic yttrium ferrite (YF-10) in charge transfer-based surface catalytic properties. Further variation of oxygen vacancies and oxygen defects in YF-7, YF-10 and YF-12 samples are also analysed from the deconvoluted PL peaks as shown in Fig. 6. 8 (a-c). Variation of relative percentage of each peak in the 3 samples were calculated from the area under the curve of individual peaks. Amount of oxygen vacancies and oxygen defects are become maximum in the YF-10 sample as shown in in Table- 6. 1 and Table- 6. 2. Thus, the

findings of XPS study corroborates with PL analysis which can suitably explain the enhancement of sensitivity for YF-10 sample.

Further, effect of phase transition of $YFeO_3$ in enhancement of the acetone sensing behaviour at the atomistic scale and the corresponding alterations in electronic structures were theoretically investigated using DFT calculation. Adsorption energy is the major influential parameter for evaluating the gas sensing performance of any material [55,81]. To demonstrate the electronic interaction between $YFeO_3$ and the acetone molecule, the adsorption energy (E_{ads}) has been investigated using the following equation:

$$E_{ads} = E_{YFeO_3+acetone} - (E_{YFeO_3} + E_{acetone}) \quad (8)$$

where, $E_{YFeO_3+acetone}$, E_{YFeO_3}, $E_{acetone}$, represent the energies of gas molecule adsorbed $YFeO_3$ system, the pristine $YFeO_3$ and acetone molecule respectively. Being most pronounced and exposed (121) surface of orthorhombic $YFeO_3$ and (101) surface of hexagonal $YFeO_3$ were chosen for the calculations. The binding energies of the acetone gas molecule for the Fe-terminated and O-terminated orthorhombic $YFeO_3$ structure are found to be -1.8 eV and -4.00 eV respectively. On the other hand, the binding energy of the acetone on the hexagonal $YFeO_3$ structure is calculated as -2.79 eV. The more negative value of E_{ads} suggests that the adsorption of acetone gas molecule is more energetically favourable [82]. Fig. 6. 12 (a) shows the binding of acetone molecule on the (121) surface of O-terminated orthorhombic $YFeO_3$ and Fig. 6. 12 (b) shows the binding of acetone molecule on the (101) surface of O-terminated hexagonal $YFeO_3$. Theoretical calculation suggests orthorhombic phase of yttrium ferrite has to be more energetically favourable than the hexagonal phase for acetone adsorption and corresponding sensitivity towards acetone has to be maximum for the orthorhombic phase, which exactly matches with our experimental results. Further, based on the difference in binding energies on different configurations, O-terminated orthorhombic $YFeO_3$ is considered for calculating the gas sensing mechanism at the atomistic scale. To analyse the adsorption properties of acetone gas molecule on $YFeO_3$, Bader charge analysis and planar averaged charge density calculation have been performed to demonstrate quantitatively the charge transfer between the substrate and adsorbed molecule. The charge transfer has been evaluated by the following:

$$\Delta\rho = \rho_{YFeO_3+acetone} - (\rho_{YFeO_3} + \rho_{acetone}) \quad (9)$$

Where, the terms represent the charge densities of acetone adsorbed $YFeO_3$, pristine YFeO3 and acetone gas molecules respectively [83]. Here, the substrate $YFeO_3$ will gain 0.20 e^- by being adsorbed of acetone gas molecule. This is in accordance with the planar average charge

density distribution, as shown in Fig. 6. 12 (c). Here positive and negative values indicate accumulation and depletion of charge densities respectively. It appears that the substrate $YFeO_3$ is depleted of charge near the interface while the adsorbate has charge accumulation, leading to a charge transfer from adsorbate (C_3H_6O) to the substrate ($YFeO_3$). Hence, theoretical charge transfer results exactly justifies surface electronic charge transfer mechanism for acetone sensing which has been discussed in details in earlier section 6. 3. 3 (i).

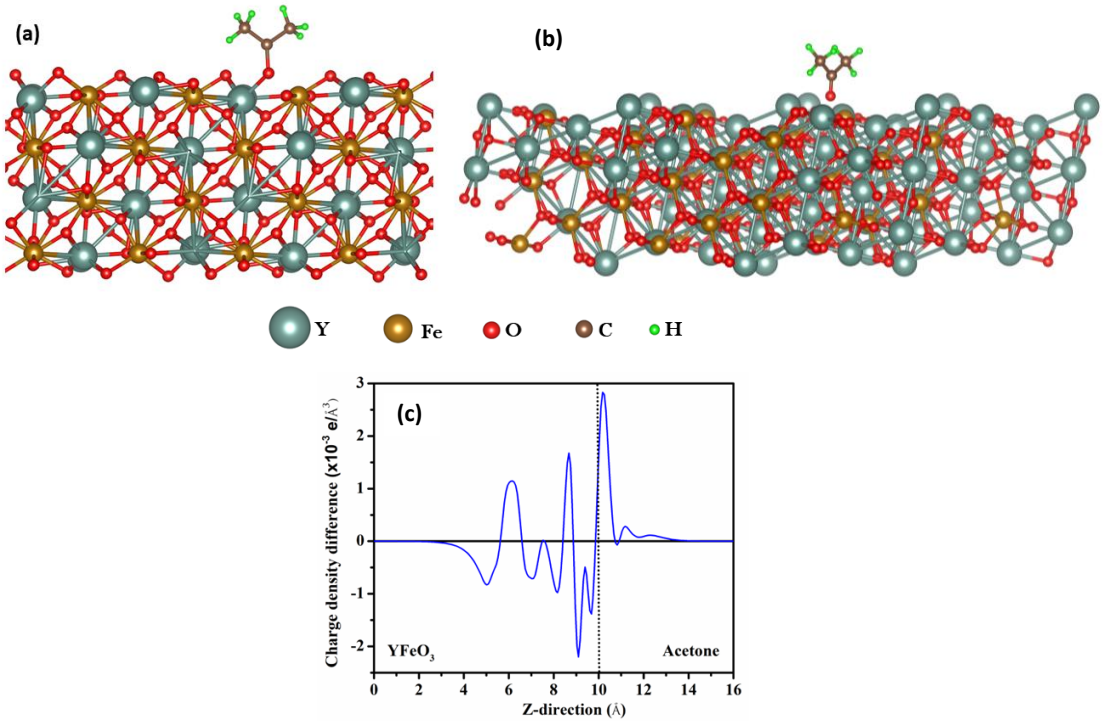

Fig. 6. 12. (a) optimized structure of acetone adsorbed orthorhombic $YFeO_3$. (b) optimized structure of acetone adsorbed hexagonal $YFeO_3$. (c) Planar average charge density difference in the acetone adsorbed orthorhombic $YFeO_3$.

(iii) Gas sensing kinetics

As elaborately discussed in the section 3.3.(i), SMO based chemiresistive gas sensing is primarily a surface catalytic activity where successive adsorption and desorption of environmental oxygen molecule and target gas molecule over the surface of the sensing material results in changing resistance of the sensor. Eley-Rideal mechanism is employed to justify the redox reactions over the surface of the sensing material and subsequently to analyze gas sensing kinetics. Possible surface reactions can be formulated as follows

$$\frac{1}{2}O_2 + \Delta_{ads} + e^- \xrightarrow{R_1} O^-_{ads} \qquad (10.1)$$

$$O_{ads}^{-} \overset{R_2}{\rightarrow} \frac{1}{2}O_2 + \Delta_{ads} + e^{-} \quad (10.2)$$

$$O_{ads}^{-} + \hat{G} \overset{R_{kr}}{\longrightarrow} \bar{O} + \Delta_{ads} + e^{-} \quad (10.3)$$

Where, Δ_{ads} is the surface adsorption site, $R_1$is kinetic rate constant of adsorption, R_2 is kinetic rate constant of desorption of O_2 molecule, and R_{kr} is kinetic rate constant for analyte gas.

The number density of analyte molecules interaction mostly depends on preabsorbed oxygen molecule and incoming gas concentration. If at any specific time 't' total adsorption sites are S_0 over the sensor surface and the no of occupied sites is S_1, then the simultaneous de-adsorption will be linearly dependent on then number of occupied sites (S_1). So, at any fixed temperature reaction rates can be expressed as follows;

$$\frac{dS_1}{dt} = R_1(S_0 - S_1)\rho_o - R_{kr}S_1\rho_g - R_2N_1 \quad (11)$$

Where ρ_o and ρ_g are the concentration of incoming environmental oxygen and the particular gas respectively [84,85].

dividing both side of equation (11) by S_0,

$$\frac{d\left(\frac{S_1}{S_0}\right)}{dt} = R_1\left(1 - \frac{S_1}{S_0}\right)\rho_o - R_{kr}\frac{S_1}{S_0}\rho_g - R_2\frac{S_1}{S_0}\ ; \quad (12)$$

Taking, $\frac{S_1}{S_0} = \emptyset$,which is the surface convergence then,

$$\frac{d\emptyset}{dt} = R_1(1 - \emptyset)\rho_o - R_{kr}\emptyset\rho_g - R_2\emptyset; \quad (13)$$

$$\int \frac{d\emptyset}{R_1(1-\emptyset)\rho_o - R_{kr}\emptyset\rho_g - R_2\emptyset} = \int dt \quad (14)$$

$$\emptyset = \left(\frac{R_1\rho_o}{R_1\rho_o + R_{kr}\rho_g + R_2}\right)\left(1 - e^{-(R_1\rho_o + R_{kr}\rho_g + R_2)t}\right) \quad (15)$$

Moreover, change in conductance is linearly proportional to the surface convergence. Hence, transient gas sensing response of the YF-10 sensor can be conveyed as follows,

$$C_{res}(t) = C_O + C\left[1 - e^{-\left(\frac{t}{\tau_{res}}\right)}\right] \quad (16)$$

Where, C_O is the base conductance in ambient air background, C is a constant, and τ_{res} is response time [85].

Comparing equation (15) and (16) τ_{res} can be expressed as

$$\tau_{response} = \frac{1}{(R_1\rho_o + R_{kr}\rho_g + R_2)} \quad (17)$$

For the transient recovery part gas concentration will be equal to zero ($\rho_g = 0$) and only environmental oxygen will be present over the surface of the sensing material. The reaction rate over the active surface sites then can be presented as follows,

$$\frac{d\emptyset}{dt} = R_1(1-\emptyset)\rho_o - R_2\emptyset; \quad (18.1)$$

$$\frac{d\emptyset}{dt} = R_1\rho_o - R_1\emptyset\rho_o - R_2\emptyset; \quad (18.2)$$

$$\frac{d\emptyset}{dt} = R_1\rho_o - \emptyset(R_1\rho_o + R_2) \quad (18.3)$$

$$\int \frac{d\emptyset}{R_1\rho_o - \emptyset(R_1\rho_o + R_2)} = \int dt \quad (18.4)$$

$$\emptyset = \frac{R_1\rho_o}{R_1\rho_o + R_2}[1 - e^{-(R_1\rho_o + R_2)t}] \quad (19)$$

Further the transient conductance in the recovery part is correlated with this surface convergence equation and can be presented as follows,

$$C_{rec}(t) = C_O^{/} + C^{/}[e^{-(\frac{t}{\tau_{rec}})}] \quad (20)$$

Comparing equation (19) and (20) τ_{res} can be expressed as

$$\tau_{recovery} = \frac{1}{(R_1\rho_o + R_2)} = \frac{1}{R_{-kr}} \quad (21)$$

Where, R_{-kr} is the inverse kinetic rate constant corresponding to the re-adsorption of environmental oxygen molecules again over the sensor surface.

Comparing equation (17) with (21), sensor response time can be represented as follows,

$$\tau_{response} = \frac{1}{(R_{kr}\rho_g + R_{-kr})} \quad (22)$$

The response and recovery times ($\tau_{response}$ and $\tau_{recovery}$) are calculated by fitting the transient conductance curve by Eqs. (16) and (20). (ref. Fig. 6. 13(a-h))

The equation (22) can be expressed as follows,

$$\frac{1}{\tau_{response}} = (R_{kr})\rho_g + R_{-kr} \quad (23)$$

Kinetic rate constants and the inverse kinetic rate constant for the redox reaction for each interfering gasses including acetone are calculated by fitting impinging gas concentration vs $\frac{1}{\tau_{response}}$ plot. Equilibrium kinetic rate constants R_{eq} can be defined as $(\frac{R_{kr}}{R_{-kr}})$ which measures the strength of the reaction. Value of R_{eq} for different interfering gases are calculated by above mentioned method and shown in Fig. 6. 13(j).

The operating temperature of any sensor is the major controlling kinetic parameter for determining the sensor response time. For a fixed gas concentration, the relation between operating temperature and response time can be expressed as

$$\tau_{res} = \frac{e^{E_s/_{2KT}}}{f} \tag{24}$$

$$\log(\tau_{res}) = E_s\left(\frac{1}{2KT}\right) - \log(f) \tag{25}$$

Where, f is the vibrational frequency of the interacting gas molecules, E_s is the activation energy for the the redox reaction, T is the operating temperature of the sensor in kelvin and K is the Boltzmann's constant [85,86]. Response time of YF-10 sensor for fixed 1 ppm gas concentration at different operating temperature had been estimated by the above discussed method in equation (2) and (5) for all five interfering gases (viz. acetone, ethanol, ammonia, CO, formalin). The activation energy (E_s) values for each interacting gas at a fixed 1ppm concentration of gas estimated from the slope of the fitted straight line of $\log(\tau_{res})$ versus $\left(\frac{1}{2KT}\right)$ plot as shown in Fig. 6. 13(k). The calculated activation energies (slope) for all the interfering gases are listed in Table- 6. 4.

As shown in the Table- 6. 4 Sensitivity (η) and the strength of the catalytic reaction (R_{eq}) of the YF-10 sensor are maximum for the acetone gas, whereas the value of the same (η, R_{eq}) are significantly low for all other interfering gases. At the same time, activation energy (E_s) for the surface reaction above the sensor surface became least for the acetone than any other interfering gases. Thus, sensing kinetic study justifies the selective acetone sensing properties of the YF-10 sensor over the other interfering gases.

6.4 Simulated breath study

To investigate the application potential of the as prepared YF-10 sensor, a simulated acetone sensing analysis using exhaled human breath was conducted. Simulated breath samples having

different trace acetone concentration were prepared by a kind of desiccator dilution method. 1000 ppm acetone vapour was prepared from liquid acetone in a large size mother desiccator separately. Healthy exhaled breath was collected in a Tedlar gas sampling bag (1L) through one of its valves. The exhaled healthy human breath contains N_2, CO_2, water vapor and thousand different kinds of VOCs including acetone. This was taken to base sample for the entire study [35,62]. Calculated volumes of acetone vapour were collected from the mother desiccator and injected to the Tedlar bag through the other valve and kept overnight to prepare certain concentration of acetone vapour mixed simulated breath. Following this technique simulated breath having acetone concentration 0.5ppm, 1ppm, 2ppm and 5ppm were prepared in different Tedlar bags. The detail experimental procedure is shown in Fig. 6. 14 (c-e). Sensing performance of YF-10 sensors towards this different simulated breath were measured as shown in Fig. 6. 14 (a). The YF-10 sensor showed magnificent resolution between the base sample (healthy exhaled breath=H.B.) and the other simulated breath having different acetone concentrations (viz. H.B.+ 0.5 ppm acetone, H.B.+ 1 ppm acetone, H.B.+ 2 ppm acetone, H.B.+ 5 ppm acetone). Sensing response of YF-10 sensor towards each concentration of simulated breath samples were little lower than that of standard acetone concentration. Little reduction in sensing response of the YF-10 sensor towards the simulated breath could be caused by the presence of high amount of saturated moisture content in the exhaled human breath. To ensure the reliability of the simulation, the breath samples from five different healthy people were collected, and similar sensing study was performed using YF-10 sensor for each individual. Result of each set of experiment were negligible variation for all the cases as shown in Fig. 6. 14 (b), which confirms the credibility of the sensor towards practical application.

Table- 6. 4: Variation of Sensitivity (η), strength of the catalytic reaction (R_{eq}) and activation energy (E_s) of the YF-10 sensor for different interfering gases.

Different gases	**Sensitivity (η)**	**Reaction Strength (R_{eq})**	**Activation energy (E_s)**
Acetone	0.26	0.031	0.22
Ethanol	0.15	0.014	0.33
Ammonia	0.16	0.026	0.41
Formalin	0.07	0.021	0.44
CO	0.15	0.022	0.61

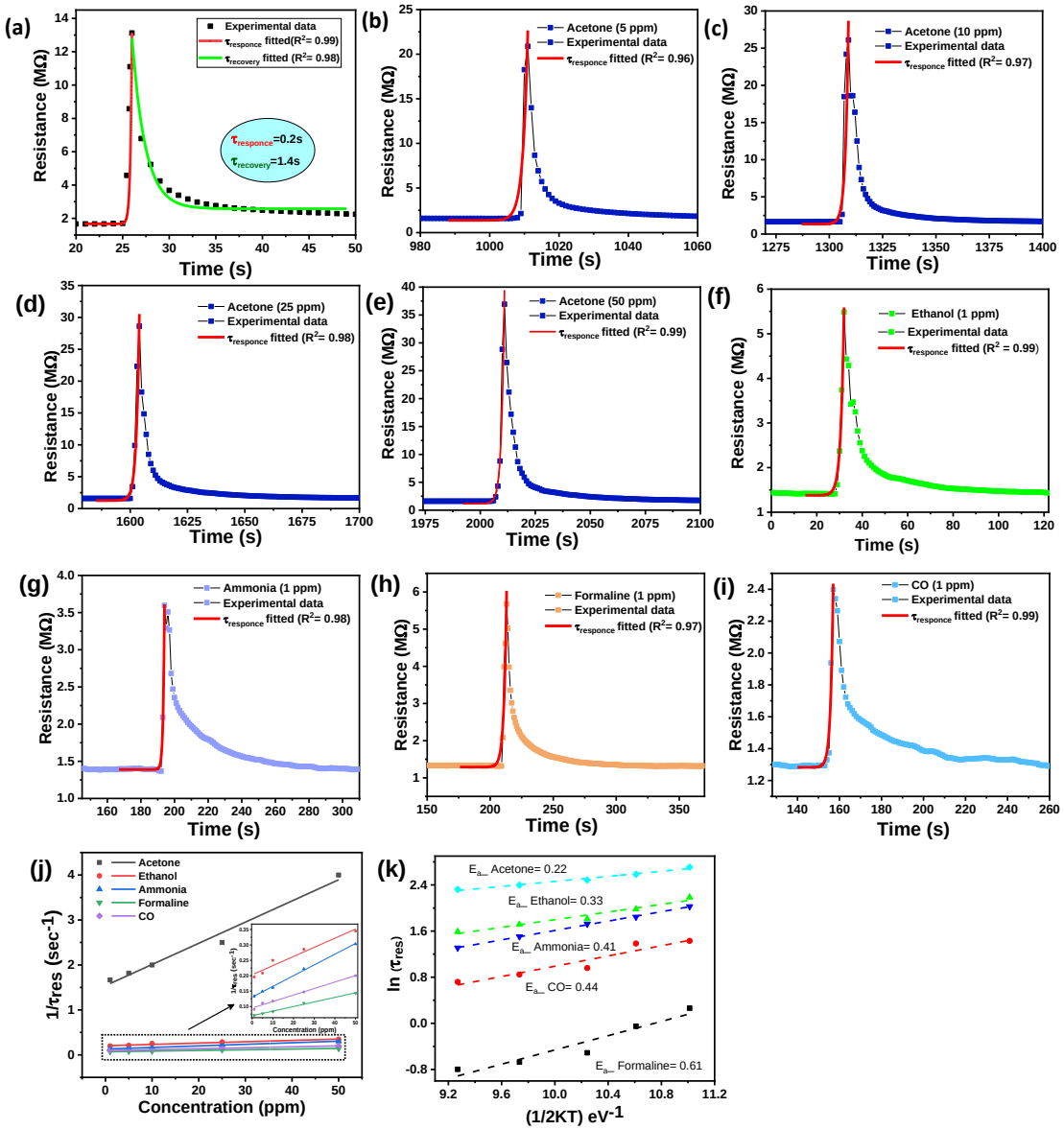

Fig. 6. 13. Fitting of dynamic resistance curve of YF-10 sensor in response to (a) 1 ppm acetone at 300 ◦C for response and recovery time measurement. (b) 5 ppm acetone, (c) 10 ppm acetone, (d) 25 ppm acetone, (e) 50 ppm acetone, (f) 1 ppm ethanol, (g) 1ppm ammonia, (h) 1 ppm formalin, (h) 1 ppm CO at 300 ◦C for response time measurement. (i) Variation of $1/\tau_{res}$ with varying concentration of different gases for obtaining kinetic rate constant for different VOCs at 350 ◦C operating temperature. (j) Variation of response time of YF-10 sensor for different gases of 1ppm concentration at350 ◦C operating temperature for obtaining activation energy (E_a) values for different interfering gases.

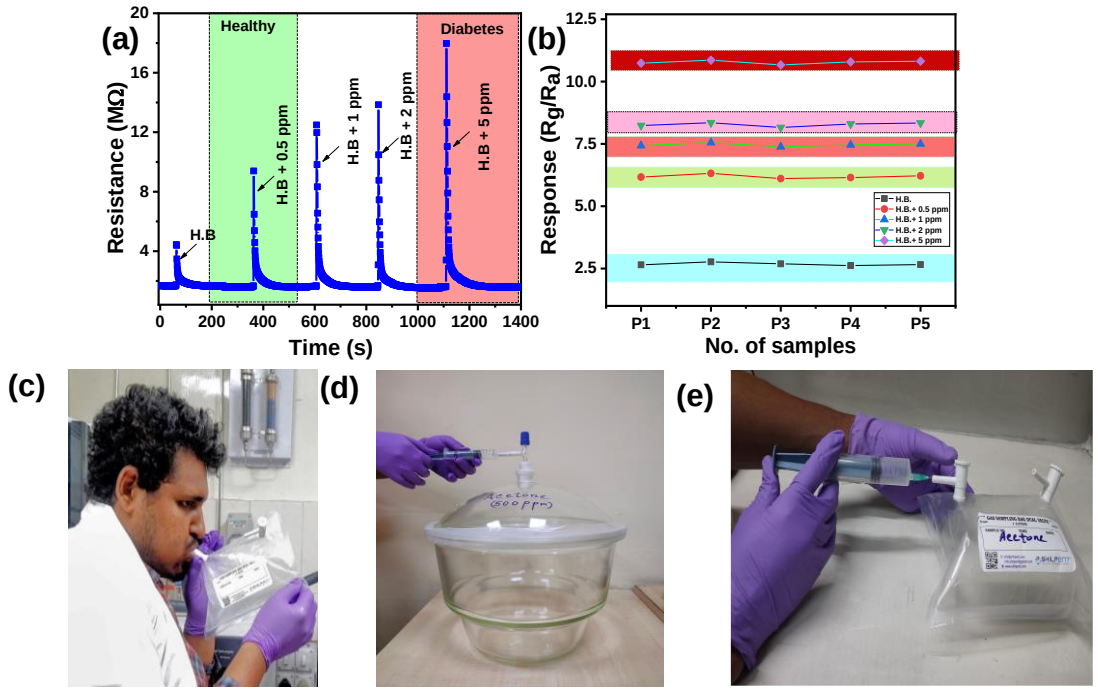

Fig. 6. 14. (a) Dynamics response curve of YF-10 sensor towards healthy breath (H.B.) and simulated breath of simulated breath having different concentration at 300º C operating temperature. (b) Response of YF-10 sensor towards 5 different simulated breath samples. (c) Breath sample collection in 1lt. tedlar bag. (d-e) Preparation of simulated breath sample.

6.5 Conclusion

In summary, different crystalline phases of crystalline perovskite $YFeO_3$ were synthesized using solution combustion method. Experimental results delineate that orthorhombic $YFeO_3$ (YF-10) shows highest sensitivity towards acetone amongst other phase. At optimum operating temperature orthorhombic YF-10 shows maximum 7.9-fold response towards 0.5 ppm acetone having significant resolution, excellent repeatability, nearly stable response in different humid background, good selectivity among different interfering gases and long-term stability for more than 180 days. Enhanced sensitivity of orthorhombic YF-10 sensor over other phases was explained in terms of morphology, oxygen vacancies and ferric bivalency in different phases of yttrium ferrite. DFT calculation was utilized to explain the enhanced sensitivity of orthorhombic phase by comparing the adsorption energy for acetone gas of different phases. Further, selective acetone sensing of YF-10 over other interfering gases are explained by invoking Eley-Rideal model. Finally, simulated breath study using different trace acetone concentration manifest the potential of YF-10 sensor as breath analyser for detecting diabetes in non-invasive way.

6.6 References

[1] X . Yang, X. Hao, T. Liu, F. Liu, B. Wang, C. Ma, X. Liang, C. Yang, H. Zhu, J. Zheng, T. He, G. Lu, CeO_2-based mixed potential type acetone sensor using $La_{1-x}Sr_xCoO_3$ sensing electrode, Sens. Actuators B Chem. 269 (2018) 118–126

[2] A. T. Güntner, S. Abegg, K. Königstein, P. A. Gerber, A. S. Trucksäss, S. E. Pratsinis, Breath Sensors for Health Monitoring. ACS Sens. 4 (2019) 268−280.

[3] K. Yuan, C.Y. Wang, L.Y. Zhu, Q. Cao, J.H. Yang, X.X. Li, W. Huang, Y.Y. Wang, H.L. Lu, D. W. Zhang, Fabrication of a Micro-Electromechanical System-Based Acetone Gas Sensor Using CeO_2 Nanodot-Decorated WO_3 Nanowires, ACS Appl. Mater. Interfaces 12 (2020) 14095−14104.

[4] S.-J. Choi, I. Lee, B.-H. Jang, D.-Y. Youn, W.-H. Ryu, C. O. Park, I.-D. Kim, Selective Diagnosis of Diabetes Using Pt-Functionalized WO_3 Hemitube Networks as a Sensing Layer of Acetone in Exhaled Breath, Anal. Chem. 85 (2013) 1792−1796.

[5] P. Puchalska, P.A. Crawford, Multi-dimensional roles of ketone bodies in fuel metabolism, signaling, and therapeutics, Cell Metab 25(2) (2017) 262–284

[6] X. Liu, X. Tian, X. Jiang, L. Jiang, P. Hou, S. Zhang, X. Sun, H. Yang, R. Cao, X. Xu, Facile preparation of hierarchical Sb-doped In_2O_3 microstructures for acetone detection. Sens. Actuators B Chem. 270 (2018) 304–311.

[7] P . Ariyageadsakul, V. Vchirawongkwin, C. Kritayakornupong, Determination of toxic carbonyl species including acetone, formaldehyde, and phosgene by polyaniline emeraldine gas sensor using DFT calculation, Sens. Actuators B Chem. 232 (2016) 165–174.

[8] G. T. Fan, C. L. Yang, C.H. Lin, C.C. Chen, C.H. Shih, Applications of Hadamard transform-gas chromatography/mass spectrometry to the detection of acetone in healthy human and diabetes mellitus patient breath, Talanta 120 (2014) 386–390.

[9] A. Mirzaei, S. G. Leonardi, G. Neri, Detection of Hazardous Volatile Organic Compounds (VOCs) by Metal Oxide Nanostructures-based Gas Sensors: A review., Ceram. Int. 42 (2016) 15119−15141.

[10] Y. Pan, Q. Zhang, W. Zhou, X. Zou, H. Wang, C. Huang, C. Shen, Y. Chu, Detection of Ketones by a Novel Technology: Dipolar Proton Transfer Reaction Mass Spectrometry (DP-PTR-MS), J. Am. Soc. Mass Spectrom. 28 (2017) 873–879.

[11] V.V. Kondalkar, L. T. Duy, H. Seo, K. Lee, Nanohybrids of Pt-Functionalized Al_2O_3/ZnO Core−Shell Nanorods for High-Performance MEMS-Based Acetylene Gas Sensor. ACS Appl. Mater. Interfaces 11 (2019) 25891−25900.

[12] Y. Wang, C. Liu, Z. Wang, Z. Song, X. Zhou, N. Han, Y. Chen, Sputtered SnO_2:NiO Thin Films on Self-assembled Au Nanoparticle Arrays for MEMS Compatible NO_2 Gas, Sens. Actuators B Chem. 2019 (278) 28−38.

[13] P.J. Cao, Q.G. Huang, S.T. Navale, M. Fang, X.K. Liu, Y.X. Zeng, W.J. Liu, F. J. Stadler, Y.M. Lu, Integration of mesoporous ZnO and Au@ZnO nanospheres into sensing device for the ultrasensitive CH_3COCH_3 detection down to ppb levels, Appl. Surf. Sci. 518 (2020) 146223.

[14] J. Huang, J. Zhou, Z. Liu, X. Li, Y. Geng, X. Tian, Y. Du, Z. Qian, Enhanced acetonesensing properties to ppb detection level using Au/Pd-doped ZnO nanorod, Sens. Actuators B Chem. 310 (2020), 127129.

[15] H. Du, W. Yang, W. Yi, Y. Sun, N. Yu, J. Wang, Oxygen-plasma-assisted enhanced acetone-sensing properties of ZnO nanofibers by electrospinning, ACS Appl. Mater. Interfaces 12 (2020) 23084–23093.

[16] C-H. Kwak, T-H. Kim, S-Y. Jeong, J-W. Yoon, J-S. Kim, and J-H. Lee, Humidity-Independent Oxide Semiconductor Chemiresistors Using Terbium-Doped SnO_2 Yolk−Shell Spheres for Real-Time Breath Analysis, ACS Appl. Mater. Interfaces, 10 (2018) 18886−18894.

[17] G.Li, Z. Cheng, Q. Xiang, L. Yan, X. Wang, J. Xu, Bimetal Pd Au decorated SnO_2 nanosheets based gas sensor with temperature-dependent dual selectivity for detecting formaldehyde and acetone, Sens. Actuators B Chem., 283 (2019) 590-601.

[18] X. Kou, F. Meng, K. Chen, T. Wang, P. Sun, F. Liu, X. Yan, Y. Sun, F. Liu, K. Shimanoe, G. Lu, High-performance acetone gas sensor based on Ru-doped SnO_2 nanofibers, Sens. Actuators B Chem., 320 (2020) 128292.
[19] R. Xing, Q. Li, L. Xia, J. Song, L. Xu, J. Zhang, Y. Xie, H. Song, Au modified three-dimensional In_2O_3 inverse opals: synthesis and improved performance for acetone sensing toward diagnosis of diabetes, Nanoscale, 7 (2015) 13051-13060.

[20] W. Liu, L. Xu, K. Sheng, X. Zho, B. Dong,G. Lu, H. Song, A highly sensitive and moisture-resistant gas sensor for diabetes diagnosis with Pt@In_2O_3 nanowires and a molecular sieve for protection NPG Asia Materials 10 (2018) 293–308.
[21] M. Karmaoui, S. G. Leonardi, M. Latino, D. M. Tobaldi, N. Donato, R. C. Pullar, M. P. Seabra, J. A. Labrincha, G. Neri, Pt-decorated In_2O_3 nanoparticles and their ability as a highly sensitive (<10 ppb) acetone sensor for biomedical applications, Sens. Actuators B: Chem., 230 (2016) 697-705.

[22] G. T. Santos, A. A. Felix, M. O. Orlandi, Ultrafast Growth of h-MoO_3 Microrods and Its Acetone Sensing Performance, Surfaces, 4 (2021) 9–16.
[23] W. Jiang, L. Meng, S. Zhang, X. Chuai, P. Sun, F. Liu, X. Yan, Y. Gao, X. Liang, G. Lu, Enhanced resistive acetone sensing by using hollow spherical composites prepared from MoO_3 and In_2O_3, Microchim Acta 186 (2019) 359.

[24] S. Kim, S. Park, S. Park, C. Lee, Acetone sensing of Au and Pd-decorated WO_3 nanorod sensors, Sens. Actuators B: Chem., 209 (2015) 180–185.

[25] H. Song, S. Yan, Y. Yao, L. Xia, X. Jia, J. Xu, 3D α-Fe_2O_3 nanorods arrays@graphene oxide nanosheets as sensing materials for improved gas sensitivity, Chem. Eng. J. 370 (2019) 1331–1340.

[26] S. Chakraborty, M. Pal, Highly selective and stable acetone sensor based on chemically prepared bismuth ferrite nanoparticles, J. Alloys Compd., 787 (2019) 1204-1211.

[27] S. Neogi, R. Ghosh, Behavioral remodeling of perovskite $BiFeO_3$ by Ag-doping strategies for enhanced and ppb level acetone sensing performance: An advanced enlightenment for selectivity and sensing mechanism, Appl. Mater. Today, 29 (2022) 101611.
[28] P. Song, H. Zhang, D. Han, J. Li, Z. Yang, Q. Wang, Preparation of biomorphic porous $LaFeO_3$ by sorghum straw biotemplate method and its acetone sensing properties, Sens. Actuators B: Chem., 196 (2014) 140–146.
[29] W. Qin, Z. Yuan, Y. Shen, R. Zhang, F. Meng, Phosphorus-doped porous perovskite $LaFe_{1-x}P_xO_{3-\delta}$ nanosheets with rich surface oxygen vacancies for ppb level acetone sensing at low temperature, Chem. Eng. J. 431 (2022) 134280.
[30] H. Zhang, J. Xiao, Y. Wang, L. Zhang, G. Zhao, H. Yang, H. Wang, A portable acetone detector based on $SmFeO_3$ can pre-diagnose diabetes through breath analysis, J. Alloys Compd., 922 (2022) 166160.
[31] S. Pei, S. Ma, X. Xu, X. Xu, O. Almamoun, Modulated $PrFeO_3$ by doping Sm^{3+} for enhanced acetone sensing properties, J. Alloys Compd. 856 (2021) 158274.

[32] L. Ma, S.Y. Ma, X.F. Shen, et al., $PrFeO_3$ Hollow Nanofibers as a Highly Efficient Gas Sensor for Acetone Detection, Sens. Actuators, B 255 (2018) 2546–2554.
[33] Z. Wu, R. Zhang, M. Zhao, S. Fang, Z. Han, J. Hu, K. Wang, Effect of Pd doping on the acetone-sensing properties of $NdFeO_3$, Int. J. Miner. Metall. Mater. 19 (2012) 141–145.
[34] H. Liu,T. Miao,W. Liu,J. Chen,B. Cheng,H. Qin,J. Hu, Highly sensitive acetone gas sensor based on $YFeO_3$ planar electrode under multi-wavelength light illumination, Mater. Lett. 333 (2023) 133596.
[35] F. Meng,J. Hu,C. Liu,Y. Tan, Y. Zhang, Highly sensitive and low detection limit of acetone gas sensor based on porous YbFeO3 nanocrystallines, Chem. Phys. Lett. 780 (2021) 138925.

[36] H. Liu, D. Zhu, T. Miao, W. Liu, J. Chen, B. Cheng, H. Qin, J. Hu, Highly Sensitive p-$SmFeO_3$/p-$YFeO_3$ Planar-Electrode Sensor for Detection of Volatile Organic Compounds, Chemosensors 2023, 11, 187.
[37] K. Wua, Y. Lua, Y. Liua, Y. Liuc, M. Shenb, M Debliquyd, C. Zhanga, Synthesis and acetone sensing properties of copper (Cu^{2+}) substituted zinc ferrite hollow micro-nanospheres, Ceram. Int., 46 (2020) 28835–28843.
[38] C. Zhang, Q.D. Wu, B.B. Zheng, J.J. You, Y.F. Luo, Synthesis and acetone gas sensing properties of Ag activated hollow sphere structured $ZnFe_2O_4$, Ceram. Int. 44 (2018) 20700–20707.
[39] C.H. Zhao, W.Z. Lan, H.M. Gong, J.L. Bai, R. Rarnachandran, S. Liu, F. Wang, Highly sensitive acetone-sensing properties of Pt-decorated $CuFe_2O_4$ nanotubes prepared by electrospinning, Ceram. Int. 44 (2018) 2856–2863.
[40] T. Das, S. Das, M. Karmakar, S. Chakraborty, D. Saha, Mrinal Pal, Novel barium hexaferrite based highly selective and stable trace ammonia sensor for detection of renal disease by exhaled breath analysis, Sens. Actuators B: Chem. 325 (2020) 128765.

[41] S. Mojumder , T. Das , S. Das , N. Chakraborty , D. Saha , M. Pal, Y and Al co-doped ZnO-nanopowder based ultrasensitive trace ethanol sensor: A potential breath analyzer for fatty liver disease and drunken driving detection, Sens. Actuators B: Chem. 372 (2022) 132611.

[42] N. Chakraborty, S. Das, A. Hossain, D. Saha, S. Mondal, Poly aniline (PANI) loaded hierarchical $Ti_{1-x}Sb_xO_2$ rutile phase nanocubes for selective room temperature detection of benzene vapor, Sens. Actuators B: Chem. 347 (2021) 130622.

[43] T. Das, S. Mojumder, S. Chakraborty, D. Saha, M. Pal, Beneficial effect of Sn doping on bismuth ferrite nanoparticle-based sensor for enhanced and highly selective detection of trace formaldehyde, Appl. Surf. Sci. 602 (2022) 154340.
[44] G. Kresse, J. Furthmu¨ller, Efficient iterative schemes for ab initio total-energy calculations using a plane-wave basis set, Phys. Rev. B: Condens. Matter Mater. Phys. 54 (1996) 11169–11186.

[45] G. Kresse, J. Furthmu¨ller, Efficiency of ab initio total energy calculations for metals and semiconductors using a plane-wave basis set, Comput. Mater. Sci. 6 (1996) 15–50.

[46] B. H. O'Connor, Mark D. Raven, Application of the Rietveld Refinement Procedure in Assaying Powdered Mixtures, Powder Diffraction. 3(01) (1998) 2-6.

[47] P. Zhao, L. Lu, X. Liu, A. G. De la Torre, X. Cheng, Error Analysis and Correction for Quantitative Phase Analysis Based on Rietveld-Internal Standard Method: Whether the Minor Phases Can Be Ignored?, Crystals 8 (2018) 110.

[48] D. D. Boulay, E.N. Maslen, V. M. Streltsov, A Synchrotron X-ray Study of the Electron Density in $YFeO_3$, Acta Cryst. B51 (1995) 921-929.

[49] N. T. K. Thanh, N. Maclean, S. Mahiddine, Mechanisms of Nucleation and Growth of Nanoparticles in Solution, Chem. Rev. 114 (2014) 7610−7630.

[50] M. H. Alotaibi, G. A. El-Hiti, H. Hashim, A. S. Hameed, D. S. Ahmed, E. Yousif, SEM analysis of the tunable honeycomb structure of irradiated poly (vinyl chloride) films doped with polyphosphate, Heliyon, 4 (2018) e01013.

[51] J.F. Moulder, W.F. Stickle, P.E. Sobol, K.D. Bomben, Handbook of X-ray Photoelectron Spectroscopy, Perkin Elmer Corp, Eden Prairie, MN, 1992.
[52] S. Mathur, H. Shen, N. Lecerf, A. Kjekshus, H. Fjellvag, G.F.Goya, Adv. Mater. 14 (2002) 1405.
[53] L. Feng, S. Gai, F. He, P. Yang, Y. Zhao, Multifunctional bismuth ferrite nanocatalysts with optical and magnetic functions for ultrasound enhanced tumor theranostics, ACS Nano. 14(6) (2020) 7245–7258.
[54] H. Aono, M. Sato, E. Traversa, M. Sakamoto, Y. Sadaoka, J. Am. Ceram. Soc. 84 (2001) 341.

[55] M. Wu, S. Chen, W. Xiang, Oxygen vacancy induced performance enhancement of toluene catalytic oxidation using $LaFeO_3$ perovskite oxides, Chem. Eng. J. 387 (2020) 124101.

[56] J.L. Li, M. Zhang, Z.J. Guan, Q.Y. Li, C.Q. He, J.J. Yang, Synergistic effect of surface and bulk single-electron-trapped oxygen vacancy of TiO_2 in the photocatalytic reduction of CO_2, Appl. Catal. B-Environ. 206 (2017) 300–307.
[57] X.W. Li, W.D. Zhang, J.Y. Li, G.M. Jiang, Y. Zhou, S.C. Lee, F. Dong, Transformation pathway and toxic intermediates inhibition of photocatalytic NO removal on designed Bi metal@defective $Bi_2O_2SiO_3$, Appl. Catal. B-Environ. 241(2018) 187–195.

[58] X. Yu, X. An, Enhanced magnetic and optical properties of pure and (Mn, Sr) doped $BiFeO_3$ nanocrystals, Solid State Commun. 149 (2009) 711–714.
[59] R. Moubah, G. Schmerber, O. Rousseau, D. Colson, M. Viret, Photoluminescence investigation of defects and optical band gap in multiferroic $BiFeO_3$ single crystals. Appl. Phys. Express 5 (2012) 035802.
[60] V. Surdu, R. D. Trus, ca, Bogdan, T. Vasile, O. C. Opre, E. Tanasa, L. Diamandescu, E. Andronescu, A. C. Ianculescu, $Bi_{1-x}Eu_xFeO_3$ Powders: Synthesis, Characterization, Magnetic and Photoluminescence Properties, Nanomater. 9 (2019) 1465.
[61] S. Acharya, D.K. Padhi, K.M. Parida, Visible light driven $LaFeO_3$ nano sphere/RGO composite photocatalysts for efficient water decomposition reaction, Catal. Today 353 (2020) 220-231.
[62] X. Chen, H. Zhang, T. Wang, F. Wang, W. Shi, Optical and photoluminescence properties of $BiFeO_3$ thin films grown on ITO-coated glass substrates by chemical solution deposition, Phys. Status Solidi A, 2012, 1–5.
[63] A. R. Vázquez-Olmos, M. E. Sánchez-Vergara, A. L. Fernández-Osorio, A. Hernández-García, R. Y. Sato-Berrú, J. R. Alvarez-Bada, Mechanochemical Synthesis of $YFeO_3$ Nanoparticles: Optical and Electrical Properties of Thin Films, J. Clust. Sci. 29 (2018) 225–233.

[64] P. S. J. Bharadwaj, S. Kundu, V. S. Kollipara, K. Varma, Structural, optical and magnetic properties of Sm^{3+} doped yttrium orthoferrite ($YFeO_3$) obtained by sol–gel synthesis route, J. Phys.: Condens. Matter, 32 (2020) 035810.

[65] O. M. Lemine, M. Bououdina, M. Sajieddine, A. M. Al-Saie, M. Shafi, A. Khatab, M. Alhilali, M. Henini, Synthesis, structural, magnetic and optical properties of nanocrystalline
$ZnFe_2O_4$, physica B: condensed matter. 406 (2011) 1989-1994.
[66] A. Manikandan, S.A. Antony, R. Sridhar, S. Ramakrishna, M. Bououdina, A Simple Combustion Synthesis and Optical Studies of Magnetic $Zn_{1-x}Ni_{(x)}Fe_2O_4$ Nanostructures for Photoelectrochemical Applications, J. Nanosci. Nanotechnol. 15 (2015) 4948-4960.
[67] S. Das, S. Mojumder, D. Saha, M. Pal, Influence of major parameters on the sensing mechanism of semiconductor metal oxide based chemiresistive gas sensors: A review focused on personalized healthcare, Sens. Actuators B Chem. 352 (2) (2022) 131066.
[68] B. Liu, K. Li, Y. Luo, L. Gao, G. Duan, Sulfur spillover driven by charge transfer between AuPd alloys and SnO_2 allows high selectivity for dimethyl disulfide gas sensing Chem. Eng. J. 420 (2021) 129881.
[69] S. Sen, S. Maity, S. Kundu, Fabrication of Fe doped reduced graphene oxide (rGO) decorated WO_3 based low temperature ppm level acetone sensor: Unveiling sensing mechanism by impedance spectroscopy, Sens. Actuators B Chem. 361 (2022) 131706.
[70] J. Guo, Y. Li, B. Jiang, H. Gao, T. Wang, P. Sun, F. Liu, X. Yan, X. Liang, Y. Gao, J. Zhao, G. Lu, Xylene gas sensing properties of hydrothermal synthesized SnO_2-Co_3O_4 microstructure, Sens. Actuators B: Chem. 310 (2020) 127780.
[71] F. Yin, Y. Li, W. Yue, S. Gao, C. Zhang, Z. Chen, Sn_3O_4/rGO heterostructure as a material for formaldehyde gas sensor with a wide detecting range and low operating temperature, Sens. Actuators B: Chem. 312 (2020), 127954.
[72] N. Yamazoe, K. Shimanoe, Theory of power laws for semiconductor gas sensors. Sens. Actuators B: Chem. 128 (2008) 566−573.

[73] H.J. Song, S.W. Yan, Y.L. Yao, L.X. Xia, X.H. Jia, J.S. Xu, 3D α-Fe_2O_3 nanorods arrays@graphene oxide nanosheets as sensing materials for improved gas sensitivity, Chem. Eng. J. 370 (2019) 1331–1340.
[74] K. O. Moura, R. Lima, A. Coelho, E. Souza-Junior, J. Duque and C. Meneses, Tuning the Surface Anisotropy in Fe-doped NiO Nanoparticles, Nanoscale, 2014,6, 352-357.
[75] Y. Li, Y. Ma, Z. Wang, H. Liu, X. Wang, Y. Dong, W Qian, Morphologically distinctive $YFeO_3$ with near-infrared reflection and ferromagnetic characteristics, J Mater Sci: Mater Electron. 33 (2022) 11318–11331.
[76] X. Qiao, Y. Xu, K. Yang, J. Ma, C. Li, H. Wang, L. Jia, Mo doped $BiVO_4$ gas sensor with high sensitivity and selectivity towards H2S, Chem. Eng. J. 395 (2020) 125144,
[77] N. Chakraborty, P. K. Ghose, P. Rudra, S. Das, D. Saha, A. K. Mishra, A. Sanyala, S. Mondal, Dopant-induced cationic bivalency in hierarchical antimony-doped tin oxide nano-particles for room temperature SO_2 sensing, J. Mater. Chem. A 9 (2021) 21824-21834.
[78] N. Chakraborty, S. Mondal, Dopant Mediated Surface Charge Imbalance in Enhancing Performance of Metal Oxide Chemiresistive Gas Sensors, J. Mater. Chem. C 10 (2022) 1968-1976.

[79] L. Song, K. Dou, R. Wang, P. Leng, L. Luo, Y. Xi, C. C. Kaun, N. Han, F. Wang, Y. Chen, Sr-Doped Cubic In_2O_3/Rhombohedral In_2O_3 Homojunction Nanowires for Highly Sensitive and Selective Breath Ethanol Sensing: Experiment and DFT Simulation Studies, ACS Appl. Mater. Interfaces 12 (2020) 1270−1279.
[80] A. Shanmugasundaram, D.S. Kim, N. D. Chinh, J. Park, Y.J. Jeong, J. Piao, D. Kim, D. W. Lee, N-/S- dual doped C@ZnO: An excellent material for highly selective and responsive NO_2 sensing at ambient temperatures, Chem. Eng. J. 421 (2021) 127740
[81] Y. H. Zhang, Y. L. Li, F.L. Gong, K. F. Xie, M. Liu, H. L. Zhang, S. M. Fang, Al doped narcissus-like ZnO for enhanced NO_2 sensing performance: An experimental and DFT investigation, Sens. Actuators B Chem. 305 (2020) 127489
[82] K. Sun, G. Zhan, L. Zhang, Z. Wang, S. Lin, Highly sensitive NO_2 gas sensor based on ZnO nanoarray modulated by oxygen vacancy with Ce doping, Sens. Actuators B Chem. 379 (2023) 133294.
[83] M. Mukherjee, R. Jana, A. Datta, Designing C_6N_6/C_2N van der Waals heterostructures for photogenerated charge carrier separation, Phys. Chem. Chem. Phys. 23 (2021) 3925.
[84] D. R. Jones, T. G. G. Maffeïs, Analysis of the kinetics of surface reactions on a zinc oxide nanosheet-based carbon monoxide sensor using an Eley-Rideal model, Sens. Actuators B Chem. 218 (2015) 16−24.
[85] N. M. Vuong, D. Kim, H. Kim, Surface gas sensing kinetics of a WO_3 nanowire sensor: Part 2-Reducing gases., Sens. Actuators B Chem. 224 (2016) 425−433.
[86] H. Hu, M. Trejo, M. E. Nicho, J. M. Saniger, A.G. Valenzuela, Adsorption kinetics of optochemical NH_3 gas sensing with semiconductor polyaniline films, Sens. Actuators B Chem. 82 (2002) 14−23.

CHAPTER-VII

Band Gap Engineered n-n Type Zinc Oxide-Zinc Ferrite Heterostructure for Enhanced CO Sensing: An Experimental Study Supported by Theoretical Calculation

[Part of the manuscript is under review]

7.1 Introduction

The exponential increase in demand driven by the continuously expanding global population has given rise to two major challenges: the depletion of fossil fuel resources and the onset of overall environmental pollution. Overutilization of fossil fuels releases various toxic pollutant gases in the environment such as NO_x, SO_x, CO, greenhouse gases, which leads to global warming. Carbon monoxide (CO) is a colourless and odourless gas that is primarily generated through the incomplete combustion of fossil fuels. Diesel and gasoline-powered vehicles, thermal power plants, coal-fired furnaces, and gasoline engines are the primary sources responsible for the emission of CO into the environment.[1,2] Exposure to elevated levels of carbon monoxide (CO) can have detrimental effects on animals. Inhalation of excessive CO in the environment leads to its absorption into the bloodstream through the respiratory system. CO exhibits a 250 to 300 times greater binding affinity to human blood, higher than that of oxygen. Carbon monoxide reacts with haemoglobin to generate carboxy haemoglobin (COHb), which is primarily incapable of delivering oxygen to bodily tissues and essential cells. Thus, exposure to high concentrations of CO can result in a variety of health risks, including headaches, nausea, fast breathing, weakness, tiredness, disorientation, and confusion. The health risks posed by carbon monoxide are particularly severe for unborn babies, children, and older adults, as they may be more vulnerable to brain damage and life-threatening heart issues. Additionally, exposure to CO can worsen symptoms for individuals with asthma and chronic pulmonary conditions. As per United States Occupational Safety and Health Administration (OSHA) guidelines maximum exposer limit for a healthy person is 35 ppm. Hence development of highly sensitive and selective CO sensor is need of the society. [3–5]

Semiconductor metal oxide based chemiresistive CO sensor plays crucial role for their easy to fabricate and cost effectiveness. Moreover, metal oxide heterostructure-based materials have distinctive electrical properties, they also have demonstrated very selective and sensitive gas sensing performance in the realm of chemiresistive gas sensing. Over the decades, researcher had tried to enhance efficacy of all such gas sensing performance by strategically modulating many factors such as particle surface to volume ratio, morphology, shape, electronic properties, energy band gap, and defect states through doping in the pristine materials. However, there are still a few major drawbacks associated with both pristine and doped materials such as insufficient charge separation, immobility of charge carriers, and charge recombination. In order to address these drawbacks, scientists have experimented with heterojunction catalysts,

which are synthesized by combining two distinct semiconducting materials with dissimilar band structures for generating free charge carrier and the separation of charge at the interface.

Among different binary SMOs zinc oxide (ZnO) serves as a wide-band gap n-type metal oxide, extensively employed in catalysis and sensing applications due to its-proficient light absorption and photo response characteristics.[6–9] Despite its advantageous properties, pure ZnO faces challenges such as a wide band gap, increased electron-hole recombination rates, and pronounced photobleaching effects when utilized as a surface catalyst. To address these limitations and enhance its gas sensing and surface catalytic capabilities, different light sensitizers with lower band gaps are integrated with ZnO. Recently, the spinel ferrites such as MFe_2O_4 (M = Ni, Mg,Cu, Ca, Zn, Co etc.) were extensively studied in the field of gas sensing because of their lower bandgap energy, enhanced surface activity.[10–15] Although gas sensing performance of pure ferrites has not showed much efficient result due to their high recombination rate.

Herein this work, the cooperative integration of n-type ZnO with n-type spinel $ZnFe_2O_4$ (ZFO) in different molar ratio is poised to elucidate the effective establishment of a heterostructure to elevate its sensing performance. The creation of a heterojunction interface not only augments the active surface area of the catalyst but also adjusts the band structure of the composite material, facilitating the optimization of the catalyst's energy levels for specific reactions. Additionally, the formation of the heterojunction significantly reduces photo-corrosion in the catalyst, thereby extending its operational lifetime. These design modifications collectively minimize the likelihood of charge carrier recombination, resulting in an amplified gas sensing performance. Detailed gas sensing study reveals that 50% ZnO - 50% $ZnFe_2O_4$ based sample (ZZF-11) showed highest response to 1ppm CO gas (S= 29.4%).

Presence of highest ferric bivalence state, increased defects and chemisorbed oxygen content, donor defect states, higher surface area, stable photocurrent in ZZF-11 sample play combining effect in showing best sensing performance. DFT study revealed changes of electronic band structure due to formation of ZnO-ZFO heterostructure. Electron density distribution at the interface of ZnO and ZFO was calculated which shows the presence of abundant of electrons at the heterojunction interface. The simulation results also indicate that electrons transfer from ZFO to ZnO, which aligns precisely with the experimental findings. Moreover, enhanced CO sensing of heterostructure compared to the pure samples is theoretically validated by adsorption energy calculation using DFT simulations.

7.2 Experimental section

7.2.1 Chemical and reagents

Zinc nitrate hexahydrate ($Zn(NO_3)_2 \cdot 6H_2O$), Iron(III) nitrate nonahydrate ($Fe(NO_3)_3 \cdot 9\ H_2O$), citric acid ($HOC(COOH)(CH_2COOH)_2$), Poly ethylene glycol-400 (PEG-400 $H(OCH_2CH_2)_nOH$), ethanol were purchased from Merck chemicals and used directly without further purification. Customized lab prepared Deionized (DI) water was used to prepare all aquas solution.

7.2.2 Synthesis of ZFO

Pristine Zinc ferrite (ZFO) was synthesized by solution evaporation method. 0.5 mmol of ($Zn(NO_3)_2 \cdot 6H_2O$) was dissolved in 100ml DI water to prepare solution-I and 1 mmol of ($Fe(NO_3)_3 \cdot 9\ H_2O$) was dissolved in 100 ml DI water separately to prepare solution-II. Then, the above solutions were transferred to a larger beaker and 1.5 mmol of citric acid was mixed to it. The final solution was kept under continuous stirring with 350 rpm at a fixed 90 ºC temperature nearly for 6 hrs until a brown flappy ash formed after complete burning of the solution which was next grinded to fine dust. The brown fappy ash then transferred to 120 ºC oven for 24 h for thermal etching. Finally, the material was calcined at 600 ºC for 2 h to get phase pure ZFO nano powder.

7.2.3 Synthesis of ZnO-ZFO

ZnO-ZFO heterostructures were prepared by the facile refluxing method. Calculated amount of as synthesized ZFO was mixed in 50ml DI water using magnetic stirrer to prepare solution-III. 1mmol ($Zn(NO_3)_2 \cdot 6H_2O$) was mixed in 150ml DI water and 10 ml PEG-400 was added to the aquas solution, which was named as solution-IV. Next, solution-III and solution-IV were mixed together and kept on a magnetic stirrer for 2 h at 60 ºC. The final solution was transferred to customised reflux unit for 4 h at 120 ºC. After completion of the refluxing process the precipitate was centrifuged at 7000 rpm for 20 min and washed several times with DI water and ethanol. The solid precipitate was finally sintered at 500 ºC for 1 h to achieve the ZnO-ZFO composites. Based on the molar ratio of ZnO and ZFO, composite materials were marked with ~~a~~ unique name as given in Table- 7. 1. Schematic of the synthesis procedure is shown in the Fig. 7. 1.

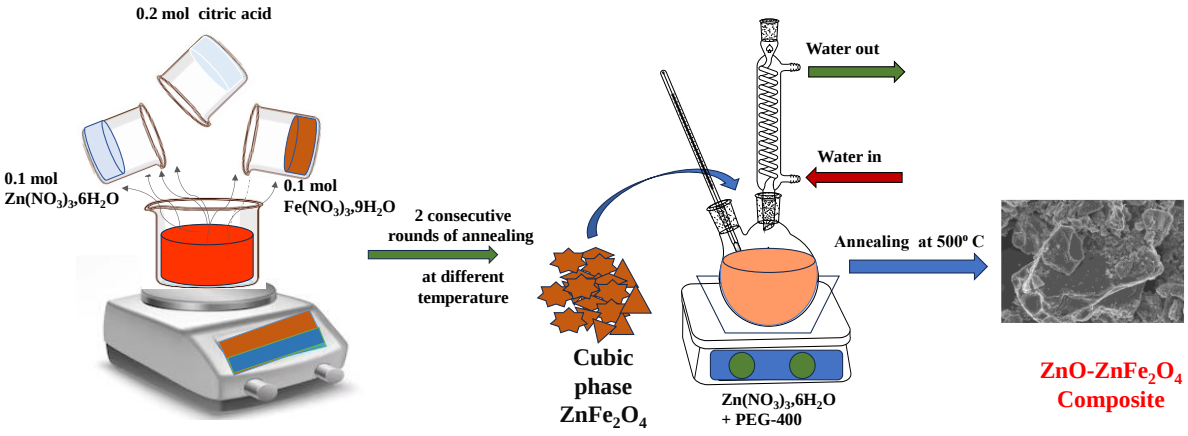

Fig. 7. 1. Schematic of synthesis procedure of ZnO- ZFO heterostructure.

Table- 7. 1: Composition details, elemental atomic % details as calculated from EDX , Surface electronic states details from XPS analysis, BET surface area, Band gap energy, details of donor defect density as calculated from PL analysis of all the synthesized samples

Sample name	**Composition in synthesized condition (in wt.-%)**		**Elemental analysis from EDX analysis. (in atomic %)**			**Surface electronic states details from XPS analysis**				**BET surface area (m^2/g)**	**Band gap energy (eV)**	**Donor defect density as calculated from PL analysis**
	ZnO	**ZFO**	**Zn**	**Fe**	**O**	**O_L**	**O_D**	**O_C**	**Fe^{2+}/Fe^{3+}**			
ZnO	100	0	48.6	-	51.4	62.7%	26.4%	10.9%		7.0	3.10	24.4%
ZFO	0	100	14.4	24.7	60.9	68.0%	26.2%	5.8%	0.06	12.5	2.05	24.3%
ZZF-31	75	25	28.5	14.1	57.4	58.2%	30.4%	11.4%	0.22	17	2.40	28.5%
ZZF-11	50	50	23.9	20.5	55.5	28.9%	53.3%	17.8%	0.36	27	2.30	34.2%
ZZF-13	25	75	17.2	22.0	60.8	54.8%	34.9%	10.3%	0.15	24	2.15	29.1%

7.2.4 Material characterizations

The crystal diffraction pattern and the purity of crystalline phase were analysed using X-ray diffractometer (PANalytical X′ Pert pro MPD XRD, Cu Kα, λ =1.5418 Å). Morphology of the synthesized samples were examined from field emission scanning electron microscopy (FESEM, Carl Zeiss, Supra 35 V P microscope) and transmission electron microscope (TEM, FEI Tecnai G230ST). Elemental composition of the samples was analysed by Energy-dispersive X-ray spectroscopy (EDX Oxford Instrument and EDAX Inc.) equipped-with the FESEM. Optical properties, energy band gap, presence of different defects states were investigated utilizing UV–Visible spectrophotometer (UV-3600) and fluorescence spectrophotometer (PL, Horiba FluoroMax-4 spectrometer). Presence of different chemical bonds in the synthesized materials were obtained by the Fourier transform infrared spectrometry (FTIR, Nicolet 380). The chemical states of Zn, Fe and O were analysed using X-ray Photoelectron Spectroscopy (XPS microprobe, ULVAC-PHI 5000 Versa Probe II, U.S). Brunauer-Emmett-Teller (BET) surface area, pore size distribution, the N_2-adsorption/ desorption isotherms of the samples were obtained using NovaWin, Quantachrome Instrument.

7.2.5 Fabrication and measurement of gas sensors

Taguchi type thick film sensor was fabricated using Al_2O_3 made cylindrical substrate and inhouse customized drop coating set up. Detailed fabrication procedures were shown in earlier reports. [16,17] Commercially available gas cylinders, N_2 cylinders and Alicat made mass flow meter (MFC) were used for gas sensing measurement of various gas concentration. Keysight made digital multimeter (Model No. 34470A) and the allied data acquisition software was used to record dynamic resistance of the chemiresistive sensors. The sensor was heated until a stable resistance was achieved (indicated as R_{air}) and consequently specific gas was purged on to the sensor. Detailed gas sensing measurement set up is depicted elsewhere. [18,19] In presence of specific gas resistance of the sensor was decreased which was indicated as R_{gas}. Response of the sensor was calculated as,

$$S_g = \left(\frac{R_{gas}-R_{air}}{R_{air}}\right) \times 10 \quad \ldots\ldots\ldots\ldots\ldots\ldots(1)$$

7.2.6 Computational Methods

The Vienna *Ab-Initio* Simulation Package (VASP) was used to perform the Density Functional Theory (DFT) calculations. Projector-Augmented Wave (PAW) pseudopotentials were utilized to model the interactions between valence electrons and ionic cores. The electronic properties were studied using the Perdew-Burke-Ernzerhof (PBE) parameterized exchange-correlation (ε_{xc}) functional within the generalized gradient approximation (GGA). The Dudarev formalism [20], incorporating U_{eff} values of 10 eV, 7 eV, and 5.3 eV for Zn (d), O (p), and Fe (d) orbitals, respectively, was used to apply the Hubbard U correction[21,22]. The structures were optimized until the Hellmann-Feynman forces were smaller than 10^{-3} eV/Å. Self-consistent energy calculations were performed with a tolerance of 10^{-5} eV and a kinetic energy cutoff of 600 eV. To integrate the Brillouin zone, we used a Gamma-centered *k*-grid of 10 x 10 x 6, 6 x 6 x 6, and 8 x 8 x 2 for ZnO, ZFO, and ZnO-ZFO (ZZF-11), respectively. When studying carbon monoxide (CO) adsorption, we selected the most stable surface for each composition. For ZnO, the $(10\bar{1}0)$ non-polar surface was chosen based on previous studies. [21–24] For ZFO, we carefully evaluated the DFT energies for the reported most stable slabs, i.e., (110) and (111) ZFO.[25,26] The (110) ZFO slab is more stable than the (111) slab due to its more negative energy. For ZnO and ZFO, we used a 32-unit cell slab with a = 43.87 Å, b = c = 20 Å and a 16-unit cell slab with a = b = 11.93 Å, c = 23.66 Å, respectively. We prepared the ZZF-11 heterostructure with a = b = 8.56 Å, and c = 31.99 Å. A 15 Å vacuum perpendicular to the surface was applied to avoid interaction between periodic images. The slabs were optimized with the GGA ε_{xc}, including the vdW correction.[27] The adsorption energies were evaluated using a 1 x 3 x 3, 3 x 3 x 1, and 1 x 3 x 3 Gamma-centered *k*-grid for ZnO, ZFO, and ZFO-11, respectively.

7.3 Results and discussion

7.3.1 XRD & FTIR analysis

The crystal structure and phase composition of pure ZnO, ZFO and the ZnO-ZFO composites were investigated using XRD. As shown in Fig. 7. 2 (a) all the diffraction peaks corresponding to pure ZnO exactly matched with wurtzite phase of ZnO (ICDD card no. 01-079-0207), whereas all the diffraction peaks corresponding to pure ZFO perfectly matched with the Cubic phase of ZFO (ICDD card no. 01-087-1230). For the three composite materials (ZZF-31, ZZF-11, ZZF-13) characteristic peaks of both the ZnO (wurtzite) and ZFO (cubic) were found which

indicates co-existence of ZnO and ZFO in the composite samples. Diffraction peaks of all five samples in the 2θ range from 34.5º to 37º is shown in Fig. 7. 2 (b) to analyse the shift and change in relative intensity of the most intense characteristics peak of ZnO (at 2θ=35.8º) and ZFO (at 2θ=35.22º) in the composite materials. Both the peaks got shifted slightly in all the composite samples from their original position which indicates the formation of heterostructure materials. Additionally, it can be observed from the Fig. 7. 2 (b), relative intensity of the ZnO peak (at 2θ=35.8º) gradually diminished from ZZF-31 to ZZF-13 which exactly matches with the molar weight ratio of ZnO and ZFO in the composite samples.

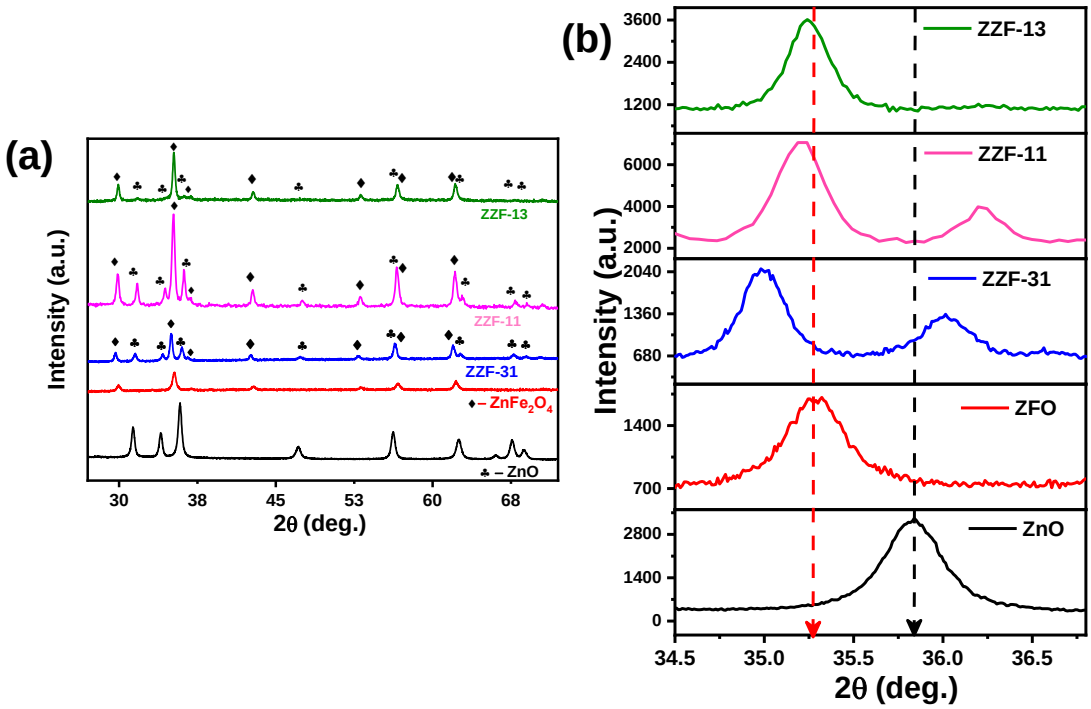

Fig. 7. 2. (a) XRD pattern of all the samples, (b) Magnified XRD pattern of all the samples in the 2θ=34.5º-37º

FTIR spectra in the range of 400-4000 cm^{-1} of all pure and composite nanoparticles are shown in Fig. 7. 3 (a). In Fig. 7. 3 (b) FTIR spectra of ZZF-11 sample is shown elaborately by indicating the centre of each transmission peak. For the pristine ZnO sample a major characteristic peak at 478 cm^{-1} was found corresponding to the stretching of Zn-O bond. For the pure ZFO sample 2 major characteristic peaks were observed at 467cm^{-1} and 543 cm^{-1} which are attributed to the Zn-O bond stretching vibration at octahedral site and Fe-O bond stretching vibration at the tetrahedral site of the spinel ferrite respectively. Whereas in all three composite samples (ZZF-31, ZZF-11, ZZF-13) two major characteristic peaks were identified

corresponding to the Zn-O bond stretching vibration and Fe-O bond stretching vibration respectively. Interestingly, the transmission intensity corresponding to Zn-O bond gradually decreases with respect that of the Fe-O bond from ZZF-31 to ZZF-13 which also indicates that amount of ZnO decreases as it transforms from ZZF-31 to ZZF-13. Moreover, in all five samples few major transmission peaks were observed at 1108 cm^{-1}, 1315 cm^{-1},1384 cm^{-1}, 1627 cm^{-1},2923 cm^{-1}, and 3436 cm^{-1}. Peaks at 1108 cm^{-1}, and 1315 cm^{-1} are attributed to the primary, secondary alcohol vibration. Peak at 1384 cm^{-1} is corresponding to the C-H bond vibration originated due to organic surfactant (PEG-400). Peaks at 1627 cm^{-1} was originated due to the bending vibration of absorbed water on the surface of the material. Whereas peaks at 2923 cm^{-1}, and 3436 cm^{-1} were corresponding to the hydroxyl compounds and stretching and bending vibration of surface – OH group respectively.[28–31]

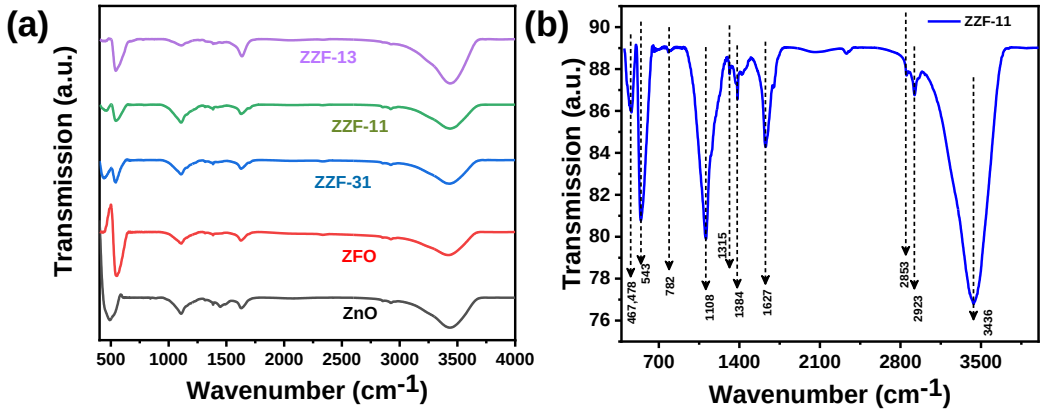

Fig. 7. 3. (a) FTIR spectra of all the samples, (b) FTIR spectra of ZZF-11 sample.

7.3.2 Morphology studies

Morphology of the synthesized pure and composite materials were examined using FESEM and TEM analysis as shown in Fig. 7. 4, Fig. 7. 6. Pure ZFO was formed in nearly spherical shape (ref. Fig. 7. 4 (a)). Radius of the ZFO nano sphere as measured using ImageJ software was ~ 20 nm. FESEM micrographs of ZZF-11 composite suggest that, spherical ZFO particles were densely coated on the ZnO nanosheet. It can be interfered from the micrographs that the ZnO nanosheet was grown around the dispersed spherical zinc ferrite nanoparticles in the suspension following the well-known heterogeneous seeded growth technique. Overall, the FESEM micrographs of ZZF-11 sample indicates the successful formation of ZnO-ZFO heterostructure.

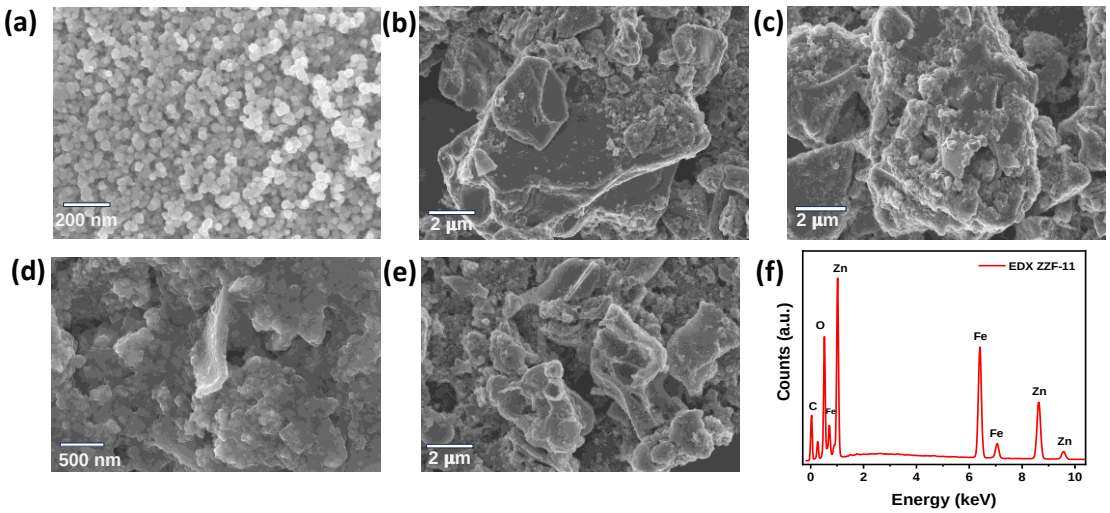

Fig. 7. 4. FESEM micrographs of (a) ZFO, (b) ZZF-31, (c-d) ZZF-11, (e) ZZF-13, (f) EDX spectra of ZZF-11.

Quantitative EDX and corresponding elemental mapping were taken for the pure and composite samples. The composite samples exhibit a consistent distribution of Zn, Fe, and O, as indicated by elemental mapping, confirming the successful preparation of ZnO-ZFO heterojunctions (ref. Fig. 7. 5.). The atomic percentage of Zn, Fe, and O atoms in the sample were measured from EDX analysis as presented in Table- 7. 1. The molar ratio of Zn/Fe in the composite samples indicates ZFO dissolved completely in the zinc nitrate precursor solution while ZnO had formed in pure crystalize form during synthesise reaction. Additionally, the Zn/Fe molar ratio shows that the theoretically calculated molar ratio of the composite material is almost identical to the value that was measured experimentally.

Transmission electron microscopy (TEM) images was taken for pure ZFO and ZZF-13, ZZF-11, ZZF-31 sample as shown in Fig. 7. 6 (a-d). Micrograph clearly indicates spherical shape ZFO was formed. Whereas for the composite samples sheet like ZnO was grown and spherical ball shaped ZFO are distributed surrounding the ZnO sheet. It is noteworthy that the ZZF-11 composite sample comprises an intimate interface between ZnO and ZFO, indicating the successful establishment of a heterojunction-catalyst boundary. HRTEM images further demonstrate the effective generation of the ZnO-ZFO composite. Where, two distinct lattice spacings of 0.25 nm and 0.35 nm are seen in Fig. 7. 6 (e), which correspond to the ZFO (311) and ZnO (220) planes, respectively.

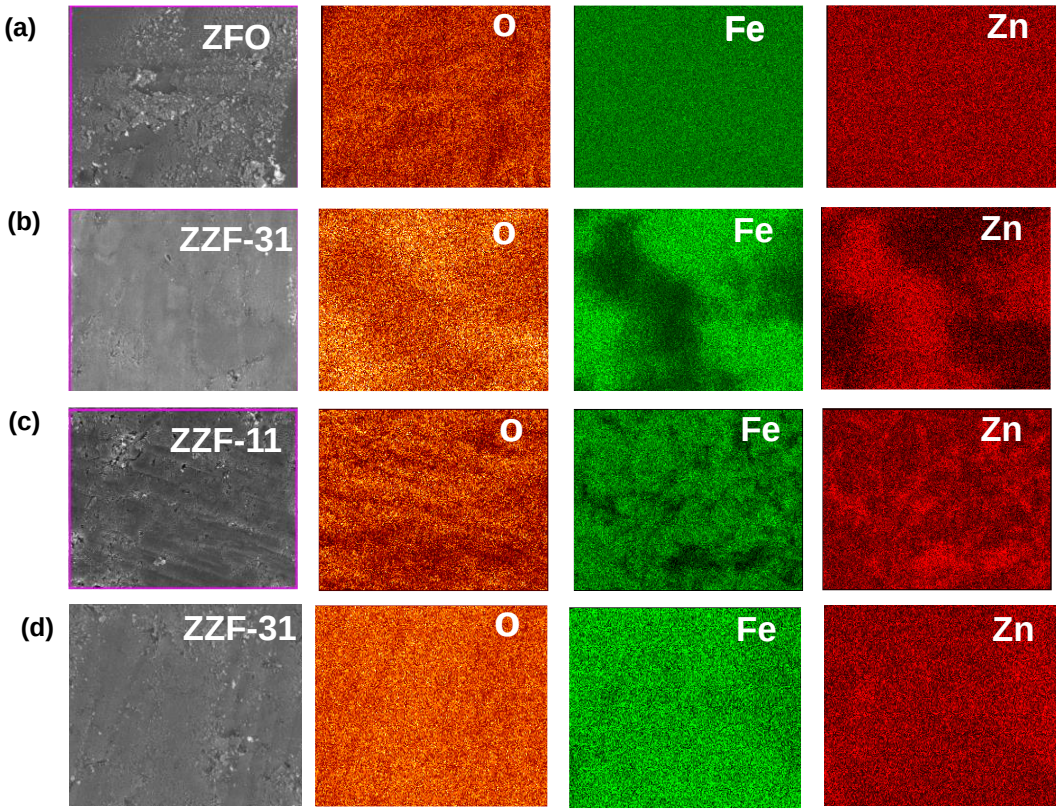

Fig. 7. 5. EDS selected elemental colour mapping area of (a) ZFO, (b) ZZF-31, (c) ZZF-11 (d) ZZF-31 (O, Fe, Zn elements are shown in different colours).

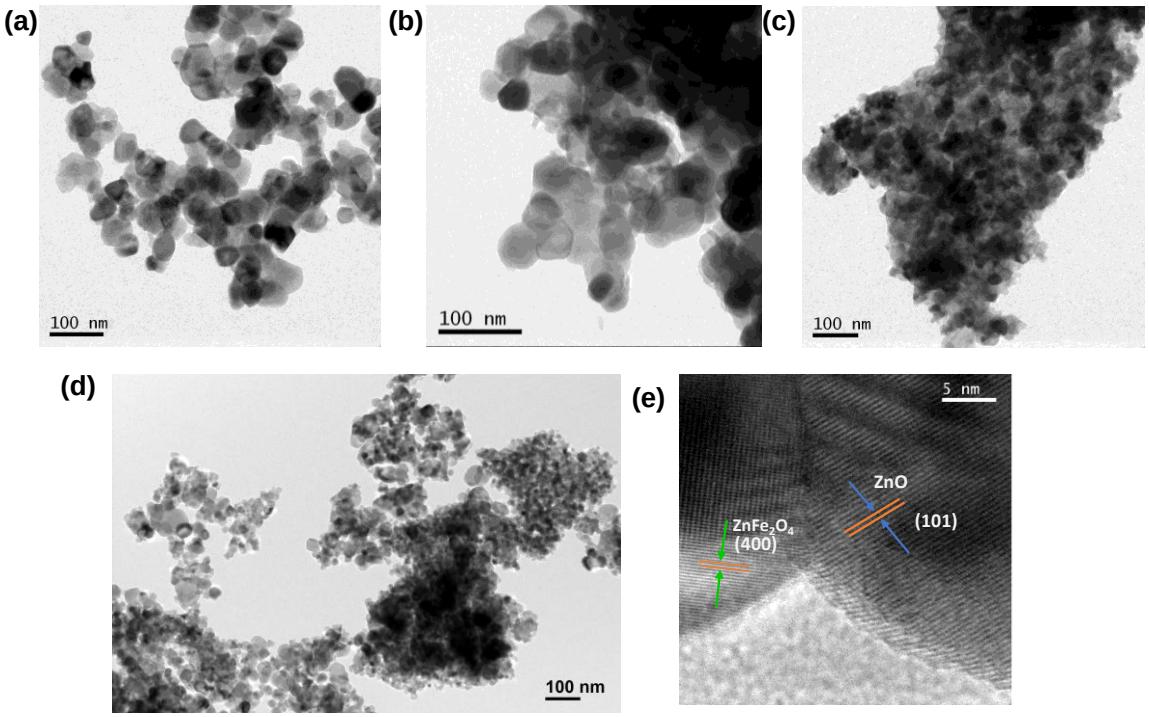

Fig. 7. 6. TEM micrographs of (a) ZFO, (b) ZZF-31, (c) ZZF-13, (d) ZZF-11, (e) HRTEM image of ZZF-11.

7.3.3 X-ray photoelectron spectroscopy and surface compositions

X-ray Photoelectron Spectroscopy (XPS) analyses were employed to conduct a quantitative investigation of the electronic structures and chemical states of both the pure and heterojunction catalyst. The XPS survey scan spectra illustrated in Fig. 7. 7 (a) reveal the simultaneous presence of Zn, Fe, O, and adventitious C.

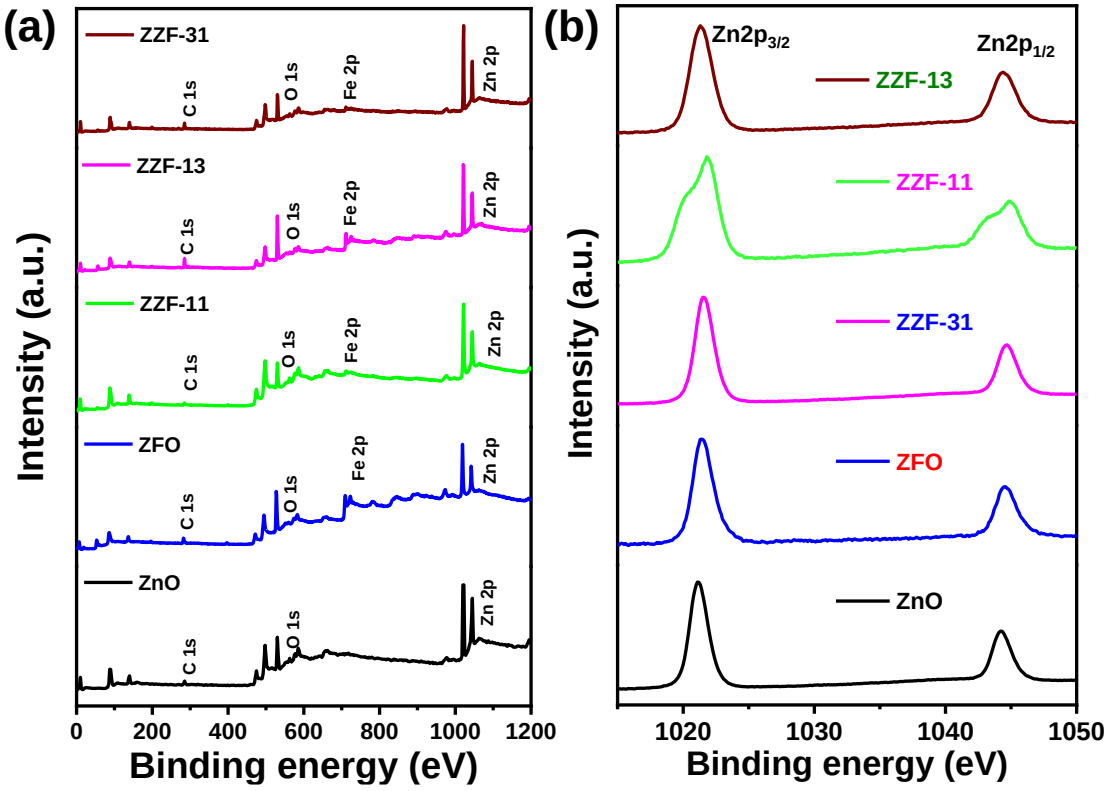

Fig. 7. 7. (a) XPS survey scan of ZnO, ZFO, ZZF-11, ZZF-13, ZZF-31. (b) HR-XPS spectra of Zn2p region of all the samples.

In the High-Resolution X-ray Photoelectron Spectroscopy (HR-XPS) spectra of Zn 2p (Fig. 7. 7 (b)), the peaks observed at approximately 1021.3 eV and 1044.4 eV correspond to Zn $2p_{3/2}$ and Zn $2p_{1/2}$, respectively which indicates the presence of the Zn^{2+} oxidation state in all the samples. Interestingly, Zn 2p peak in ZZF-11 sample clearly has asymmetric Zn2p peak, which exhibits spin-orbit split peaks corresponding to Zn $2p_{3/2}$ and Zn $2p_{1/2}$. Both the Zn $2p_{3/2}$ and Zn $2p_{1/2}$ peaks are separately fitted with two Gaussian peaks situated at around 1021.7, 1022.9, 1044.8 and 1046.35 eV respectively which confirms that Zinc is present in 2+ oxidation state at the octahedral site of ZFO and ZnO in the composite sample. As shown in Fig. 7. 8 (a-d), HRXPS spectra illustrate the presence of Fe 2p electronic state in pure and composite samples. Two distinct peaks were observed at 710.1 eV and 724.7 eV, respectively in all the samples

corresponding to Fe $2p_{3/2}$ and Fe $2p_{1/2}$ spectra which were generated due to the presence of Fe-O bond in the samples. Further both the Fe $2p_{3/2}$ and Fe $2p_{1/2}$ were deconvoluted in several gaussian peaks centred at 710.8 eV and 724.4 eV, 724.6 and 736.7eV. Asymmetry in Fe $2p_{3/2}$ and Fe $2p_{1/2}$ peak signifies that the iron in present in bivalent oxidation state in the samples. Peaks corresponds to 710.8, 724.6 eV are attributed to Fe^{2+} species whereas peaks centered at 724.4 and 736.7eV signifies the presence of Fe^{3+} species in the samples. Detail XPS analysis indicates that the Fe^{3+} ion states are predominant in both the pure ZFO and composite samples, with the presence of Fe^{2+} as a consequence of electron hopping at the octahedral site. Relative percentage of each peaks are calculated from the fitted curves and shown in Table-7.1.

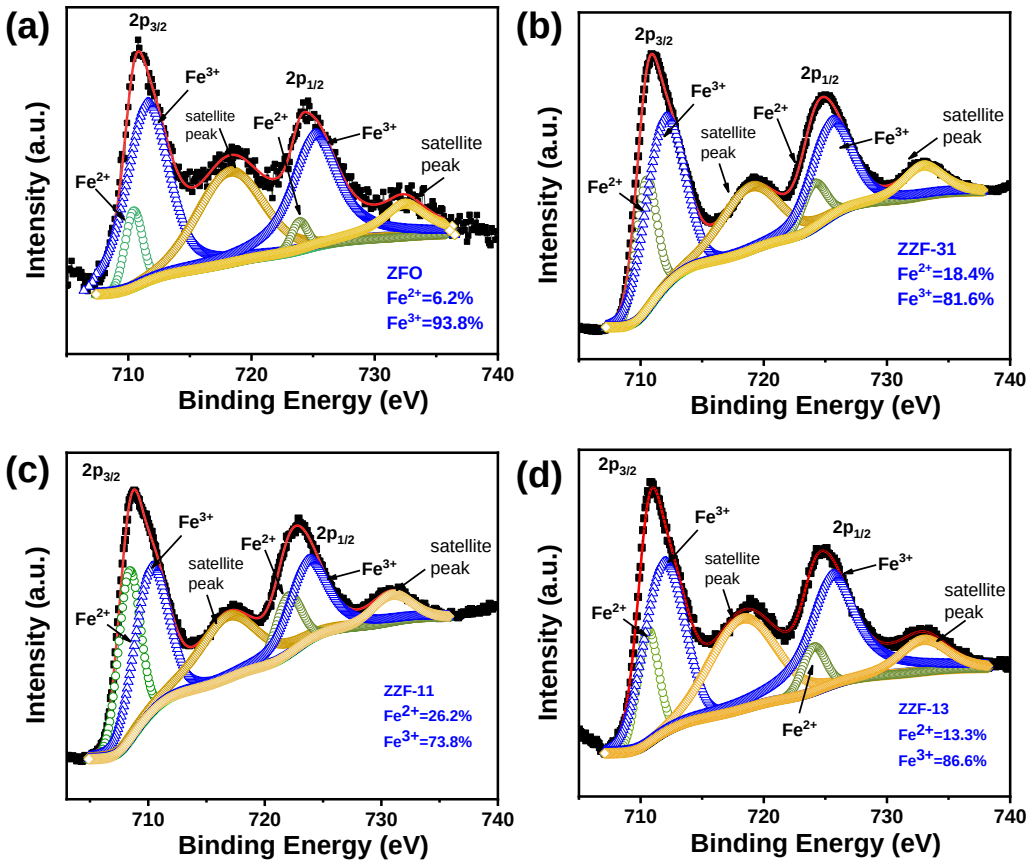

Fig. 7. 8. HR-XPS spectra of Fe2p region corresponding to (a) ZFO (b)ZZF-31, (c) ZZF-11, (d) ZZF-13.

In Fig. 7. 9 (a-e), the O 1s peaks were deconvoluted into three distinct peaks at 529.1, 531.3, and 532.6 eV respectively in all the synthesized samples which are attributed to lattice oxygen, defective oxygen, and surface-adsorbed oxygen, respectively [35,36]. Variation of each oxygen species in pure and composite samples are calculated and presented in Table- 7. 1.

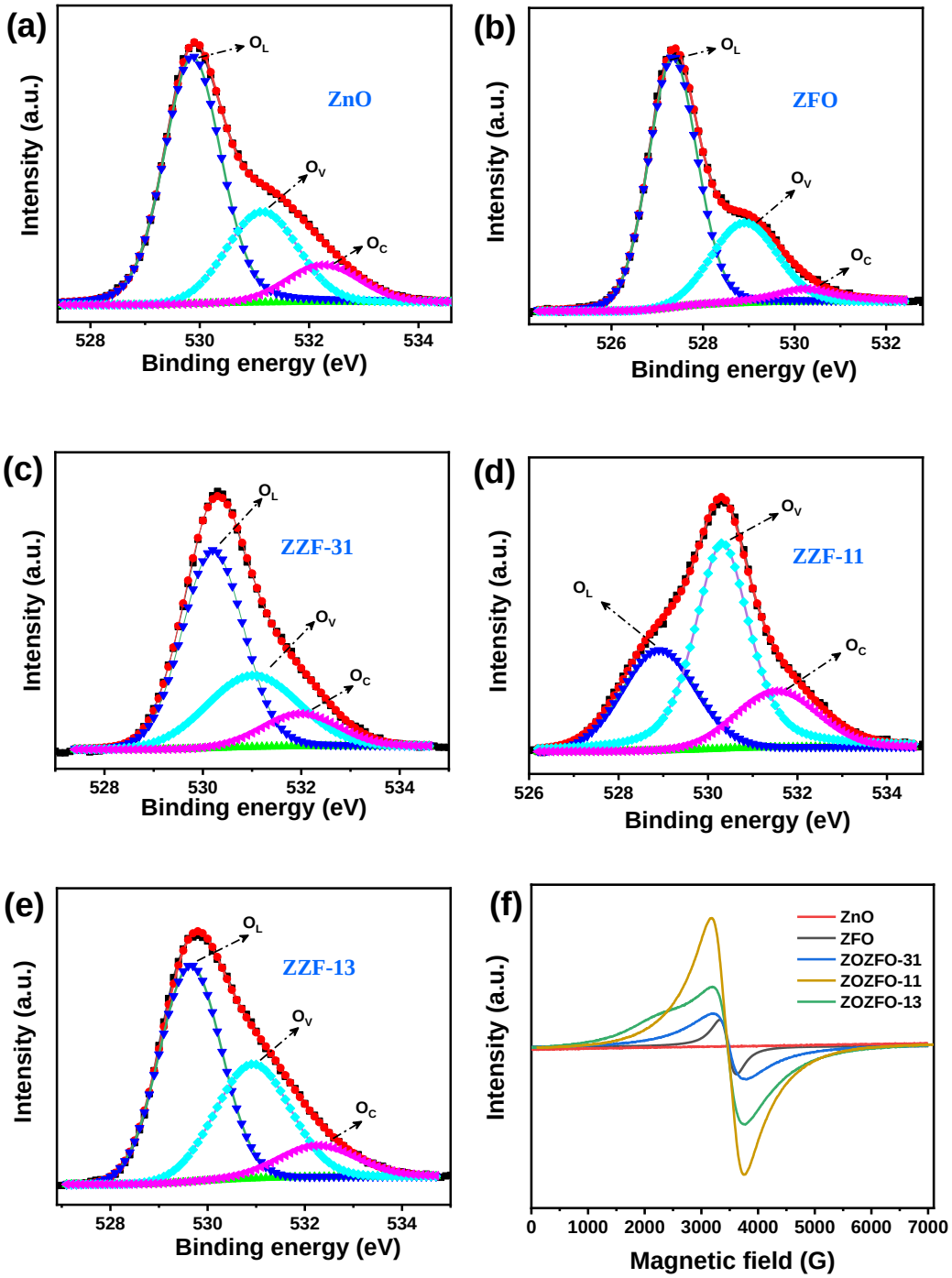

Fig. 7. 9. HR-XPS spectra of O 1s region corresponding to (a) ZnO, (b) ZFO, (c) ZZF-31, (d) ZZF-11, (e) ZZF-13, (f) EPR spectra of all the samples.

Electron paramagnetic resonance (EPR) spectra were utilized to validate the presence and progression of oxygen vacancies in both pure and composite samples (ref. Fig. 7. 9 (f)). No signal was detected in the pure ZnO sample, whereas a symmetrical signal at g = 2.003 was

observed in both the pure ZFO and the composite samples. By functioning as a trapping centre for photogenerated electrons, the oxygen vacancy centre reduces the possibility of recombination of these electrons with holes in the composite samples. Additionally, out of all the samples, ZZF-11 exhibits the highest EPR signal, indicating the sample's largest oxygen vacancies centre, which precisely aligns with the XPS O1s spectral analysis

7.3.4 Surface area analysis

The porosity and effective surface area of the synthesized samples were assessed through Brunauer−Emmett−Teller (BET) analysis utilizing the N_2 adsorption/desorption method, aiming to determine their potential as photocatalysts. The isotherm plots depicted in the Fig. 7. 10 (a) exhibit type-4 hysteresis behaviour, specifically of type IV classification, confirming the mesoporous nature of the synthesized samples. The BET surface areas for pure ZnO and ZFO are 7 and 12.5 m^2/gm, respectively. In contrast, for the heterostructure samples, the surface area significantly increased, reaching 17 m^2/g, 27 m^2/g, and 24 m^2/g for ZZF-31, ZZF-11, and ZZF-13, respectively. This notable augmentation in the specific surface area of heterojunction photocatalysts offers more reactive sites, thereby enhancing light absorption capacity during photocatalytic reactions compared to pure metal oxides. BJH method was used to calculate Pore size distribution of the pure and composite samples which indicates pore sizes and volume also became maximum for ZZF-11 among other samples. BJH curve of ZZF-11 sample is shown in Fig. 7. 10 (b). Variation of surface area, pore volume and pore diameter of in ZnO, ZFO, ZZF-31, ZZF-11, ZZF-13 samples is shown in Fig. 7. 10 (c).

7.3.5 Optical studies

Uv-vis adsorption spectra of the pure ZnO, ZFO and the heterostructures and the corresponding Tauc plots are shown in Fig. 7. 11 (a-f). Band gap energy of the samples were determined using classical Kubelka−Munk equation as follows,

$$\alpha h\upsilon = C(h\upsilon - E_g)^{1/2} \quad \text{.....(2)}$$

Where, α is the absorption coefficient and (hυ) indicates the energy of the incident photon in a direct-band semiconductor. The band gap of pure ZnO and ZFO were turned out to be 3.10 and 2.05 eV respectively which matches exactly with the previously reported values. Whereas, in the heterostructures the band gap values showed a systematic decreasing trend the with

increasing amount of zinc ferrite. Calculated values of band gap for ZZF-31, ZZF-11, ZZF-13 are 2.40 eV, 2.3 eV, 2.15 eV respectively. It is possible that the creation of a heterostructure between ZnO and ZFO, which would facilitate photon absorption, photogenerated charge carrier production, and separation. As a result, it causes the band gap energy to decrease with increasing ZFO content in the composite samples.[32–34]

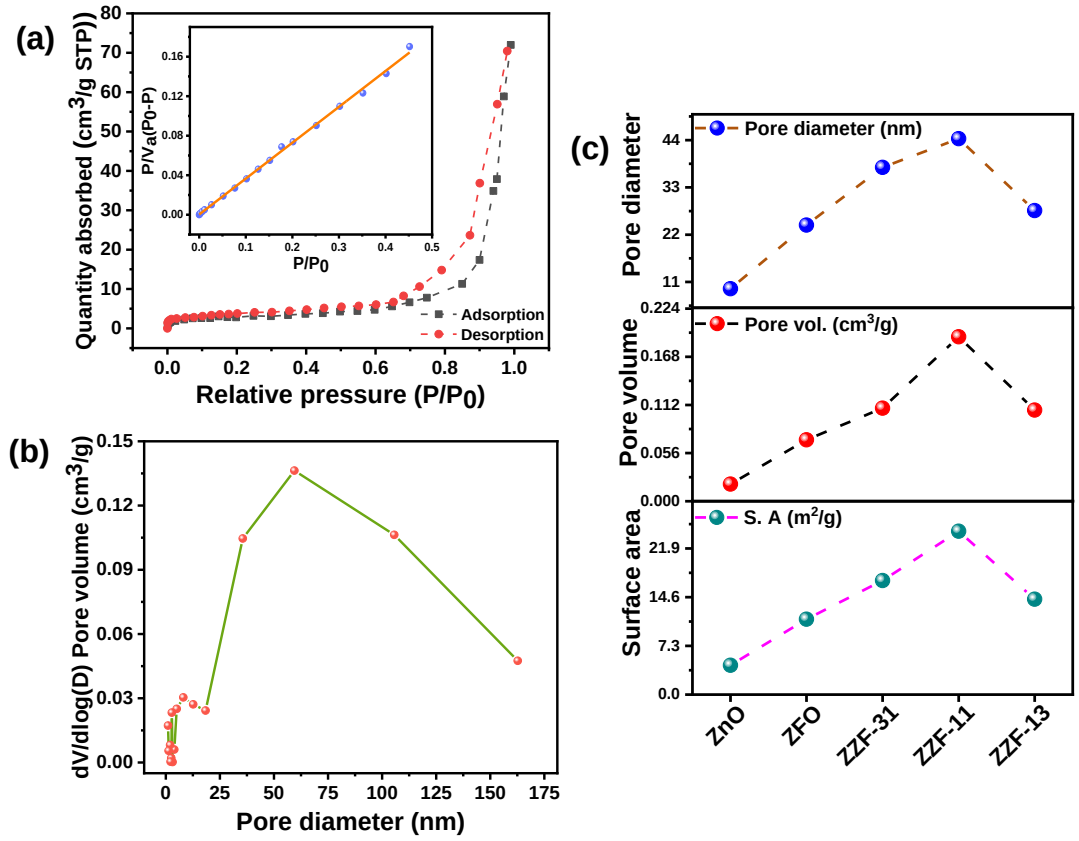

Fig. 7. 10. (a) N_2 adsorption-desorption isotherm of ZZF-11 (inset BET surface area curve of ZZF-11), (b) BJH pore size distribution curve of ZZF-11 sample, (c) Variation of surface area, pore volume and pore diameter of in ZnO, ZFO, ZZF-31, ZZF-11, ZZF-13 samples.

Photoluminescence (PL) spectra of both pure and composite samples were obtained at room temperature, with excitation at 325 nm. Photoluminescence (PL) are useful tool for measuring the effectiveness of the separation and recombination of photoinduced carriers of the as synthesized catalysts. As indicated by the photoluminescence (PL) spectra in Fig. 7. 12 (a), the ZZF-11 heterojunction exhibits a significantly reduced PL intensity compared to all other pure and composite samples. The reduction implies that the ZZF-11 heterojunction efficiently inhibits the recombination of electron-hole pairs.

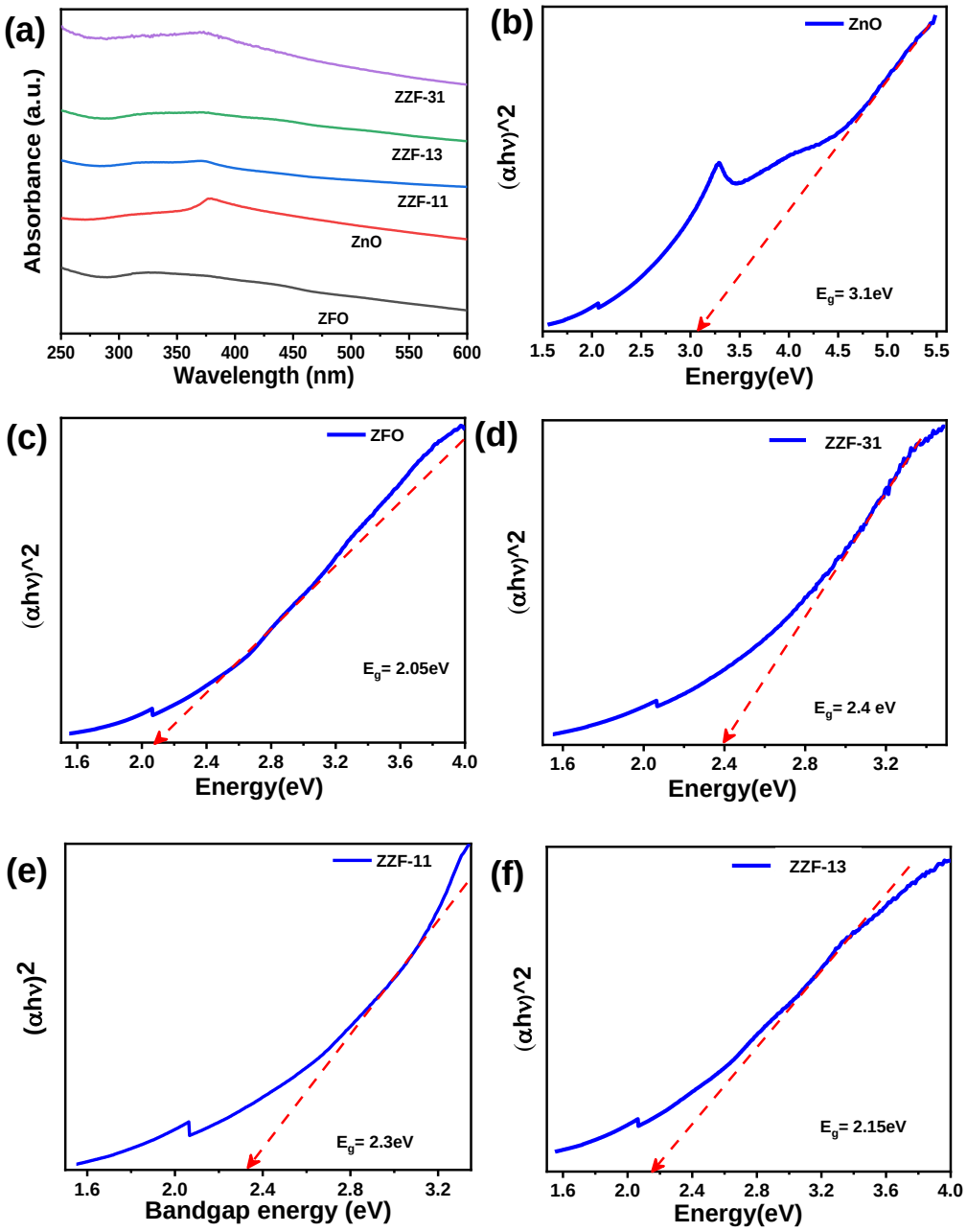

Fig. 7. 11. (a) UV-Vis adsorption spectra of all the samples, Tauc plot of (b) ZnO, (c) ZFO, (d) ZZF-31, (e) ZZF-11, (f) ZZF-13.

Moreover, the formation and evolution of various defect states in different samples were meticulously analysed by deconvoluting the Photoluminescence (PL) emission spectra.This process involved utilizing a Gaussian-Lorentzian fit to distinguish and identify six different peaks, providing detailed insights into the characteristics of defect states in the samples, as illustrated in Fig. 7. 12 (b-d). The initial prominent peak observed in the range of 398-402 nm

can be ascribed to the near-band-edge emission of the material. The violet-blue emissions observed in the range of 408-412 nm can be associated with zinc interstitials (Z_{ni}) or lattice deformation. The strongest blue emission peak, detected at 428–432 nm, is associated with the presence of extra iron (Fe) ions and self-activated centres in the synthesized nanomaterials. Zinc Vacancies (V_{zn}) might be responsible for the emission at 457–462 nm, whereas oxygen defects/vacancies or defect level emission (V_O) is responsible for emissions in the 495–499 nm range. Lastly, peak in range of 585-595 nm is correspond to the oxygen interstitial (O_i). Relative percentage of each emission are calculated from the area under the curve of that corresponding curve. Among these defects, Zn_i and V_o function as donor defect states, contributing free electrons to the system. Amount of donor defect content is calculated and shown in Table- 7. 1. Result indicates amount of donor defect content has increased in the heterostructure systems compared to the pure ZnO and ZFO samples and become maximum for ZZF-11 sample.

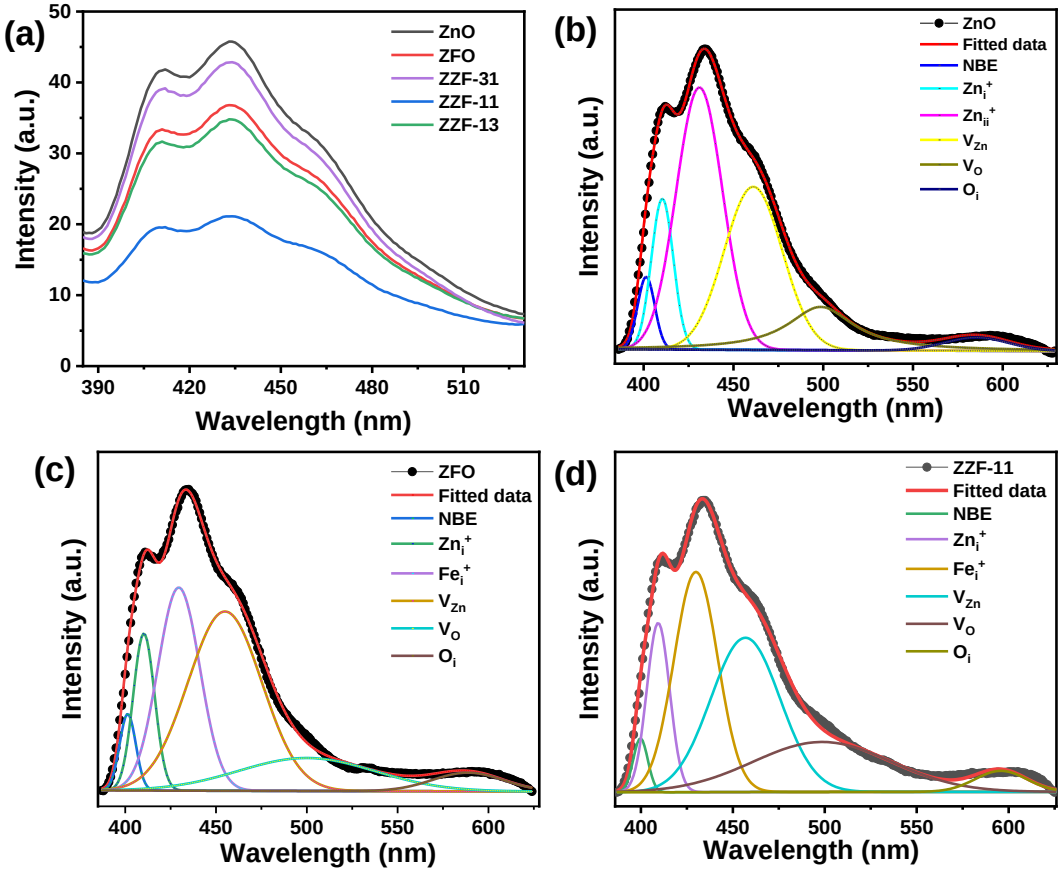

Fig. 7. 12. (a) Comparison of PL emission spectra of all the sample, Deconvoluted PL spectra of (b) ZnO, (c) ZFO, (d) ZZF-11.

7.3.6 Theoretical calculations

To gain a comprehensive understanding of the electronic properties of ZnO, ZFO, and ZZF-11, we estimated the band structures and atom-projected partial density of states (pDOS) for these materials. The investigation reveals that ZnO is a spin-unpolarized direct band gap semiconductor (ref. Fig. 7. 13 (a)), manifesting a band gap of 3.48 eV - a value in close agreement with experimental observations. The pDOS (as depicted in Fig. 7. 13 (d)) analysis further shows the composition of the valence band maximum (VBM), which mainly consists of O (p) orbitals, whereas the conduction band minimum (CBM) is primarily a result of the hybridization of Zn(s), O(s), and O(p) orbitals. In stark contrast to ZnO, ZFO emerges as a spin-polarized semiconductor, featuring distinct direct band gaps of 2.17 eV for the spin-down state and 3.14 eV for the spin-up state (ref. Fig. 7. 13 (b)). The pDOS plot depicts that the VBM is predominantly governed by O (p) orbitals, with a minor contribution from other orbitals for both spin up and down configurations. Conversely, the CBM is mainly composed of Fe (d) orbitals for spin down configuration while for spin up configuration, the CBM comprises of the hybridization of O(s), O (p), Zn (s), and Fe(s) orbitals (ref. Fig. 7. 13 (e)). The formation of the heterostructure (ZZF-11) leads to alteration of the electronic properties of these materials. We obtained a spin polarized semiconductor with spin-up and spin-down indirect band gaps of 2.19 eV and 1.66 eV, respectively (ref. Fig. 7. 13 (c)). However, there is a very small difference between the direct and indirect band gaps. The direct band gaps for spin up and down configurations are 2.43 eV and 1.69 eV, respectively. We observe a decrease in the band gap upon formation of heterostructure. Moreover, the conduction bands become more dispersive in comparison to ZnO and ZFO which results in the decrease of effective mass of electrons thereby increasing their charge carrier mobility. From Fig. 7. 13 (f), we observe that for the spin up configuration, the VBM is composed of O (p) orbitals while the CBM comprises of the hybridization of O (p) and Fe (d) orbitals. For the spin-down configuration, the VBM is mainly composed of Zn(s) orbitals with small contributions from Fe(s) and Fe (d) orbitals. However, the CBM is composed of the hybridization of Fe (d) and Zn (s) orbitals.

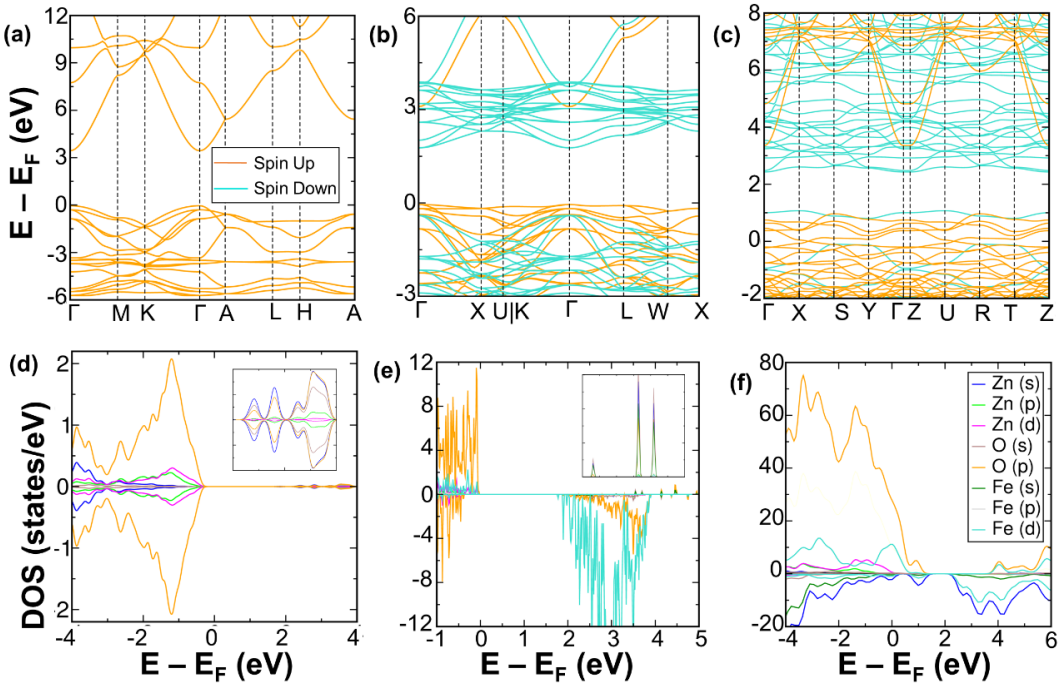

Fig. 7. 13. The electronic band structure and atom-projected partial density of states for (a, d) ZnO, (b, e) ZFO, and (c, f) ZZF-11, respectively. The inlets shown in figure (d) and (e) are the zoomed view of the conduction band edges of ZnO and ZFO.

7.3.7 Gas sensing behaviour

Gas sensing performance of the pristine ZnO, ZFO and the ZnO-ZFO composites were measured to analyse the beneficial effect of the formation of nanocomposite. Variation of the base resistance (R_{air}) of all the sensors were measure with varying operating temperature of the sensor as shown in Fig. 7. 14 (a). Base resistance of all the sensors shows an exponentially decreasing trend which delineates semiconducting nature of synthesised material. Response of any SMO sensor depends on the operating temperature of the sensor. Fig. 7. 14 (b) shows sensing response of the five sensors (ZnO, ZFO, ZZF-31, ZZF-11, ZZF-13) towards 100 ppm carbon monoxide (CO) gas at 150ºC-350ºC operating temperature. The pure ZnO, ZFO based sensors showed maximum response at slightly higher operating temperature at 320ºC and 250ºC respectively. Whereas for the composite material-based sensors shows more elevated response at relatively much lower temperature. The optimum operating temperature of ZZF-31, ZZF-11, ZZF-13 were turn out to be 240ºC, 190ºC and 220ºC respectively. Among all five

sensors ZZF-11 showed maximum 90% response towards 100ppm CO at its optimum operating temperature (at 190ºC) which was nearly 559% higher than the pure ZnO based sensor (S = 16.1%, measured at 320ºC) and 491% higher than the pure ZFO based sensor (S = 18.3%, measured at 250ºC). Presence of abundant amount of charge carriers due to the formation of the heterostructure interface plays crucial role in reducing the optimum operating temperature for the composite material-based sensors. All the further detailed gas sensing study were performed using the ZZF-11sensor. Background humidity plays an influential role in sensing response. Response of the ZZF-11 sensor was measured at different background humidity condition as shown in Fig. 7. 14 (c) which shows that at higher humid condition response of the sensor decreases slightly. In elevated humidity conditions, moisture tends to obstruct some of the active sites within the sensing material. Response of the sensors towards different CO concentrations (100, 50, 25, 10 ppm) were measured at optimum operating condition. ZZF-11 sensor showed highest response among all other sensors for all the different CO concentration (ref. Fig. 7. 14 (d)).

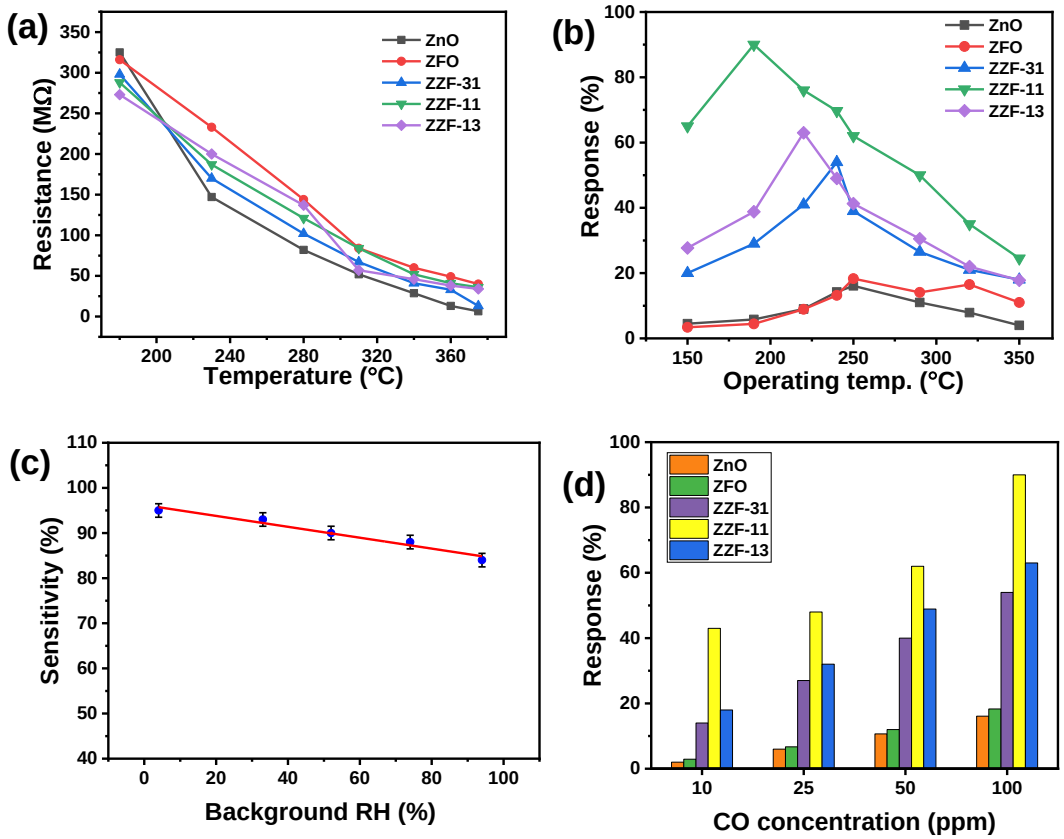

Fig. 7. 14. (a) Variation of the base resistance of the sensors with operating temperature, (b) Variatio of the response of the sensors with operating temperature, (c) Changes of the

sensitivity of the ZZF-11 sensor with background humidity, (d) Response of different sensors towards different CO concentration at their optimal operating temperatures.

Dynamic response-recovery curve of ZZF-11 sensor is shown in Fig. 7. 15 (a). Dynamic response curve of ZZF-11 also delineates the resolution of the sensor towards different CO concentration is remarkably well. Moreover ZZF-11 sensor shows significantly high response even to 1ppm CO gas (S= 29.4% at 340ºC).

Response of the sensor and concentration of the CO gas are corelated using Freundlich adsorption isotherm model as given in equation (3),

$$ln(S_g) = \ln(\alpha) + \mu ln(C_g) \ldots\ldots\ldots\ldots\ldots\ldots\ldots (3)$$

Where, S_g is the response of the sensor and C_g concentration of CO gas, α is the proportionality constant and μ is an exponent. The scatter plot exhibits a strong fit with a straight line (adjusted R2 = 0.95), having a slope (μ) < 1 (μ =0.23) which suggests predominant physisorption of CO molecules on the sensor surface (ref. Fig. 7. 15 (b)). Physisorption of gas molecules on the sensor surface indicates rapid recovery and reversibility of the sensor.

Furthermore, repeatability of the ZZF-11 sensor was checked by impinging 75 ppm CO gas to the ZZF-11 sensor at optimum operating temperature for five consecutive cycles. Sensor showed no significant change in the response even after five alternative cycles which proves the repeatable stable nature of the ZZF-11 sensor as shown in Fig. 7. 15 (c). The theoretical lower detection limit (LOD) of the sensor was measured using the following equation,

$$LOD = 3 \times \left(\frac{noise_{rms}}{sensitivity}\right) \ldots\ldots\ldots\ldots\ldots\ldots\ldots\ldots\ldots\ldots\ldots\ldots (4)$$

where, $noise_{rms}$ represent the standard deviation of the sensor. The calculated LOD value indicates that the ZZF-11 sensor could detect CO upto 100 ppb with a significant response of ~10%. To determine the response and recovery time of the ZZF-11 sensor, a multi-exponential model is employed to analyse the transient resistance curve of the sensing response. This model considers the adsorption and desorption phases separately, allowing for a more comprehensive estimation of the sensor's behaviour during these distinct processes. Adsorption phase (response) and desorption phase (recovery) of the curve fitted with the equation no (5) and (6) respectively,

$$R = R_O + A_1 e^{\left((t_o - t)/\tau_{response}\right)} \ldots\ldots\ldots\ldots\ldots\ldots\ldots (5)$$

$$R^{/} = R_O^{/} + A_2 e^{\left(t/\tau_{recovery}\right)} \ldots\ldots\ldots\ldots\ldots\ldots\ldots\ldots\ldots (6)$$

Where R, $R^{/}$ are the instantaneous resistance of the ZZF-11 sensor at the time of response and

recovery respectively, R_O , $R^/$ are two constant and $\tau_{response}$, $\tau_{response}$ are response and recovery time respectively. Fitted transient response curve of ZZF-11 sensor towards 75 ppm CO is shown in Fig. 7. 15 (d). Based on the analysis of the curve fitting, the sensor ZZF-11 exhibited response and recovery times of approximately 9 seconds and 4 seconds, respectively, when exposed to 75 ppm of CO.

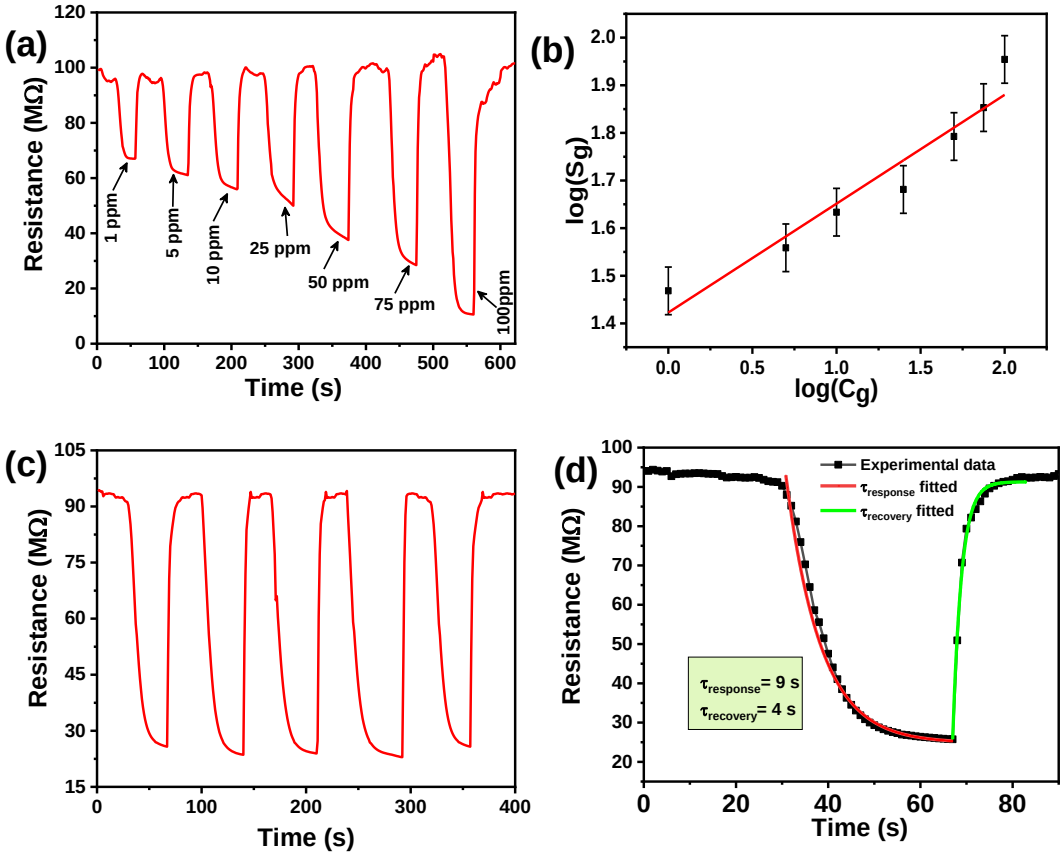

Fig. 7. 15. (a) Dynamic response curve of ZZF-11 sensor, (b) log(S_g) vs. log(C_g) curve for ZZF-11 sensor, (c) Repeatable response curve of ZZF-11 sensor towards 75 ppm CO gas at optimum operating condition, (d) Response and recovery time of ZZF-11 sensor towards 75 ppm CO gas.

Response of the ZZF-11 sensor towards 100 ppm CO was measured for more than 120 days to evaluate the long-term stability performance of the sensor. As shown in the Fig. 7. 16 (a), there was a very insignificant deviation in the response of the sensor even after 4 months. Error in long-term stability was measured which was less than 5% after 120 days which indicates the superior stability of the sensor. Further base resistance of the ZZF-11 sensor at optimum

operating conditions was also measured for 120 days interval as shown in Fig. 7. 16 (a), which delineates base resistance of the sensor also remained very stable for the longer time span. Selective gas sensing performance is one of the major parameters for practical applicability of any sensor. Response of the ZZF-11 sensor was measured towards six different relevant interfering gases such as CO, NO_2, SO_2, H_2S, NH_3, Formalin and for saturated moisture. ZZF-11 exhibits maximum sensitivity specifically to carbon monoxide (CO) and maintains almost negligible sensitivity to other gases as shown in Fig. 16 (b). This delineates the selective CO sensing characteristics of the sensor.

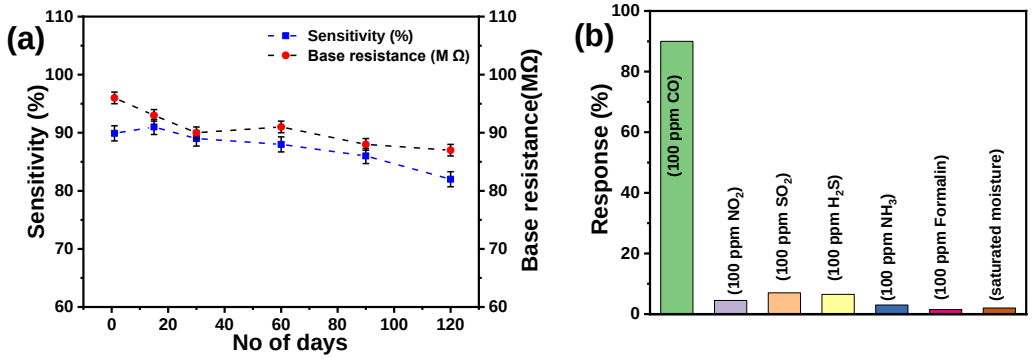

Fig. 7. 16. (a) Modulation of sensitivity and base resistance of ZZF-11 sensor over the time period of 120 days, (b) Selectivity curve of ZZF-11 sensor over other interfering gases.

7.3.8 CO sensing mechanism

Metal oxide semiconductor based chemiresistive sensor works based on the principal of surface charge model, where at ambient environmental oxygen molecules are preabsorbed on the MOS surface and capture electrons from the conduction band of the sensing material and transformed into ionized oxygen species. Out of Which a thick electron depletion region is formed and bases resistance got increased. When carbon mono oxide is parched on the sensor, surface absorbed O^{2-} ions reacts with CO molecules to create CO_2 and free electrons. These electrons come back to the conduction band of the active sensing material and reduces the resistance of the sensor as given in the following equations,

O_2 (g) $\rightarrow O_2$ (ads) …….... (7.1)

O_2 (ads) + $e^- \rightarrow O^{2-}$ (ads)……...(7.2)

CO + (1/2) O^{2-}(ads) $\rightarrow CO_2 + e^-$ …..(7.3)

Entire CO sensing procedure is schematically shown in Fig. 7. 17. Formation of heterojunction significantly changes the interfacial electronic band structure which enhances the gas adsorption ability and finally gas sensing response of the heterostructure sensors increases substantially. A detailed discussion of how heterojunction creation enhances the sensing response is discussed later.

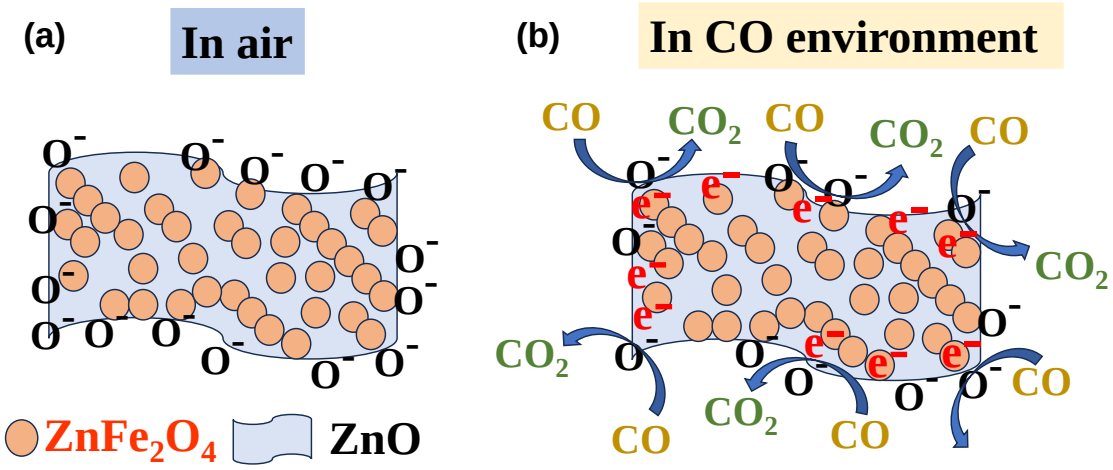

Fig. 7. 17. Schematic of the CO sensing mechanism of ZZF-11.

A possible charge transfer mechanism has been visualized and presented in Fig. 7. 18 (a) on the basis of calculated CB and VB edges positions of ZFO and ZnO. It is well observed that the band positions of two materials supports to form *n-n* type heterostructure because of both the bare semiconductors are n type in nature which also supported by MS plot. Photoelectrochemical response implies photoinduced electron-hole pair generation, separation and free charge carrier migration mechanism within ZFO-ZnO n–n heterojunction. [35]As both ZFO and ZnO exhibit n-type conductivity, the fermi level (E_f) of these semiconductors lies near the CB, marked by dark red dotted line. Potential of CB minima (CBM) for both ZFO and ZnO has negative value and ZFO has higher potential energy compared to ZnO so electrons will transfer from CBM of ZFO to CBM of ZnO. Hence, the upward and downward band bending occurs which creates space charge layer with certain capacitance generate internal potential gradient to oppose the charge migration. After light irradiation, fast generated electrons are gone through the bending CB with the help of the induced electric field at the interface of the composites. Hence, n-n heterojunction may boost charge separation and migration which effectively restrict electron-hole recombination that helps to enhance gas sensing performance.

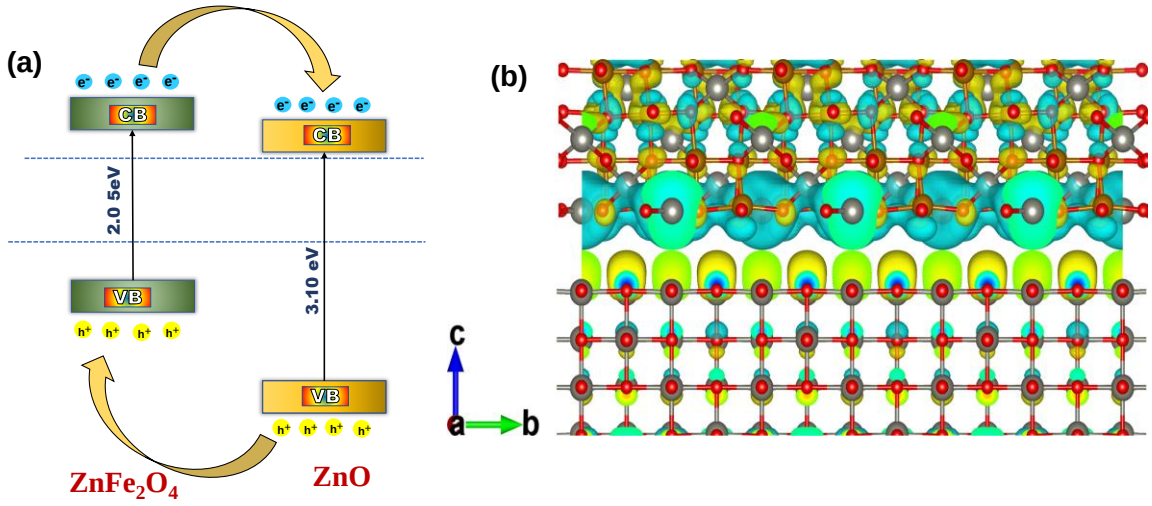

Fig. 7. 18. (a) Schematic presentation of band diagram of ZFO/ZnO heterostructure. (b) 3D picture of the differential charge density of the ZFO/ZnO interface, where the yellow and blue areas denote the gain and the loss of electrons, respectively, with the isosurface value of 0.4253 e/Å^3

The heterostructure is further investigated by plotting the planar-averaged charge density difference along the slab direction Z as shown in the Fig. 7. 18 (b). It shows that the electrons are mainly accumulated on the bottom layer of the ZnO surface, while ZFO layer acts as an electron donor. It implements that electrons are transferred from the ZFO to the ZnO surface. The quasi-direct suitable band gaps and more dispersive nature of the conduction band edges make the heterostructure a favourable material for exhibiting enhance sensing activity. For understanding of the synergistic effect of heterostructure formation in enhancing CO sensing performance, the adsorption effect of CO adsorption on ZnO, ZFO and ZZF-11 samples were evaluated through DFT. Adsorption energies (E_{ad}) of CO on ZnO, ZFO, and ZFO-11 were found to be -0.30 eV, -0.49 eV, and -0.73 eV, respectively. Calculated E_{ad} values established that the adsorption capacity of the heterostructure material for CO gas significantly increases (ref. Fig. 7. 19 (a-c)). Hence, the sensing performance also remarkably improvises for the ZZF-11 sample.

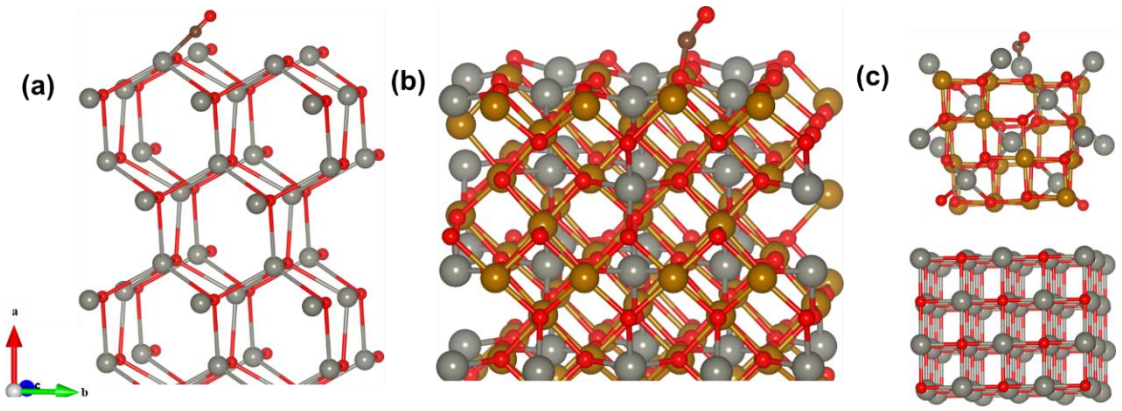

Fig. 7. 19. Adsorption of CO on (a) ZnO. (b) ZFO. (c) ZZF-11 in a favorable configuration.

In addition to the interfacial charge transfer mechanism, various intrinsic properties of the heterostructure material collectively contribute to making ZZF-11 the most effective CO sensor. The BET surface area study indicates a substantial increase in the surface area of the composite samples. ZZF-11 demonstrates the largest surface area among all compositions, as illustrated in Fig. 7. 10 (c). A larger specific surface area provides more active sites for catalytic reactions, enhancing its effectiveness as a catalyst. The elevated surface area induces a greater number of surface reactions, thereby playing a significant role in demonstrating the highest sensing response. Detail XPS analysis indicates that ferric bivalency emerged when the heterostructure contact between the spherical zinc ferrite particles and ZnO sheet started to form. In the pure ZFO sample, the majority of iron atoms predominantly exist in the Fe^{3+} oxidation state, characterized by the electronic configuration $1s^2\ 2s^2\ 2p^6\ 3s^2\ 3p^6\ 3d^5$. However, during the formation of the heterojunction, a notable phenomenon occurs wherein a portion of electrons gets trapped by diverse defect sites on the zinc oxide nanoparticle. Consequently, this electron trapping leads to the conversion of some Fe^{3+} ions into Fe^{2+}. The elevated level of charge imbalance contributes to an enhanced charge mobility in the ZZF-11 sample when compared to the pristine samples (ref. Fig. 7. 8 (a-d)). Further these imbalances in the iron oxidation states induces more oxygen defect states in the composite samples. Detail XPS O1s spectra analysis showed that amount of oxygen defect increases monotonically and become maximum for the ZZF-11 sample (ref. Fig. 7. 9 (a-e)). The Electron Paramagnetic Resonance (EPR) spectra of both the pure and composite samples demonstrate that the oxygen vacancy reaches its maximum in the ZZF-11 sample (ref. Fig. 7. 9 (f)). Oxygen vacancies create substantial defect states within the bandgap which promote more electrons across the conduction band of the samples which also shift the fermi level towards the conduction band.

Furthermore, active sites are generated due to higher oxygen vacancy content which stabilize the reaction intermediates.[36,37] Collectively, these factors contribute to the modification of the electronic properties of the ZZF-11 sample, enabling novel functionalities. This modification plays a crucial role in enhancing CO sensing.

7.4 Conclusion

In summary, a n-n type heterojunction of ZnO-ZFO was synthesized by sol-gel assisted reflux method. ZZF-11 sensor showed highest response to CO gas. Experimental and theoretical analyses reveal that the ZZF-11 heterojunction interface exhibits the largest specific surface area, along with the highest concentration of ferric balance states and oxygen defect states. Additionally, this interface also demonstrates a maximized content of donor defects within the same sample. PL studies indicate that the heterostructure enhances the separation of charge carriers. Further the DFT analysis indicates that adsorption energy of CO becomes least for the ZnO-ZFO composite sample in comparison with the pure ZnO or pure ZFO based sensor. This study presents a unified approach to for fabricating a highly sensitive and selective CO sensor for environment monitoring through heterostructure formation.

7.5 Reference

[1] Y. Bing, Y. Zeng, S. Feng, L. Qiao, Y. Wang, W. Zheng, Multistep assembly of Au-loaded SnO2 hollow multilayered nanosheets for high-performance CO detection, Sens Actuators B Chem 227 (2016) 362–372. https://doi.org/10.1016/j.snb.2015.12.065.

[2] M. Tonezzer, L.T.T. Dang, H.Q. Tran, S. Iannotta, Multiselective visual gas sensor using nickel oxide nanowires as chemiresistor, Sens Actuators B Chem 255 (2018) 2785–2793. https://doi.org/10.1016/j.snb.2017.09.094.

[3] K. Wetchakun, T. Samerjai, N. Tamaekong, C. Liewhiran, C. Siriwong, V. Kruefu, A. Wisitsoraat, A. Tuantranont, S. Phanichphant, Semiconducting metal oxides as sensors for environmentally hazardous gases, Sens Actuators B Chem 160 (2011) 580–591. https://doi.org/10.1016/j.snb.2011.08.032.

[4] S. Mahajan, S. Jagtap, Metal-oxide semiconductors for carbon monoxide (CO) gas sensing: A review, Appl Mater Today 18 (2020) 100483. https://doi.org/10.1016/j.apmt.2019.100483.

[5] Y. Zeng, L. Qiao, Y. Bing, M. Wen, B. Zou, W. Zheng, T. Zhang, G. Zou, Development of microstructure CO sensor based on hierarchically porous ZnO nanosheet thin films, Sens Actuators B Chem 173 (2012) 897–902. https://doi.org/10.1016/j.snb.2012.05.090.

[6] M.T. Vijjapu, S.G. Surya, S. Yuvaraja, X. Zhang, H.N. Alshareef, K.N. Salama, Fully Integrated Indium Gallium Zinc Oxide NO_2 Gas Detector, ACS Sens 5 (2020) 984–993. https://doi.org/10.1021/acssensors.9b02318.

[7] B. Jiang, J. Lu, W. Han, Y. Sun, Y. Wang, P. Cheng, H. Zhang, C. Wang, G. Lu, Hierarchical mesoporous zinc oxide microspheres for ethanol gas sensor, Sens Actuators B Chem 357 (2022) 131333. https://doi.org/10.1016/j.snb.2021.131333.

[8] S. Jaballah, M. Benamara, H. Dahman, D. Lahem, M. Debliquy, L. El Mir, Formaldehyde sensing characteristics of calcium-doped zinc oxide nanoparticles-based gas sensor, Journal of Materials Science: Materials in Electronics 31 (2020) 8230–8239. https://doi.org/10.1007/s10854-020-03358-y.

[9] Q.A. Drmosh, I. Olanrewaju Alade, M. Qamar, S. Akbar, Zinc Oxide-Based Acetone Gas Sensors for Breath Analysis: A Review, Chem Asian J 16 (2021) 1519–1538. https://doi.org/10.1002/asia.202100303.

[10] J. George, A. K.E., Gas sensing characteristics of magnesium ferrite and its doped variants, Physica B Condens Matter 610 (2021) 412958. https://doi.org/10.1016/j.physb.2021.412958.

[11] P.L. Mahapatra, S. Das, N.A. Keasberry, S.B. Ibrahim, D. Saha, Copper ferrite inverse spinel-based highly sensitive and selective chemiresistive gas sensor for the detection of formalin adulteration in fish, J Alloys Compd 960 (2023) 170792. https://doi.org/10.1016/j.jallcom.2023.170792.

[12] R.R. Powar, V.D. Phadtare, V.G. Parale, S. Pathak, K.R. Sanadi, H.-H. Park, D.R. Patil, P.B. Piste, D.N. Zambare, Effect of zinc substitution on magnesium ferrite nanoparticles: Structural, electrical, magnetic, and gas-sensing properties, Materials Science and Engineering: B 262 (2020) 114776. https://doi.org/10.1016/j.mseb.2020.114776.

[13] T. Ravikumar, L. Thirumalaisamy, S. Madanagurusamy, K. Sivaperuman, Substrate temperature dependent ammonia gas sensing performance of zinc ferrite thin films prepared by spray pyrolysis technique, J Alloys Compd 959 (2023) 170568. https://doi.org/10.1016/j.jallcom.2023.170568.

[14] A. Rezaeipour, S. Dehghani, S. Hoghoghifard, VOC Sensors Based on Nanoparticles and Nanorods of Nickel Ferrite, IEEE Sens J 22 (2022) 16464–16471. https://doi.org/10.1109/JSEN.2022.3188541.

[15] R. Kashyap, R. Kumar, S. Devi, M. Kumar, S. Tyagi, D. Kumar, Ammonia gas sensing performance of nickel ferrite nanoparticles, Mater Res Express 6 (2019) 125034. https://doi.org/10.1088/2053-1591/ab55b5.

[16] S. Mojumder, T. Das, S. Das, N. Chakraborty, D. Saha, M. Pal, Y and Al co-doped ZnO-nanopowder based ultrasensitive trace ethanol sensor: A potential breath analyzer for fatty liver disease and drunken driving detection, Sens Actuators B Chem 372 (2022) 132611. https://doi.org/10.1016/j.snb.2022.132611.

[17] T. Das, S. Mojumder, D. Saha, M. Pal, Enhanced ammonia sensing performance of barium hexaferrite enabled through Zn doping: Mechanistic study considering modulation of Fe2+/Fe3+ ratio and oxygen vacancy, Sens Actuators B Chem 406 (2024) 135358. https://doi.org/10.1016/j.snb.2024.135358.

[18] S. Mojumder, T. Das, D. Saha, M. Pal, koHighly sensitive and selective chemiresistive temperature-dependent trace formalin sensor using hydrothermally grown hexagonal yttrium ferrite, Mater Chem Phys (2024) 129329. https://doi.org/10.1016/j.matchemphys.2024.129329.

[19] S. Mojumder, T. Das, M. Mukherjee, D. Saha, A. Datta, M. Pal, Development of highly sensitive and selective trace acetone sensor using perovskite yttrium ferrite: Mechanism, kinetics and phase dependence study, Chemical Engineering Journal 477 (2023) 146855. https://doi.org/10.1016/j.cej.2023.146855.

[20] S.L. Dudarev, G.A. Botton, S.Y. Savrasov, C.J. Humphreys, A.P. Sutton, Electron-energy-loss spectra and the structural stability of nickel oxide: An LSDA+U study, Phys Rev B 57 (1998) 1505–1509. https://doi.org/10.1103/PhysRevB.57.1505.

[21] J.B.L. Martins, J. Andrés, E. Longo, C.A. Taft, A theoretical study of (1010) and (0001) ZnO surfaces: molecular cluster model, basis set and effective core potential dependence, Journal of Molecular Structure: THEOCHEM 330 (1995) 301–306. https://doi.org/10.1016/0166-1280(94)03853-D.

[22] S.C. Abrahams, J.L. Bernstein, Remeasurement of the structure of hexagonal ZnO, Acta Crystallogr B 25 (1969) 1233–1236. https://doi.org/10.1107/S0567740869003876.

[23] S.A.S. Farias, E. Longo, R. Gargano, J.B.L. Martins, CO2 adsorption on polar surfaces of ZnO, J Mol Model 19 (2013) 2069–2078. https://doi.org/10.1007/s00894-012-1636-4.

[24] J.S. Gordijo, N.M. Rodrigues, J.B.L. Martins, CO_2 and CO Capture on the ZnO Surface: A GCMC and Electronic Structure Study, ACS Omega 8 (2023) 46830–46840. https://doi.org/10.1021/acsomega.3c06378.

[25] S. Furukawa, M. Endo, T. Komatsu, Bifunctional Catalytic System Effective for Oxidative Dehydrogenation of 1-Butene and *n* -Butane Using Pd-Based Intermetallic Compounds, ACS Catal 4 (2014) 3533–3542. https://doi.org/10.1021/cs500920p.

[26] H. Guo, A.C. Marschilok, K.J. Takeuchi, E.S. Takeuchi, P. Liu, Essential Role of Spinel $ZnFe_2O_4$ Surfaces during Lithiation, ACS Appl Mater Interfaces 10 (2018) 35623–35630. https://doi.org/10.1021/acsami.8b12869.

[27] S. Grimme, J. Antony, S. Ehrlich, H. Krieg, A consistent and accurate *ab initio* parametrization of density functional dispersion correction (DFT-D) for the 94 elements H-Pu, J Chem Phys 132 (2010). https://doi.org/10.1063/1.3382344.

[28] A. Manohar, C. Krishnamoorthi, K.C.B. Naidu, C. Pavithra, Dielectric, magnetic hyperthermia, and photocatalytic properties of ZnFe2O4 nanoparticles synthesized by solvothermal reflux method, Applied Physics A 125 (2019) 477. https://doi.org/10.1007/s00339-019-2760-0.

[29] E. Sarala, M. Madhukara Naik, M. Vinuth, Y. V. Rami Reddy, H.R. Sujatha, Green synthesis of Lawsonia inermis-mediated zinc ferrite nanoparticles for magnetic studies and anticancer activity

against breast cancer (MCF-7) cell lines, Journal of Materials Science: Materials in Electronics 31 (2020) 8589–8596. https://doi.org/10.1007/s10854-020-03394-8.

[30] S. Alamdari, M. Sasani Ghamsari, C. Lee, W. Han, H.-H. Park, M.J. Tafreshi, H. Afarideh, M.H.M. Ara, Preparation and Characterization of Zinc Oxide Nanoparticles Using Leaf Extract of Sambucus ebulus, Applied Sciences 10 (2020) 3620. https://doi.org/10.3390/app10103620.

[31] S. Yedurkar, C. Maurya, P. Mahanwar, Biosynthesis of Zinc Oxide Nanoparticles Using Ixora Coccinea Leaf Extract—A Green Approach, Open Journal of Synthesis Theory and Applications 05 (2016) 1–14. https://doi.org/10.4236/ojsta.2016.51001.

[32] L. Xue, E. Liang, J. Wang, Fabrication of magnetic ZnO/ZnFe2O4/diatomite composites: improved photocatalytic efficiency under visible light irradiation, Journal of Materials Science: Materials in Electronics 33 (2022) 1405–1424. https://doi.org/10.1007/s10854-021-07568-w.

[33] K. Davis, R. Yarbrough, M. Froeschle, J. White, H. Rathnayake, Band gap engineered zinc oxide nanostructures *via* a sol–gel synthesis of solvent driven shape-controlled crystal growth, RSC Adv 9 (2019) 14638–14648. https://doi.org/10.1039/C9RA02091H.

[34] M.A. Golsefidi, M. Abrodi, Z. Abbasi, A. Dashtbozorg, M.E. Rostami, M. Ebadi, Hydrothermal method for synthesizing ZnFe2O4 nanoparticles, photo-degradation of Rhodamine B by ZnFe2O4 and thermal stable PS-based nanocomposite, Journal of Materials Science: Materials in Electronics 27 (2016) 8654–8660. https://doi.org/10.1007/s10854-016-4886-6.

[35] S. Ghosh, S. Bera, A. Singh, S. Basu, R.N. Basu, Hierarchical Bi2WO6/BiFeWO6 n-n heterojunction as an efficient photocatalyst for water splitting under visible light, J Alloys Compd 919 (2022) 165700. https://doi.org/10.1016/j.jallcom.2022.165700.

[36] Md.S. Islam, J. Lee, S. Ganguli, A.K. Roy, Effect of oxygen vacancy and Si doping on the electrical properties of Ta2O5 in memristor characteristics, Sci Rep 13 (2023) 16656. https://doi.org/10.1038/s41598-023-43888-z.

[37] Z. Deng, J. Ji, M. Xing, J. Zhang, The role of oxygen defects in metal oxides for CO_2 reduction, Nanoscale Adv 2 (2020) 4986–4995. https://doi.org/10.1039/D0NA00535E.

CHAPTER-VIII

Conclusions and Future Perspectives

8.1 Conclusions

In this thesis, variety of pure, doped, and composite semiconductor metal oxides were synthesized, and different cost-effective, flexible, and highly sensitive chemiresistive gas sensors were developed utilizing them. The research primarily focuses on fabricating Taguchi-type chemiresistive sensors aimed at creating breath analyzers for health monitoring and gas sensors for environmental monitoring. A thorough literature review revealed that although numerous chemiresistive sensors based on metal oxides have been reported, they often suffer from limitations such as low sensitivity, poor selectivity, high operating temperatures, low detection limits, inadequate resolution between different gas concentrations, and long-term instability. To address these challenges, this thesis explores the synthesis of various metal oxides, including binary oxides, ferrites, and binary oxide-ferrite heterojunctions. Comprehensive material characterizations were performed using various sophisticated techniques.

Initially, binary metal oxide (ZnO) based gas sensors were synthesized. To improve the performance of these pure binary metal oxide sensors, different dopants were incorporated into the pure crystals. Subsequently, perovskite ferrites were explored as active sensing materials. Transition metal ions within the perovskite ferrite material ($YFeO_3$) were selected for their multiple valence states, efficient charge transport ability, abundant morphology, and porous structure. Overall, the sensing capabilities of perovskite showed significant improvement over the binary metal oxide-based sensors. Finally, a metal oxide heterostructure material (ZnO-$ZnFe_2O_4$) was synthesized due to its disparate energy band gaps and electronic structures, which facilitated enhanced charge separation and efficient charge transport. As a result, the gas sensing abilities of this heterostructure material were significantly improved. Along with the experimental result theoretical studies were performed in different stages of the thesis to explain the gas sensing mechanism more precisely.

The first chapter explores various gas sensing techniques and the diverse applications of gas sensors. It emphasizes the significant role of chemiresistive semiconducting metal oxide (SMO) based gas sensors in the field, highlighting their ease of fabrication, cost effectiveness, and user-friendliness. A comprehensive literature review of previously reported gas sensing materials is presented, detailing their advantages and limitations, which informed the selection of specific SMOs for this thesis. The second chapter provides a concise overview of different

material synthesis and characterization techniques. The third chapter details the development of a chemically synthesized aluminium (Al) and yttrium (Y) co-doped zinc oxide (ZnO) nanopowder-based ethanol sensor, designed for highly sensitive and selective exhaled breath analysis. The sensor, comprising 1 wt% Al and 5 wt% Y co-doped ZnO, exhibited a significant n-type response of 62.8% to 1 ppm ethanol, outstanding selectivity against other gases, rapid response and recovery times (0.77 s and 8.1 s, respectively), and long-term stability of at least 10 months. The enhanced sensitivity of the co-doped sensor is attributed to the high surface-to-volume ratio and dopant-induced point defects. Furthermore, the optimized sensor successfully differentiated between healthy breath and simulated breath with varying ethanol levels, proving its potential for applications in detecting drunken driving and fatty liver disease. In the fourth chapter, the development of a Li-doped ZnO nanoparticle-based ammonia sensor with a cauliflower-like morphology is presented. The sensor, with 5 wt% Li-doped ZnO (LZ-5), demonstrated the highest sensitivity, showing a 43% response to 1 ppm ammonia with rapid response and recovery times of 1.7 s and 17 s, respectively. This optimized sensor showed high selectivity for ammonia, resistance to moisture, and stability over six months. The enhanced performance is attributed to increased surface area, excess oxygen defects, and higher donor content. The ammonia sensing mechanism was further theoretically elucidated through density functional theory (DFT) calculations at the microscopic level. The sensor exhibited promising results for detecting ammonia in human exhaled breath, indicating its potential for monitoring kidney-related ailments. In the fifth chapter, a chemiresistive sensor based on hexagonal $YFeO_3$, highly sensitive and selective to formalin vapor, is reported. The sensor achieved a response of approximately 3.12 times for 1 ppm formalin at 240°C, with rapid response and recovery times of 2.3 s and 13.1 s, respectively. The enhanced sensing performance is attributed to factors such as higher surface area, bivalent iron states, oxygen defects, and small bandgap energy. In the sixth chapter, various sensors were developed using YFeO3 in different pure and mixed crystalline phases of perovskite YFeO3. Among these, the orthorhombic YFeO3 (YF-10) demonstrated the highest response, exhibiting a 7.9-fold increase in sensitivity to 0.5 ppm acetone, along with excellent repeatability, selectivity, and long-term stability. The enhanced sensitivity of orthorhombic YF-10 is attributed to its specific morphology, presence of oxygen vacancies, and ferric bivalency. The mechanism underlying the increased acetone sensitivity of orthorhombic YFeO3 on a microscopic scale was elucidated using DFT calculations across different phases. Additionally, the selectivity of the YF-10 sensor towards acetone was explained using the Eley-Rideal model. Simulated breath studies were also conducted with a

simulated breath sample to evaluate the sensor's potential as a non-invasive breath analyzer for diabetes detection.

Finally, in the seventh chapter, n-n type ZnO-ZnFe2O4 heterojunction-based sensors were fabricated. Among various combinations, the ZZF-11 sensor exhibited the highest response to CO gas. Experimental and theoretical analyses reveal that the ZZF-11 heterojunction interface possesses the largest specific surface area, the highest concentration of ferric states and oxygen defects, and a maximized content of donor defects. DFT analysis indicates that the ZnO-ZFO composite has the lowest CO adsorption energy compared to pure ZnO or ZFO sensors. This study highlights the advantages of heterostructure materials over pure semiconductor metal oxides.

Throughout this thesis, various novel sensors were developed, demonstrating superior performance compared to previously reported sensors in terms of sensitivity, selectivity, and response and recovery times. The enhancements in sensitivity were elucidated through advanced characterization techniques. In addition to experimental work, some studies incorporated density functional theory (DFT) to explore the gas sensing mechanism at the molecular level. In three studies (Chapters III, IV, VI) focused on VOC sensors for breath analysis, simulated breath studies were conducted alongside standard gas sensing experiments. These simulated studies underscore the practical applicability of the fabricated sensors.

8.2 Future Perspectives

In this section, I have classified the future aspects of my research into three distinct parts. While metal oxides have played a pivotal role in gas sensing over the past few decades, they still exhibit significant drawbacks such as poor sensitivity and selectivity. In this research, I have employed various techniques to enhance the sensing performance of semiconductor metal oxide (SMO) based sensors. However, a major limitation of this work is the high operating temperature required for optimal sensor performance. Recent research has explored the use of various carbon-based polymer materials in conjunction with pure semiconductor metal oxides (SMOs) to fabricate composite material-based sensors. Due to the presence of pi electrons in carbon-based polymer materials, these sensors demonstrate a sensing response at room temperature. However, a major drawback of these sensors is their lack of stability. Pure polymer-based sensors suffer from issues of repeatability and stability. Therefore, the primary objective moving forward will be to identify cutting-edge materials beyond SMOs that can

address the issue of high operating temperatures. Perovskite halide materials are relatively unexplored in the field of gas sensing. These materials possess long carrier diffusion lengths and efficient charge separation and transport properties, making them excellent candidates for catalysis. Additionally, their superior light absorption and light harvesting properties render them highly useful in optical studies. The combined effects of efficient charge transport, structural stability, and flexibility make perovskite halides promising materials for gas sensing applications as well. Metal-organic framework (MOF) based materials represent another promising, yet relatively unexplored, group of materials in the field of gas sensing. MOFs typically possess high surface areas and large pore sizes, providing ample opportunities for structural tailoring by incorporating various metal centres or functional groups within their porous frameworks. Consequently, the development of MOF-based sensors presents a significant potential future direction in gas sensing research.

There is significant potential for a deeper theoretical understanding of the gas sensing mechanism. Although my research has incorporated some theoretical insights, much more can be explored. Specifically, DFT studies can be employed to precisely identify the adsorption sites of gas molecules on the active sensing surface and to elucidate the nature of the chemical bonds between the gas molecules and the sensing material. Furthermore, DFT calculations can provide a detailed analysis of reaction pathways and the sensing mechanism at the molecular level. Additionally, DFT can accurately predict the selectivity of a sensor towards a specific gas, facilitating the selection of materials for targeted studies. Therefore, incorporating comprehensive DFT calculations in gas sensing research holds tremendous potential for developing more efficient sensors with enhanced sensitivity and selectivity.

Finally, a handheld device can be developed using Arduino-based microelectromechanical systems (MEMS) for real-time breath analysis, enabling the early and non-invasive detection of diseases. A clinical trial should be conducted using the fabricated sensor before it is commercialized as breath analyser.

Appendix I

List of publications

Thesis related publications

[1] **S. Mojumder**, T. Das, S. Das, N. Chakraborty, D. Saha, M. Pal, Y and Al co-doped ZnO-nanopowder based ultrasensitive trace ethanol sensor: A potential breath analyzer for fatty liver disease and drunken driving detection, Sens Actuators B Chem 372 (2022) 132611. https://doi.org/10.1016/j.snb.2022.132611.

[2] **S. Mojumder**, T. Das, M. Mukherjee, D. Saha, A. Datta, M. Pal, Development of highly sensitive and selective trace acetone sensor using perovskite yttrium ferrite: Mechanism, kinetics and phase dependence study, Chemical Engineering Journal 477 (2023) 146855. https://doi.org/10.1016/j.cej.2023.146855.

[3] **S. Mojumder**, T. Das, D. Saha, M. Pal, Highly sensitive and selective chemiresistive temperature-dependent trace formalin sensor using hydrothermally grown hexagonal yttrium ferrite, Mater Chem Phys 319 (2024) 129329. https://doi.org/10.1016/j.matchemphys.2024.129329.

[4] **S. Mojumder**, T. Das, T. Mondal, S. Ghosh, D. Saha, C.K. Ghosh, M. Pal, Improved ammonia sensing performance achieved through defect modulation by Li doping in cauliflower-like ZnO for exhaled breath analysis towards renal diseases detection: An experimental venture supported by DFT calculation, TrAC Trends in Analytical Chemistry 180 (2024) 117896. https://doi.org/10.1016/j.trac.2024.117896.

[5] **S. Mojumder**, T. Das, S. Monga, D. Sarkar, S. Bhattacharya, S. Ghosh, M. Pal, Tuning of important parameters for enhanced CO sensing of Zinc Oxide-Zinc Ferrite based n-n type heterostructure: An experimental study supported by theoretical calculation. [Manuscript-Under Review]

Other published articles

[1] S. Das, **S. Mojumder**, D. Saha, M. Pal, Influence of major parameters on the sensing mechanism of semiconductor metal oxide based chemiresistive gas sensors: A review focused on personalized healthcare, Sens Actuators B Chem 352 (2022) 131066. https://doi.org/10.1016/j.snb.2021.131066.

[2] T. Das, **S. Mojumder**, S. Chakraborty, D. Saha, M. Pal, Beneficial effect of Sn doping on bismuth ferrite nanoparticle-based sensor for enhanced and highly selective detection of trace formaldehyde, Appl Surf Sci 602 (2022) 154340. https://doi.org/10.1016/j.apsusc.2022.154340.

[3] T. Das, **S. Mojumder**, D. Saha, M. Pal, Enhanced ammonia sensing performance of barium hexaferrite enabled through Zn doping: Mechanistic study considering modulation of Fe^{2+}/Fe^{3+} ratio and oxygen vacancy, Sens Actuators B Chem 406 (2024) 135358. https://doi.org/10.1016/j.snb.2024.135358.

[4] N. Chakraborty, A. Ghosh, **S. Mojumder**, A.K. Mishra, S. Mondal, Selectively activated suppressed quantum networks in self-assembled single atom-Ag catalyst-based room temperature sensors for health monitoring, J Mater Chem A Mater (2024). https://doi.org/10.1039/D4TA01888E.

[5] T. Das, **S. Mojumder**, D. Sarkar, S. Ghosh, M. Pal, Multifunctional n-n Type α-MoO_3/$BiFeO_3$ Heterostructures for Enhanced Charge Transfer Induced Photocatalytic Water Splitting and H_2S Gas Sensing. [Manuscript- Under Review]

[6] S. Dash, **S. Mojumder**, T. Das, D. Saha, M. Pal, Highly sensitive and selective rGO-$LaFeO_3$ nanocomposite based formaldehyde sensors towards air quality monitoring. [Manuscript- Under Review]

Appendix II

List of Conference attended

[1] 2ND Indian Materials Conclave and 31st AGM of MRSI, February 2020, MRSI Kolkata chapter, India.

[2] International Symposium on Materials of the Millennium: Emerging Trends and Future Prospects (MMETFP-2021), November 2021, Gandhinagar, Gujarat, India. [Topic of the talk: highly sensitive and stable copper chromite ($CuCr_2O_4$) thick film-based trace ethanol sensor for analyzing exhaled human breath]

[3] 85th annual session of the Indian Ceramic Society, Indian Ceramic Society, December 2021, Karnataka Chapter, Bengaluru, Indian. [Topic of the talk: Zinc Chromite Ceramic Spinel Nanoparticle Based Trace Acetone Sensor]

[4] Young Scientist Colloquium, MRSI, Kolkata Chapter, 16th December 2022, CSIR-Central Glass and Ceramic Research Institute, Kolkata, Presented a poster.

[5] 3rd Symposium on "Sensors for Society" Jawaharlal Nehru University, New Delhi, 12 January, 2023, presented a talk.

[6] International Conference on Thin Films & Nanotechnology: Knowledge, Leadership, & Commercialization, July 6-8, 2023, Indian Institute of Technology Madras, India, presented a poster.

[7] Young Scientist Colloquium, MRSI, Kolkata Chapter, 1st December 2023, Jadavpur University, Presented a poster.

[8] 34th AGM of MRSI (December 12-15, 2023), Indian Institute of Technology (BHU) Varanasi, presented a poster.

[9] 67th DAE Solid State Physics Symposium, Bhabha Atomic Research Centre, Mumbai, December 2023, presented a paper.

[10] International Conference on Fundamental and Advanced Research in Chemistry 2024, (8-10 June, 2024), Indian Institute of Technology Mandi, presented a paper.